

Microfluidic investigation of dynamic surfactant rearrangement on water-oil interfaces during single droplet formation

by

IOANNIS KIRATZIS

A thesis submitted to the University of Birmingham for the degree of

DOCTOR OF PHILOSOPHY

College of Engineering and Physical Sciences

School of Chemical Engineering

University of Birmingham

UNIVERSITY OF
BIRMINGHAM

University of Birmingham Research Archive

e-theses repository

This unpublished thesis/dissertation is copyright of the author and/or third parties. The intellectual property rights of the author or third parties in respect of this work are as defined by The Copyright Designs and Patents Act 1988 or as modified by any successor legislation.

Any use made of information contained in this thesis/dissertation must be in accordance with that legislation and must be properly acknowledged. Further distribution or reproduction in any format is prohibited without the permission of the copyright holder.

Abstract

The formation of droplets within a continuous phase is most commonly referred to as dispersion and is a key process present in industry and nature. If the produced dispersion is stabilised then it is referred to as an emulsion. One method for the formation of emulsions involves the addition of surfactants that stabilise the interface to prevent drop coalescence. One of the challenges in emulsification is the competition between the rapid timescales of droplet break-up (interface formation) and surfactant mass transport. This suggests that emulsification might evolve under non-equilibrium conditions. This study investigates the dynamic aspects of emulsification using microfluidics, by studying the formation of an emulsion droplet by droplet in a range of capillary numbers from 10^{-4} to 10^{-1}.

The process of droplet formation was studied using a flow focusing microfluidic device, with a channel width of 200 μm, for a range of surfactant solutions using continuous phases with a range of viscosities. The emulsion droplets formed were found to decrease in size with an increase in the quantity of surfactant in the system, the continuous phase flow rate and the continuous phase viscosity. Notably it was shown that different solutions which possess the same equilibrium properties (e.g. solutions above the critical micelle concentration), produce droplets of different sizes suggesting that the dynamic (non-equilibrium) properties of the system dominate the governing physics. Finally, the satellite droplets formed from the liquid filaments between the primary drops increase in size with an increase in the surfactant concentration.

Emulsification was further investigated by examining the thinning rate of the liquid filament connecting the expanding droplet to the bulk of the dispersed phase. In all cases the thinning rate follows two stages: initially, the thinning rate is slow and the surfactant solutions exhibit a thinning behaviour which is different from a surfactant free fluid. As the break-up process advances the thinning rate increases and the solutions with surfactant concentrations below the

cmc exhibit a thinning behaviour similar to a surfactant free system. This presents more evidence that the droplet formation process evolves under non-equilibrium conditions when small quantities of surfactants are present and the process diverts from equilibrium as it reaches its final stages.

Furthermore, the flow fields in the dispersed phase were investigated during the droplet formation process using Ghost Particle Velocimetry (GPV), an optical velocimetry technique, with the aim of understanding how the presence of surfactant affects the local hydrodynamics. During the final stages of the break-up the presence of surfactant reduces fluid velocities. This suggests that inhomogeneities in surfactant concentration create gradients in surface tension causing interfacial (Marangoni) stresses which act in the opposite direction to the prevailing flow field. However, during the initial stages of droplet formation the presence of surfactants allows for higher fluid velocities that increase the fluid recirculation. The above results showed the impact of the presence of surfactant on the hydrodynamics of the dispersed phase during droplet formation.

This study contributes to the knowledge of how the mass transport of surfactant influences the hydrodynamics and interfacial behaviour over the short timescales of emulsification. It was demonstrated that when the surfactant quantities are small the systems display properties closer to a surfactant free system and the presence of Marangoni phenomena in the last stages of the process act against droplet formation. These interfacial stresses act to oppose the prevailing flow field.

Acknowledgements

I would like to thank my academic supervisors, Dr. Daniele Vigolo and Prof. Mark Simmons, for giving me the opportunity to work with them and providing me with their guidance and experience. I also would like to thank Dr. Nina Kovalchuk for her valuable experience and time she dedicated in assisting me. Their mentoring and great knowledge helped me stay on the right course and not lose hope. I would also like to thank Dr. Federico Alberini, Dr. Andy Ingram, Dr. Alessio Alexiadis and Dr. Tom Mills for their contributions, whether material or verbal. Many thanks to the Engineering and Physical Sciences Research Council for founding this work. Lastly, many thanks go to the administrative and technical staff in the School of Chemical Engineering that helped me every time there was an issue.

I would also like to thank my friends and co-workers for standing by me and providing much needed companionship and memories to cherish. More specifically I would like to thank Alberto Almena and Alexandros Kosmidis for their friendship and willingness to abandon work and have a coffee every time I desired it.

I would also like to thank my partner, Ana, for sticking with me during the hardest part of a PhD, the writing stage. Her determination and discipline helped me complete this work.

I would also like to thank my family for supporting my decision in pursuing research. My parents for being examples of hard work, intelligence and integrity and my sister for being a wonderful friend.

Contents

Chapter 1: Introduction 1

1.1. Aims and objectives 2

1.2. Thesis outline 4

1.3. Publication and presentations arising from this work 4

Chapter 2: Review of the Literature 6

Introduction 6

2.1. Emulsions 6

2.2. Surfactants and surface/interfacial tension measuring techniques 9

2.2.1. Surfactants and surface/interfacial tension 9

2.2.2. Surface and interfacial tension measurements techniques 12

2.3. Microfluidic droplet formation 15

2.4. PDMS microfluidics 23

2.5. The presence of surfactants 26

2.5.1. Surfactant mass transport timescales 27

2.5.2. Surface tension driven flows 29

2.5.3. The effect of dynamic surface tension on droplet formation 30

2.5.4. Droplet break-up inside a continuous phase 34

2.6. Velocimetry studies 37

2.7. Summary 46

Chapter 3: Materials and Methods 48

Introduction 48

3.1. Materials 48

3.1.1. Fluids 48

3.1.2. Solution preparation 49

3.2. Methods 50

3.2.1. Equilibrium interfacial tension 50

3.2.2. Dynamic surface tension 51

3.2.3. Microfluidic device fabrication 52

3.2.4. Droplet formation experiments 54

3.2.5. Ghost Particle Velocimetry experiments 57

Chapter 4: Microfluidic droplet formation with the presence of surfactant 64

Introduction 64

4.1. Equilibrium interfacial tension of various surfactant solutions and surfactant parameters 64

4.2. Droplet sizes in the presence of surfactants 70

4.2.1. Systems with surfactant 73
4.3. Droplet sizes modelling 87
4.4. Satellite droplets 89
4.5. Conclusions 94
Chapter 5: Kinetics of the thinning neck 97
Introduction 97
5.1. Kinetics of the thinning neck of surfactant free solutions 97
5.2. Kinetics of the thinning neck of surfactant solutions 100
5.3. Neck kinetics and thinning rate of a higher viscosity dispersed phase 109
5.4. Conclusions 113
Chapter 6: Local hydrodynamic phenomena during droplet formation: velocity fields and interfacial topology 116
Introduction 116
6.1. 2-D velocity field during necking for a surfactant free system 116
6.2. 2-D velocity field during necking for systems with surfactant 119
6.3. Examination of the neck shape during the necking stage and self-similarity 128
6.4. GPV study of the droplet expansion 133
6.5. Conclusions 139
Chapter 7: Conclusions and future work 142
7.1 Conclusions 142
7.1.1. Conclusions regarding droplet sizes 142
7.1.2. Conclusions regarding the neck kinetics 143
7.1.3 Conclusions regarding the velocity fields 146
7.1.4. Conclusion regarding the self-similarity of the neck 148
7.2. Future work 149
Appendix: Encapsulation of hydroxyapatite microparticles in a solid and impermeable shell using microfluidics 152
A.1. Introduction 152
A.2. Aims and objectives 152
A.3. Literature review 152
A.4. Materials and methods 156
A.4.1. Microfluidic devices 156
A.4.2. Hydroxyapatite micro particles 157
A.4.3. Droplet formation and encapsulation 158
A.4.5. UV fluorescence 159
A.5. Results 160

A.6. Conclusions and future work 164
8. References 166

List of Figures

Figure 2.1 Schematic representation of the drag force and surface tension force during necking. Figure adapted from (Roumpea et al., 2019) 8
Figure 2.2 Schematic of a surface tension isotherm. Adopted from (Hsu et al., 2000) 10
Figure 2.3 Schematic representation of Rayleigh-Benard convection. Figure adapted from the Nonlinear physics group website in the University of Toronto (University of Toronto). 16
Figure 2.4 Illustrations of the most common geometries used in droplet microfluidics. a: Co-flow. b: Cross-flow. c: Flow-focusing. Figure adapted from (Christopher and Anna, 2007). Q_c and Q_d are the continuous and dispersed phase flows rates respectively. W_o is the width of the outlet channel. W_c and W_d are the sizes of the continuous and dispersed phase channels respectively. W_{or} in panel c is the size of the orifice while H is the distance between the dispersed phase channel and the orifice. 18
Figure 2.5 Droplet formation in a T-junction. Image adapted from (Glawdel et al., 2012a). The red arrow denotes the fluid flow while time moves from left to write. 19
Figure 2.6 Droplet formation instances in a flow focusing microfluidic device. image adapted from (Garstecki et al., 2005) 20
Figure 2.7 Flow regimes in a cross flow microfluidic device. a: Threading. b: Jetting. c: Dripping. e: Displacement. Figure adapted from (Cubaud and Mason, 2008). 21
Figure 2.8 Droplet formation under dripping. Figure adapted from (Cubaud and Mason, 2008). 22
Figure 2.9 The liquid bridge, or neck, at different instances before droplet pinch-off (Roché et al., 2009). 30
Figure 2.10 Kinetics of the thinning neck towards pinch-off. Upper inset is the final instances of the thinning. Lower inset is interfacial tension versus time. Figure adopted from (de Saint Vincent et al., 2012). 32
Figure 2.11 Schematic demonstration of cross-correlation of subsequent images. Image adapted from (Wieneke, 2017) 40
Figure 2.12 Typical micro-PIV result. Image adapted from (Lindken et al., 2009) 41
Figure 2.13 a: Flow field inside the expanding droplet during droplet formation. b: Flow field inside a moving droplet. Figures adapted from (Pirbodaghi et al., 2015) 45
Figure 3.1 Schematic and snapshot of the microfluidic device used in this study 52
Figure 3.2 Schematic of photolithography representing the difference between a negative and a positive photoresist. Adapted from the PhD thesis of Dr. Zoe Schofield by her permission. 53
Figure 3.3 a: Soft lithography steps. a: PDMS on top of silicon wafer. b: detachment of solid PDMS from silicon wafer. c: PDMS attached to a glass slide 54
Figure 3.4 Diagram of the experimental set-up. Figure adapted from (Riccomi et al., 2018) 55
Figure 3.5 Typical droplet sizing instant. 56
Figure 3.6 Typical neck diameter sizing instant 57
Figure 3.7 a. Initial image stack (video) of multiple droplet formation events. b. Separation of the droplet formation events in individual image stacks and median subtraction. c. Each stack is analysed separately and the velocity profiles on the upper(U) and lower(L) interface are extracted. d. the velocity profiles extracted from each droplet formation event are averaged. 59
Figure 3.8 Example of image processing. From left to right, original video capture, intensity median over 1000 frames, median subtracted. 59
Figure 3.9 Manual masking example using PIVLab. The highlighted red square represents the software functions that allow the masking. 60

Figure 3.10 Setting the PIV interrogation area using PIVLab. The highlighted area represents the software input fields. 60
Figure 3.11 Vector validation step using PIVLab. The red rectangle represents the software functions allowing for the vector validation. Vectors outside the black rectangle are discarded. 61
Figure 3.12 Illustration of the extraction of the velocities along the interface. The red rectangle demonstrates the functions allowing this operation. The inset is the velocity magnitudes along the length of the line. 62
Figure 4.1 Equilibrium interfacial tensions for the solution used in the study. a:(Kovalchuk et al., 2018c) 65
Figure 4.2 Dynamic surface tension for C10TAB and C12TAB solutions. Full circles are the dyed solutions, squares are the solutions with nanoparticles. 68
Figure 4.3 Droplet formation in a flow-focusing microfluidic device. (a) and (b) expansion, (c) necking, (d) pinch-off. 70
Figure 4.4 Droplet sizes for a 52% w/w glycerol-D.I. solution in various silicone oils 72
Figure 4.5 Droplet sizes for a 52% w/w glycerol-D.I. water with various surfactant concentrations .. 74
Figure 4.6 Timescales associated with the replenishment of surfactant on the interface for C10TAB solutions in 4.6 mPa s silicone oil for various flow rate ratios. 75
Figure 4.7 Timescales associated with the replenishment of surfactant on the interface for C10TAB solutions in 19 mPa s silicone oil. 77
Figure 4.8 Timescales associated with the replenishment of surfactant on the interface for C10TAB solutions in 96 mPa s silicone oil. 78
Figure 4.9 Droplet sizes for a 52% w/w glycerol-water with various surfactant concentrations. 79
Figure 4.10 Timescales associated with the replenishment of surfactant on the interface for C12TAB solutions in 4.6 mPa s silicone oil. 80
Figure 4.11 Timescales associated with the replenishment of surfactant on the interface for C12TAB solutions in 19 mPa s silicone oil. 81
Figure 4.12 Timescales associated with the replenishment of surfactant on the interface for C12TAB solutions in 96 mPa s silicone oil. 82
Figure 4.13 Droplet sizes for a 52% w/w glycerol-D.I. water with various surfactant concentrations 83
Figure 4.14 Timescales associated with the replenishment of surfactant on the interface for C16TAB solutions in 4.6 mPa s silicone oil. 84
Figure 4.15 Timescales associated with the replenishment of surfactant on the interface for C16TAB solutions in 19 mPa s silicone oil. 85
Figure 4.16 Timescales associated with the replenishment of surfactant on the interface for C16TAB solutions in 96 mPa s silicone oil. 86
Figure 4.17 Normalised droplet diameter vs a_2Ca_2 for three different continuous phase viscosities. ○:C10TAB, ◊:C16TAB, □:C12TAB. Shades of red: C12TAB, shades of green: C16TAB, Shades of blue: C10TAB. Segmented line is the scaling for d/h<2.5 for dripping from literature (Cubaud and Mason, 2008). 88
Figure 4.18 Celestial analogy of satellite droplet formation. left panel: 2 mM C16TAB in 96 mPa s silicone oil. Central panel: our solar system. Right panel: 2 mM C16TAB in 4.6 mPa s silicone oil. . 90
Figure 4.19 Satellite droplet diameters for various surfactant concentrations in 4.6 mPa s silicone oil. Vertical lines are the cmc values of the different surfactants. 90
Figure 4.20 Satellite droplet diameters for various surfactant concentrations in 19 mPa s silicone oil. Vertical lines are the cmc values of the different surfactants. 91
Figure 4.21 Satellite droplet diameters for various surfactant concentrations in 96 mPa s silicone oil. Vertical lines are the cmc values of the different surfactants. 92
Figure 4.22 Normalised satellite droplet sizes over the range of Capillary numbers studied. ○:C10TAB, ◊:C16TAB, □:C12TAB. Shades of red: C12TAB, shades of green: C16TAB, Shades of

blue: C10TAB. Solid black line is the model extracted. Dotted black lines are the prediction bounds. 94
Figure 5.1 Neck kinetics during necking for a solution without surfactant in three different continuous phase viscosities. 98
Figure 5.2 Neck kinetics during necking for C10TAB solutions in three different continuous phase viscosities. The arrow shows the increase in concentration. 101
Figure 5.3 Neck thinning rate for different C10TAB solutions in 4.6,19 and 96 mPa s silicone oil for instances close to the break-up. The black horizontal line is the slope of the surfactant free system while the red lines represent the error margins. The solid vertical line marks the cmc of the surfactant 102
Figure 5.4 Neck thinning rate for different C10TAB solutions in 4.6, 19 and 96 mPa s silicone oil for instances away from the break-up. The black horizontal line is the slope of the surfactant free system while the red lines represent the error margins. The solid vertical line marks the cmc of the surfactant 103
Figure 5.5 Neck kinetics during necking for C12TAB solutions in three different continuous phase viscosities 105
Figure 5.6 Neck thinning rate for different C12TAB solutions in 4.6, 19 and 96 mPa s silicone oil for instances close to the break-up. The black horizontal line is the slope of the surfactant free system while the red lines represent the error margins. The solid vertical line marks the cmc of the surfactant 105
Figure 5.7 Neck thinning rate for different C12TAB solutions in 4.6, 19, 96 mPa s silicone oil for instances away from break-up. The black horizontal line is the slope of the surfactant free system while the red lines represent the error margins. The solid vertical line marks the cmc of the surfactant 106
Figure 5.8 Thinning kinetics close to pinch-off for C10TAB solutions 108
Figure 5.9 Comparison between the measured and calculated interfacial tensions for C10 and C12TAB solutions in the final moments of the neck break-up. 109
Figure 5.10 Neck kinetics of 70 mPa s C10TAB concentrations. Continuous phase is 4.6 mPa s silicone oil 110
Figure 5.11 Neck thinning rate for instances away from the pinch-off for various 70 mPa s C10TAB solutions in three different continuous phases. Solid black line is the thinning rate of a surfactant free system while the red lines are the error margins. The vertical black lines mark the cmc of the surfactant. 111
Figure 5.12 Neck thinning rate instances close to the pinch-off for various 70 mPa s C10TAB in three diffrent continuous phases. Solid black line is the thinning rate of a surfactant free system while the red lines are the error margins. The vertical black lines mark the cmc of the surfactant. 112
Figure 6.1 Averaged total velocity fields during necking for a surfactant free system. Continuous phase is 4.6 mPa s silicone oil. Neck diameter is a: 100, b:80, c: 60 and d:40 μm. 117
Figure 6.2 Velocities along the interface during the necking stage for a surfactant free system in three different continuous phases. 118
Figure 6.3 Schematic representation of the neck where the velocity profiles are measured. The red line represents the length of the neck where the velocities are measured, where 0 is the start and 1 is end of neck. 119
Figure 6.4 Averaged total velocity fields during necking for a 2 mM C12TAB solution. Continuous phase is 4.6 mPa s silicone oil. Neck diameter is a: 100, b:80, c: 60 and d:40 μm. 121
Figure 6.5 Velocities along the interface during the necking stage of 2 mM C12TAB solution in three different continuous phases. 122
Figure 6.6 Maximum fluid velocity during necking for various solutions. Continuous phase is 4.6 mPa s silicone oil. 123

Figure 6.7 Velocity profiles along the interface of the thinning neck. Continuous phase is 4.6 mPa s silicone oil. a_{1-2}: 7.6 mM and 2 mM. b_{1-2}: 38.1 mM and 10 mM. 124
Figure 6.8 Maximum fluid velocity during necking for various solutions. Continuous phase is 19 mPa s silicone oil. 125
Figure 6.9 Velocity profiles along the interface of the thinning neck. Continuous phase is 19 mPa s silicone oil. a_{1-2}: 7.6 mM and 2 mM. b_{1-2}: 38.1 mM and 10 mM. 126
Figure 6.10 Maximum fluid velocity during necking for various solutions. Continuous phase is 96 mPa s silicone oil. 127
Figure 6.11 Velocity profiles along the interface of the thinning neck. Continuous phase is 96 mPa s silicone oil. a_{1-2}: 7.6 mM and 2 mM. b_{1-2}: 38.1 mM and 10 mM. 128
Figure 6.12 Rescaled thinning neck interface profiles for a surfactant free system in three different continuous phase viscosities 129
Figure 6.13 Rescaled thinning neck interface for various surfactant solutions in 4.6 mPa s continuous phase. a_{1-2}: 7.6 mM and 2 mM. b_{1-2}: 38.1 mM and 10 mM..... 130
Figure 6.14 Rescaled thinning neck interface for various surfactant solutions in 19 mPa s continuous phase. a_{1-2}: 7.6 mM and 2 mM. b_{1-2}: 38.1 mM and 10 mM..... 131
Figure 6.15 Rescaled interface profiles for 5 cmc surfactant solutions in three different continuous phases. a_{1-3}: neck diameter is 80 μm. b_{1-3}: neck diameter is 40 μm. 132
Figure 6.16 Expansion stage of a surfactant free system. Continuous phase is 4.6 mPa s silicone oil. a: 3 ms b: 7 ms. c:10 ms. d: 13 ms after the previous droplet pinch-off..... 133
Figure 6.17 Expansion stage of a surfactant free system. Continuous phase is 19 mPa s silicone oil. a: 3 ms b: 7 ms. c:10 ms. d: 13 ms after the previous droplet pinch-off..... 134
Figure 6.18 Expansion stage of a 38.1 mM C10TAB solution. Continuous phase is 4.6 mPa s silicone oil. a: 3 ms b: 7 ms. c:10 ms. d: 13 ms after the previous droplet pinch-off..... 135
Figure 6.19 Expansion stage of a 381 mM C10TAB solution. Continuous phase is 4.6 mPa s silicone oil. a: 3 ms b: 7 ms. c:10 ms after the previous droplet pinch-off 137
Figure 6.20 Expansion stage of a 38.1 mM C10TAB solution. Continuous phase is 19 mPa s silicone oil. a: 3 ms b: 7 ms. c:10 ms after the previous droplet pinch-off 138
Figure A.1 microfluidic devices used is this project. From top to bottom: straight, serpentine and double serpentine channels 156
Figure A.2 Schematic of experimental set-up..... 158
Figure A.3 Water droplet diameters using three different continuous phases 160
Figure A.4 NOA89 droplet sizes in three different continuous phases..... 161
Figure A.5 Residence times of NOA89 Droplets for various flow rate conditions 162
Figure A.6 Microparticle inside a liquid NOA89 droplet..... 163
Figure A.7 Fluorescent images of rhodamine-NOA89 solid capsules in various times after formation. a: 0 hours. b: 8 hours. c: 16 hours. d: 32 hours. 164

List of tables

Table 2.1 Dynamic surface and interfacial tension methods (Mucic et al., 2011). 15
Table 3.1 Physical properties of the fluids involved. a: (Kovalchuk et al., 2018c), b:(Sigma-Aldrich, 2020), c: (Sigma-Aldrich, 2017), d:(Merck, 2020i)..... 49
Table 3.2 Surfactant solutions used in this study..... 50
Table 4.1 Cmc in water and in a 52% wt. glycerol-water solution. a: (Kovalchuk et al., 2016), b:(Kovalchuk et al., 2018c), c: measured value..... 66
Table 4.2 Limiting adsorption and adsorption constants for the surfactants used in this study 67
Table 5.1 Thinning exponents for solutions without surfactant in three different continuous phase viscosities for time close and away from the pinch-off 100

Table 6.1 Equilibrium interfacial tension of the solution used 120

The search for truth is more important than the truth

-Gotthold Ephraim Lessing-

Chapter 1: Introduction

Droplet formation is a process present in nature, industry and everyday life, from the dispersions made while cooking, to high end cosmetic products and to the constant rain here in the UK. Nevertheless, such a simple and common process still holds many secrets. Emulsification can be defined as the formation of a kinetically or thermodynamically stable dispersion of droplets in a liquid continuous phase. One method enabling the production of an emulsion relies on the addition of a surface-active agent (surfactant) to stabilise the produced droplets and prevent coalescence. Providing kinetic energy to these components results in an emulsion. The emulsification process is complex as the timescales of droplet/interface formation are often of similar magnitude to the timescales associated with the surfactant mass transport. This gives rise to dynamic effects at the interface and a process that evolves under non-equilibrium conditions.

Microfluidics can be defined as the study of fluid flow in systems in which the behaviour differs from conventional systems due to the small length scales of the system (Nguyen and Wereley, 2006). The miniaturization of engineering components is not only found in fluid systems; more people are familiar with the miniaturisation of electronics systems which started in the early 1990's which, until recently, allowed for a doubling of the system's capacity every 18 months (Moore, 1980). The introduction of the term microfluidics, the study of phenomena in fluid based devices in submillimetre length scales, occurred in the late 1980's (Manz et al., 1990). Initially, microfluidic research mainly considered continuous flowing streams of completely miscible liquids. This was carried out in the context of minimisation of reactant volumes and process times (Weibel and Whitesides, 2006). Despite the advantages that these smaller scales offered, a number of problems were observed. For example, the boundary layers on the channel walls dominate the developing flow field, while the low Reynolds number allows for minimal

mixing of the components in the system (Haeberle and Zengerle, 2007, Ottino, 1990). This sparked the emergence of droplet microfluidics in order to segment the flow using droplets, or gas bubbles (Günther and Jensen, 2006). The mechanism behind droplet formation has been described by Garstecki et al. (Garstecki et al., 2005). The droplet formation process in a microfluidic device is a competition between the interfacial tension force that acts against droplet break-up and the drag force of the continuous phase that pulls the droplet downstream (Husny and Cooper-White, 2006). Due to the smaller length scales of microfluidics, body forces, such as gravity and inertia become less dominant, while, surface tension and viscosity become more important forces (Bruus, 2007).

Droplet based microfluidics have applications in cell cultures, biological macromolecules characterisation, DNA studies, chemical synthesis, nanoparticle fabrication and many more (Clausell-Tormos et al., 2008, Zheng et al., 2004, Agresti et al., 2010, Mashaghi et al., 2016). The applications are numerous and the ease of observation, due to advancements in camera and microscope technology the past years, allow for the study of a multitude of different systems. Microfluidics technology allows for constant engineering innovation which can be observed by the number of start-up companies developing microfluidics applications. The applicability of microfluidic systems on different fields coupled with the plethora of physical processes present drive the need for further study. Specifically, in the field of emulsification, the ability to completely describe the surfactant mass transport and better understand the underlying physics will lead to huge improvements in the field.

1.1. Aims and objectives

This project aims to better understand the surfactant mass transport during emulsification and visualise the fluid flows that rearrange the surfactant molecules along the interface of a forming droplet. Furthermore, it aims at increasing the knowledge on the break-up of liquid inside a

viscous continuous phase in timescales comparable to the timescales of industrial processes. Using a microfluidic platform, the emulsification process is isolated and studied drop by drop and the local flow field will be determined using Ghost Particle Velocimetry (GPV). GPV is a velocimetry technique that relies on cross-corelating the speckle pattern generated by the light scattering produced by flowing nanosized tracers in the sample fluid (Buzzaccaro et al., 2013). GPV has been established as a technique to investigate rapid microscale phenomena such as droplet formation or flows in microchannels (Pirbodaghi et al., 2015). This microfluidic platform will be used to better understand the surfactant mass transport on the water-oil interface during emulsification and how it affects droplet formation, shed light on the complex hydrodynamics of liquids jets and further advance the capabilities of GPV. Therefore, the aims and objectives of the study are:

1. Explore how the droplet formation process is affected by critical parameters including surfactant type and concentration, continuous and dispersed phase flow rate, and continuous phase viscosity.
2. Determine the relative importance of the timescales associated with the droplet formation process and the surfactant mass transport.
3. Examine the thinning rate of the neck under various conditions to determine the effects of the presence of surfactant.
4. Improve the knowledge on the local hydrodynamics of liquids jets by examining the local velocity field at timescales not yet accessed experimentally. More GPV will be used to determine the impact of the surfactant presence on the local hydrodynamics and visualise the effect of Marangoni phenomena

1.2. Thesis outline

The thesis is divided into 7 Chapters, with Chapter 1 being the introduction. Chapter 2 provides a review of the literature relevant to the research presented in this thesis, covering, microfluidics, multiphase flows, surfactants and velocimetry studies. Following this, Chapter 3 contains the materials and methods, where the material properties, the microfluidic device and the techniques used in the study are described. Chapter 4 is the first results chapter and details measurements of equilibrium interfacial tension and dynamic surface tension laying the foundations for the upcoming work. Droplet size distributions for different surfactant solutions over a range of conditions are presented and used to extract a mathematical model describing the system. Chapter 5, the second results chapter, focuses on the neck kinetics of the thinning neck during pinch-off for the various systems examined. These kinetics are used to extract information about the presence of surfactant during the necking stage. The final part of Chapter 5, examines the effect of the diffusion coefficient of the surfactant. The third and final result chapter, Chapter 6, describes velocimetry measurements made using GPV. This chapter details information on the local velocity field during the droplet formation process and presents an analysis of the shape of the interface of the thinning neck. The work concludes in Chapter 7 where the conclusions and the future work are presented. The thesis also contains an appendix describing the work carried out on the encapsulation of PEPT tracer particles using microfluidics.

1.3. Publication and presentations arising from this work

Conference papers and presentations

Kiratzis, I., Vigolo, D., Simmons, M.J.H. Microfluidic investigation of dynamic surfactant rearrangement at water-oil interfaces during single droplet formation, 71st Annual Meeting of the APS Division of Fluid Dynamics, Atlanta, Georgia, USA, 18-20 November 2018

Kiratzis, I., Kovalchuk, N.M., Simmons, M.J.H., Vigolo, D. Marangoni phenomena during droplet formation in microfluidics, 2019 AIChE Annual Meeting, Orlando, Florida, USA, 10-15 November 2019

Journal papers

Detachment mechanism for water-in-oil droplets in microfluidic flow-focusing devices in the presence of soluble surfactant. Leo Turnell-Ritson, Mehdi Jangi, **Ioannis Kiratzis**, Nina M. Kovalchuk, Daniele Vigolo. (in preparation)

Chapter 2: Review of the Literature

Introduction

The aim of this chapter is to provide a review of the current knowledge on microfluidic droplet formation and emulsification, the techniques used to investigate it and build the case for the motivation and aims for this study. This chapter begins by giving the basic information on emulsions and their preparation methods followed by a review of surface/interfacial tension. This is followed by droplet formation in microfluidics where the different microfluidic configurations for droplet formation are presented. Next the effect of the presence of surfactant on emulsification in microchannels is presented which is followed by a review on the velocimetry techniques used to examine physical systems.

2.1. Emulsions

Emulsions consist of two immiscible liquids with one phase being dispersed in the form of small droplets in the other (McClements, 2016). Emulsions are an example of a colloidal system, defined as a dispersion of two substances where one substance is finely and uniformly distributed in the other (Levine, 2007). In food applications for example the size of emulsion droplets ranges from 100 nm to 100 μm (McClements, 2016).

Many emulsion systems consist of an organic (oil) and an aqueous phase, though water-in-water two phase systems are also possible as a means of fat replacement to reduce the calorific value of food (Vis et al., 2015). An emulsion that contains oil droplets dispersed in an aqueous continuous phase is referred to as an oil-in-water (O/W) emulsion. The opposite is referred to as a water-in-oil emulsion (W/O). In addition to the above types of emulsions, it is possible to create multiple emulsions, for example oil-in-water-in-oil (O/W/O). Such emulsions are used

in the food industry for the gradual release of ingredients, or for the isolation of microorganism (McClements and Li, 2010, Kadri et al., 2016).

The process of forming an emulsion is referred to as emulsification. Apart from the two liquid phases, a surfactant, or surface-active agent, or stabiliser is added to the process. Surfactants are amphiphilic molecules that adsorb at the interface and provide kinetic stability against coalescence due to the presence of steric or electrostatic repulsion between droplets in a dispersion (Tadros, 2013). Surfactants can either be non-ionic or ionic. Ionic surfactants are those who carry a group of positive or negative charge (Toofan and Toofan, 2015). Surfactants that carry a negatively charged functional group on their head, are referred to as anionic while surfactants that carry a positively charged group are referred to as cationic (Porter, 2013).

Some of the methods for emulsion formation include homogenisers, high shear mixers and more recently microfluidics (Liu et al., 2020, McClements, 2016). In all cases, the device creates disturbances on the interface between the fluids forcing the formation of droplets (McCabe et al., 2005). In most industrial applications the emulsification process begins with an initial mixing of the two immiscible phases so that fairly large droplets of the dispersed phase are produced inside the continuous phase. The next stages of homogenization allow for the break-up of these larger droplets into smaller ones. The break-up of a droplet is determined by the balance between interfacial forces, that hold the droplet together, and the disruptive forces generated by the emulsification equipment. The break-up of the droplets happens due to high shear and pressure gradients (McClements, 2016).

Emulsification in microchannels happens one droplet at a time and the local flow fields that deform the interface are precisely controlled by the pumping equipment and the microfluidic channel geometry (Christopher and Anna, 2007). Emulsions offer the ability to enclose reactant species and act as vessels for carrying out reactions (Griffiths and Tawfik, 2006). Microfluidics offer the additional advantage of preventing sample dispersion and fouling of the channel walls

(Christopher and Anna, 2007). The ability to precisely control droplet volume allows for tuning of the stoichiometry of reactant species. Furthermore the velocities, sorting, coalescence and internal mixing of the droplets can be controlled allowing for the study of rapid time dependant phenomena (Ismagilov, 2003, Song et al., 2006).

In the case of microfluidics flow conditions are laminar and the break-up happens due to the interface experiencing normal and tangential stresses (Walstra, 1991). The disruptive force in this case is the drag force exerted on the dispersed phase by the continuous phase (Roumpea et al., 2019). This force acts in the flow direction and is described by

$$F_D = 4\pi\mu_c \frac{2n+3}{n+1} D_d(u_c - u_d) \tag{2.1}$$

Where μ_c is the continuous phase viscosity (Pa s), n is the viscosity ratio, D_d is the droplet diameter and $u_c - u_d$ (m s^{-1}) is the relative velocity between the continuous phase and the droplet velocity. The drag force acts against the interfacial tension force and is described by

$$F_\sigma = \gamma \left(\frac{1}{R} + \frac{2}{h}\right)\left(\pi \frac{W_d^w}{4}\right) \tag{2.2}$$

Where γ is interfacial tension (N m^{-1}), R is the leading-edge radius of the drop, h is the channel depth (m) and W_d is the neck width (m). Figure 2.1 displays the above force balance during droplet formation.

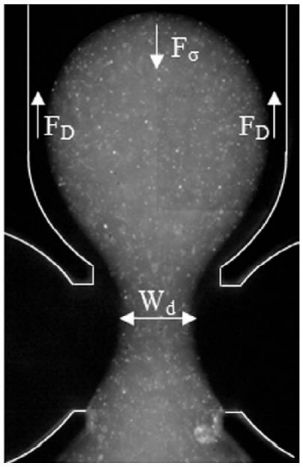


Figure 2.1 Schematic representation of the drag force and surface tension force during necking. Figure adapted from (Roumpea et al., 2019)

2.2. Surfactants and surface/interfacial tension measuring techniques

2.2.1. Surfactants and surface/interfacial tension

Surfactants are amphiphilic molecules, meaning they have hydrophobic and hydrophilic groups. Surfactant molecules are adsorbed on the interface and lower surface (or interfacial) tension on the medium they are dissolved (Nic et al., 2005). The first studies were carried out in the early 20th century (Frumkin and Gorodetzkaya, 1928, Szyszkowski, 1908). The first surfactants used were fatty acids and since the 1930´s sodium lauryl (dodecyl) sulfate became one of the most commonly used and studied surfactants (Mucic et al., 2011). Other important families of surfactants are the Alkyl trimethyl ammonium bromide (Cx-TAB), Polyethylene glycol tert-octylphenyl ethers (Tritons), Polyoxyethylenesorbitans (Tweens) and alkyl dimethyl phosphine oxides.

The addition of a surfactant leads to a reduction in surface (or interfacial) tension, which is the energy required to increase surface area or conversely, is the property of a liquid interface to resist deformation due to an external force (Nic et al., 2005). Fluid molecules feel mutual attraction. If a free surface of a liquid and a gas is considered, a molecule in the bulk of the liquid feels attraction from all directions while a molecule on the interface feels attraction from a reduced number of neighbours. This leaves the molecules on the interface in an energetically unfavourable position. Therefore, the creation of new interface is energetically costly, and this is the reason why fluids tend to minimise their surface areas. If the total cohesive energy a molecule feels is U, then a molecule on the interface will feel U/2. If the characteristic dimension of the molecule is R, then its characteristic surface area is R^2, then surface tension is proportional to $U/2R^2$. According to the above definition surface tension is energy per unit area which is equivalent to force per unit length. Surface tension increases as the cohesive energy increases and as the characteristic dimension of the molecules decreases (Israelachvili,

2011). For example the surface tension of water in air is 72 mN m^{-1} (DeGennes et al., 2002). The representation of surface tension as a function of surfactant concentration for a set and constant temperature is known as an isotherm. Figure 2.2 is a typical example of a surface tension isotherm.

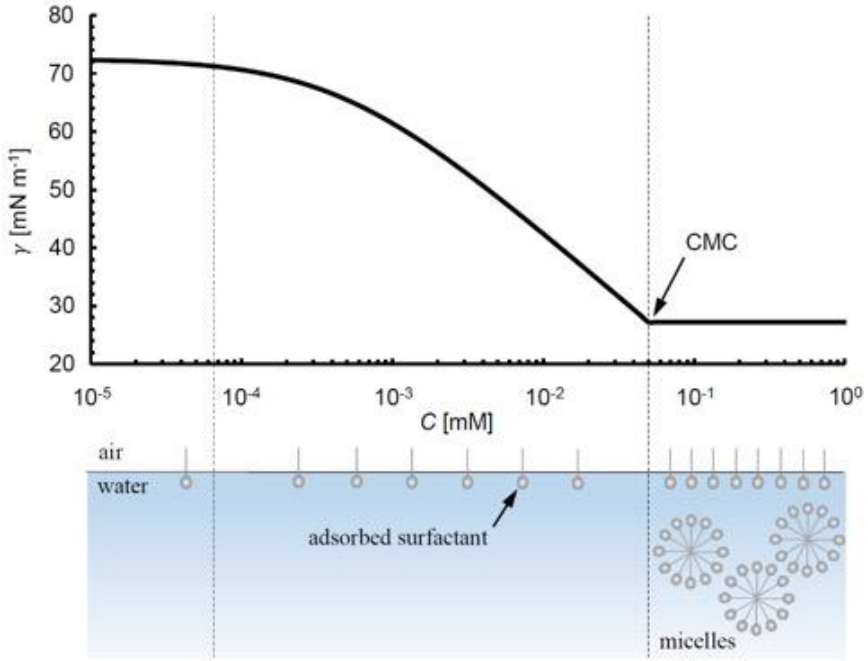


Figure 2.2 Schematic of a surface tension isotherm. Adopted from (Hsu et al., 2000)

The first notable aspect of the isotherm is that an initial increase of the surfactant concentration reduces surface tension. Beyond a critical concentration, the critical micellar concentration (cmc), the value of surface tension plateaus. The cmc denotes the concentration limit at which the additional quantity of surfactant will form aggregates in the bulk called micelles. The shape and structure of micelles depends on the nature of the surfactant and the solution. Micelles are not surface active and they do not get adsorbed on the interface, nevertheless they affect adsorption by being in equilibrium with surfactant monomers present in the system (Miller et al., 2008). Micelles can be spherical, ellipsoidal or cylindrical, while also bilayer configurations exist. The micelle shape is a function of concentration, surfactant molecular geometry and pH (Hamley, 2007).

The location of the isotherms on the horizontal axis can be used as a measure of the surfactant strength. For example, Hexanol requires large concentrations to produce significant differences in surface tension, meaning that in small concentrations, the presence of Hexanol will not produce any significant differences in surface tension. The range of concentrations that the isotherms span is characteristic for each surfactant. This range represents the molar area that the adsorbed molecules require. The smaller this area is the steeper is the curve (Mucic et al., 2011).

The first adsorption model was described by Langmuir (Langmuir, 1918). The adsorption isotherm for the Langmuir model is

$$\Gamma = \Gamma_{\infty} \frac{bc}{1+bc} \tag{2.3}$$

While the corresponding equation of state is

$$\gamma - \gamma_0 = RT\Gamma_{\infty} \ln (1 + bc) \tag{2.4}$$

Here, Γ is the adsorption (mol m^{-2}) which represents the amount of adsorbed species on an interface, b is the adsorption constant (m^3 mol^{-1}) which is the slope of the isotherm, c (mol m^{-3}) is the surfactant bulk concentration and Γ_{∞} is the maximum adsorption (mol m^{-2}), R is the ideal gas law constant and T is absolute temperature (K). The Langmuir model assumes that adsorption on a liquid interface is a similar chemical phenomenon as adsorption on a solid substrate (Langmuir, 1917).

An expansion of this model was described by Frumkin that also included the interaction between molecules at the adsorption layer improving the correlation between theory and experiments. In this case the equation of state and the isotherm are given by:

$$bc = \frac{\theta}{1-\theta} \exp(-2a\theta) \tag{2.5}$$

and

$$-\frac{\Pi\omega_0}{RT} = \ln(1-\theta) + a\theta^2 \tag{2.6}$$

Where α is a constant describing intermolecular interaction, θ is the surface coverage, defined as $\theta = \Gamma\omega$, and ω is the molar area (m^2) of the adsorbed molecule. Another extension of the above models is the reorientation model (Fainerman et al., 2009). The model assumes that some molecules change their orientation as they are adsorbed on the adsorption layer in order to reduce their molar area.

Different surfactants have different surface activities and therefore measurable differences in surface tension are expected only when a certain concentration is reached. The lower limit is dictated by the adsorption constant b. The upper concentration limit is the critical micelle concentration (Mucic et al., 2011). Surfactant can still be dissolved in the system but the excess in monomers present in the solution form micelles. Micelles are assembles formed by surfactant molecules after no more surfactant can be adsorbed on the interface (Menger, 1979). The critical micellar concentration is the concentration at which the surfactant stops being adsorbed on the interface and no more changes in surface tension are recorded. A micelle is a particle of colloidal dimension and is comprised of the surfactant molecules present in the solution (McNaught and Wilkinson, 1997).

2.2.2. Surface and interfacial tension measurements techniques

The main techniques used for measuring equilibrium surface tension are divided into two categories, force tensiometry and optical tensiometry. Force tensiometry utilises the force experienced by a probe from the interface. The main techniques used are the Du Nouy ring and the Wilhelmy plate (Mucic et al., 2011). These techniques can measure surface, or interfacial tension on the timescale of 1s to several hours (Mucic et al., 2011).

When using the Du Nouy ring method a platinum ring is submerged on the liquid and then pulled towards the interface. As the ring approaches the interface a meniscus is formed which pulls the ring towards the liquid. Before the rupture of the meniscus and the release of the ring the interface has exerted a maximum force which is used to measure surface tension (Du Noüy,

1919). Using the Wilhelmy plate method a plate is submerged into the liquid and the initial position is recorded. After that, the plate is fully submerged and then brought back to the initial position. The force exerted on the plate is measured and from that surface tension is measured (Neumann, 1979).

Optical methods rely on droplet or bubble profiles to measure surface tension and generally these techniques perform drop shape analysis. These techniques can be divided into pendant drop methods, where a droplet is formed at the tip of a capillary, sessile drops, where a droplet rests on a flat surface, and liquid bridge methods, where a droplet forms a bridge between two solid interfaces. Respectively these techniques measure surface, or interfacial tension successfully from 1s to several minutes (Mucic et al., 2011). The methods analyses the interface shape using the Young-Laplace equation (Finn, 1999).

$$\Delta P = -\sigma(\frac{1}{R_1} + \frac{1}{R_2}) \tag{2.7}$$

Where ΔP is the Laplace pressure, which describes the pressure difference between the interior of the droplet and its surrounding phase, σ is surface tension (N m^{-1}) and R_1 and R_2 are the principal radii of curvature. The pendant drop method can be used to measure interfacial tension as well. The above methods, both optical and force, can be used to measure dynamic surface tension or interfacial tension but the experimental timescales are above 1 s (Mucic et al., 2011).

In contrast to equilibrium surface (or interfacial) tension stands dynamic surface tension. The most common methods for determining dynamic surface tension are the maximum bubble pressure tensiometry, capillary pressure tensiometry, drop volume tensiometry, drop and bubble profile tensiometry and ring/plate tensionemetry (Mucic et al., 2011). These dynamic surface, or interfacial tension measuring techniques, allow access to very short timescales, from 10^{-1} ms to several seconds (Mucic et al., 2011).

Maximum bubble pressure tensiometry relies on the formation of a bubble at the tip of a capillary. The capillary is submerged in the solution intended for study. The method relies in measuring the maximum pressure that can be applied to a bubble at the tip of the capillary before it detaches (Schramm, 2006). The surface tension can be calculated from the measured maximum capillary pressure (Fainerman and Miller, 2004). In most experimental settings the equipment measures the bubble pressure for different bubble formation frequencies. The maximum pressure is then determined from the measured signal and from that the surface tension can be calculating using

$$P = {}^{2\sigma}/_{r_{cap}} + \Delta\rho g h + P_{dyn} \quad (2.8)$$

Where r_{cap} is the radius (m) of the capillary, $\Delta\rho$ is the difference in density (kg m^{-3}) between the solution and air, g is the gravitational acceleration (m s^{-2}), h is the immersion depth (m) and P_{dyn} represents the dynamic pressure contribution (Javadi et al., 2013).

Capillary pressure tensiometry relies on measuring the pressure difference across the interface of a forming drop at the tip of a capillary using a pressure transducer and monitoring the pressure shape using imaging. Using this data, the surface tension can be calculated using

$$\Delta P_{cap} = 2\sigma/R \quad (2.9)$$

Where σ is surface tension (N m^{-1}), ΔP_{cap} is the pressure difference (Pa) and R is the radius (m) of the bubble (Passerone et al., 1991).

Drop volume tensiometry is a method that can give dynamic interfacial tension information for liquid-liquid systems. It relies on measuring the volume of droplets detaching from a capillary of a given diameter. Using the density of the liquid and the diameter of the capillary the surface tension can be calculated (Tate and London, 1864). Table 2.1 summarises the above information.

Table 2.1 Dynamic surface and interfacial tension methods (Mucic et al., 2011).

Method	Time range	Liquid-gas	Liquid-liquid
Maximum bubble pressure tensiometry	$2x10^{-4}$ - 10^{2} s	X	-
Capillary pressure tensiometry	10^{-2} – 10^{3} s	X	X
Drop volume tensiometry	1 s – 30 mins	X	X
Drop and bubble profile tensiometry	1 s – to hours	X	X
Ring tensiometry, plate tensiometry	10 s to hours	X	X

2.3. Microfluidic droplet formation

Microfluidic droplet formation is an example of a phenomenon which occurs in systems that are under constant non-equilibrium conditions. These systems, in experimental and natural settings, produce spatial structures in steady state; microfluidic droplet formation is such a structure (Cross and Hohenberg, 1993). More generally fluid systems display a plethora of spatiotemporal formations. Some examples are the Rayleigh-Bénard convection, Taylor-Couette flow and Bénard-Marangoni convection. During Rayleigh-Bénard convection, a fluid is placed between two flat plates. The bottom plate is held at a temperature higher than the top plate. The fluid near the bottom plate heats up and due to thermal expansion, a difference in density arises between the lower and upper fluid layers. Since both fluids are in the same gravitational field the lighter fluid would move towards the top. This upwards fluid flow drives a downwards movement, due to mass conservation, and stable structures can arise (Gollub and Langer, 1999).

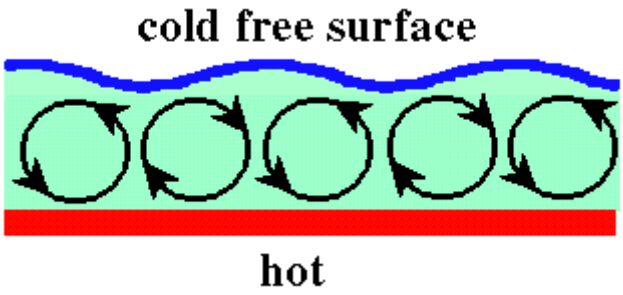


Figure 2.3 Schematic representation of Rayleigh-Benard convection. Figure adapted from the Nonlinear physics group website in the University of Toronto (University of Toronto).

In the case of the Bénard-Marangoni convection, the flow is caused due to a difference in surface tension. Surface tension at a constant temperature is a function of concentration. Solvent evaporation from a free surface may create concentration differences on the interface which translate to surface tension differences. Consequently, fluid motion is expected (Pearson, 1958). Due to mass conservation, fluid movement along the interface causes fluid from the bulk to move towards the interface. In the experiments carried out by Bénard in 1900 the surface patterns observed were hexagonal. The fluid motion created flow patterns in which it rose in the centre, moved towards the edges and fell along the sides of the cells (Bénard, 1900). These types of cells can also arise due to differences in concentration that give rise in differences in surface tension and can produce corrugated surfaces (Yiantsios et al., 2015). More specifically, in the context of drying thin films, the evaporation of the solvent leads to differences in surface tension along the interface of the film. These differences in surface tension drive Bénard-Marangoni convection that creates peaks and valleys on the interface. At the same time the evaporation of the solvent leads to an increase in the viscosity of the film which helps to freeze in place the corrugated surface (Yiantsios et al., 2015).

The common thread connecting these phenomena is instability. These complex patterns arise when systems are pushed into unstable states by very small perturbations. In such systems is possible to have steady spatial structures (Cross and Hohenberg, 1993). In fluid mechanics fluid motion is generally described by the Navier-Stokes equations. These non-linear partial

differential equations, having multiple steady solutions for a set of parameters, can give rise to a plethora of new steady states (Gollub and Langer, 1999). Droplet formation in microfluidics occurs as a steady solution to the Navier-Stokes equations.

Emulsification in microchannels is an efficient way to produce highly monodisperse emulsions. Microfluidics offer excellent control over the size and the frequency of the produced droplets due to the miniaturisation of the experimental scales (Anna, 2016). The most common microfluidic channel geometries used are co-flow geometries (Figure 2.4a), where two fluids move in parallel to each other, cross-flow junctions in which the continuous phase meets the dispersed phase perpendicularly at an intersection (Figure 2.4b), and flow-focusing (Figure 2.4c) where a constriction in the channel accelerates the fluids (Anna, 2016). In each case the dispersed phase is driven into a channel due to the action of a pump or a pressure controller creating a pressure difference between the inlet and outlet channel. The continuous phase is similarly driven into another channel. Droplets are formed where these two channels meet. The volumetric flow rate of the pumps and the geometry of the junction determine the flow field which is responsible for the deformation of the interface and ultimately the droplet formation (Anna, 2016). Under constant flow of the two liquid phases droplets form periodically at the intersection. Generally this process is a competition between local fluid stresses that seek to deform the interface and surface tension which resists the interface deformation (Christopher and Anna, 2007). There are no inherent advantages or disadvantages to a specific microfluidic channel geometry, the choice of microfluidic device depends on the materials used in applications and the available fabrication methods. For example, a co-flow microfluidic device can be chosen for example in a case where the produced droplets need to be as further away from the wall as possible (Christopher and Anna, 2007). In the case of this study a flow focusing channel geometry was chosen due to the ability to clearly observe the droplet formation process while the shearing forces that deform the growing droplet are symmetrical

in nature due to the geometry of the junction (Cubaud and Mason, 2008, Pirbodaghi et al., 2015).

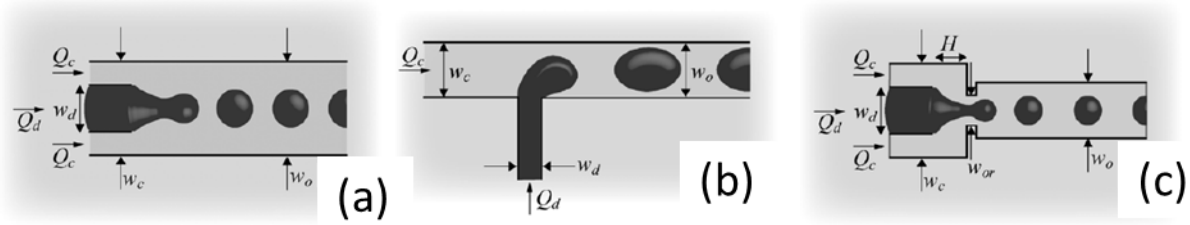


Figure 2.4 Illustrations of the most common geometries used in droplet microfluidics. a: Co-flow. b: Cross-flow. c: Flow-focusing. Figure adapted from (Christopher and Anna, 2007). Q_c and Q_d are the continuous and dispersed phase flows rates respectively. W_o is the width of the outlet channel. W_c and W_d are the sizes of the continuous and dispersed phase channels respectively. W_{or} in panel c is the size of the orifice while H is the distance between the dispersed phase channel and the orifice.

Co-flow geometries have been established to create droplets at a tip of a tapered capillary which is used to introduce the dispersed phase into the co-flowing continuous phase (Umbanhowar et al., 2000). Droplets grow spherically at the tip of the capillary and detach when they reach a critical size where the drag of the continuous phase surpasses interfacial tension. Through this method researchers were able to achieve monodispersities, higher than previous experimental methods. In most droplet formation microfluidics experiments droplet monodispersities are above 97% (Umbanhowar et al., 2000).

Cross-flow microfluidic droplet formation was first implemented by Thorsen and their colleagues in 2001. The researchers used a T-shaped microfluidic device with a depth of 6.5 μm and a width of 35 μm. They demonstrated that droplet sizes depend on the dispersed phase pressure and no droplets are formed if the pressures are significantly different. Initial studies focused on exploring the concept of droplet formation with this geometry and reported that the size of the droplets is controlled by the flow rates of the two phases used (Nisisako et al., 2002). Later, researchers were also able to divide the process in three stages, the lag stage, where the interface retracts after the previous break-up, the filling stage, where the expanding droplet starts invading the outlet channel, and a final stage, necking, where the filament connecting the

expanding droplet to the bulk of the dispersed phase thins and releases the droplet (Glawdel et al., 2012a).

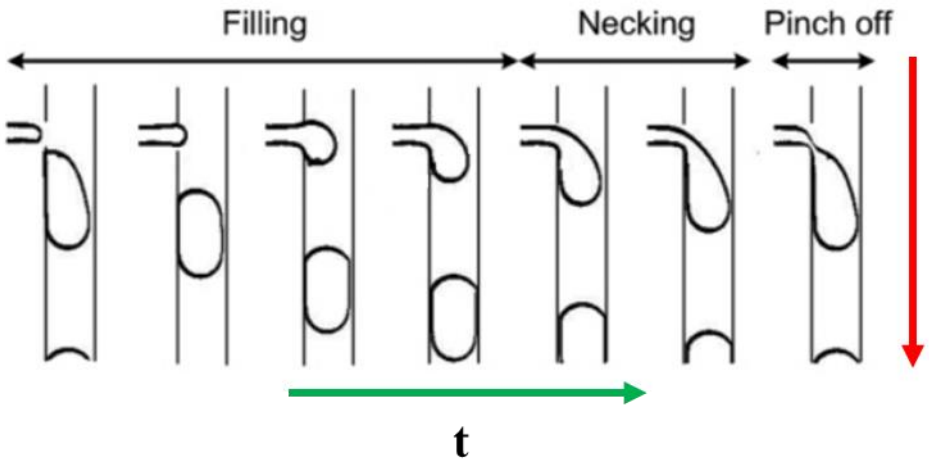


Figure 2.5 Droplet formation in a T-junction. Image adapted from (Glawdel et al., 2012a). The red arrow denotes the fluid flow while time moves from left to write.

Further work showed that the break-up outcome is dictated by the capillary number and the flow rate ratio (Glawdel et al., 2012b). The capillary number is a dimensionless quantity that demonstrates the relative importance of viscous forces over surface tension forces.

In the case of the flow focusing geometry, researchers demonstrated that droplet sizes are comparable to the orifice width (Shelley et al., 2003). Initial studies on flow focusing devices showed that, by increasing the continuous phase flow rate the viscous stresses start controlling the break-up and the liquid thread thins and extends towards the outlet channel. At low continuous phase flow rates the geometry of the orifice controls droplet formation (Anna and Mayer, 2006). Furthermore, the addition of surfactant leads to the formation of a thread which increases in length with increasing oil flow rate (Anna and Mayer, 2006). Further studies expanded on the mechanism of detachment stating it follows three distinct steps. The first step is after the previous break-up where the interface of the dispersed phase evolves and its width is bound by the width of the orifice. In the second step the interface gradually thins due to the

action of the continuous phase and in the third and final step it breaks releasing the droplet downstream (Garstecki et al., 2005).

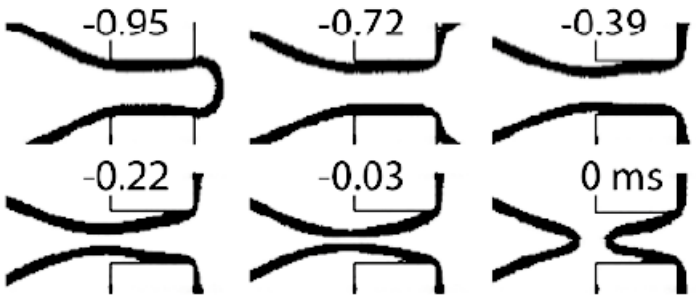


Figure 2.6 Droplet formation instances in a flow focusing microfluidic device. image adapted from (Garstecki et al., 2005)

Further studies demonstrated the capabilities of flow focusing devices by expanding on the regimes that can be present. Studies using more viscous dispersed phases showed that there exist clear boundaries between regimes (Cubaud and Mason, 2008). Using the same microfluidic device and by altering the continuous phase flow rates and the viscosity ratio between the two phases, researchers were able to produce five regimes, threading, jetting, dripping, tubing, and displacement (Cubaud and Mason, 2008) as presented in Figure 2.7. They were able to deduce qualitative empirical laws based on their results and that the regime present clearly depends on the capillary number of the two phases and identified a critical capillary number of 0.1. When capillary numbers are below the critical value, droplets are formed in the dripping regime and they are larger than the channel depth. Above the critical value of capillary number jetting is present and the production of subchannel size droplets is possible. When the capillary number of the dispersed phase is much higher than the capillary number of the continuous phase a steady thread is formed (Cubaud and Mason, 2008). Figure 2.7 illustrates the flow regimes mentioned above.

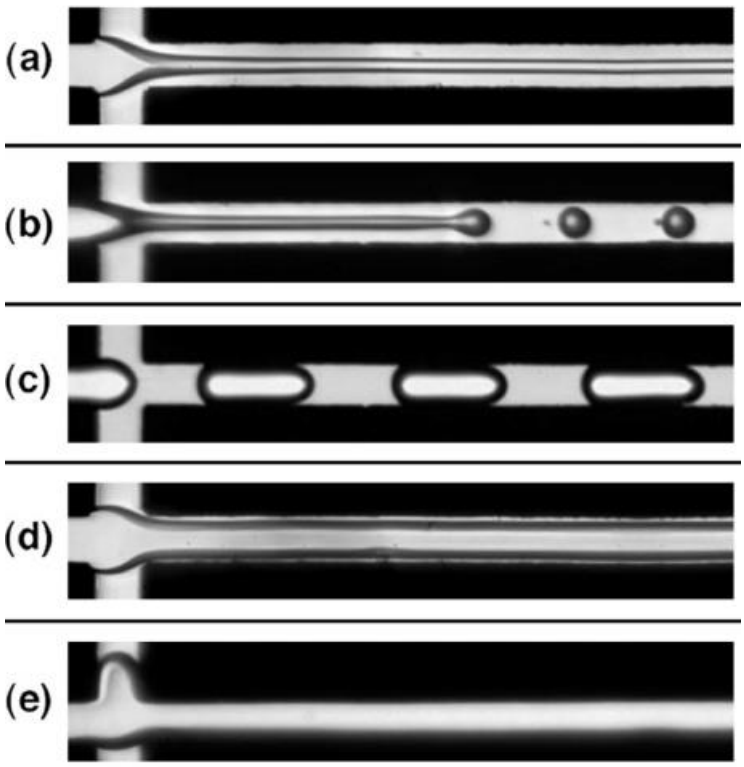


Figure 2.7 Flow regimes in a cross flow microfluidic device. a: Threading. b: Jetting. c: Dripping. e: Displacement. Figure adapted from (Cubaud and Mason, 2008).

In the dripping regime (Figure 2.7 c), which is of particular interest for this study, the droplet formation process is dominated by the competition between the drag force exerted by the flow field and the interfacial tension force resisting the break-up of the interface (Roumpea et al., 2019). After the pinch-off of the previous droplet, the dispersed phase retracts slightly into the dispersed phase channel due to interfacial tension and then it moves again towards the main channel. In the first stage, referred to as ***expansion***, the dispersed phase invades the junction and expands into the main channel. After the dispersed phase has invaded the junction the droplet expands mainly in the radial direction towards the side channels. In some cases, the expanding drop completely blocks off the side channels. As the pressure in the side channels keep increasing the expanding drop is forced to recede and starts growing mainly in the axial direction towards the main channel forming a neck connecting the expanding droplet to the bulk of the dispersed phase. The start of the ***necking*** stage occurs when the curvature of the neck changes. As the necking stage progresses the neck becomes thinner as it buckles under

the flow of the continuous phase. The droplet during the necking stage expands in the axial direction. As the neck becomes thinner it ruptures in what is defined as the ***pinch-off*** stage (Kovalchuk et al., 2018d, Cubaud and Mason, 2008).

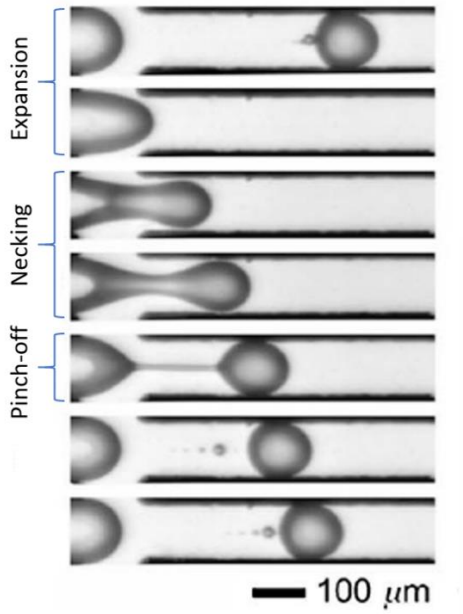


Figure 2.8 Droplet formation under dripping. Figure adapted from (Cubaud and Mason, 2008).

In the final stages of this regime, interfacial tension acts against droplet break up, since the stretching of the neck creates more interfacial area between the two fluids (Cubaud and Mason, 2008). Furthermore, the Laplace pressure in the thinnest part of the neck is a function of surface tension (Brochard-Wyart and Quéré, 2004). The higher the local interfacial tension component, the larger the Laplace pressure will be in the thinnest part of the neck, making the break-up of the neck harder. In the initial stages it has been shown that the presence of surfactants reduces surface velocities due to the presence of Marangoni phenomena along the interface (Roumpea et al., 2019). After the necking stage and the break-up of the droplet happens, the interface of the dispersed phase recoils back due to the action of interfacial tension. After the recoil, the dispersed phase starts invading the junction of the microfluidic device once again, this stage is called expansion. As expansion progresses the dispersed phases invades and blocks the movement of the continuous phases in the junction. Once the expansion is complete the action

of the continuous phase leads to the necking stage. Studies on the expansion stage in a flow focusing microfluidic device have shown that there is strong recirculation at the tip of the expanding droplet as the expansion stage advances. In a recent study that used μPIV in order to analyse the 2-D velocity field that develops during droplet formation in the squeezing regime, researchers demonstrated that when surfactant is present in the system there is no recirculation during the expansion stage of droplet formation (Roumpea et al., 2019).

2.4. PDMS microfluidics

The first microfluidic devices were made from glass and the process involved costly equipment and time-consuming procedures. Initial fabrication methods involved etching on glass and silicon (McDonald et al., 2000). Significant advancements in microfluidics occurred after the introduction of Polydimethylsiloxane, or more commonly referred to as PDMS. PDMS is a synthetic polymer and its versatility and low cost made it a vital component of microfluidics (Raj M and Chakraborty, 2020). Other elastomers used for the fabrication of microchannels include polymethyl methacrylate (PMMA) and polyurethane (Zhu and Wang, 2017). The technique used to create micro and nanostructures using elastomers is referred to as soft lithography (Xia and Whitesides, 1998). The advantageous use of PDMS elastomers lies in the fact that they are liquid at room temperature due to their low glass transition temperatures making them easy to handle. PDMS is poured on a master (mould) prepared by photolithography or other micropatterning techniques (Xia and Whitesides, 1998). The most common commercial form of PDMS is provided by DOW Corning and it consist of two parts, the PDMS elastomer and the crosslinker. Another major advantage of PDMS is its transparency allowing optical observation, excellent biocompatibility and permeability. The use of PDMS has also its downsides which are its tendency to swell in the presence of hydrocarbon based solvents and the ability of water to permeate through it (Raj M and Chakraborty, 2020).

Since the first demonstration of the ease of use of PDMS it has become a standard in microfluidics. Due to the myriad of microfluidic applications that exploit a number of different physical phenomena it is important to tune the chemical and material properties of the microfluidic device to allow for the desired phenomena to occur. The most common surface modification is the changing the hydrophobic nature of PDMS to hydrophilic. This is most commonly carried out by plasma modification which introduces polar groups to the surface (Bhattacharya et al., 2005). In this case, oxygen plasma, reacts with the PDMS surface, forming silicone atoms with one missing electron from the initial Si-CH_3 groups. These silicone atoms will combine with hydrogen atoms forming Si-OH groups. When the PDMS surface is brought into contact with a glass slide, or another PDMS surface, treated in the same way, the Si-OH groups of the two parts bond forming Si-O-Si bonds (Elveflow, 2017). Plasma modification is also used for the patterning of surface with hydrophobic/hydrophilic parts (Barbier et al., 2006). The tendency of PDMS to interact with solvents is countered by coating the PDMS surface with glass using sol-gel methods or by altering the ratio of polymer-to-crosslinker along with the baking times (Huang et al., 2014, Abate et al., 2008). Lastly, UV modification is also used quite frequently. UV modification allows for the formation of thin layer of un-crosslinked oligomers on the channel walls by altering the UV intensity (Dendukuri et al., 2008). The change in crosslinker quantity will also result in alteration of the mechanical properties of the PDMS by increasing its elastic modulus (Wang et al., 2014). Similarly, to the hydrophobicity/hydrophilicity patterning, PDMS can be modified with a gradient in elasticity which can be useful in a variety of fields (Darhuber et al., 2003).

The tuning of the elasticity of PDMS has a major impact on organ on a chip applications (Moyer, 2011). Changes in the elasticity for example affect the adhesion of fibroblasts (Fuard et al., 2008). PDMS also allows for the growth of cells on its surface, serving as a backbone (Das and Chakraborty, 2013). Another example is the work carried out at the University of

Birmingham studying the mechanism behind deep vein thrombosis using microfluidics (Schofield et al., 2018). In this work, researchers, used PDMS microfluidic devices fitted with leaflet valves in order to study the flow around them and determine the conditions under which clots are formed. PDMS microfluidics have been used to create biocompatible grafts with better cell viability, improved hyaline cartilage formation and enhanced mechanical properties (Li et al., 2014). In other cases, PDMS has been used to create an intra-cochlear electrode with better adhesion to the walls of the inner ear. Furthermore, PDMS microfluidic devices have been employed for the study of microorganisms such as E. coli and C. elegans (Samanta et al., 2017, Ben-Yakar et al., 2009). In the case of E. coli, microfluidics has been successfully employed to study chemotaxis, which is the directed motion in the presence of some chemicals. In this case the microfluidic device allowed for a better control of the chemical gradient and allowed researchers to develop a theoretical model of chemotactic drift (Samanta et al., 2017). C. elegans on the other hand is a model organism for the study of neurobiological processes in in-vivo settings. Microfluidics in this case allowed for better manipulation of the microorganisms. Lastly, PDMS is employed in the field of biomimetics, where the aim is to construct materials that mimic their biological counterparts (Vincent et al., 2006). An example of microfluidics being employed in this field is the study of silk fibres. In this case a microfluidic approach was used to study the silk fibre assembly process. In nature the fibre is formed with a complex mechanism involving changes in ionic concentration and pH within the micrometre sized spinning duct possessed by the organism. This approach allowed researchers to identify that colloidal aggregation is a requirement for the formation of the fibre under shear (Rammensee et al., 2008).

In terms of droplet microfluidics PDMS has been employed for the creation of T-Junctions, flow focusing and co-flow geometries (Cramer et al., 2004, Christopher and Anna, 2007, Anna and Mayer, 2006). The first implementation of droplet formation in a microfluidic T-junction

made out of PDMS was carried out in 2005 by Garstecki and his colleagues and improved on the scaling provided by previous research on droplet formation in a similar device. They provided an empirical scaling law over a vast range of flow rate conditions (Garstecki et al., 2006). In the case of PDMS based flow focusing devices researchers used a three-flow system operating under laminar conditions to break-up a more viscous stream. Researchers were able to create highly monodisperse droplets, smaller than the junction width, which can be controlled by manipulating the flow rates of the two fluids (Xu and Nakajima, 2004).

Another technological field where PDMS is used is sensors. Simple PDMS sensors have been fabricated for the detection of heat and measurement of temperature (Chuang and Wereley, 2009). More commonly PDMS is used for the creation of pressure and tactile sensors due to the ability of PDMS to withstand large amounts of stress without failing (Wu et al., 2011). Other types of sensors employing PDMS have also been developed for the measurements of physical properties, such as the refractive index of liquids (Polynkin et al., 2005).

In summary, the introduction of PDMS based devices as a simpler, faster and bench-top alternative to previous methods of microfluidic device fabrication, has made microfluidics much more accessible. Researchers no longer needed to rely on specialised methods requiring technicians and clean room technologies in order to fabricate their microfluidics systems. This made microfluidics much more accessible to scientists.

2.5. The presence of surfactants

As mentioned above surfactants are mainly used as stabilisers and as means of reducing interfacial tension to facilitate break-up. In most applications the amount of surfactant far exceeds the cmc (critical micelle concentration). The addition of surfactant enables, the lowering of interfacial tension, the capability to maintain, or change the wetting conditions of the channel walls and ultimately, the prevention of droplet or bubble coalescence. In other

cases, surfactants have been engineered for specific applications involving biomolecules and the encapsulation of cells. In these cases the surfactants are biologically inert and provide long term stability (Holtze et al., 2008).

2.5.1. Surfactant mass transport timescales

Droplet formation timescales compete with the surfactant mass transport timescales which might lead to the development of interfacial tension gradients, especially at intermediate surfactant concentrations. Under flow conditions the mass transport of surfactant is affected by the local flow fields. The relative importance between convective and diffusive mass transport can be described using the Peclet number defined as (Bruus, 2007)

$$Pe = \frac{Lu}{D} \tag{2.10}$$

Where, L is a characteristic length (m), u is the local fluid velocity (m s^{-1}) and D is the diffusion coefficient (m^2 s^{-1}) of the surfactant present. For a microfluidic device with a channel depth of 200 μm, a fluid velocity of 0.045 m s^{-1} (Roumpea et al., 2019) and a diffusion coefficient of 10^{-10} m^2 s^{-1} (Nowak et al., 2017), the calculated value of the Peclet number in the order of 10^4, suggesting that convective mass transport is important during microfluidic droplet formation. The transport of surfactant on the interface due to diffusion-controlled adsorption from the bulk is can be estimated using

$$\tau_\gamma = \frac{\Gamma_m^2}{Dc^2} \tag{2.11}$$

Where Γ_m is the maximum adsorption (mol m^{-2}) which describes the maximum amount of surfactant that can be adsorbed on the interface, D is the surfactant diffusion coefficient (m^2 s^{-1}) and c the concentration of the surfactant (mol m^{-3}). Equation 2.10 is derived by examining the time dependence of diffusion controlled adsorption (Mucic et al., 2011), researchers were able to show that it depends on the surfactant bulk concentration, the maximum adsorption and the diffusion coefficient of the surfactant (Ziller and Miller, 1986). Using the maximum

adsorption in equation 2.11, the calculated time scale reflects the amount of time it takes for the diffusion-controlled adsorption phenomena to populate the available interface with the amount of surfactant dictated by the Langmuir isotherm model (Ziller and Miller, 1986). The limiting adsorption timescale is inversely proportional to concentration, suggesting a rapid replenishment of surfactant in a highly concentrated solution. Replenishment of surfactant on the interface can also happen due to rearrangement of surfactant molecules due to Marangoni phenomena that create fluid motion. The time scale associated with these phenomena is given by

$$\tau_M = \frac{(\mu_1 + \mu_2) D_d}{\Delta\gamma} \tag{2.12}$$

Where μ_1 and μ_2 are the viscosities (Pa s) of the dispersed and continuous phases respectively D_d is a characteristic length (m) and $\Delta\gamma$ is the difference in interfacial tension (N m^{-1}) driving the fluid motion (Kovalchuk et al., 2019b).

Furthermore the smaller length scales are a perfect setting for the development of Marangoni phenomena due to the gradients in interfacial tension (Alvarez et al., 2010, Jin et al., 2004). Generally, the presence of surfactant leads to a production of smaller droplets in comparison to a surfactant free system due to the reduction of interfacial tension, this has been verified both experimentally and computationally (Van der Graaf et al., 2006). These studies assumed a uniform surfactant presence and a droplet formation process that evolved under equilibrium conditions, since there is no description of the dynamic surfactant effects on droplet formation. On the other hand, the main challenges that computational studies face are the coupling of the changes in interfacial curvature with the mass flux of the surfactant, something that can be simplified by studying non-soluble surfactants (Jin and Stebe, 2007).

2.5.2. Surface tension driven flows

The first cases of flow driven by surface tension differences was documented in 1855. The first observations were made on a resting body of water placed in a glass when a small quantity of liquor was placed in the centre of it. What was observed was a rapid rushing of the surface away from that spot (Thomson, 1855). The effect was made more apparent if fine powder particles were dusted on the surface of the water, maybe the first instance of particle tracking. These, yet not called Marangoni, phenomena became more famous due to the "tears of wine" effect. In this case the spirit is introduced close to the sides of the vessel. What is observed is that the liquid climbs the wall, accumulates and then due to its weight flows down again, hence the name "tears" (Thomson, 1855). The first systematic study of these phenomena was carried out by Italian physicist Carlo Marangoni during his doctorate and the results were published afterwards (Marangoni, 1865). More generally, similarly to a pressure gradient driving fluid motion, a gradient is surface tension can produce the same effect. The difference between the two lies in the fact that a gradient force per volume (pressure gradients) tend to maximise volume, while a gradient force per area (surface tension gradient) tends to minimise surface area (Bruus, 2007). In nature Marangoni forces are used as propulsion systems by bacteria (Bruus, 2007). The characteristic magnitude of such forces is proportional to $\Delta\sigma/L$ (De Gennes et al., 2013). Another quite notable result of Marangoni phenomena is the "coffee stain" problem. In this case a droplet containing dispersed solids dries on a surface. The result of the drying is a stain along the perimeter of the drop (Deegan et al., 1997). The liquid evaporating at the edge drives a fluid flow towards it that pushes material along with it. This has been exploited in patterning applications and the convective flow pushing material to the edge has been supressed by evaporating the drop in an ethanol vapor environment (Majumder et al., 2012). Another way Marangoni phenomena, impact engineering applications is their presence in lubricant oil mixtures. In that case foaming is sustained due to the presence of soluto-

capillary Marangoni phenomena arising due to the preferential evaporation of some of the components. This preferential evaporation of one of the components drives Marangoni flows that help regenerate the foam film (Rodríguez-Hakim et al., 2019).

2.5.3. The effect of dynamic surface tension on droplet formation

Returning to droplet formation, it was observed that the produced droplet sizes are larger in the cases where the adsorption of surfactant is slow (Xu et al., 2012). It was shown, by using saturated surfactant systems as models and comparing them to less concentrated systems, that for low surfactant concentrations and small formation times, the dynamic interfacial tension is more important that the equilibrium interfacial tension. Emulsification studies with the presence of surfactant showed that the regimes previously described by Cubaud and Mason are still present (Cubaud and Mason, 2008). The effects of the surfactant depend on the concentration, if the surfactant has a large cmc then the solution will most likely behave like a pure liquid displaying its equilibrium surface tension, while if the quantity is small the solution behaves like a solution without surfactant (Kovalchuk et al., 2018c). Other studies focused on the examination of the liquid bridge, the fluid filament that connects the expanding droplet to the bulk of the dispersed phase (Figure 2.9).

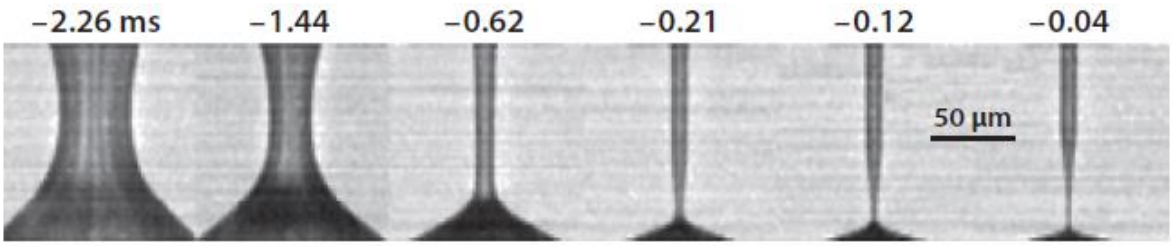


Figure 2.9 The liquid bridge, or neck, at different instances before droplet pinch-off (Roché et al., 2009).

The thinning behaviour of a fluid neck undergoing rupture is governed by viscosity, density and interfacial tension. According to Eggers, as the neck radius is reduced and the singularity is approached, the radius of the neck is given by

$$R(z,t) = l_v t'^{\alpha_1} \varphi(z'/t'^{\beta}) \tag{2.13}$$

Where R is the neck radius (m), l_v is the viscous length scale, z′ and t′ are the distance and time away from the singularity, a_1 and β and φ are constants (Eggers, 1993). For unconfined surfactant free liquids, the kinetics close to pinch off follow regimes dependant on the physical properties of the fluid.

When viscous effects can be neglected, the thinning behaviour is inertial and the radius of the neck follows

$$R(t) = 0.35(\gamma/\rho)^{1/3}(t_c - t)^{2/3} \quad (2.14)$$

Where, R is the neck radius (m), t is time (s), t_c is the time (s) at which the neck ruptures, γ is interfacial tension (N m^{-1}) and ρ (kg m^{-3}) is density (Eggers and Villermaux, 2008). When viscous effects are dominant the thinning behaviour is described by

$$R(t) = C(\gamma/\mu)(t_c - t) \quad (2.15)$$

Where, μ is the dynamic viscosity (Pa s) of the fluid undergoing pinch-off and C is a constant that takes the values 0.07 if the Reynolds number is negligible. For later stages of the break-up, as fluid velocities increase, the constant takes the value of 0.03 (Papageorgiou, 1995). The cross-over between these regimes is defined by the Ohnesorge number

$$Oh = \frac{\mu_d}{\sqrt{\rho_d \gamma h}} \quad (2.16)$$

Where μ_d is the viscosity of the dispersed phase (Pa s), ρ is density (kg m^{-3}), γ is interfacial tension (mN m^{-1}) and h is a characteristic length (m). Very close to pinch-off both inertia and viscosity become important and the kinetics follow the visco-inertial regime given by

$$D = A_{VI}\,\frac{\gamma}{\mu_d}\,(t_c - t) \quad (2.17)$$

Where, A_{VI} a is constant that takes the value 0.0608. Transition between these regime occurs when the neck diameter and time become of the order of magnitude of the viscous length and time scales given by

$$l_v = \mu_d^2/\gamma\rho_d \quad (2.18)$$

$$\tau_v = \mu_d^3 / \rho_d \gamma^2 \quad (2.19)$$

Lastly, if the break-up occurs inside an outside liquid of non-negligible viscosity the break-up can follow the two-fluid Stokes regime. In this case the neck radius is given by

$$R(t) = (H\gamma/\mu_c)(t_c - t) \quad (2.20)$$

Where, H is constant which is a function of the viscosity ratio and μ_c is the viscosity of the continuous phase (Cohen and Nagel, 2001).

By examining the evolution of the width of this region over time, researchers were able to identify different regimes of neck thinning (de Saint Vincent et al., 2012, Roché et al., 2009). In this case it was show that in the initial stages of the break-up interfacial tension is close to the equilibrium values, while when the formation process approaches pinch-off interfacial tension increases, Figure 2.10 displays this behaviour.

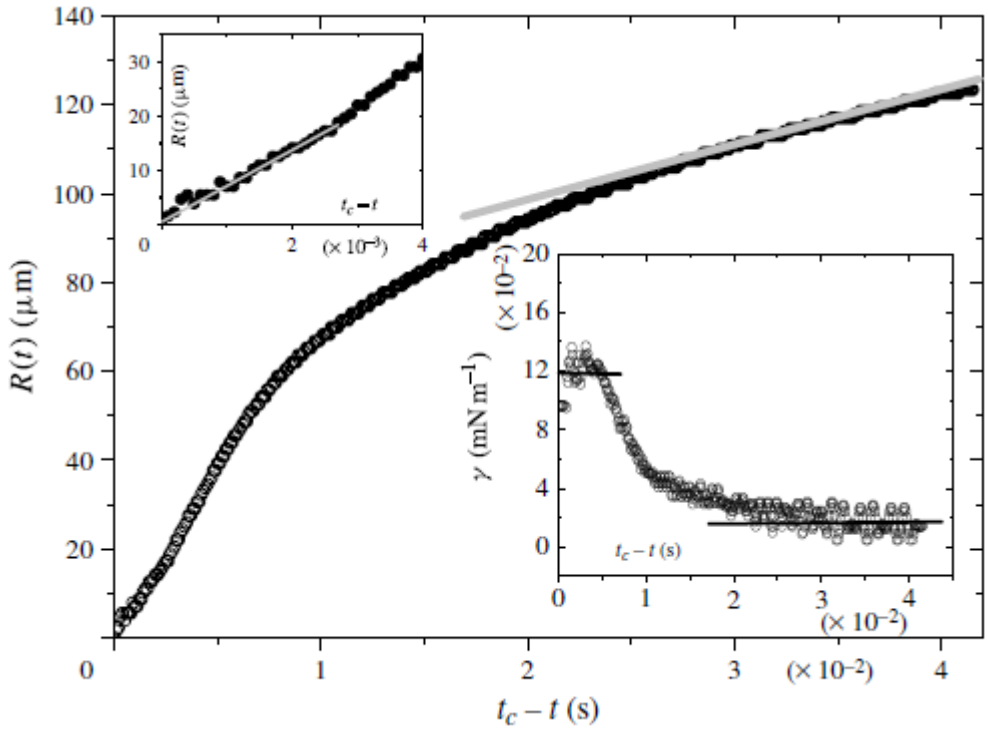


Figure 2.10 Kinetics of the thinning neck towards pinch-off. Upper inset is the final instances of the thinning. Lower inset is interfacial tension versus time. Figure adopted from (de Saint Vincent et al., 2012).

Figure 2.10 displays the neck radius as a function of time as droplet pinch off is approached. Two distinct behaviours are observed, one for time scales away from the pinch-off, where the

thinning rate is slower, and a faster thinning rate at timescales closer to pinch-off. The bottom right inset displays the acting interfacial tension at the timescales of droplet pinch-off. It is observed that when the thinning rate is slow, interfacial tension has values very close to the equilibrium values while in the final instances before droplet pinch-off, interfacial tension increases. This suggests depletion of surfactant from the neck on the timescales of droplet formation (de Saint Vincent et al., 2012). A similar study was carried out for droplet formation at the tip of a capillary under the effect of gravity. In this study researchers investigated the formation of liquid drops and the thinning kinetics of various soluble surfactants solutions for various concentrations, above and below the cmc. It was found that for surfactants present in high concentrations the liquid behaves like a pure solution with an apparent surface tension equal to the equilibrium value. In contrast, surfactants with lower values of cmc display dynamic properties close to the pinch off, and their surfactant transport dynamics cannot be ignored (Kovalchuk et al., 2016).

The evolution of the fluid interface is responsible for droplet sizes, formation times and the distribution of secondary break-ups (Tjahjadi et al., 1992, Zhu et al., 2016). In the case of break-up in air the rescaled interface profiles fall over a single curve and are universal regardless of boundary and initial conditions (Eggers and Villermaux, 2008). For two liquid pinch-off the shape of the interface depends on the viscosity ratio between the two liquids (Cohen and Nagel, 2001) while a similar universality has been observed for droplet formation in microfluidic devices (Eggers and Villermaux, 2008). This universality suggests that the profiles of the liquid interface of the thinning neck during pinch-off will be self-similar and collapse on the same curve. Deviation from this have been observed for systems where the droplet break-up happens under pressure fluctuations (Zhu and Wang, 2019).

The above studies used models for the thinning of liquid filaments derived by universal scaling laws that depend only on the physical properties of the fluid (Eggers, 1993). Eggers in his study

was able to show that during the thinning of a thin filament of glycerol the maximum velocity of the fluid exiting the neck in any time during the break-up can be predicted independent from the experimental conditions (Eggers, 1993).

2.5.4. Droplet break-up inside a continuous phase

The problem becomes more complex when an external fluid is present, such as in the case of microfluidic droplet formation. In this case, researchers were able to prove that the thinning process depends on the viscosity ratio between the two fluids (Cohen and Nagel, 2001). The effect of the outer fluid can be neglected if the liquid bridge consists of a higher viscosity liquid than the external phase and if the process evolves significantly slowly (Eggers, 1997). Furthermore, other numerical studies showed that the thinning process depends on surface tension and density when considering the break of a thin sheet of liquid (Keller and Miksis, 1983). All the above studies have not considered the dynamic effect of surfactant mass transport and only considered pure systems with fixed equilibrium properties. The studies presented above used models that described the neck thinning process and tried to reverse engineer interfacial tension by measuring the neck diameter over time. The interfacial tension calculated is not the actual value of interfacial tension, but an estimate, and can give an indication of the dynamic properties of the fluid in these short timescales.

It is important to point out here that there exists no dynamic surface tension measurement capability for the timescales of droplet formation in microfluidics (Mucic et al., 2011). The most common experimental method that reaches sub-milliseconds timescales and can measure dynamic surface tension for surfactant solutions is maximum bubble pressure tensiometry (Table 2.1). Despite the advances in measuring capabilities the technique is still limited to air-liquid interfaces. Therefore, there exists no dynamic surface (or interfacial) tension measurement capabilities for the short timescales of droplet formation in microchannels. There have been microfluidic attempts to measure dynamic interfacial tension. Researchers used a Y-

junction channel to quantify the apparent interfacial tension during droplet formation. In their study they used hexadecane as a dispersed phase and water-ethanol solutions in a range of ethanol concentrations to derive a calibration curve which was used to estimate the dynamic interfacial tension of Sodium Dodecyl Sulfate (SDS) and Poly(ethylene glycol)-*block*-poly(propylene glycol)-*block*-poly(ethylene glycol) (PEF108) solutions (Steegmans et al., 2009). They used the droplet sized of the model systems and compared that to the surfactant laden systems. They showed that surfactant transport is dominated much more by advection rather that diffusion (Steegmans et al., 2009). Another study, by Xu and his colleagues, used a co-flow microfluidic device and analysed the force balance during droplet formation. They as well used model systems with a variety of interfacial tensions and compared these to the surfactant-laden cases. Similarly they used the droplet sizes of the model systems to estimate the interfacial tension of the surfactant cases (Xu et al., 2008). Other studies incorporated the dynamic surfactant effects into previously existing models (Glawdel and Ren, 2012) and showed that droplet sizes were larger than the predicted values which suggested an increase in surface tension during the droplet formation process. In the study by Xu et al. surfactants with larger and smaller molecular weights were used in order to control diffusion (Einstein, 1905). The diffusion coefficient of dissolved species is very important since it regulates their mass transport. Studies have been performed where the addition of glycerol, in order to increase viscosity, showed that the spreading of droplets is enhanced when the diffusive transport of surfactant is suppressed (Kovalchuk et al., 2019a).

Other studies have shown that the shape of the deforming neck is different between a surfactant free and a surfactant laden case. More specifically, the equilibrium shapes of surfactant laden bridges, appears to be different than the shape of a surfactant free system, while the length of the bridge is also affected (Liao et al., 2004). The break-up of the thinning necks is also important due to the presence of secondary break-ups. Researchers showed that the increase in

surfactant concentration increases the size of satellite droplets (Kovalchuk et al., 2018b). This was also predicted by numerical work that studied cases with a concentration of surfactant above the cmc. It was demonstrated that Marangoni phenomena are responsible for the increase in satellite droplet size even for cases of surfactant solutions above the cmc (Craster et al., 2009). In experimental studies a retardation of the thinning process and an increase in interfacial tension has been monitored in microfluidic or gravity break-up. In the case of break up under gravity the fluid has been shown to slow down due to the effects of Marangoni stresses close to the pinch off (Kovalchuk et al., 2018b).

Similar studies have been done for droplet coalescence. During coalescence two bodies of the same liquid come closer within a second liquid and a film of the outer liquid is formed between them. This film eventually drains and coalescence is initiated due to Van der Waals forces (Chinaud et al., 2016). Studies performed in a Hele-Shaw cell showed that the neck expands linearly in the first stages of the break-up and the local surfactant concentration is double the bulk surfactant concentration. More detailed studies using fluorescent surfactants showed that the draining of the film affects the distribution of the surfactant (Dong et al., 2019). A drop was created at the tip of a capillary inserted in the continuous phase. The drop was left to stand at the tip for various times and then released. This controlled the amount of surfactant absorbed on the drop interface. Once the drop was released and rested on the interface, the draining of the film between the drop and the interface swept the surfactant along the interface. For drops that rested at the tip of the capillary for larger times the amount of surfactant swept was larger. The above study helped to cement previous findings that showed that the partial coalescence can be controlled due to the action of Marangoni phenomena along the interface (Weheliye et al., 2017). The expanding neck during coalescence contains much more surfactant due to the merging of the interfaces. The top part of the merging droplet contains less surfactant. This creates a surface tension gradient along the interface that acts against partial coalescence (Dong

et al., 2017). Marangoni phenomena have also been found to enhance convective mixing in merging droplets (Nowak et al., 2017). The mixing produced by the difference in surface tension is found to be considerably higher than the one produced by the difference in capillary pressure.

From the above is clear that the surfactant mass transport during droplet formation is quite important and complicated to describe. The majority of the above studies used models derived for pure systems or the observation of droplet sizes in order to observe the results of the dynamic aspect of droplet formation. The neck kinetics model presented by equations 2.11, 2.12 and 2.13 perform well when the break-up occurs in a continuous phase of negligible viscosity and when surface tension is constant. When droplet formation occurs inside a viscous continuous phase the neck kinetics deviate from these models. Furthermore, when dynamic conditions are present and since dynamic interfacial tension in the timescales of emulsification is unknown the behaviour is challenging to describe. The studies presented above focused on the physicochemical aspect of surfactant mass transport during droplet formation. They stressed the importance that the quantity of surfactant present in the system has in allowing for dynamic conditions to manifest. They were able to calculate the acting surface tension during the process through the observation of the final outcome of droplet formation, either the thinning neck kinetics or the droplet sizes. Using the above findings, this work attempted to incorporate the effect of the hydrodynamics present during droplet formation, affecting the surfactant mass transport.

2.6. Velocimetry studies

In more recent approaches researchers applied velocimetry techniques for the study of the surfactant mass transport. Researchers used Planar Laser Induced Fluorescence (PLIF) to describe the spatiotemporal distribution of surfactant. Despite the successes, PLIF has its

limitations since it relies on the use of a laser and the presence of fluorescent surfactants which limits the general applicability of the results (Crimaldi, 2008). Other studies have resorted to the use of velocimetry techniques such as micro-PIV. Recently it was demonstrated that surfactant free systems undergoing droplet formation in a flow focusing microfluidic device display large velocities along the interface and the presence of recirculation patterns after the drop detaches. In the surfactant laden case the velocities appear to be smaller and the recirculation patters are not present (Roumpea et al., 2019).

But before an overview of these studies is presented, it is reasonable to review velocimetry techniques in general. One of the first flow visualisation experiments was performed by Osborne Reynolds in which he studied the transition from laminar to turbulent flow. In the context of this study what is important is that Reynolds in his experiments used a very simple way to visualise flow, he introduced a dye in the flow direction which followed the fluid and revealed the flow conditions (Reynolds, 1883). Despite the ingenuity of this experiment, he was not able to extract any quantitative information from it. Flow visualisation experiments date far before Reynolds, there is evidence that Leonardo da Vinci performed fluid visualisation experiments where he flowed seeds inside a glass vessel (Gharib et al., 2002). Newton wrote about similar observations as well (Adrian, 2005).

Even though flow visualisation experiments are quite important, they only provide researchers with qualitative information about the observed flow fields. Engineering applications, research and industry require quantification of the velocity fields present in physical systems. The velocimetry techniques applied in microfluidics exploit the transparent nature of the channel and fluids. These methods are generally the most comprehensive in enabling the spatial distribution of the fluid motion to be obtained, at high spatial and temporal resolution. Specifically, the fluid motion can be tracked via the addition of small neutrally buoyant

particles whose behaviour can be assumed to match that of the fluid. This can be assumed if the particle Stokes number, St, is less than 10^{-1},

$$St = \frac{\rho D^2 / 18\mu}{D_0 U_0} \tag{2.21}$$

Where ρ is the density of the particle (kg m^{-3}), D is the diameter of the particle (m), μ is the fluid viscosity (Pa s), D_0 is a reference length (m) and U_0 is the velocity (m s^{-1}) of the fluid (Krstić, 2006). The Stokes number is the particle's momentum response time over the flow field timescale. Two approaches can be taken to track the motion of particles in modern velocimetry, Particle Tracking Velocimetry, that relies on tracking individual particles via a Lagrangian approach (Maas et al., 1993), while Particle Image Velocimetry (PIV) uses an Eulerian method where the flow is observed in a specific region in space and the motion of the fluid is observed through that region in time.

Quantifications of the flow field using Particle Tracking Velocimetry (PTV) rely on tracking individual particles that are optically resolvable (Maas et al., 1993). The particles have to be neutrally buoyant which is achieved by matching their density with the density of the fluid and their sizes are in the micrometre scale (Chang et al., 1985). The technique allowed researchers to better observe turbulence and better determine the flow field developed (Kasagi and Nishino, 1991). A particular challenge for microfluidics applications is the size of the PTV tracer particles which need to be orders of magnitude smaller than the channel dimensions, making the technique almost impossible to implement for the study of flows in submillimetre channels. A technique more suited for smaller scale systems is particle image velocimetry (PIV) (Adrian, 1986). The first attempts were carried out by the use of laser speckle methods that used double exposure images and correlated the speckle pattern between pairs of images (Dudderar and Simpkins, 1977, Barker and Fourney, 1977, Grousson and Mallick, 1977). These first methods were referred to as laser speckle velocimetry. A speckle pattern is the pattern arising from the superposition of light with random phases scattered from different portion of the sample

(Brogioli et al., 2002). The term particle image velocimetry was coined later, in 1984, due to the presence of particles in the speckle images (Adrian, 1984). The motion of the particles is evaluated using an autocorrelation function between a pair of images

$$R = \prec I_s(t) \times I_s(t + \Delta t) \succ = \lim_{T \to \infty} \frac{1}{2T} \int_{-T}^{T} I_s(t) I_s(t + \Delta t) dt \qquad (2.22)$$

This function allows us to cross-correlate the intensity field between two frames and extract a measure of the displacement. This function has three components. A component associated with the mean image intensity, one associated with the noise due to the recording, the light source etc, and a component dependant on the intensity associated with the presence of the particles. The function displays a peak when $\Delta x = V\Delta t$. Figure 2.11 shows the cross-correlation between two individual frames when performing PIV.

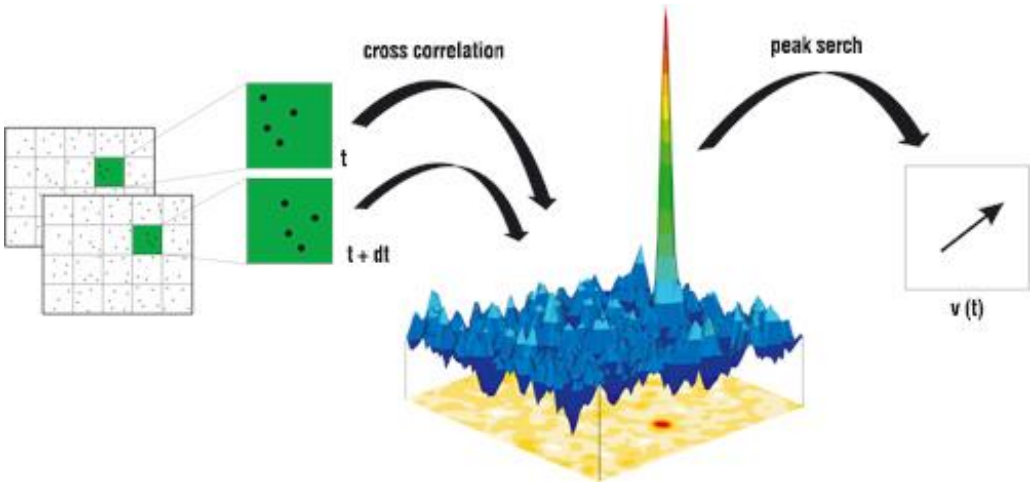


Figure 2.11 Schematic demonstration of cross-correlation of subsequent images. Image adapted from (Wieneke, 2017)

The first PIV systems where employed to study turbulent systems and they relied on illuminating particles that were 20-30 μm in diameter (Adrian, 2005). Since then the evolution of computer technology, memory storage capabilities and cameras has led to significant advancements in PIV. This allowed for the study of flow patterns between trailing bubbles in millimetre sized capillary tubes and the study of the streamlines of viscous fluids being expelled from a tube (Cox, 1964, Thulasidas et al., 1997).

In the context of microfluidics, the first velocimetry studies involved the use of X-rays and optical doppler tomographic imaging. X-ray imaging was used to analyse the velocity contours in the nozzle of an ink-jet printer (Lanzillotto et al., 1997) while Optical Doppler Tomography (ODT) was used to investigate the flow patterns inside a 1 mm circular channel (Chen et al., 1997). In the first case the motion of 1-20 μm emulsion droplets was recorded. The advantages of using an X-ray system lie in the fact that observations can be made in opaque systems. In the case of the ODT particle sizes were 1-7 μm. In both cases particle sizes are comparable to the dimension of the channel therefore their ability to faithfully follow the flow field is limited. The first micro-PIV systems used for microfluidics were developed using 100-300 nm fluorescent particles and were employed to measure the velocity field around an elliptical cylinder (Santiago et al., 1998). A volume of the fluid is illuminated with light and the objective collects the light from the plane that is in focus (Breuer, 2005). One of the drawbacks of micro-PIV is the need of an expensive set-up and control system. Figure 2.12 represents a typical micro-PIV result (Lindken et al. 2009).

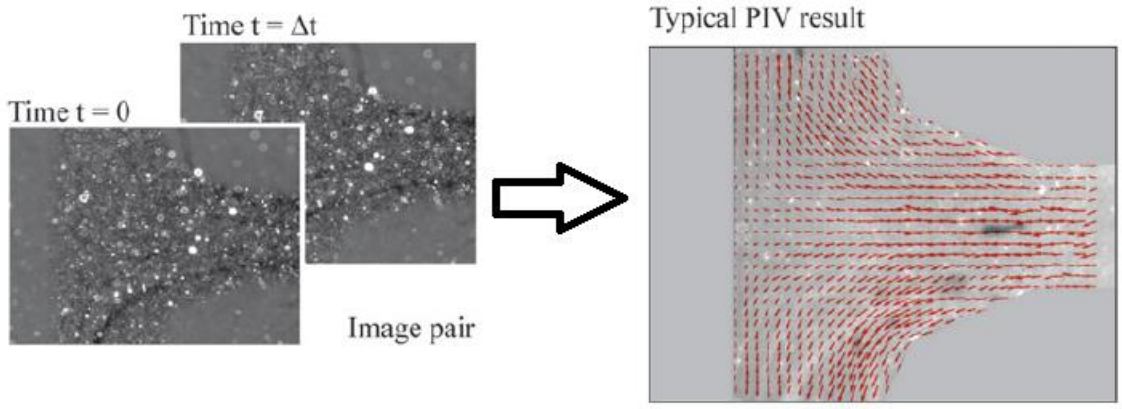


Figure 2.12 Typical micro-PIV result. Image adapted from (Lindken et al., 2009)

In microfluidics systems micro-PIV allowed for the study of the velocity field in a T-junction due to the interest in convective mixing (Lindken et al., 2006) and in a straight channel when a counter flow is present (Shinohara et al., 2004). Other studies focused on the evolution of the

flow around the detaching droplet showing the impact of the flow conditions in the velocity field and on the droplet formation process (van Steijn et al., 2007).

As mentioned before, techniques that track individual particles are referred to as particle tracking velocimetry techniques. In these cases, the particles are large enough and are optically resolvable. These techniques fall behind in resolution but perform well when the system is large enough (Adrian, 2005). Furthermore, the average displacement of the fluid is calculated by measuring the displacement of the individual particle assuming it faithfully follow the flow. In contrast, micro-PIV techniques, can rely on cross-corelating consecutives frames using the intensity of the emitted light of the particles or their interaction with the light (Lindken et al., 2009). More specifically, the techniques work by seeding the fluid with the tracer particles. For microfluidic applications these particles are between 0.2-2 μm and they should have matching densities with the fluid in order to follow the flow.

More recently a technique called Ghost Particle Velocimetry was developed that uses sub-optical resolution tracers and only requires a bright-field illumination, a Köhler illumination and the ability to operate the condenser lens (Buzzaccaro et al., 2013). By reducing the numerical aperture of the condenser the coherence of the light source is increased similarly to differential dynamic microscopy (Cerbino and Trappe, 2008). Closing the condenser lens allows us to transform the random diverging light produced from our source into a parallel beam, increasing its coherence (Watson, 1998). The condenser consists of a diaphragm with a variable aperture and as the light passes through it, it is focused on the sample (Payne, 1950). The opening and closing of the condenser iris regulates the angle at which the wavefronts shine on the sample (ZEISS Microscopy). This works in a similar way as a spatial filter would work for a laser beam by removing the high frequencies (Thompson, 1969). The basic concept of the technique is that if a uniform distribution of particles is considered, traveling with the fluid and illuminated in a thin layer perpendicular to the axis of observation, then the speckle pattern

produced between two consecutive frames can be used to estimate the average displacement of the fluid. The particle size is below the diffraction limit, so they are invisible to the eye, but they still interact with the light. As the light gets scattered from the particles in the near field it interacts either constructively or destructively (Brogioli et al., 2002). What is observed in the far field, is a speckle pattern, that can give us information about the fluid motion.

The advantages of using the produced speckle pattern to analyse the fluid dynamics lie in the fact that it is possible to extract information without needing individually resolvable particles. Cerbino et. al. used this to measure the diffusion coefficients of nanometre-sized particles in a suspension. They were able to accurately measure the diffusion coefficient of their suspension particles and match them to the calculation using the Stokes-Einstein equation (Cerbino and Trappe, 2008). In other cases the analysis of speckle patterns using Differential Dynamic Microscopy (DDM) allowed for the study of cell behaviour, tissues, suspension and soft matter (Cerbino and Cicuta, 2017). In its first microfluidic application GPV was used to analyse the flow around an obstacle in a microfluidic channel (Buzzaccaro et al., 2013).

The speckle pattern produced at a time t is compared to the speckle pattern a time $t+\Delta t$. The time-correlation function of the normalised intensity displays a peak when $\Delta x = V\Delta t$ allowing for the extraction of the velocity field. The cross-correlation is carried out using PIV-lab (Thielicke and Stamhuis, 2014). When cross-correlating two consecutive frames the cross-correlation function R(s) has three components similarly to PIV. The median subtraction serves the purpose of reducing the contribution of the noise and average intensities during cross-correlation (Brossard et al., 2009). The limitation of GPV are found in the fact that due to the spatial coherence of the light used the observation plane has a certain longitudinal depth and if the time window between two individual frames becomes large enough, the Brownian motion of the particles affects the results (Buzzaccaro et al., 2013).

Following the establishment of GPV one of the implementations was to study the trapping of particles in a T-junction and the analysis of flow patterns inside moving droplets in microchannels (Vigolo et al., 2014, Pirbodaghi et al., 2015). T-junctions are very common piping elements that allow for the bifurcation of the flow and is assumed that particles entering the bifurcation will leave it following the flow. In reality, the flow conditions at the bifurcation allow for the trapping of any suspended species leading to undesirable results. More specifically, low density suspended species present in the continuous phase interact with a vertical flow created at the T-junction and are unable to leave the intersection for a variety of flow conditions (Vigolo et al., 2014). In this study millimetre-sized channels were employed and the suspended species were bubbles formed by electrolysis. In a more recent instance, the same study was carried out in a microfluidic environment using GPV. The researchers were able to recreate previous work while also proving the capabilities of GPV. They showed that increasing the Reynolds number leads a formation of recirculation zone that can create particle trapping (Riccomi et al., 2018). Furthermore, the researchers used micro-PIV to validate their results and try to understand the limits of the technique. They were able to demonstrate that GPV and micro-PIV perform very well for low Reynolds numbers, while GPV, starts underperforming as the Reynolds number increases. This is mainly attributed to the fact that as flow conditions become faster a higher frame rate is required for GPV (Riccomi et al., 2018).

A more important implementation of GPV is the velocimetric analysis of high-speed small-scale phenomena like emulsification. Researchers first analysed the flow around a rectangular obstacle in a microchannel and compared the results to simulations validating the GPV results. In the same study they employed a simple cross-flow microfluidic device and studied the formation of droplets. They were able to resolve the flow field during droplet formation. More specifically they showed that as the droplet moves towards the outlet channel, a stagnation zone is formed at the tip of the droplet. As the pinch-off moment is approached, this stagnation zone

moves to the centre of the droplet as fluid moves towards the tip of the droplet from the sides. Furthermore, they were able to resolve the flow field inside a moving droplet showing that there are two hydrodynamically isolated recirculation zones. As the droplet is pushed forward from the action of the continuous phase, liquid at the interface of the droplet is dragged by the action of the continuous phase. This fluid is pushed along the interface and towards the tip of the droplet and then towards the centre (Pirbodaghi et al., 2015). The results are presented in Figure 2.13.

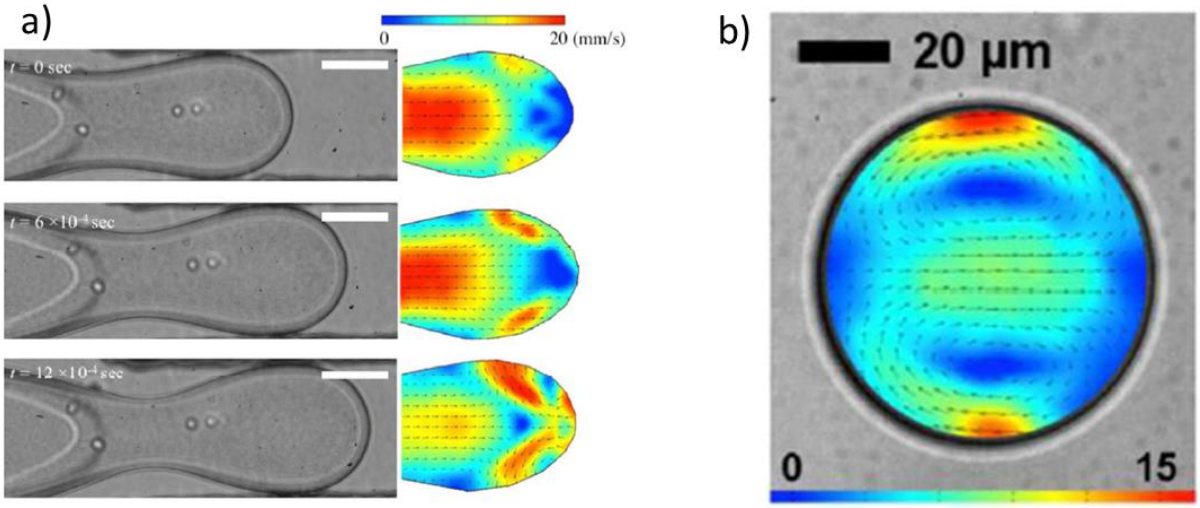


Figure 2.13 a: Flow field inside the expanding droplet during droplet formation. b: Flow field inside a moving droplet. Figures adapted from (Pirbodaghi et al., 2015)

These results are especially significant in the context of convective mixing in droplet generation applications. In a similar context GPV has been used to analyse the flow field during droplet formation in stop-flow lithography applications. In this case the researchers were able demonstrate how the oscillating flow dynamics produced by droplet formation affect the shape of the produced polymerised structures (Martino et al., 2016). Stop-flow lithography is the creation of polymerised hydrogels in flow environments (Dendukuri et al., 2006).

GPV has also been employed in the study of coalescence in microchannels. Firstly, the researchers analysed the recirculation happening inside a plug moving in a microchannel. Similarly, to the case of a moving droplet, there are two hydrodynamically isolated

recirculation zones caused by the drag of the continuous phase. During coalescence investigators were able to identify strong convective mixing. More specifically during the first instances of coalescence of similar drops there is two vortexes formed on the sides of the droplets. These vortexes do not mix the contents of the different drops but aid coalescence by bringing surfactant from the bulk to the interface (Kovalchuk et al., 2018a). The motivation of this study was the merging of drops in microchannels with the presence of surfactant. In a follow up study GPV was used to analyse coalescence events between a surfactant free and a surfactant laden droplet. The study showed that in the case of merging droplets there is two significant flows arising. One is close to the interface and is caused due to the difference in interfacial tension of the droplets. This fluid flow is cause by Marangoni phenomena and it results in the surfactant laden drop spreading around the surfactant free droplet. The second flow is caused by the difference in capillary pressure and it results in the surfactant free drop invading the surfactant laden droplet. The researchers also studied the effect of the sequence of droplets. It was found that when the surfactant laden droplet precedes the surfactant free drop along the flow direction the merging is accompanied by strong convective mixing. If the order is reversed, the convective mixing during merging is significantly smaller. Close to the channels walls the flow of the continuous phase is smaller and the Marangoni flow can either be in the same or the opposite direction, depending on the order of the droplets. When the Marangoni flow is in the opposite direction, the convective mixing is much smaller. GPV showed that the maximum velocity inside the droplets during coalescence is significantly smaller in this case (Kovalchuk et al., 2019b).

2.7. Summary

The main pillars on which this study rests have been made clear in the present literature review. The main challenge that emulsification applications face is the timescales over which they

happen. Droplet formation is a rapid process that evolves in timescales shorter than the timescales available for the surfactant to redistribute on the interface. This allows for the presence of dynamic conditions which affect the process and alter the expected results. Furthermore, the lack of measuring capabilities in these short timescales makes it impossible to precisely know the behaviour of a given system. Industrial and research applications have tried to counter this by increasing the amount of surfactant above the cmc, which can be damaging to the environment and reduce the cost-effectiveness of processes.

From a physical perspective droplet formation presents researchers with a variety of challenges. It is a process that evolves over decreasing length scales, where observation becomes very difficult if not impossible. Therefore, the observation of the hydrodynamic phenomena present is really challenging. Local velocity fields change rapidly and as smaller and smaller length scales are approached the behaviour of fluids has never been observed experimentally. Furthermore, the fact that the droplet formation process occurs inside a continuous phase with a comparable viscosity to the dispersed phase further complicates the surfactant mass transport on the interface.

The emergence of new techniques, like GPV, capable of addressing these challenges pave the way for a better understanding of these complex physics and an expansion of our measuring capabilities. This study paves the way towards better understanding surfactant mass transport during rapid fluid phenomena and lays the foundation for on-line dynamic surface tension measurements in shorter and shorter timescales. The fundamental question that droplet formation holds is whether the presence of surfactant affects the process or the process affects the presence of surfactant. Most likely they both affect each other.

Chapter 3: Materials and Methods

Introduction

Chapter 3 describes the experimental materials used and the main methods for the analysis of the results. It begins with describing the preparation of the solutions used in the study and then describes the methods used for the measurement of equilibrium interfacial and dynamic surface tension. Following that the details of photolithography and soft-lithography are explained which form the basis for microfluidic device fabrication. Finally, the experimental procedure for measuring droplet sizes and neck kinetics is described alongside with the theory behind GPV.

3.1. Materials

3.1.1. Fluids

Due to the nature of this study and the interest in examining interfacial phenomena there is a need to have a close look at the interface. When light encounters the interface between two fluids it changes its speed and direction (Hecht, 2012). This creates the impossibility of closely examining the interface between two fluids due to differences in their refractive indices. The curvature of the interface redirects the light away from the objective and the interface appears dark. To counter this there is a need to match the refractive index of the fluids used. The continuous phases used in the study are 4.6, 19, 96 mPa s silicone oil provided by Merck with a refractive index of 1.403 (Sigma-Aldrich, 2020, Merck, 2020i, Sigma-Aldrich, 2017). Table 3.1 summarises the physical properties of the fluids used.

Table 3.1 Physical properties of the fluids involved. a: (Kovalchuk et al., 2018c), b:(Sigma-Aldrich, 2020), c: (Sigma-Aldrich, 2017), d:(Merck, 2020i)

	Density ($Kg\ m^{-3}$)	Dynamic viscosity (mPa s)	Kinematic Viscosity (cSt)
52%-48% Glycerol-D.I. water	1133[a]	6[a]	5.3
5 cSt silicone oil	913[b]	4.6	5
20 cSt silicone oil	950[c]	19	20
100 cSt silicone oil	960[d]	96	100

The dispersed phase is a mixture of Millipore distilled water and glycerol. Glycerol is added to manipulate the refractive index of water (Takamura et al., 2012). Glycerol (>99%) , is provided by Merck (Merck, 2020d). Water has a refractive index of 1.33 (Hale and Querry, 1973), and a 52% by weight glycerol-water solution will have a refractive index of 1.403 (Pala Rosas et al., 2017) closely matching that of the continuous phase.

3.1.2. Solution preparation

The protocol followed in every case to prepare the solution is the following. 10.8 g of glycerol are added to 10 g of distilled water. This produces 18.6 mL of solution that contains 52% glycerol by weight. To this solution 1 g L^{-1} (Kovalchuk et al., 2018c) of methyl violet (Merck, 2020f) is added to produce a large enough contrast for optical observation, or 0.2% by weight (Pirbodaghi et al., 2015) of 200 nm polystyrene nanoparticles as provided by Merck (Merck, 2020g). After the addition of the dye or the nanoparticle the solution is mixed well using a whirl mixer. It was found experimentally that the addition of the dye does not affect interfacial tension above the level of experimental error (Kovalchuk et al., 2018c). Similarly, the effect on interfacial tension due to the addition of nanoparticle will be explored in Chapter 4.

The surfactants used are provided by Merck and are used as purchased without any modification. The surfactants used are Decyltrimethylamonium Bromide (C10TAB), Dodecyltrimethylamonium Bromide (C12TAB), and Hexadexyltrimethylamonium Bromide

(C16TAB) with purities of 98% and above (Merck, 2020e, Merck, 2020c, Merck, 2020b). After the addition of surfactant, the solution is placed in a rotary agitator overnight to allow for the complete dissolution of the surfactant. It is advisable to add the surfactant after the addition of the dye or the nanoparticles. It was observed that if the surfactant was added before the nanoparticles, the nanoparticles formed aggregates. Therefore, the nanoparticles were always added first and allowed to mix well. All solutions were placed in 25 mL plastic vials. Table 3.2 summarises the surfactant solutions used in this study.

Table 3.2 Surfactant solutions used in this study

	Concentration (mM)		
C/cmc	**C10TAB**	**C12TAB**	**C16TAB**
0.1	7.6	2	0.2
0.2	15.2	4	0.4
0.5	38.1	10	1
1	76	20	2
2	152	40	4
5	381	100	10
10	760	200	20

3.2. Methods

3.2.1. Equilibrium interfacial tension

Equilibrium interfacial tension measurements were carried out using a SINTERFACE PAT1P optical tensiometer (SINTERFACE, 2020). The method relies on analysing the droplet profile as it rests in a continuous phase. Due to the nature of the measurement the method requires high refractive index differences or the presence of a dye to detect the interface profile. In this case, measurements were carried out using dyed solutions due to the matching refractive indexes of the solutions. The nanoparticle solution used for GPV using the pendant drop method and an optical tensiometer provide insufficient contrast for the equipment to detect the

interface profile. The analysis of the interface relies on the Gauss-Laplace equation (Spelt, 1996). In order to extract interfacial tension values the coordinates of the interface from the experimental images are fitted to the Gauss-Laplace equation (Karbaschi et al., 2012).

Before each measurement the syringe and needle were placed in isopropanol beakers and placed in a sonic bath to be cleared from any previous residue. The syringe is left in the sonic bath for 10 minutes and then rinsed with isopropanol and distilled water repeatedly. After rinsing, the syringe and needle were assembled and they were rinsed several times with the desired solution. The capillary needle had a diameter of 1 mm and the syringe could hold 0.5 mL in volume. The continuous phase was inserted into the provided cuvette and placed in the chamber. The needle was then inserted and the camera and software were set up as to get a clear image of the tip of the capillary. Next a calibration was performed using the capillary diameter as a reference length. After the calibration was complete a droplet was created manually at the tip of the capillary and left to rest for 5 minutes. After that the measurement started with a duration of 10 minutes. The measurement lasted for 10 minutes since after that no differences in interfacial tension were recorded.

3.2.2. Dynamic surface tension

Dynamic surface tension measurements were carried out using the maximum bubble pressure method. The equipment used is the maximum bubble pressure tensiometer BPA-1S by SINTERFACE (SINTERFACE).

Before each measurement the capillary was rinsed for 15 minutes and the dynamic surface tension of pure water was measured to ensure there were no impurities left over from previous experiments. The dynamic surface tension of water is constant and it should measure 72 mN m^{-1} (Lange and Forker, 1967). After the value for water was verified the solution under study is placed in 25 or 50 mL clean beaker and the capillary is submerged in the solution. The measuring time was 10 minutes since no notable differences were recorded for longer times.

3.2.3. Microfluidic device fabrication

The microfluidic device used in the study is a cross-flow junction that can produce water-in-oil droplets in the squeezing regime under various flow rate conditions. The height of the microfluidic device is 150 μm. Figure 3.1 displays a schematic and a snapshot of the microfluidic device used.

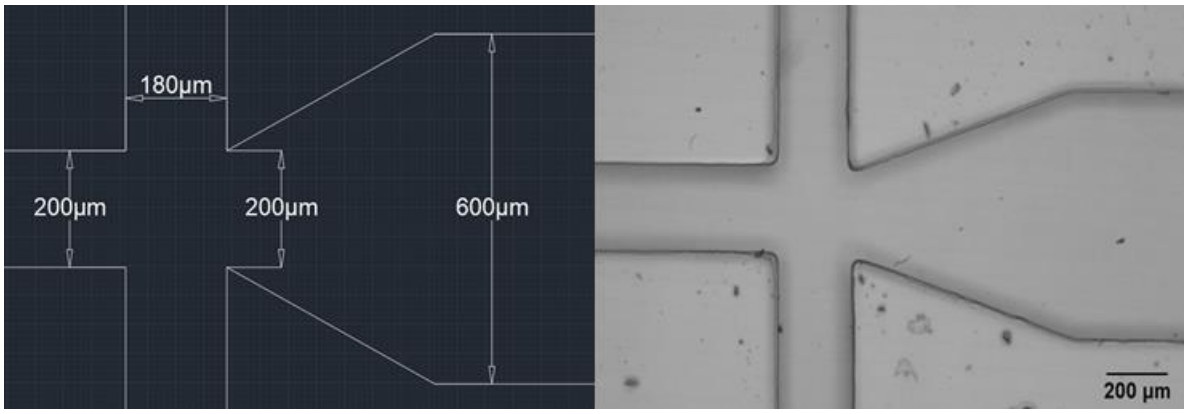


Figure 3.1 Schematic and snapshot of the microfluidic device used in this study

The creation of the microfluidic devices starts with the design of the channel using a computer aided design software (AutoCAD) (AUTODESK, 2020). The channel is designed in 2-D and the design is exported and sent to an external supplier (Micro Lithography Services Ltd) that provided a high definition photomask of the design. A solid mould of the microfluidic device is produced with photolithography, the process is illustrated in Figure 3.2.

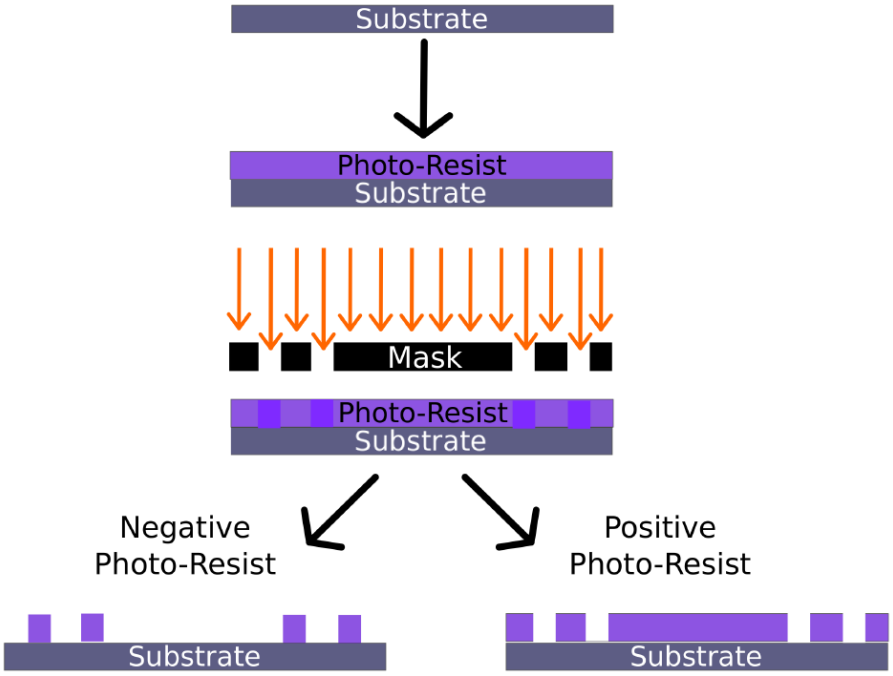


Figure 3.2 Schematic of photolithography representing the difference between a negative and a positive photoresist. Adapted from the PhD thesis of Dr. Zoe Schofield by her permission.

A 100 mm silicon wafer (Si-Mat, 2020) is spin coated with 5 g of the negative photoresist SU8-2075 (MicroChem, 2019). The rpm of the spin coater dictates the height of the microfluidic device and for this study the spin coating speed was 1750 rpm which resulted in a device height of 150 µm (MicroChem, 2019). The silicon wafer is then baked at 95 ºC for 30 minutes on a hot plate. After the baking is complete the wafer is placed in the mask aligner (Canon PLA-501FA Mask Aligner), the mask is placed above the wafer and exposed to UV light for two distinct intervals of 40 s, the energy required to solidify the photoresist is 240-260 mJ cm^{-2} (MicroChem, 2019). After the exposure another baking step followed at 95 ºC for 12 minutes. After this baking step is complete the wafer is immersed in a SU8 developer solution until the residual SU8-2075 is washed off. Finally, the device is washed with isopropyl alcohol (IPA) and dried. The wafer is then glued to a petri dish using an epoxy adhesive (Araldite professional adhesives, 2020) and left to properly attach overnight.

The microfluidic device is then created using soft-lithography (Figure 3.3), were PDMS (SYLGARD 184 (DOW, 2020)) is mixed with the curing agent in a mixture of 10 parts to 1 (MIT, 2013), then poured on the negative mould created by photolithography in a petri dish.

The dish is placed in a vacuum chamber in order to remove any gas bubbles present, and then placed in an oven for 90 minutes at 70 ^{o}C (DOW, 2020). After the curing is complete the device is cut using a knife and peeled of the wafer and inlet holes are punched in the PDMS chip using a 1.5 mm biopsy puncher. The device is then attached to a plain glass slide using oxygen plasma treatment (Zhou et al., 2010). After attaching the device on the glass slide it is placed on a hot plate for 15 minutes at 100 ^{o}C. The final steps consist of the surface treatment of the microfluidic channel with Aquapel (Aquapel Glass Treatment, 2020) in order to make is hydrophobic (Rotem et al., 2012). The microfluidic device is now ready to be used. The process is illustrated in Figure 3.3.

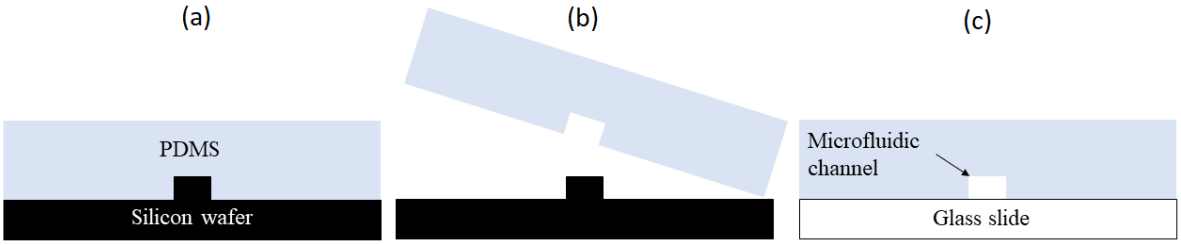


Figure 3.3 a: Soft lithography steps. a: PDMS on top of silicon wafer. b: detachment of solid PDMS from silicon wafer. c: PDMS attached to a glass slide

3.2.4. Droplet formation experiments

For the droplet formation experiments two syringe pumps (WORLD PRECISION INSTRUMENTS, 2020) were employed. The fluids used are injected using 5 mL syringes (Merck, 2020a). The solutions used are described in Table 3.2. For these experiments the dispersed phase flow rate was kept constant at 5 µl min^{-1} and the continuous phase flow rate was varied from 5 to 50 µL min^{-1}. The syringe was then connected to the microfluidic device using a syringe needle tip and Tygon microbore tubing (Cole-Parmer, 2020). The flow rate conditions were set and the flow was left to stabilise for 15 minutes before any observation were made. The microfluidic device was placed on the stage of an inverted optical microscope Nikon Ti-U (Nikon, 2020). The observation was carried out using a Photron Fastcam SA-5

(Photron). For the droplet formation experiments the solutions used were dyed with methyl violet, the objective used had a 10× magnification and the frame rate selected was 2,000 fps. The recordings are of sufficient duration to contain a significant number of droplet formation events. In the case of the neck kinetics experiments the frame rate selected was 30,000 fps and the objective used had a magnification of 40×. Figure 3.4 is a schematic representation of the experimental set-up.

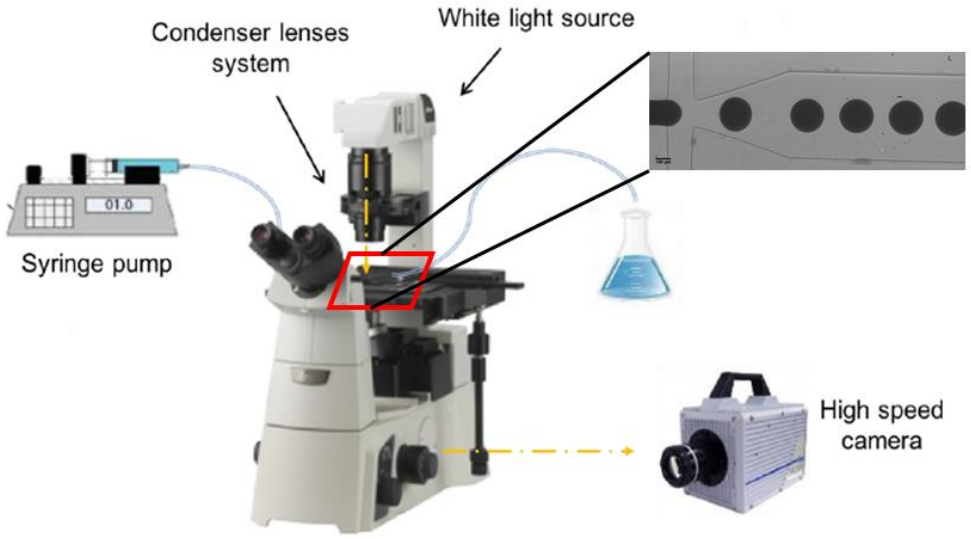


Figure 3.4 Diagram of the experimental set-up. Figure adapted from (Riccomi et al., 2018)

The analysis of the results was carried out using ImageJ (Schindelin et al., 2012). The video recording is imported on ImageJ and the pixel width and heigh values are changed according to the magnification in order to reflect the actual distance. For the droplet formation and neck kinetics experiments the diameter of the droplet and neck respectively parallel to the plane of observation are measured as shown by the red arrow in figures Figure 3.5 Figure 3.6. In the case of the droplet formation experiments the size of the droplets was measured in the outlet channel further away from the junction to minimise any effects of the velocity field in the droplet size. In each case ten droplets were sized and the measurements averaged. In the case of the neck kinetics experiments, three different neck thinning instances were measured over the same timescale.

Droplet sizes are measured downstream in the main channel of the microfluidic device. The red line in Figure 3.5 represents a typical droplet diameter measurement.

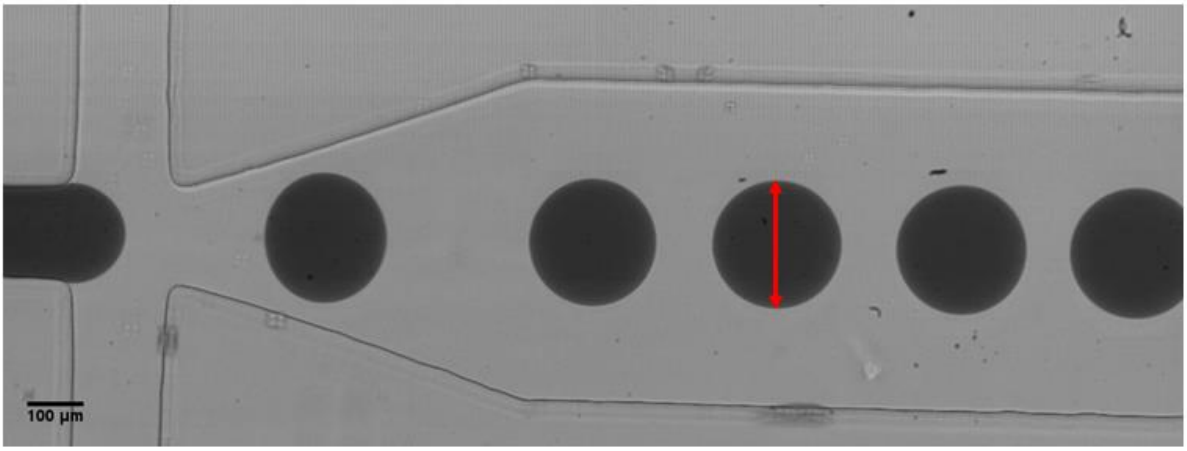


Figure 3.5 Typical droplet sizing instant.

Droplets are sized downstream to mitigate the effects of the channel expansion. The expansion reduces local fluid velocities deforming the moving droplets, therefore affecting the droplet size measurement (Bruus, 2007). The pixel to µm ratio was calibrated using a stage micrometre. With a magnification of 10× and using the Photron FastCam SA5, 1 pixel is equivalent to 2 µm. For the neck kinetics experiments, both the flow rates of the dispersed and continuous phases were kept constant at 5 and 25 µL min^{-1} respectively. Using the 40× magnification objective, 1 pixel is equivalent to 0.5 µm. A typical neck diameter measurement is presented in **Error! R eference source not found.**, where the red line represents the measured neck diameter. The error used is the standard experimental error. It represents the difference between the measured value and the true value of the measurement and is calculated by

$$E = \frac{\sigma}{\sqrt{N}} \tag{3.1}$$

where E is the error, σ is the standard deviation and N is the number of observations (Everitt and Skrondal, 2002).

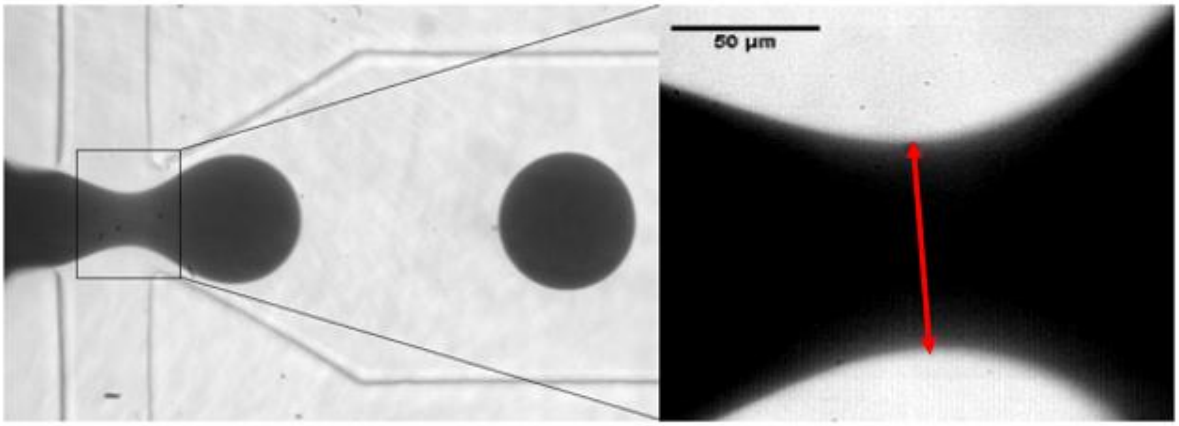


Figure 3.6 Typical neck diameter sizing instant

3.2.5. Ghost Particle Velocimetry experiments

For the velocimetry experiments, the same microfluidic device, pumps, syringes and tubing were employed. The flow rates chosen for these experiments are 5 µL min^{-1} for the dispersed phase and the 25 µL min^{-1} for the continuous phase. These experiments were carried out using a Nikon Ti-U inverted microscope and a Photron Fastcam SA-5 as previously. The frame rate selected was 30,000 fps and the numerical aperture of the condenser was set to $0.15 < NA_c < 0.5$. In each case ten droplet formation events were recorded and analysed.

Closing the condenser increases the depth of the focal plane ($\delta = Na_c/\lambda^2$, where λ is the wavelength (nm) of the light), meaning that the observation carried out contains information from a volume of fluid around the focal plane. For a microscope light source with a mean wavelength of 500 nm and the NA_c set at 0.15 the depth of the field of view is 20 µm (Buzzaccaro et al., 2013). The resolution of GPV is determined by the size of the speckles (Alaimo et al., 2006). The size of the speckles is determined by the maximum scattering angle and the wavelength of light source ($\sim\lambda/2\theta_{max}$). For particles with sizes smaller than the incident light wavelength, such as in this study, the maximum scattering angle is determined by the numerical aperture of the collection optics (NA_c). Therefore, the size of the speckles produced in this study is approximately 3 µm which determines the spatial resolution of the technique.

In order to examine if the polystyrene nanoparticles used for GPV faithfully follow the flow the Stokes number is calculated. The density of the nanoparticles is 1.05 g cm^{-3} as per the manufacturer specification while their nominal diameter is 200 nm. As a characteristic length the device depth is used while for the fluid velocity an average value of 0.05 m s^{-1} taken from the study of Roumpea et al. The viscosity of the dispersed phase is given in Table 3.1. Using equation 2.21 the Stokes number for the nanoparticles used is 0.04, therefore it can be assumed that the momentum response of the nanoparticles is small enough and they faithfully follow the flow of the dispersed phase.

The steps carried out during the post processing of the videos were the following. Initially the droplet formation events are separated in individual recording for better handling. Each of these videos contained enough frames to allow the observation of the necking stage up to the moment of pinch-off. The median is calculated for each of these videos using ImageJ and then subtracted. The videos are analysed separately and the velocity profiles along the interface are extracted. In each case two velocity profiles are extracted, one from the upper and one from the lower interface since the system is axisymmetric. This procedure is illustrated in Figure 3.7 and is carried out with purpose written scripts in ImageJ and Matlab.

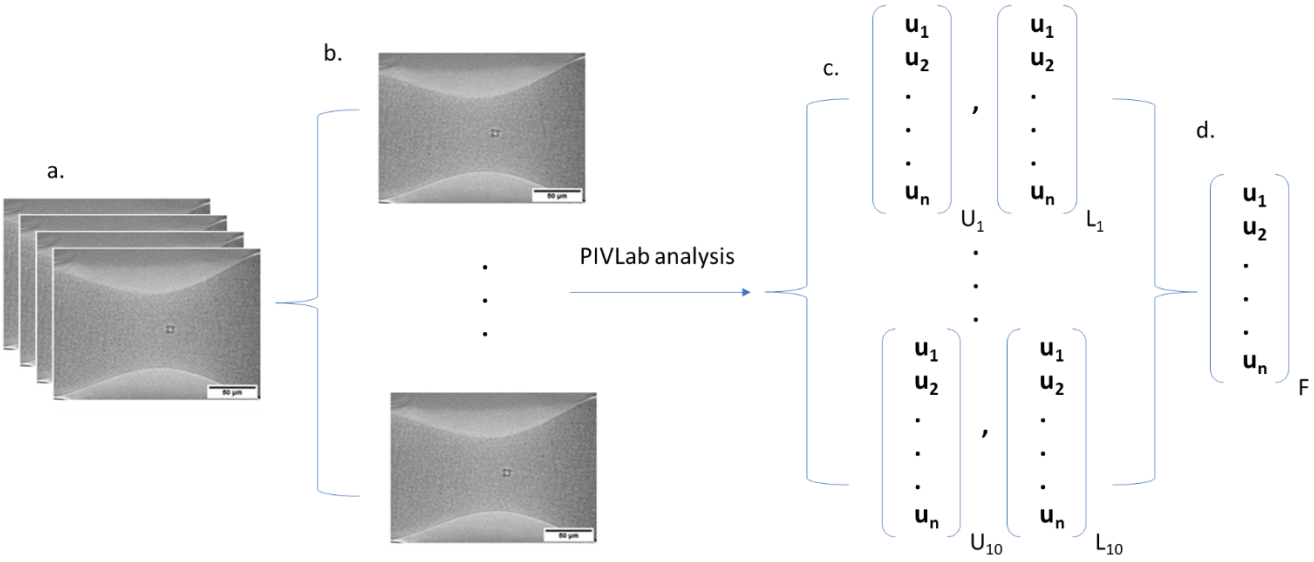


Figure 3.7 a. Initial image stack (video) of multiple droplet formation events. b. Separation of the droplet formation events in individual image stacks and median subtraction. c. Each stack is analysed separately and the velocity profiles on the upper(U) and lower(L) interface are extracted. d. the velocity profiles extracted from each droplet formation event are averaged.

In each case the median was calculated and then subtracted from each frame in order to bring forward the speckle pattern. The intensity at each point of these observations is the sum of the time independent background contribution and the scattering caused by the presence of the nanoparticles. An example of this analysis is displayed in Figure 3.8.

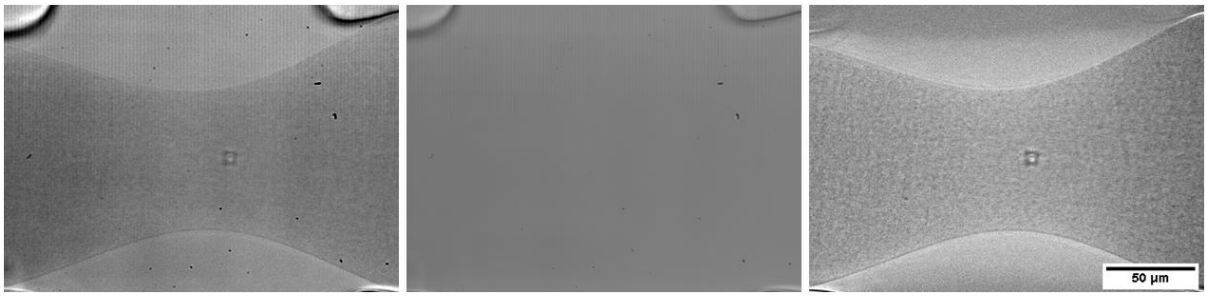


Figure 3.8 Example of image processing. From left to right, original video capture, intensity median over 1000 frames, median subtracted.

The speckles are analysed using PIVLab and the analysis consists of three steps, the pre-processing, the analysis and the post-processing. The pre-processing step consist of choosing a region of interest or setting a mask and choosing the area over which the vectors will be averaged over. An example of manual masking using PIVLAb is presented in Figure 3.9.

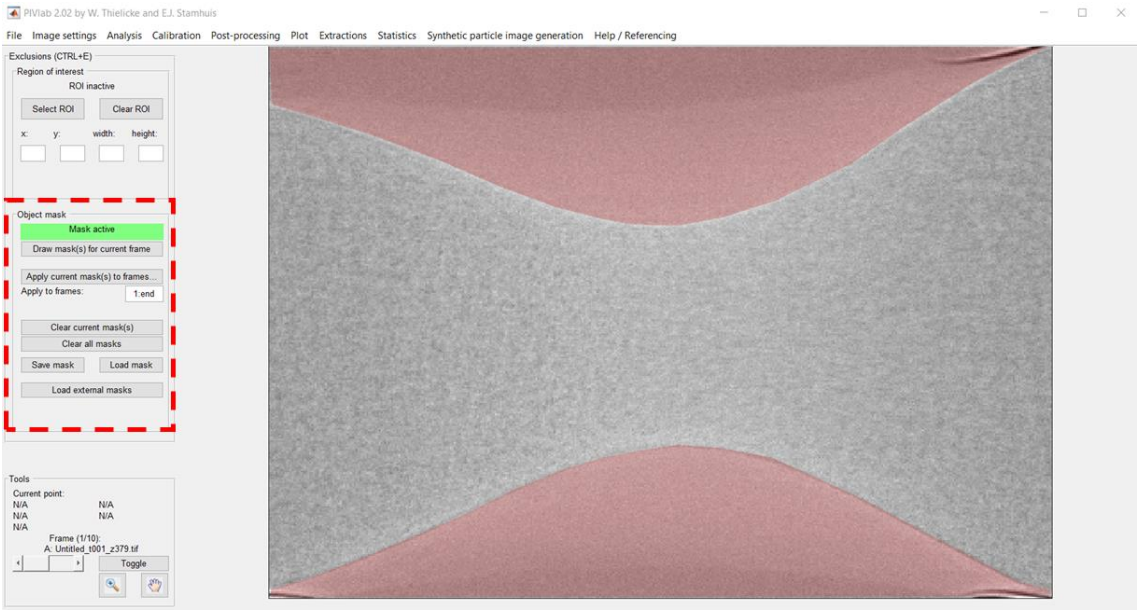


Figure 3.9 Manual masking example using PIVLab. The highlighted red square represents the software functions that allow the masking.

The final pre-processing step consists of choosing the interrogation area. This is presented in Figure 3.10.

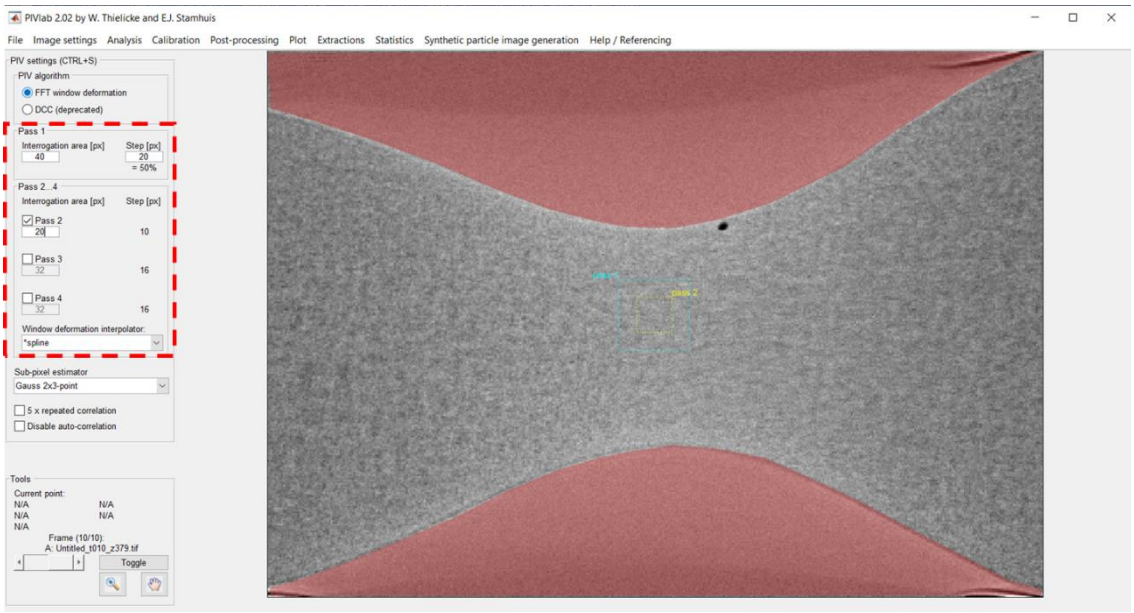


Figure 3.10 Setting the PIV interrogation area using PIVLab. The highlighted area represents the software input fields.

The interrogation area dictates the area over which the vectors are averaged. In this study the interrogation area selected has a size of 40 μm while a second pass was done over an interrogation area of 20 μm. After completing all pre-processing settings, the images are cross-

correlated producing the velocity field. The next step consists in validating the produced velocity vectors. The validation is carried out manually, this is presented in Figure 3.11.

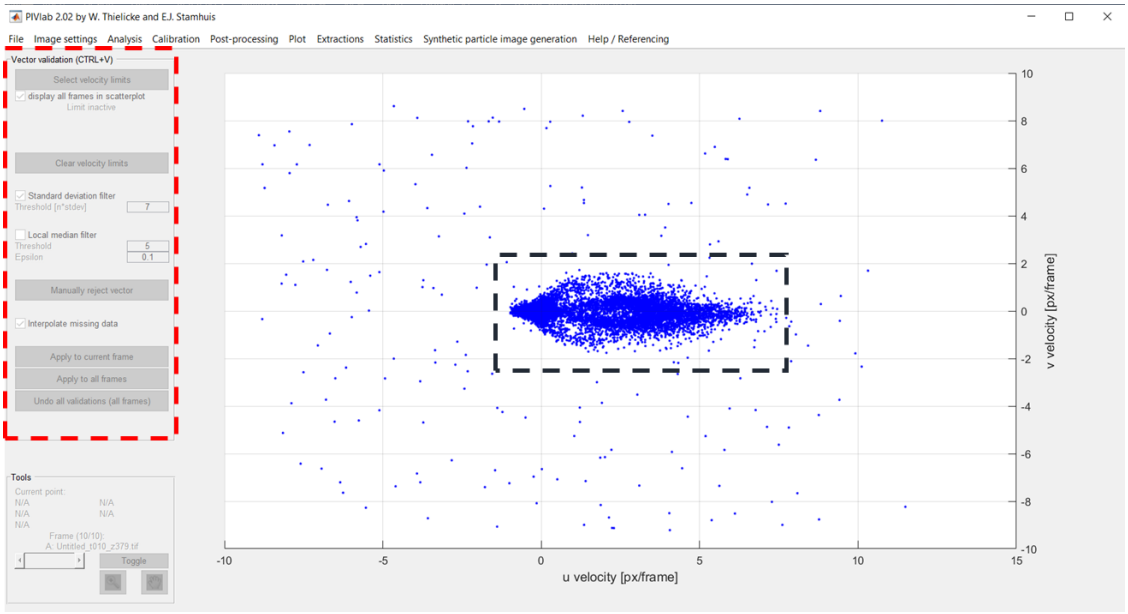


Figure 3.11 Vector validation step using PIVLab. The red rectangle represents the software functions allowing for the vector validation. Vectors outside the black rectangle are discarded.

The velocities extracted are validated by calculating the theoretical velocity (Watson, 1998)

$$u = \frac{Q}{A} \tag{3.2}$$

where u is the average fluid velocity (m s^{-1}), Q is the volumetric flow rate (m^3 s^{-1}) and A is the cross-sectional area. For a dispersed phase flow rate of 5 µL min^{-1} and a neck diameter of 50 µm, the average fluid velocity is 42 mm s^{-1} which very close to the velocities extracted using PIVLab. The final step is extracting the velocity magnitudes along the interface. This process is illustrated in Figure 3.12. A line is drawn as close to the interface as possible while the number of 300 interpolated points is selected. This value is the default value and changing it doesn't produce any significant change in the velocity profile as presented in Figure 3.12.

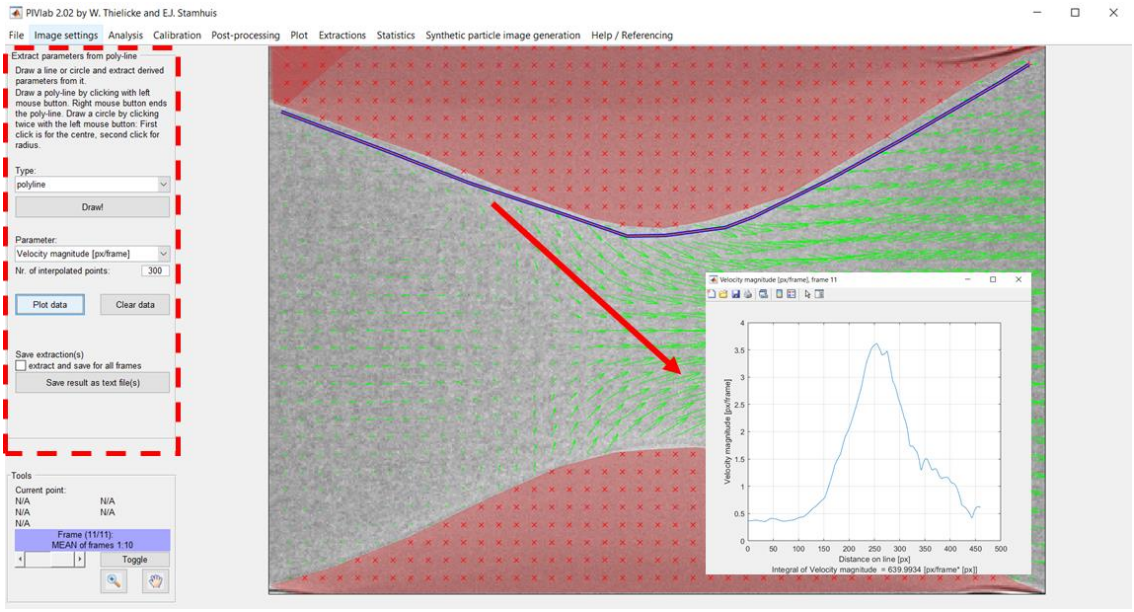


Figure 3.12 Illustration of the extraction of the velocities along the interface. The red rectangle demonstrates the functions allowing this operation. The inset is the velocity magnitudes along the length of the line.

The values of the extracted parameter are extrapolated on the line. This process is repeated for each frame separately and the final velocity profiles are averaged.

GPV has been found to produce comparable results to μPIV for Reynolds numbers smaller than 350 (Riccomi et al., 2018). The Reynolds number is defined as (McCabe et al., 2005)

$$Re = \frac{uL\rho}{\mu} \tag{3.3}$$

where u is the fluid velocity (m s^{-1}), L is a characteristic length (m), ρ is the density of the fluid (Kg m^{-3}) and μ is the viscosity (Pa s). Using the fluid velocity calculate using equation 3.1, the channel depth as the characteristic length and the fluid properties presented in Table 3.1 the Reynolds number for this study is in the order 10^0. Other sources of error when implementing GPV arise in the fact that the light collected by the microscope optics comes from an area with a depth proportional to the numerical aperture of the condenser. As the droplet pinch-off approaches, the neck diameter becomes comparable to the depth of the field of view, therefore information is collected from a variety of fluid layers having different velocities decreasing accuracy. Furthermore, fluid velocities increase as the pinch-off approaches and the Reynolds

number increases by one order of magnitude increasing the experimental error. Another source of error is the high frame rate used to capture rapid phenomena. Using the current camera set up, the increase in acquisition frame rate increases the electronic noise which reduces the contrast that the speckles produce, reducing the resolution of GPV.

Chapter 4: Microfluidic droplet formation with the presence of surfactant

Introduction

In this Chapter, results of equilibrium interfacial tension measurements made between the continuous and dispersed phases used in the study are discussed. Measurements of the dynamic surface tension of surfactant solutions below the cmc for the C10TAB and C12TAB are then presented. Then, the effect of surfactant concentration and continuous phase flow rate in the emulsification process in microchannels is discussed including the presentation of a scaling law derived from the droplet size distributions observed. Finally, this chapter concludes by studying the satellite droplet sizes under the current experimental conditions.

4.1. Equilibrium interfacial tension of various surfactant solutions and surfactant parameters

The equilibrium interfacial tension between the dispersed aqueous phase and each of the three different oil phases used was measured using the pendant drop method described in §3.2.1. Figure 4.1 shows the isotherms for 52% by weight glycerol-water solutions at various surfactant concentrations. The solutions were chosen to represent a various range of surfactant concentrations, below and above the cmc. The continuous phases used were 4.6, 19 and 96 mPa s silicone oil.

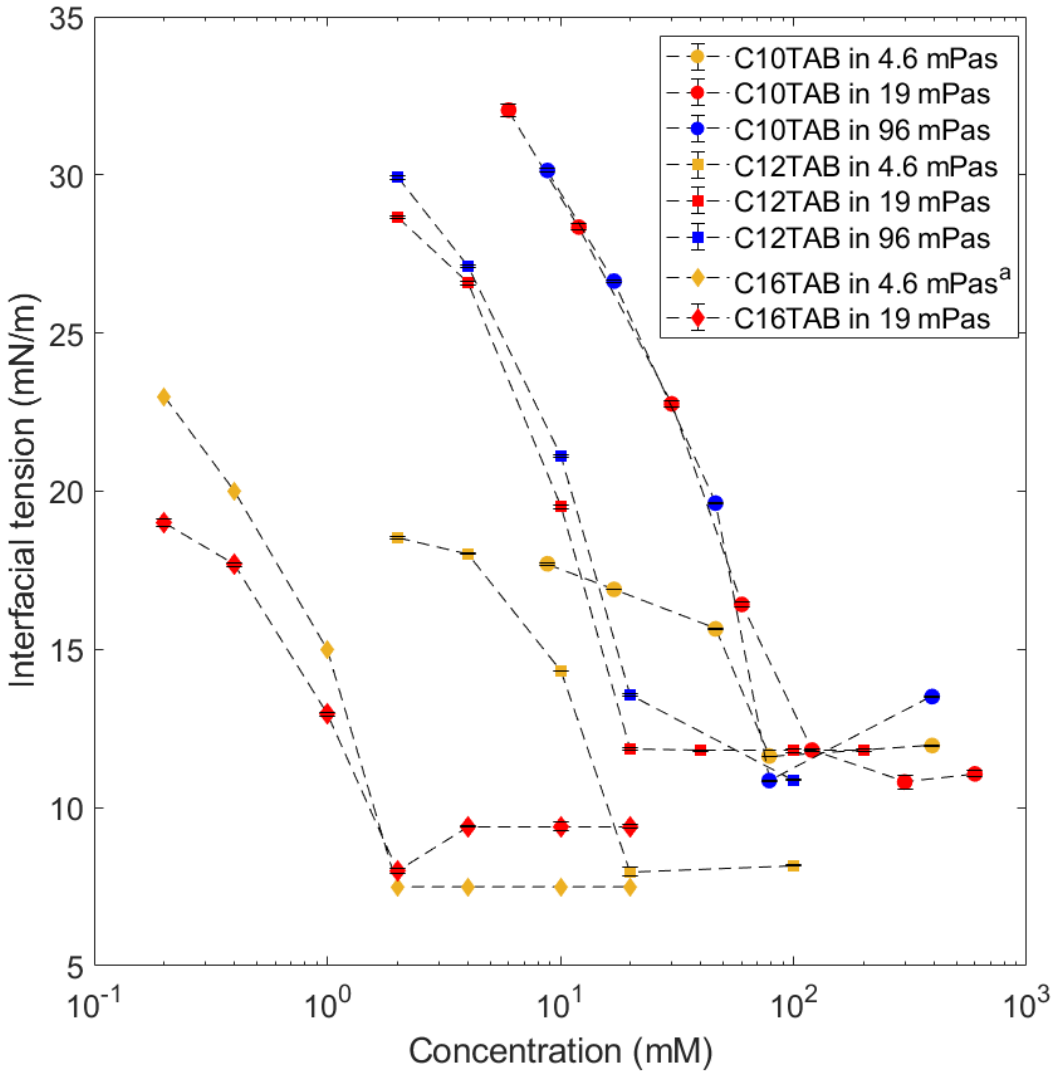


Figure 4.1 Equilibrium interfacial tensions for the solution used in the study. a:(Kovalchuk et al., 2018c)

It is observed that the increase in surfactant concentration leads to a reduction in equilibrium interfacial tension. For surfactants with higher values of cmc the interfacial tension levels off at higher concentrations. The cmc of the surfactant is affected by the presence of glycerol (Porter, 2013). The presence of glycerol leads to an increase in the cmc for all surfactants. The cmc of C10TAB in 52% glycerol solution can be calculated from the isotherm in Figure 4.1. Once the cmc is reached the interfacial tension remains constant despite the increase in surfactant concentration. Table 4.1 summarises the cmcs of the surfactants used in the study.

Table 4.1 Cmc in water and in a 52% wt. glycerol-water solution. a: (Kovalchuk et al., 2016), b:(Kovalchuk et al., 2018c), c: measured value

	Cmc in water (mM)	Cmc in 52% wt. glycerol (mM)
C10TAB	60[a]	78.7[c]
C12TAB	15[b]	20[b]
C16TAB	0.9[b]	2[b]

For the interfacial tension of the C16TAB solutions in 96 mPa s silicone oil it is assumed that since there is not a significant change between the 4.6 mPa s and 19 mPa s isotherms the values are going to be similar. For the purposes of this study the 19 mPa s equilibrium interfacial tension values will be used for any calculations where the values for the 96 mPa s are needed. From the equilibrium interfacial tension data, it appears that increasing the surfactant concentration should lead to a reduction in droplet sizes. This is because when two immiscible liquids are brought in contact, they will tend to maintain the smallest interface between them in order to reduce their interfacial energy. When a surfactant is introduced, the interfacial tension is reduced, reducing interfacial energy allowing for a larger interface between the two phases. This suggest that the lower the interfacial tension the smaller the forming droplets are (Graf and Kappl, 2003).

The data presented in Figure 4.1 is fitted to the Langmuir isotherm model using the IsoFit free software (Möbius et al., 2001). The calculated isotherm parameters are presented in Table 4.2. The adsorption isotherm for the Langmuir model is given by

$$\Gamma = \Gamma_m \frac{bc}{1+bc} \tag{4.1}$$

Where Γ_m (mol m^{-2}) is the surfactant surface concentration, Γ_∞ (mol m^{-2}) is the limiting adsorption, b (m^3 mol^{-1}) is the adsorption constant and c (mol m^{-3}) is the surfactant bulk concentration. For each surfactant the isotherm data from different continuous phases is combined since there is minimal effect of viscosity. The calculated values are in good agreement with data for the same surfactant at water-air interfaces (Mucic et al., 2011) and with data for C10TAB in water in contact with 50 cSt silicone oil (Kovalchuk et al., 2019a).

Table 4.2 Limiting adsorption and adsorption constants for the surfactants used in this study

	C10TAB	C12TAB
Γ_∞ (mol m^{-2})	$1.4 \cdot 10^{-5}$	$1 \cdot 10^{-5}$
b (m^3 mol^{-1})	$9 \cdot 10^{-3}$	$6 \cdot 10^{-2}$

For the C16TAB surfactant parameters an average of C10TAB and C12TAB is used. The dynamic surface tension was then measured using a maximum bubble pressure tensiometer described in §3.2.2. Dynamic Interfacial tension measurements for the time-scales typical of microfluidic droplet formation are not available in literature. Instead dynamic surface tension measurements for air-water interfaces can reveal important information about the dynamic surfactant behaviour in the microfluidic system studied (Kovalchuk et al., 2018c). Figure 4.2 displays the dynamic surface tensions for different surfactant solutions at concentration below the cmc.

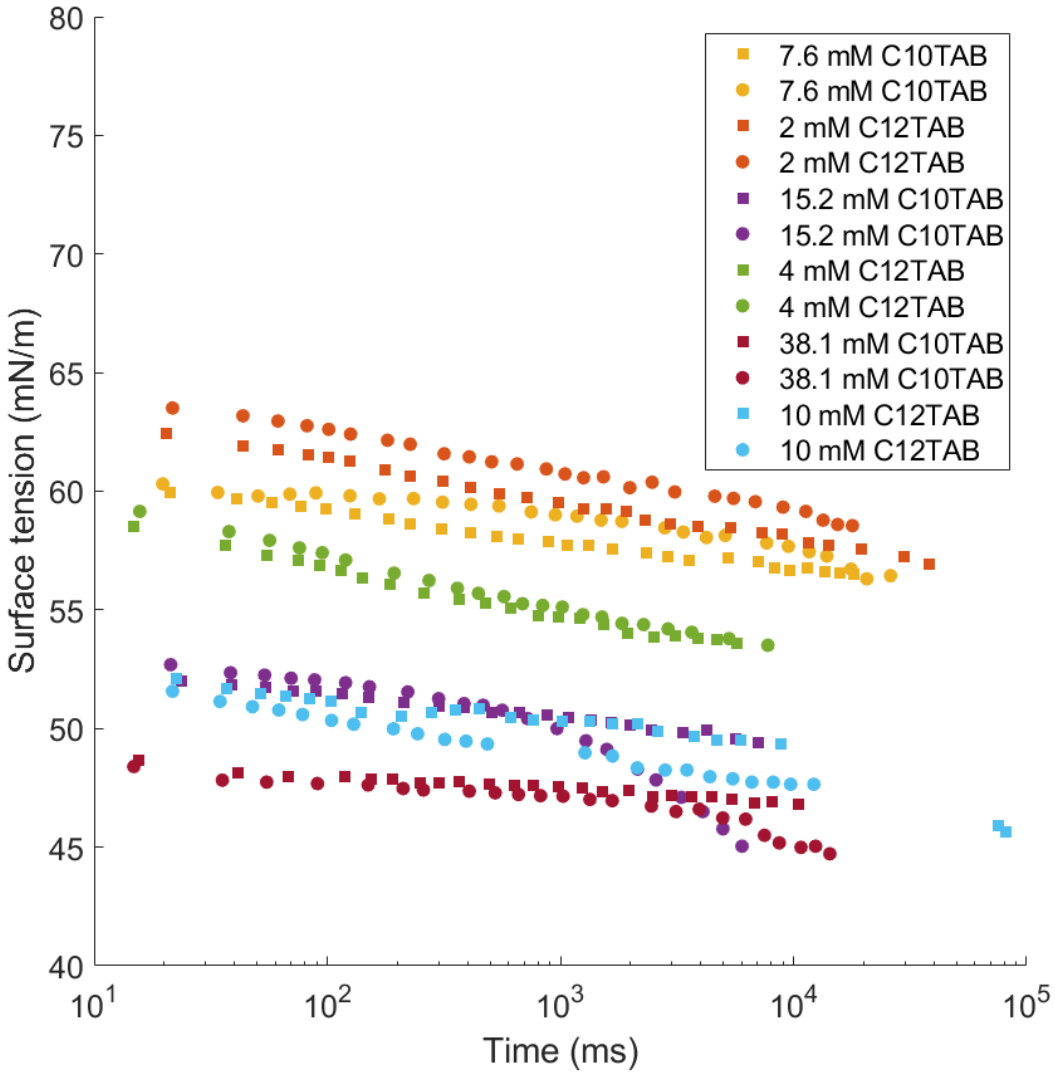


Figure 4.2 Dynamic surface tension for C10TAB and C12TAB solutions. Full circles are the dyed solutions, squares are the solutions with nanoparticles.

Timescales of droplet formation in microfluids are in the range of 10^1-10^2 ms and no dynamic interfacial tension measurements exist for these timescales. In the case of dynamic surface tension measurements, both dyed solutions and nanoparticle solutions were investigated. This is important to quantify the effect of additives on the behaviour of interfacial tension. In Figure 4.2 is observed that the dynamic surface tension is very similar between dyed and nanoparticles solutions. The only solution that displays a distinct behaviour is the 15.2 mM C10TAB dyed solution. It is most probable that this behaviour is caused by surface active impurities present in the studied solution. If this behaviour was caused by the effect of surfactant, it would be

expected also for the 38.1 mM C10TAB solution as well. Nonetheless, the reduction in interfacial tension occurs at timescales that are beyond the scope of this study and therefore do not affect the droplet formation process. Other studies performing similar experiments determined that for less active surfactants (high cmc values) like C10TAB the effective interfacial tension during droplet formation is determined by their equilibrium properties (Kovalchuk et al., 2016). The most notable aspects of the above experiments are the fact that for small timescales, in the range of microfluidic droplet formation, there is a reduction in surface tension as time increases, suggesting that for these timescales and for small surfactant concentrations the solutions display a dynamic surface tension different from the equilibrium surface tension. This is an indication that these solutions might display a dynamic interfacial tension during droplet formation. Furthermore, it is notable that C12TAB solutions appear to always display larger dynamic surface tension values than the respective C10TAB solution of the same cmc percentage. For example, the dynamic surface tension values for the 7.6 mM (0.1cmc) C10TAB solution are smaller than the 2 mM (0.1cmc) C12TAB solution. The above suggests that surfactant quantity is an important factor when it comes to dynamic surface, or interfacial, tension.

Another important parameter associated with the surfactant mass transport is the surfactant's diffusion coefficient. The diffusion coefficient of the surfactant is present in equation 2.11. increasing the diffusion coefficient of the surfactant leads to a reduction of the diffusion limited adsorption timescale. The diffusion coefficient can be calculated using (Perkins and Geankoplis, 1969)

$$D_{Am}^{o} n_{m}^{0.8} = \sum_{j=1}^{n} x_j \, D_{Aj}^{o} n_{j}^{0.8} \tag{4.2}$$

Where D_{Am}^{o} is the effective diffusion coefficient for a dilute solute A into the mixture ($cm^2 \cdot s^{-1}$), D_{Aj}^{o} infinite dilution binary diffusion coefficient of solute A into solvent J ($cm^2 \cdot s^{-1}$), x_j molar

fraction of j, n_m is the viscosity of the mixture (cP) and n_j is component's J viscosity (cP). D_{Aj}^{o} is given by

$$D_{Aj}^{o} = \frac{7.4\times10^{-8}((\varphi M_j)^{1/2})T}{n_j V_A^{0.6}} \quad (4.3)$$

Where M_j is the molecular weight of solvent j (g·mol^{-1}), T is temperature (K), n_B is the viscosity of the solvent j (cP), V_A is the molar volume of solute A (cm^2·mol^{-1}) and φ is an association factor equal to 2.6 (Perkins and Geankoplis, 1969). The calculated diffusion coefficients are $1\cdot10^{-10}$, $9.4\cdot10^{-11}$ and $8.2\cdot10^{-11}$ m^2 s^{-1} for the C10TAB, C12TAB and C16TAB respectively.

4.2. Droplet sizes in the presence of surfactants

The aim of these experiments is to characterise the system in terms of droplet formation by recording droplet sizes under various flow rate conditions. Table 3.2 summarised the solutions used. Under the experimental conditions described in Chapter 3, droplets are formed in the dripping regime as described in §2.3. Figure 4.3 displays representative instances of droplet formation under dripping.

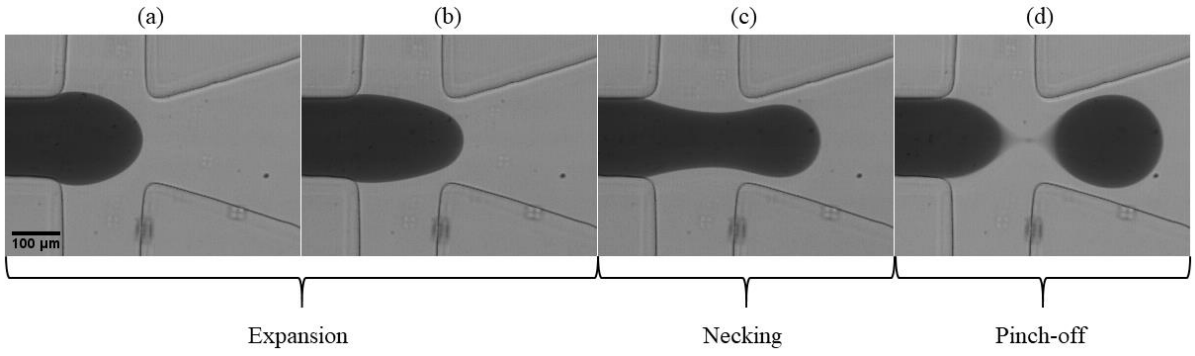


Figure 4.3 Droplet formation in a flow-focusing microfluidic device. (a) and (b) expansion, (c) necking, (d) pinch-off.

A reduction in droplet sizes with an increase in the flow rate of the continuous phase is expected, since this will increase the drag force acting against the interfacial tension force (Kovalchuk et al., 2018d). Furthermore, an increase in surfactant concentration will lead to a reduction in droplet sizes since interfacial tension is reduced which in turn reduces the

interfacial tension force acting against the break-up (Kovalchuk et al., 2018d). Lastly an increase in the viscosity of the continuous phase will also lead to a reduction in droplet sizes, since it will lead to an increase in the drag force (Cubaud and Mason, 2008). Droplet sizes are measured downstream in the main channel of the microfluidic device.

Initially, the droplet sizes for a solution without surfactant under various continuous phase flow rate conditions and a constant dispersed phase flow rate are presented. Droplets produced in this type of microfluidic device are not spherical, they are "squeezed" in the z-direction and closer to a "pancake" shape (Kovalchuk et al., 2018d). This holds as long as the droplet diameter is larger than the channel depth, which in this case is 150 μm. In this case the droplet size is the diameter of the drop visible in the plane of observation. The flow rate ratio is given by

$$\varphi = \frac{Q_d}{Q_c} \tag{4.4}$$

Where Q is the flow rate ($m^3\ s^{-1}$). The subscripts c and d denote the dispersed and continuous phases respectively.

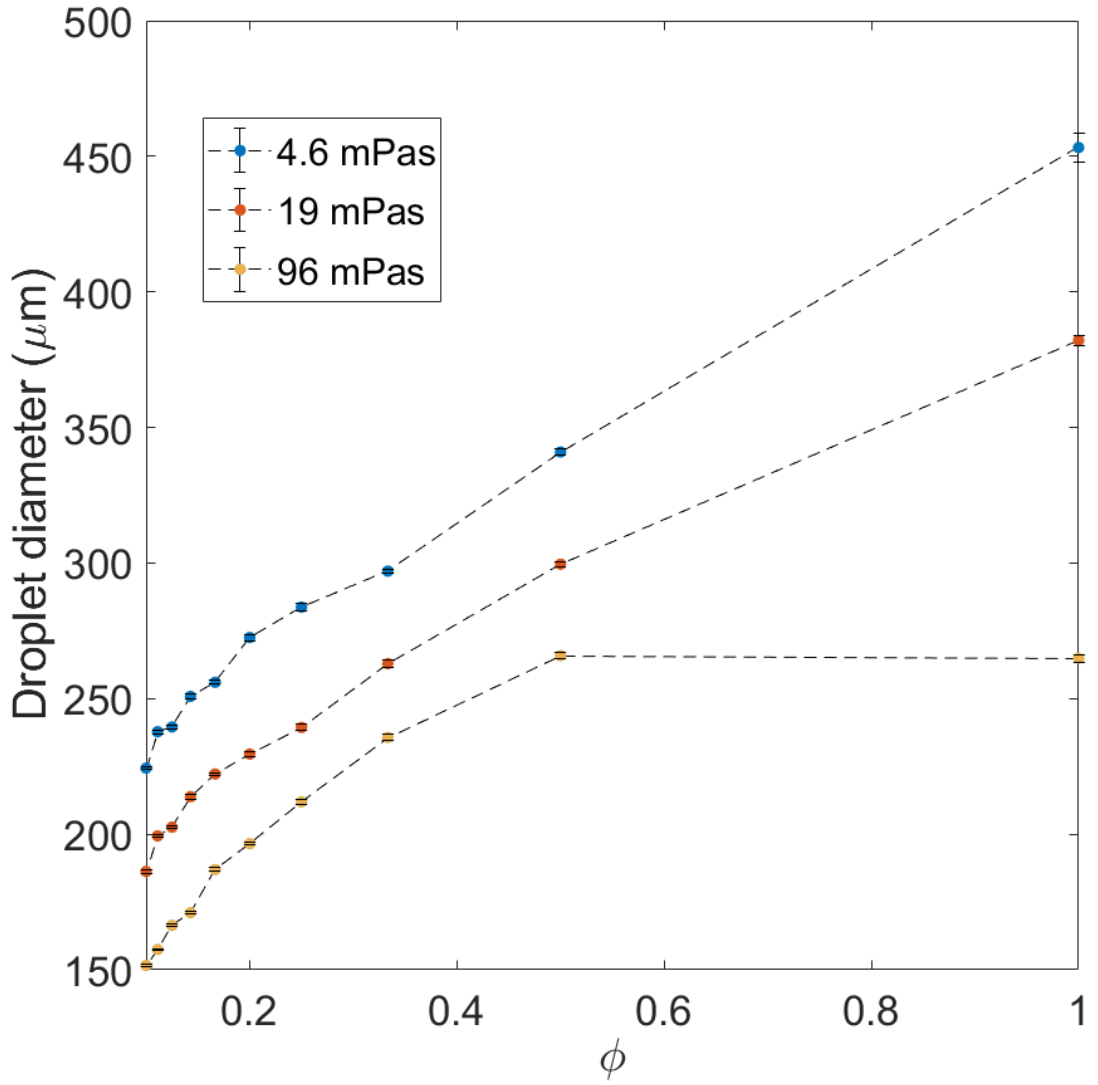


Figure 4.4 Droplet sizes for a 52% w/w glycerol-D.I. solution in various silicone oils

Figure 4.4 shows the variation of the droplet sizes versus the flow rate ratio. A clear increase in droplet sizes is observed as φ increases; this corresponds to a decrease in the continuous phase flow rate at a constant dispersed phase flow rate. Furthermore, as the viscosity of the continuous phase increases, the droplet size decreases. These results are consistent with previous experiments using surfactant-free solutions (Cubaud and Mason, 2008). Increasing the viscosity and the continuous phase flow rate increases the drag force according to equation 2.1.

$$F_D = 4\pi\mu_c \frac{2n+3}{n+1} D_d(u_c - u_d) \tag{2.1}$$

Since the drag force increases but the interfacial tension force remains the same, the droplet sizes decrease.

4.2.1. Systems with surfactant

Similarly, the emulsification outcome of various surfactant solutions is studied. The presence of surfactant leads to a reduction of interfacial tension, which leads to a smaller interfacial tension force, therefore to a smaller droplet size compared to a solution without surfactant under the same conditions. Furthermore, a reduction in droplet sizes as interfacial tension decreases with an increase in surfactant concentration is also expected. This effect should level off once the cmc of a surfactant is reached (Kovalchuk et al., 2016).

4.2.1.1. Droplet formation of C10TAB aqueous solutions in 4.6, 19 and 96 mPa s silicone oil

Similarly to Figure 4.4, the droplet diameter is represented in the y-axis and the flow rate ratio in the x-axis for various C10TAB surfactant solutions. The cmc of C10TAB in a 52% by weight glycerol solution is 76 mM. The solutions used for this study are 0.1, 0.2, 0.5, 1, 2, 5 and 10 times the cmc following previous studies (Kovalchuk et al., 2016). Figure 4.5 shows the droplet sizes for the above solutions as a function of both flow rate ratio and continuous phase viscosities. As predicted by literature droplet sizes decrease with an increase in the continuous phase flow rate and the concentration of surfactant. The increase in continuous phase flow rate increases the drag force described by equation 2.1 while the increase in the concentration of surfactant lowers the interfacial tension force described by equation 2.2.

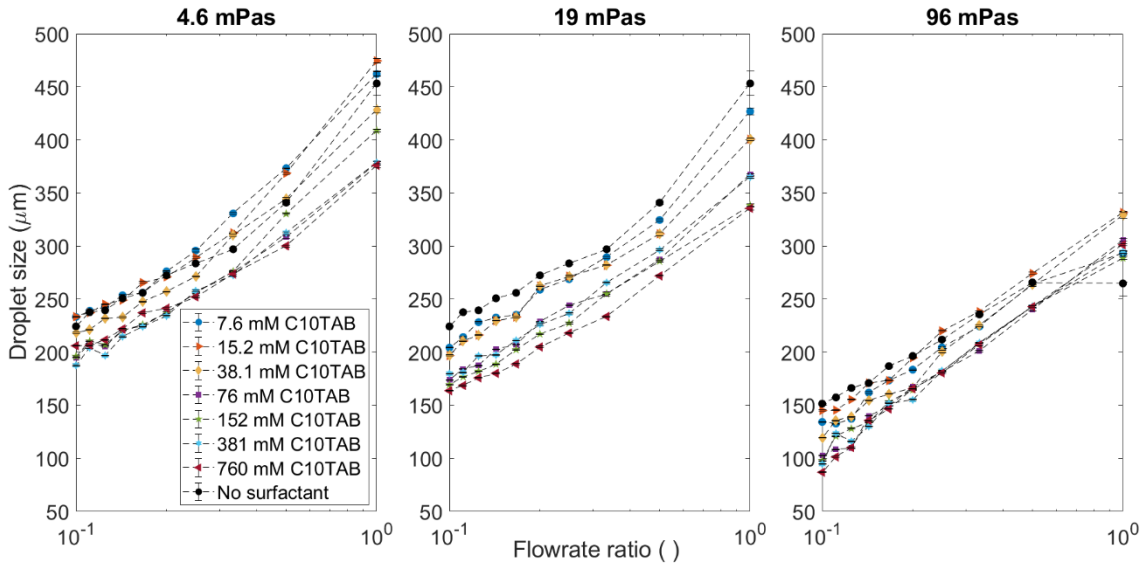


Figure 4.5 Droplet sizes for a 52% w/w glycerol-D.I. water with various surfactant concentrations

For a given viscosity of the continuous phase the droplet sizes increase with an increase in the flow rate ratio and with a decrease in surfactant concentration. It is notable that solutions with small quantities of surfactant display similar droplet size distributions, while after reaching concentrations above the cmc droplet sizes level off, suggesting a levelling off of the interfacial tension as well. In the case of 4.6 mPa s continuous phase, the clustering of the droplet size distributions observed for the solutions with small surfactant quantities can be explained by examining the equilibrium interfacial tension presented in Figure 4.1. The equilibrium interfacial tension values for these quantities of surfactant are very close to each other. This in turn means that the interfacial tension force resisting the break-up is similar in each case, therefore is reasonable that droplet sizes are similar. Furthermore, examining the dynamic surface tension from Figure 4.2 it is observed that for short timescales the solutions display a dynamic surface tension, larger than the equilibrium value.

It is useful to examine the timescales associated with the surfactant mass transport and compare them with the droplet formation timescales. The limiting adsorption timescale can be calculated using equation 2.10. Using the representatives values for the parameters of the Langmuir model of $5 \cdot 10^{-6}$ mol m^{-2} for the limiting adsorption (Γ_∞) and $5 \cdot 10^{-10}$ m^2 s^{-1} for the diffusion coefficient

for this type of surfactants (Nowak et al., 2017), the timescale associated with the replenishment of the surfactant due to adsorption on the interface from the bulk is in the range of 10^{-5}-0.8 ms depending on the surfactant concentration. Replenishment of surfactant on an expanding interface also occurs due to Marangoni phenomena. Inhomogeneities in surfactant concentration can occur due to the deformation of the interface, the action of the continuous phase and the flow of the dispersed phase. These differences in concentration create interfacial tension differences that drive fluid motion that equalise any differences in concentration along the interface. In the case of the 4.6 mPa s continuous phase, the time scale associated with these effects can be estimated using equation 2.11. Using as $\Delta\gamma$, the difference between the equilibrium interfacial tensions of the surfactant-free and surfactant solution, the Marangoni time scale is in the range of 10^{-1} ms (Kovalchuk et al., 2019b). The Marangoni timescales represents the time it takes for Marangoni phenomena, to equalise any concentration inhomogeneities.

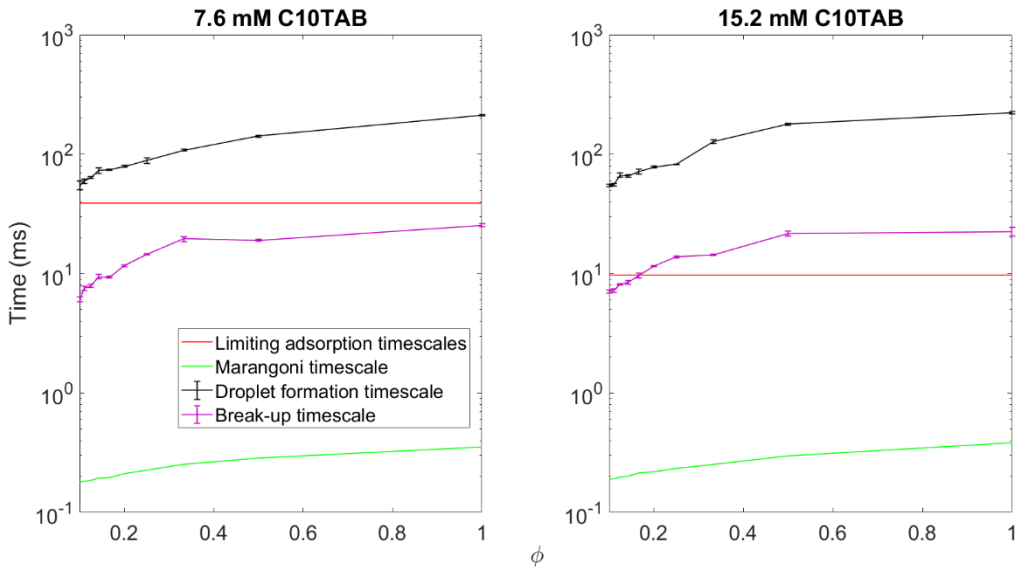


Figure 4.6 Timescales associated with the replenishment of surfactant on the interface for C10TAB solutions in 4.6 mPa s silicone oil for various flow rate ratios.

Figure 4.6 shows that, in this case, the phenomena responsible for replenishing the surfactant on the interface as it deforms, develop in time scales smaller than the time scales of droplet break-up for all C10TAB solutions when the break up occurs in the 4.6 mPa s continuous phase,

suggesting that the process evolves under equilibrium conditions in each case. Droplet formation is a periodic phenomenon and the droplet formation timescales is defined as the period of droplet formation. Experimentally it is measured as the time between each droplet formation event. The break-up time scale is the time from the beginning of the necking stage to the droplet pinch-off. During the expansion stage the droplet invades the junction, and during this stage, the curvature of the interface is positive. As the process evolves, the action of the continuous phase, squeezes the dispersed phase in the junction and the curvature of the neck interface becomes smaller. The necking stage starts when the curvature of the interface is zero. From that point in time the curvature becomes negative until the neck breaks and releases the droplet. The break-up time is defined as the time from when the neck curvature is zero until the pinch-off of the droplet.

Similarly, the timescales associated with the process for the case of 19 mPa s continuous phase are examined. The increase in the continuous phase viscosity leads to reduction in interface velocities (Kovalchuk et al., 2018d), and at the same time the increase in viscosity leads to an increase in the drag force reducing the droplet size. Viscosity is a measure of the resistance to the flow of a liquid and increasing it leads to a reduction in fluid velocities (Zhang et al., 2012). If the flow of the continuous phase is reduced it then follows that interfacial velocities will become smaller due to stress continuity on the interface. Since the continuous phase viscosity increased, the interfacial phenomena replenishing the surfactant on the interface are impacted (Kovalchuk et al., 2019b). The increase in viscosity leads to an increase in the Marangoni timescales to 10^{-1} -10 ms. Figure 4.7 compares the different timescales for these solutions.

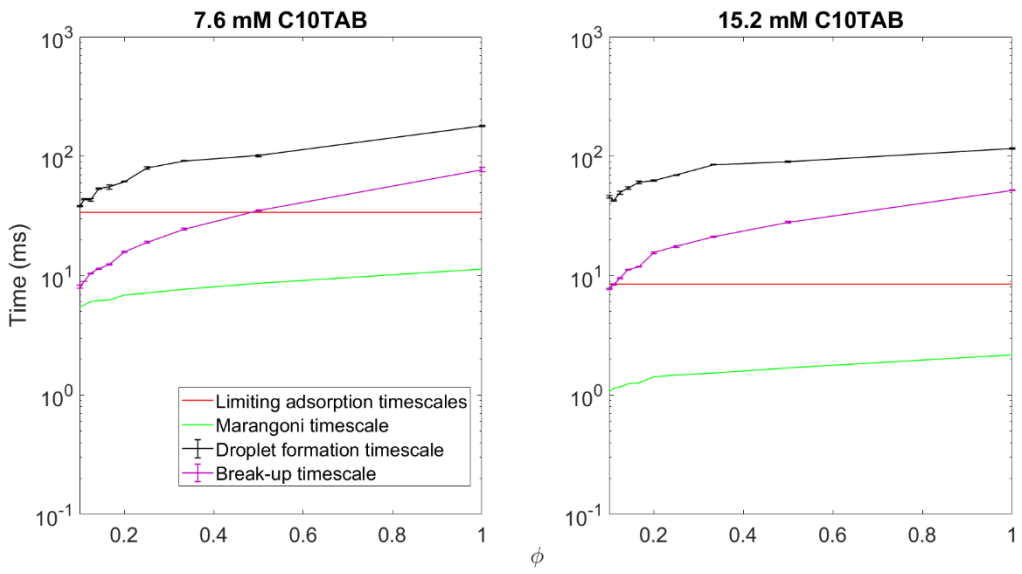


Figure 4.7 Timescales associated with the replenishment of surfactant on the interface for C10TAB solutions in 19 mPa s silicone oil.

For solutions with quantities of surfactant below the cmc the replenishment of surfactant on the interface happens due to Marangoni phenomena. The Marangoni timescale is close to the break-up timescales, suggesting that solutions below the cmc (7.6 and 15.2 mM) might behave under non-equilibrium conditions, displaying properties closer to a solution without surfactant, explaining the similarity between their droplet size distributions even though their equilibrium interfacial tensions differ (Figure 4.1). As the surfactant concentrations are increased, both the Marangoni and the limiting adsorption timescale decrease, becoming smaller than the break-up timescale. Nevertheless, a clear distinction between the droplet size distributions across all surfactant concentrations is observed. As the solution concentrations are above the cmc, equilibrium interfacial tension is constant which would suggest similar droplet formation behaviour. It can be assumed that the Marangoni phenomena play a major role in equalising interfacial tension across the interface since distinctions between the distributions are observed, even though the equilibrium interfacial tensions are the same. Any Marangoni phenomena in this case are impacted by the higher viscosity of the continuous phase allowing for a dynamic interfacial tension to manifest in each case. The effect of the quantity of surfactant was also considered. C10TAB, having the largest cmc is present in the solution in the largest quantities.

It was shown in studies that the concentration of cationic surfactants affects the viscosity of the system (Shah et al., 2016). As the surfactant concentration is increased above the cmc, the viscosity of the system is impacted, which in turns affects droplet formation.

Lastly, the case of the 96 mPa s continuous phase is examined. The limiting adsorption timescale is the same, since the same solutions are used. Figure 4.8 shows in comparison the different timescales for this case.

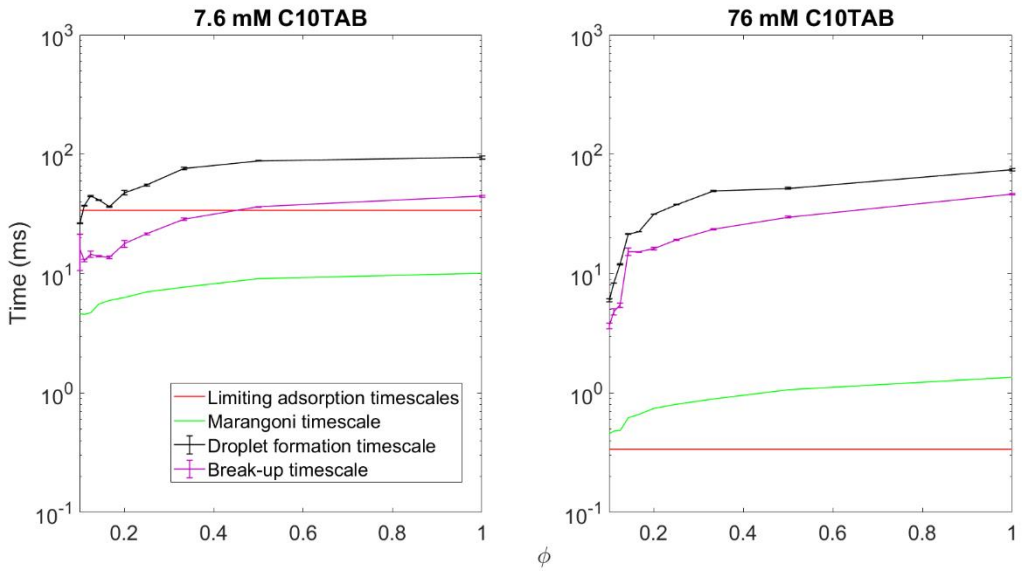


Figure 4.8 Timescales associated with the replenishment of surfactant on the interface for C10TAB solutions in 96 mPa s silicone oil.

The increase in the continuous phase viscosity has significantly increased the break-up timescales, slowing down the process. In this case the shortest time scale is the limiting adsorption time scale, suggesting that the replenishment of surfactant along the interface is controlled by adsorption/desorption phenomena. The increase in continuous phase viscosity increases the stability of the neck (Carrier et al., 2013). This means that the differences in equilibrium interfacial tensions between solutions are suppressed explaining the clustering of the droplet size distributions for the solutions up to the cmc. As the interfacial tension further decreases the distributions cluster for solutions above the cmc, suggesting a similar acting interfacial tension. For solutions with small surfactant concentration (below the cmc), the surfactant can mainly be found on the interface. The increase in continuous phase viscosity

suppresses Marangoni phenomena suggesting, that the solutions might display properties different from their equilibrium.

4.2.1.2.Droplet formation of C12TAB aqueous solutions in 4.6, 19 and 96 mPa s silicone oil

In these series of experiments the surfactant was changed to C12TAB. Droplet formation is examined using the same microfluidic device and under the same conditions. Figure 4.9 displays the droplet size distributions for various C12TAB solutions in three different continuous phase viscosities.

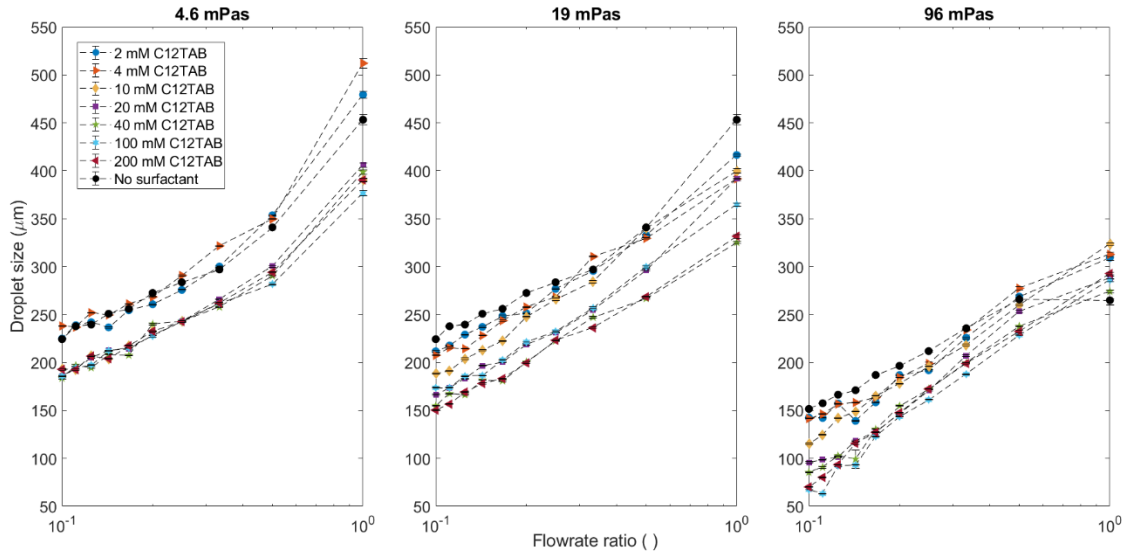


Figure 4.9 Droplet sizes for a 52% w/w glycerol-water with various surfactant concentrations

As in the case of the C10TAB solutions, an decrease in droplet sizes as φ and the surfactant concentrations decreases is observed. A levelling-off of the droplet diameter is observed as the surfactant concentration is above the cmc (20mM).

Since a different surfactant is used, the limiting adsorption time scale, compared to the C10TAB case, is larger due to the lower surfactant concentrations. Using equation 2.10 the timescale associated with the replenishment of surfactant on the interface due to adsorption from the bulk can be estimated to be between 10^{-3}-10 ms depending on concentration. The Marangoni timescale based on equation 2.11 is only affected by the difference in interfacial

tension and the difference in viscosity between the dispersed and continuous phases and is in the same order of magnitude as in the case of the C10TAB. Figure 4.10 displays the timescales in comparison for the solutions used.

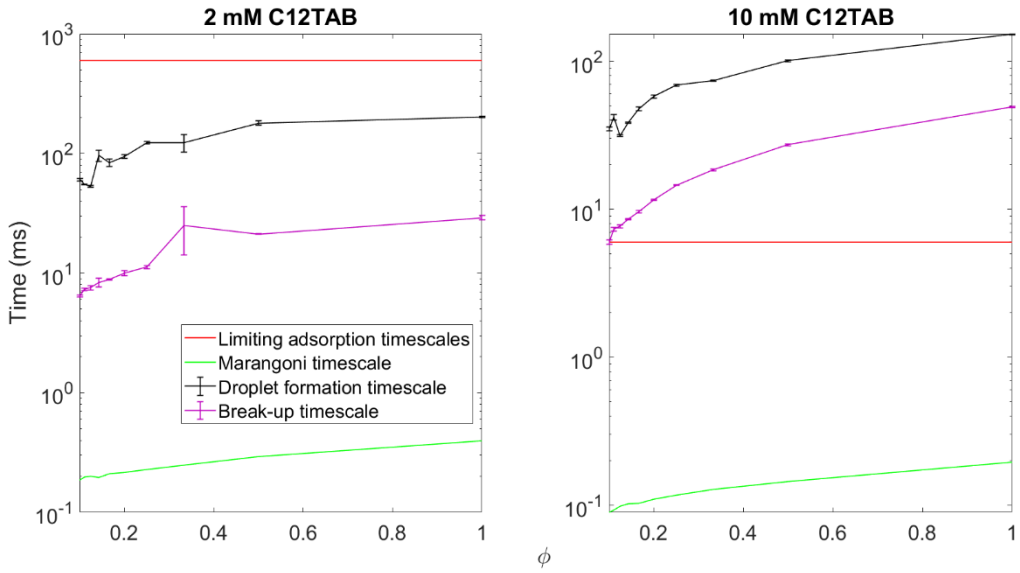


Figure 4.10 Timescales associated with the replenishment of surfactant on the interface for C12TAB solutions in 4.6 mPa s silicone oil.

From Figure 4.10 it is observed that when using solutions with small concentrations, and in the case of small flow rate ratios, the surfactant does not have sufficient time to reach the interface from the bulk. In this case, Marangoni phenomena are mainly responsible for redistributing the surfactant on the interface, since Marangoni phenomena develop in smaller time scales and the surfactant is mainly found on the interface. In the case of 4.6 mPa s, for small concentrations (2, 4 mM) of C12TAB equilibrium interfacial tensions are similar explaining the clustering of the droplet size distributions that are observed for the solutions with small surfactant concentration. As the surfactant concentration increases (10 mM), droplet sizes become smaller suggesting a smaller acting interfacial tension. As the surfactant concentration is further increased, the distributions cluster, following the levelling off of equilibrium interfacial tension.

Examining the timescales associated with the process for the 19 mPa s continuous phase is observed that the limiting adsorption timescale is larger than the break-up and Marangoni

timescale, for small concentrations of surfactant. Therefore, the surfactant mass transport is mainly dominated by the deformation of the interface and Marangoni phenomena. As the concentrations increase, the adsorption of surfactant completely overtakes the process, explaining the differences in the droplet sizes as the surfactant concentration increases. In contrast to the C10TAB case, significantly more clustering of the droplet size distributions for the smaller concentration solutions is observed, suggesting that the larger Marangoni timescale, for these solutions leads to a behaviour closer to a solution without surfactant, since the deformation of the droplet happens in a time scale smaller than the time it takes for interfacial phenomena to equalise any concentration inhomogeneities. As the surfactant quantity in the solution increases, the sizes keep decreasing for solutions above the cmc. Figure 4.11 displays the time scales associated with the surfactant mass transport and the break-up process in comparison.

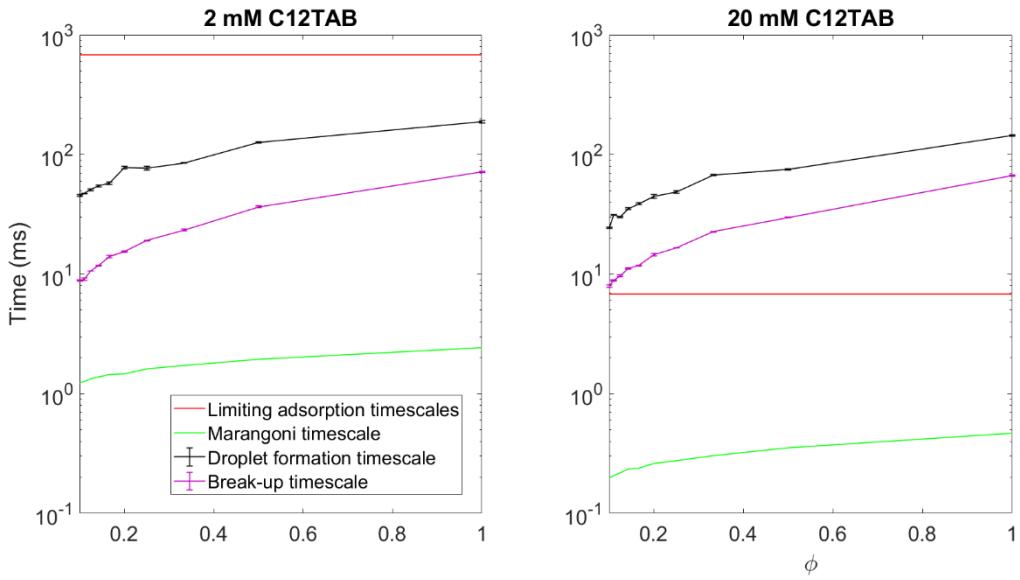


Figure 4.11 Timescales associated with the replenishment of surfactant on the interface for C12TAB solutions in 19 mPa s silicone oil.

For solutions with quantities of surfactant below the cmc, the Marangoni phenomena are mainly responsible for the replenishment of surfactant on the interface and the limiting adsorption time scale is of the same order of magnitude as the break-up time scale. This suggests that the process might be developing under non equilibrium conditions and the

solutions are displaying acting interfacial tensions similar to the solution without surfactant, explaining the clustering of results for solutions below the cmc. As the concentration increases, the solutions display properties closer to their equilibrium properties but there are distinctions between the distributions. Similarly, to the case of the C10TAB in the same continuous phase, it can be assumed that the increase in viscosity of the outer phase leads to a reduction in the magnitude of any surface flows that replenish the surfactant in these timescales explaining the difference between the distributions.

In the of case the 96 mPa s the break-up times are significantly higher, in the order of 10^1 ms. The different timescales associated with the process are examined in Figure 4.12.

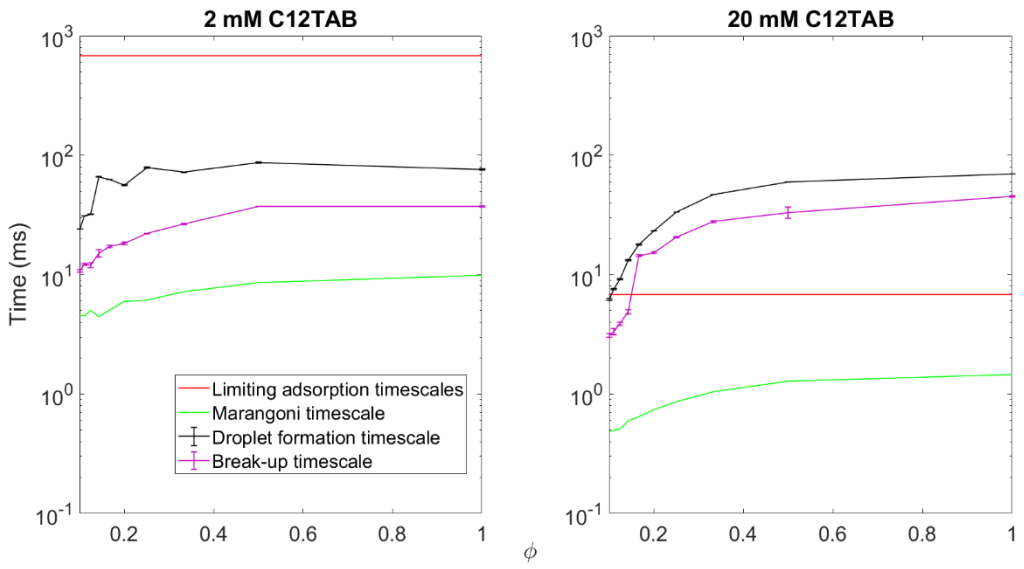


Figure 4.12 Timescales associated with the replenishment of surfactant on the interface for C12TAB solutions in 96 mPa s silicone oil.

It is observed that for the less concentrated surfactant solutions the break-up and the Marangoni timescales are comparable. This suggest that the process might behave under non equilibrium conditions and therefore explaining the droplet size clustering for these solutions. Despite the Marangoni timescale and the limiting adsorption timescale being very similar, it is reasonable to assume that the replenishment of surfactant in these cases happens mainly due to adsorption. The increase in the continuous phase viscosity inhibits surface flows (Marangoni phenomena) that contribute to the surfactant mass transport along the interface (Nowak et al., 2017).

Furthermore, the increase in the outer phase viscosity leads to an increased stability of the liquid filament suppressing any differences in interfacial tension that would produce different droplet size distributions. As the concentration of surfactant increases the surfactant mass transport timescales become significantly smaller than the break-up timescales. Therefore, solutions are expected to display equilibrium interfacial tensions explaining the clustering of the droplet size distributions.

4.2.1.3. Droplet formation of C16TAB aqueous solutions in 4.6, 19 and 96 mPa s silicone oil

In the final series for these experiments C16TAB solutions were utilised while keeping the same conditions and microfluidic device. Figure 4.13 shows the droplet size distribution for C16TAB solutions in three different continuous phase viscosities.

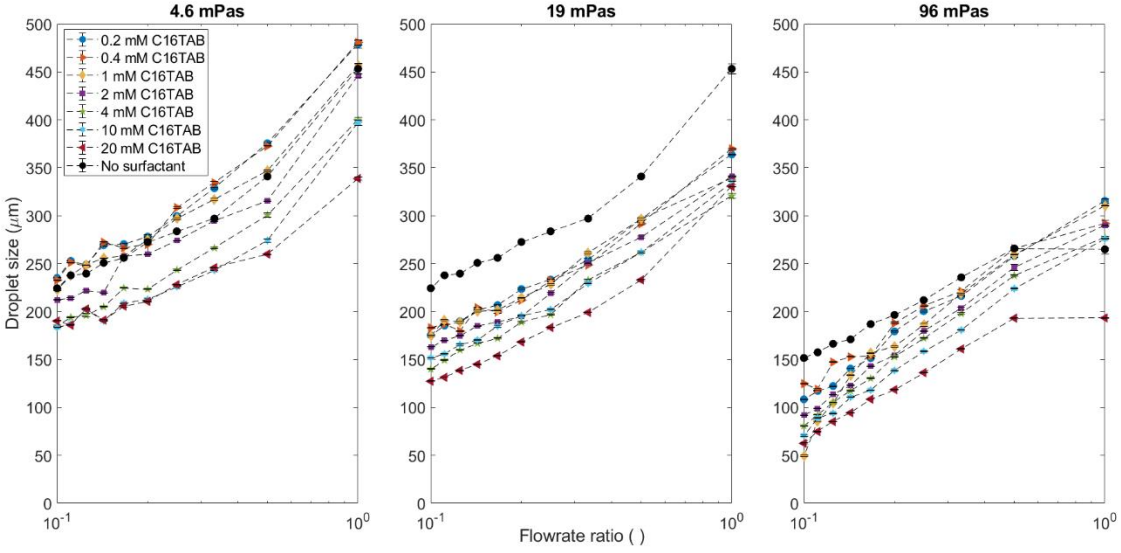


Figure 4.13 Droplet sizes for a 52% w/w glycerol-D.I. water with various surfactant concentrations

As in the previous cases a clustering of the droplet diameter distributions for solutions below the cmc (2mM) and for solutions above the cmc is observed. C16TAB is found in smaller quantities in the system, suggesting a further increase in the limiting adsorption time scale. Using equation 2.10 this time scale can be estimated to 10^{3}-10^{-1} ms, depending on

concentration. This suggests that solutions with low concentrations (0.1-0.5 cmc) will behave as solutions without surfactant in the time scale of droplet formation. Figure 4.14 shows the difference between the different timescales.

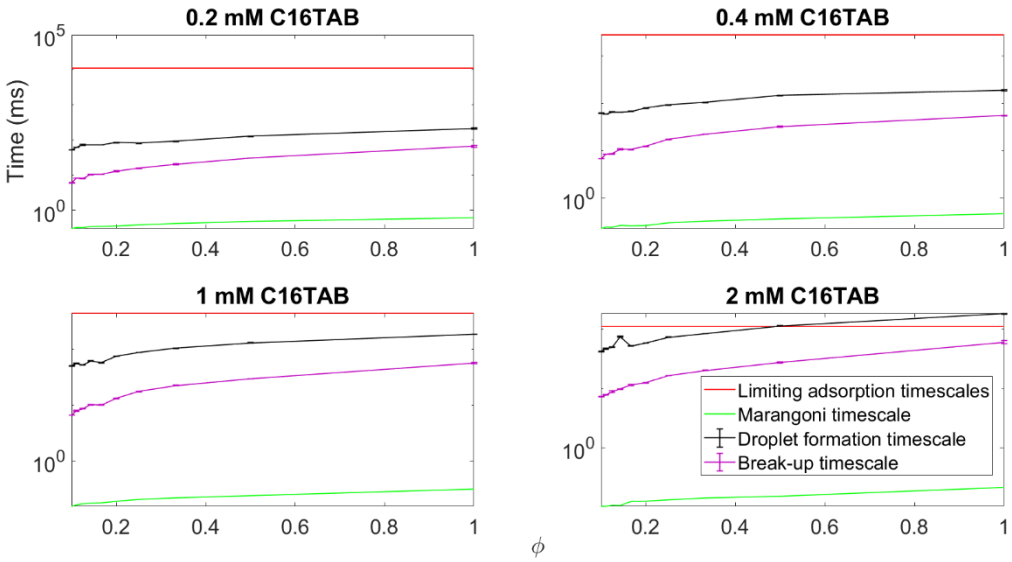


Figure 4.14 Timescales associated with the replenishment of surfactant on the interface for C16TAB solutions in 4.6 mPa s silicone oil.

For small surfactant concentrations the limiting adsorption timescale is orders of magnitude larger than the break-up or the Marangoni time scale. This means that surfactant mass transport on the interface happens mainly due to Marangoni phenomena. If the equilibrium interfacial tensions between C16TAB solutions in 4.6 mPa s silicone oil are examined, it is observed that there is a clear decrease in interfacial tension as the concentration increases suggesting that the 0.2, 0.4 and 1 mM solutions should display different droplet size distributions. As the surfactant concentration increases and the limiting adsorption timescale decreases, a clustering of the droplet size distributions for solutions above the cmc is observed. This happens for the 1 and 2 mM solutions, where the quantity of surfactant decreases the limiting adsorption timescale even further.

Examining the timescales for the case of 19 mPa s it is observed that the limiting adsorption time scales remain larger than the break-up times for solutions up to 4 mM, as seen in Figure

4.15. In these cases, Marangoni phenomena along the interface regulate the surfactant mass transport on the interface.

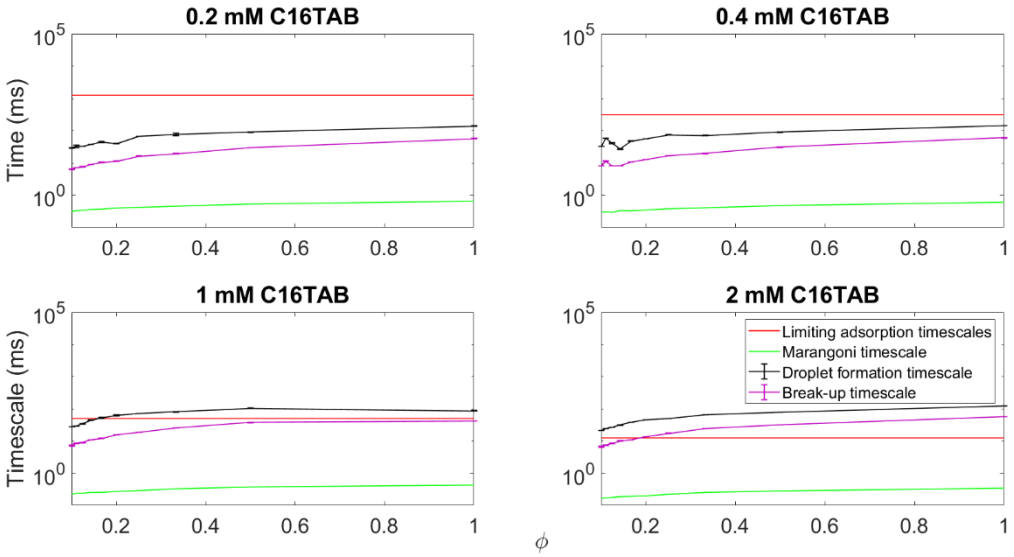


Figure 4.15 Timescales associated with the replenishment of surfactant on the interface for C16TAB solutions in 19 mPa s silicone oil.

In the case of C16TAB, the amount of surfactant in the system is limited suggesting a further reliance on Marangoni phenomena to equalise any differences in interfacial tension. Furthermore, the equilibrium interfacial tensions of these solutions are quite different from each other, pointing towards a different behaviour in each case. As the viscosity of the continuous phase increased, Marangoni phenomena that contribute to the redistribution of surfactant on the interface are impacted, which can explain the constant change in the droplet size distributions with the increase in concentration. Even solutions above the cmc display different acting interfacial tensions due to the limited quantity of surfactant in the system.

The equilibrium interfacial tension for C16TAB solutions in 96 mPa s silicone oil was extrapolated from the existing isotherm data. Looking at Figure 4.1 it can be assumed that the equilibrium values of interfacial tension for C16TAB solution in 96 mPa s silicone oil will be very similar to the existing values and therefore they are assumed to be the same as the C16TAB in 19 mPa s.

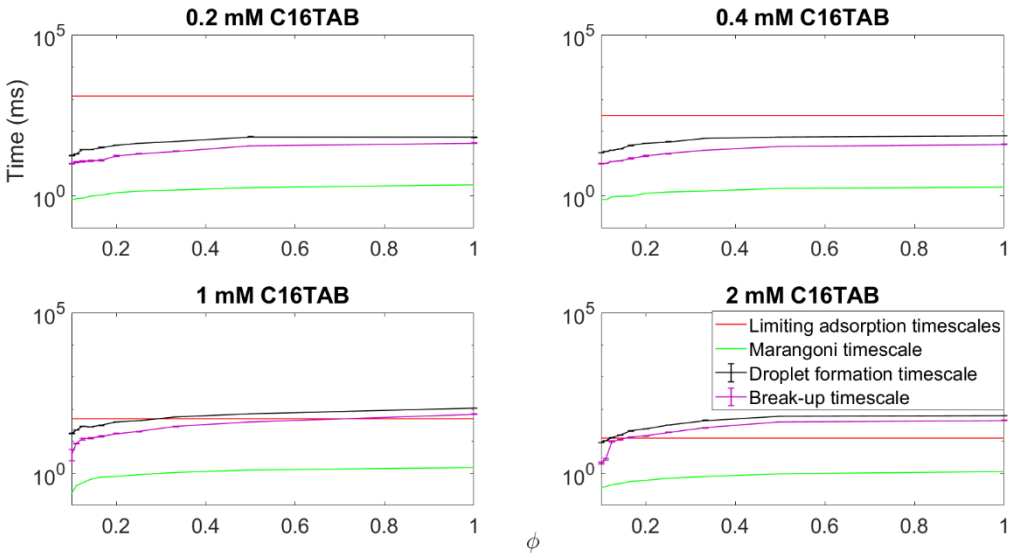


Figure 4.16 Timescales associated with the replenishment of surfactant on the interface for C16TAB solutions in 96 mPa s silicone oil.

Figure 4.16 displays the timescales associated with the surfactant mass transport for the droplet formation process of C16TAB solution in a 96 mPa s continuous phase. The Marangoni timescale is the smallest compared to the break-up and adsorption time scales. The Marangoni timescale is smaller than the deformation and droplet formation timescale, nevertheless the droplet size distributions show distinctions across all surfactant solutions. It was demonstrated in literature that the increase in the continuous phase viscosity can suppress interfacial flows which can explain the differences in the droplet size distributions. It reasonable to assume that Marangoni phenomena are more important in the replenishment of surfactant on the interface during the droplet formation process. For the three different types of surfactant is noted that for the C16TAB, as a more viscous continuous phase is used, droplet sizes fail to cluster even for solutions that the adsorption timescale becomes quite small. This is not the case for surfactants found in larger quantities, like the C10TAB and C12TAB. In those cases, the adsorption of surfactant is larger since the quantity of surfactant is far larger. The increased quantity of surfactant doesn't affect the surface concentration of surfactant (Mucic et al., 2011).

4.3. Droplet sizes modelling

The process can be mathematically modelled using the droplet size data from §4.2.1.1 - §4.2.1.3. This can be done by plotting the normalised droplet diameter, defined as the droplet diameter over the channel height, versus the capillary number times the volume fraction of the continuous phase (Cubaud and Mason, 2008). The capillary number used for this calculation is given by

$$Ca = \frac{\mu_i Q_i}{h^2 \gamma_{12}} \tag{4.5}$$

Where μ is the dynamic viscosity (Pa s), Q is the flow rate ($m^3\ s^{-1}$), h is the channel depth (m) and γ_{12} is the equilibrium interfacial tension ($N\ m^{-1}$). The subscript *i* denotes the continuous, 2, or dispersed phase, 1. The volume fraction is given by

$$\alpha_i = \frac{Q_i}{\sum_1^2 Q} \tag{4.6}$$

Where Q is the flow rate ($m^3\ s^{-1}$). The viscosity ratios used in the study are given by

$$n = \frac{\mu_d}{\mu_c} \tag{4.7}$$

and are 1.30, 0.32 and 0.06. For each different viscosity of the continuous phase, the data appears to fall over a single curve.

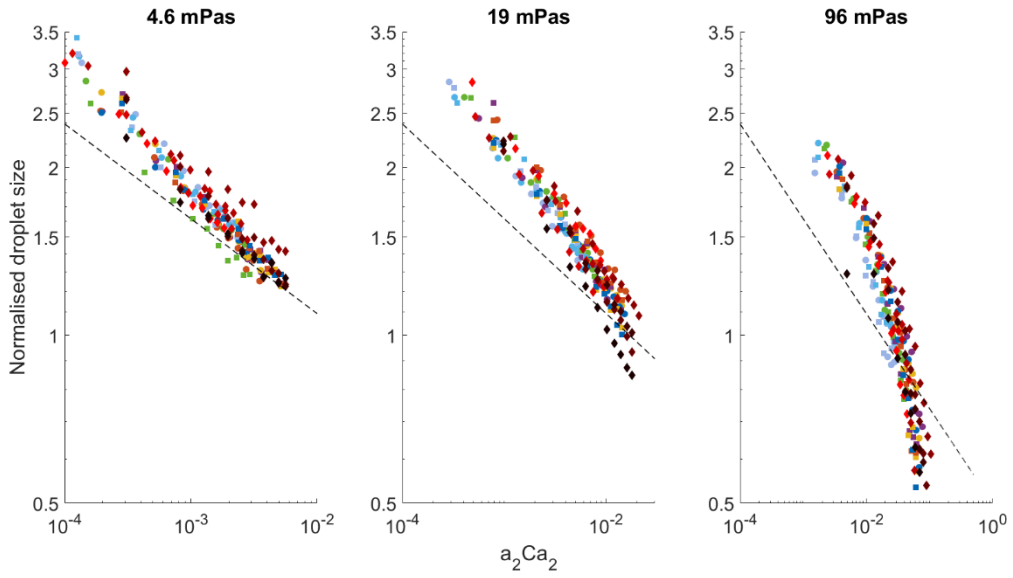


Figure 4.17 Normalised droplet diameter vs a_2Ca_2 for three different continuous phase viscosities. ○:C10TAB, ◊:C16TAB, □:C12TAB. Shades of red: C12TAB, shades of green: C16TAB, Shades of blue: C10TAB. Segmented line is the scaling for d/h<2.5 for dripping from literature (Cubaud and Mason, 2008).

Previous research showed that the scaling follows a power law (Cubaud and Mason, 2008). The data is fitted using the non-lineal least squares method for each continuous phase viscosity. For the 4.6 mPa s continuous phase viscosity the model describing the data is $d/h = 0.33\ (a_2Ca_2)^{-0.25}$. The R^2 value calculated by the non-linear least squares method is 0.96 suggesting a good fit. Literature gives the values 0.5 and -0.17 for the constant and exponent respectively (Cubaud and Mason, 2008). Differences between literature and this experimental work are expected due to the different design of the microfluidic device, flow rates, and physical properties of the fluids used. The difference between the two exponents can be qualitatively understood by arguing that in the above experiments the flow of the continuous phase plays a bigger role in the droplet break up for these length scales. For the 19 mPa s continuous phase viscosity the model is $d/h = 0.42\ (a_2Ca_2)^{-0.24}$, with an R^2 value of 0.96, suggesting a very similar behaviour for these two viscosity ratios. For the highest continuous phase viscosity, the normalised droplet diameter becomes smaller than unity, suggesting that droplet sizes are smaller than the channel depth and therefore unconfined. For this case the normalised droplet sizes above unity are fit separately from those below unity. The droplet

sizes follow the $d/h = 0.49\ (a_2Ca_2)^{-0.24}$ law for confined droplets, while the scaling law for unconfined droplets is $d/h = 0.23\ (a_2Ca_2)^{-0.40}$. The R^2 square values for these fits are 0.86 and 0.8 respectively. The reduction is the fitting quality can be explained by arguing that the transition between confined and unconfined regime is not sharp and therefore there are droplets produced in an intermediate regime. Similar studies on emulsification in square microchannels argue that the magnitude of the exponent represents the resistance to droplet formation induced by the flow in the side channels (Cubaud and Mason, 2008). The square channels used in that study are 100 μm is size. In this case the exponent is smaller, suggesting that as the dimensions of the microfluidic device decrease, the flow on the side channels, where the continuous phase travels, affects the break-up less.

The scaling laws produced in this work appear to be similar to the scaling law produced in the study of Cubaud and Mason (Cubaud and Mason, 2008). Droplet sizes follow a power law and the normalise droplet size decreases with an increase in the viscosity of the continuous phase and the increase of the continuous phase flow rate. The numerical differences in the pre-exponent and exponent values can be attributed to the presence of surfactant, which reduces droplet sizes, explaining the smaller pre-exponent factor, while the smaller exponents can be attributed to the increased contribution of the continuous phase in the break-up due to the flow focusing design of the microfluidic device.

4.4. Satellite droplets

Satellites are formed as the break-up process reaches the final moments of the pinch-off stage and the neck ruptures. As the neck thins and ruptures the liquid thread can reach atomic scales. This results in the production of secondary break-ups (Tan and Lee, 2005). For every case of droplet formation, the formation of satellite droplets is observed. The number of satellites ranges from three to six. In every case, the formation of a main satellite droplet accompanied by smaller droplets is observed and only the size of the main satellite is measured. The

distribution of the drops bears a striking celestial analogy as pointed out in previous work (Cubaud and Mason, 2008) and demonstrated in Figure 4.18.



Figure 4.18 Celestial analogy of satellite droplet formation. left panel: 2 mM C16TAB in 96 mPa s silicone oil. Central panel: our solar system. Right panel: 2 mM C16TAB in 4.6 mPa s silicone oil.

Previous work on satellites droplet stressed the importance of the viscosity ratio between the two fluids. It was shown than with an increase in viscosity ratio the size of the satellite droplets should increase (Carrier et al., 2013). The presence of surfactant alters the break-up process by affecting the adsorption dynamics and Marangoni phenomena and this can affect the satellite droplet formation. Experimental work for droplet formation under gravity at the tip of a capillary showed that, the addition of surfactant increases the size of the satellite droplets which levels of at concentrations close to the cmc (Kovalchuk et al., 2016). Similarly, to extracting droplet size distribution from our experiments, the size of the satellite droplets is also monitored. Figure 4.19 shows the main satellite droplet diameter for various concentrations of surfactant.

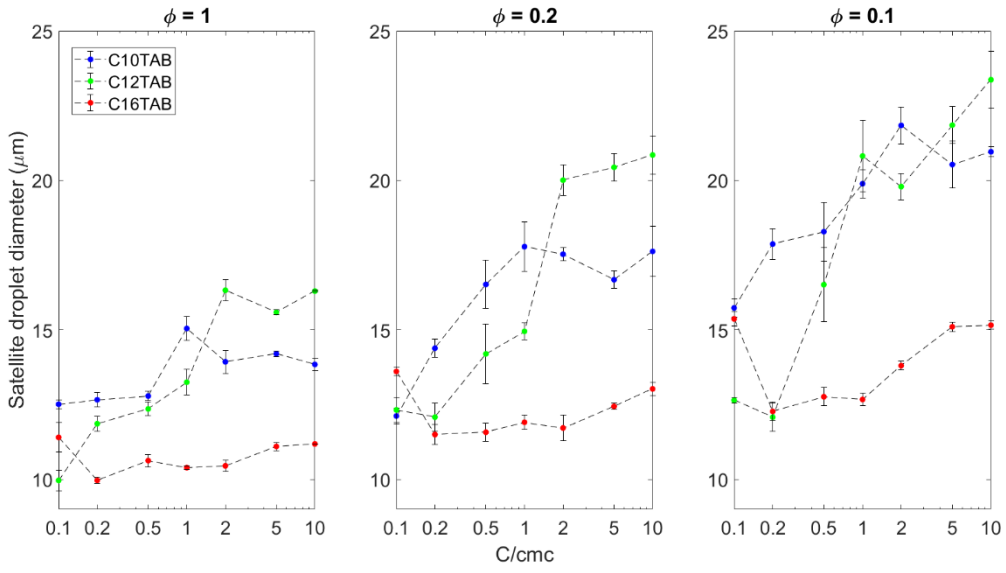


Figure 4.19 Satellite droplet diameters for various surfactant concentrations in 4.6 mPa s silicone oil. Vertical lines are the cmc values of the different surfactants.

Generally, it is observed that as the surfactant concentration increases the size of the satellite droplet increases. Similarly, it increases with an increase in the continuous phase flow rate. More specifically, for the C10TAB the size distributions peak after the concentration reaches the cmc. The surfactant mass transport process is highly dominated by adsorption, since the surfactant is in abundant quantity in the solution, explaining the plateau after the cmc. In contrast, for C12TAB solutions, the sizes keep increasing after the cmc. For this surfactant the size distributions level-off at concentration 2 times the cmc. This suggest that the size of the satellites droplets depends much more on the dynamics of surfactant mass transport in those timescales. In contrast, satellite droplet size distributions for the C16TAB solutions display very small changes. In the case of C16TAB, the amount of surfactant in the system is limited. In this case Marangoni phenomena are mainly responsible for the redistribution of the surfactant on the interface since the adsorption of surfactant from the bulk is smaller due to the smaller amount of surfactant in the system. Similarly, the satellite droplet size distributions for the 19 mPa s silicone oil continuous phase are examined. Figure 4.20 displays the results.

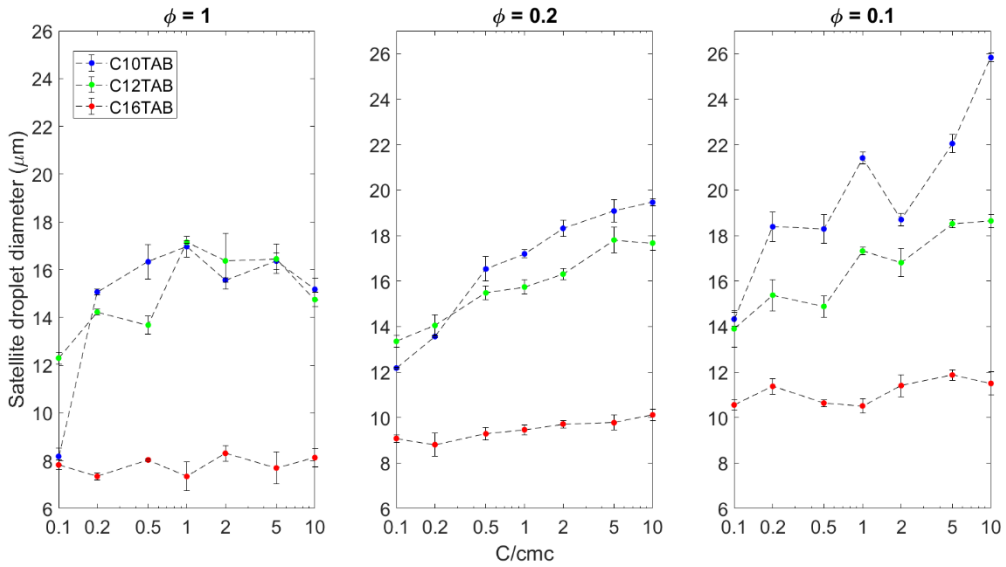


Figure 4.20 Satellite droplet diameters for various surfactant concentrations in 19 mPa s silicone oil. Vertical lines are the cmc values of the different surfactants.

As the continuous phase viscosity is increased, the satellite droplet sizes keep increasing for the C10TAB and C12TAB solutions. For the smallest flow rate ratio (larger continuous phase

flow rate), a plateau in the satellite droplet size for all surfactants is observed. In this case the break-up timescale is larger than the timescales responsible for the replenishment of surfactant on the interface. This suggests that even in the last moments before pinch-off there is enough surfactant on the interface. As the continuous phase flow rate is increased the plateau disappears. This suggests the dynamic redistribution of surfactant and an acting interfacial tension different that the equilibrium. The increase in the continuous phase viscosity leads to a suppression of surface flows, since the increase in viscosity leads to a reduction of interfacial velocities (Nowak et al., 2017). From this it can be assumed that, in those last moments of droplet formation, Marangoni phenomena are very important in the replenishment of the surfactant along the interface and highly impact the size of the satellite droplets. This becomes clearer, if the satellite sizes for the 96 mPa s continuous phase are examined. Figure 4.21 shows the results.

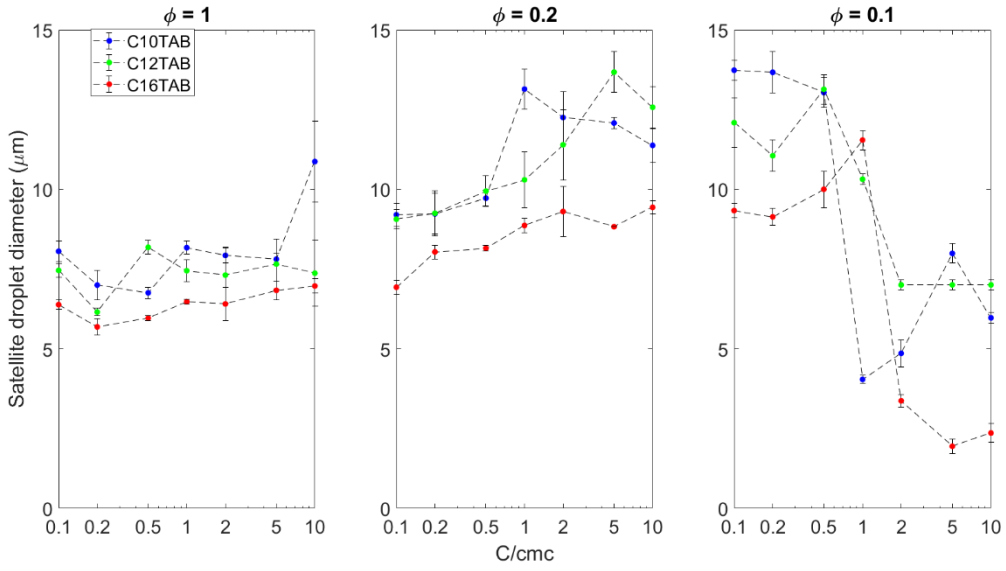


Figure 4.21 Satellite droplet diameters for various surfactant concentrations in 96 mPa s silicone oil. Vertical lines are the cmc values of the different surfactants.

For the largest flow rate ratio (largest break-up time), the replenishment of surfactant in the interface happens mainly due to adsorption explaining the plateau observed for the C10TAB and C12TAB solutions. As the continuous phase flow rate increases (central panel, Figure 4.21) the plateau vanishes suggesting that there is not enough time to allow for the replenishment of

the surfactant on the interface. Another notable aspect is the sharp decrease of satellite droplet sizes for small flow rate ratios and concentrations above the cmc. Previously, in Figure 4.17, it was demonstrated that the droplet formation scaling changes due to the effect of confinement. In a similar way, satellite droplets are impacted as well. This sharp decline in the satellite droplet size presented in Figure 4.21 is caused by the reduction of the effect of confinement. It therefore can be stated that when droplet sizes are larger than the channel depth, and are therefore confined, satellite droplet sizes are larger. From Figure 4.19 Figure 4.20 and Figure 4.21 it is observed that increasing the surfactant concentration increases the size of the main satellite droplet. In the case of the 4.6 mPa s continuous phase the increase happens even for concentrations above the cmc. This has also been recorded for the satellite droplets formed during the break-up of a droplet at the tip of a capillary under the effect of gravity (Kovalchuk et al., 2018b). In the cases where droplet formation evolves in times smaller than the time scales responsible for the replenishment of the surfactant on the interface the satellite sizes keep increasing, suggesting a strong connection of the satellite size with the dynamic aspect of surfactant mass transport.

Similarly to the droplet size scaling produced previously, a similar scaling law can be derived for the size of the satellite droplets. The diameter of the satellites is normalised as previously, by dividing it with the channel depth and plotted versus the capillary number of the continuous phase times the volume fraction of the same phase. Segmenting the satellite droplet sizes datasets based on continuous phase viscosity yields a low correlation. Figure 4.22 displays this behaviour. The main satellite droplet size is normalised using the channel depth, as done with the droplet sizes in section 4.3. the normalised sized is the plotted against the capillary number of the continuous phases times the volume fraction of the continuous phase.

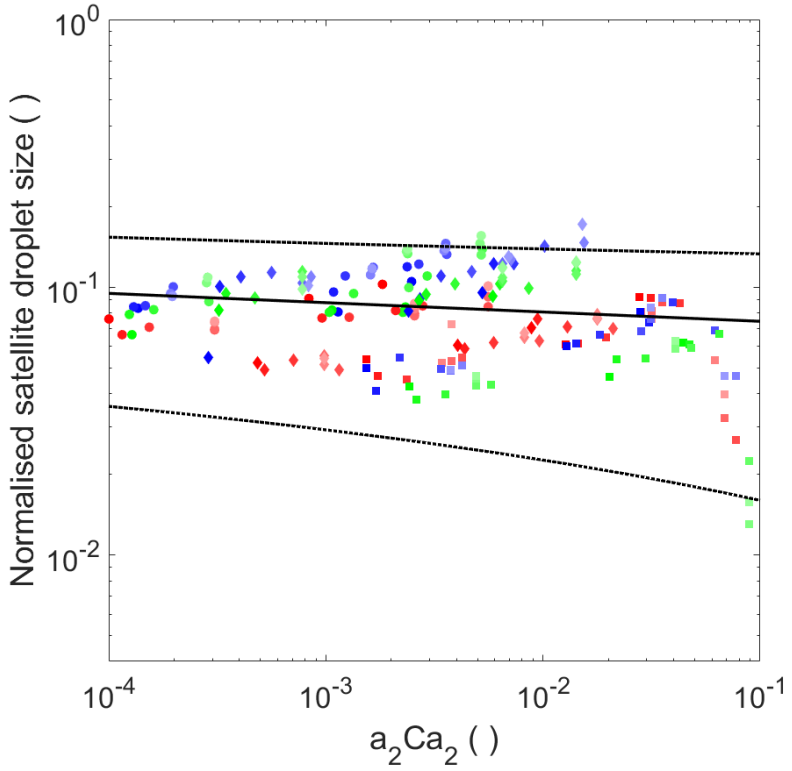


Figure 4.22 Normalised satellite droplet sizes over the range of Capillary numbers studied. ○:C10TAB, ◊:C16TAB, □:C12TAB. Shades of red: C12TAB, shades of green: C16TAB, Shades of blue: C10TAB. Solid black line is the model extracted. Dotted black lines are the prediction bounds.

This behaviour suggests that satellite droplet sizes are more affected by the local properties of the neck in the final stages of the break-up rather than the whole break-up process like droplet sizes. What is similar to the droplet size behaviour is the sharp change in sizes at very high oil viscosity and concentration, something observed in the droplet formation distributions (Figure 4.17). It is important to note that satellite droplet sizing is quite challenging, the length scales over which satellite droplets become visible are quite narrow and the time frame allowed for observation is quite small, this has contributed significantly to the measured satellite droplet size errors.

4.5. Conclusions

Key Learnings

- Droplet sizes don't level off for concentration above the cmc, suggesting a contribution of the presence of surfactant to the droplet size

- Confinement plays a major role in regulating droplet size. Under confinement droplets are larger
- The produces scaling law is similar to proposed literature scaling but with differences due to the microfluidic device design and presence of surfactant.
- Satellite droplet sizes increase with an increase in the surfactant concentration while confinement greatly increases their size

In this Chapter, the impact of the experimental conditions on the droplet sizes, and on the size of the satellite droplets was discussed. Furthermore, using the provided data, a scaling law was extracted which can be used to predict droplet sizes under various experimental conditions.

It was demonstrated that increasing the continuous phase flow rate leads to a reduction in droplet sizes. Increasing the surfactant concentration has a similar effect. It was demonstrated that for the 4.6 mPa s continuous phase, the droplet size distributions for solutions above the cmc, cluster following the levelling off of interfacial tension. This doesn't happen for the C16TAB solutions suggesting that the quantity of surfactant in the system has an impact on the droplet size distributions. Increasing the continues phase viscosity to 19 mPa s leads to droplet sizes changing for the whole range of surfactant concentrations for all studied surfactants. Increasing the continuous phase viscosity leads to a suppression of surface flows explain the lack of clustering for the droplet size distributions for the surfactant solutions above the cmc. A further increase in viscosity of the continuous phase to 96 mPa s leads to clustering of the distributions above the cmc for C10TAB and C12TAB. It generally appears that solutions below the cmc display droplet sizes very similar to each other hinting to a depletion of surfactant and an acting interfacial tension larger than the equilibrium value.

The timescales associated with the surfactant mass transport were calculated in each case and compared to the timescales of droplet formation. In each case they were smaller that the droplet formation and break-up timescales. This would suggest that the process evolves under

equilibrium conditions in each case which doesn't explain the similarity between the low surfactant concentration droplet sizes. It can be said that the time scales associated with the surfactant mass transport are not good predictors of surfactant behaviour during droplet formation. The presence and transport of surfactant is affected more by the local flow conditions in the neck and expanding droplet and therefore, time scales that describe the process entirely cannot properly predict and describe the surfactant behaviour.

Lastly, the size of the main satellite droplet follows an inverse trend compared to droplet sizes. Satellite droplets increase in size when the continuous phase flow rate and the surfactant concentration is increased. For the 4.6 and 19 mPa s continuous phase the satellite droplet sizes level off for solutions above the cmc for all surfactants when the oil flow rates are small, but keep increasing when the flow rate of the continuous phase is increased. In the case of 96 mPa s continuous phase the satellite droplet size distributions appear to be similar to each other for all flow rate conditions and surfactant concentrations. The above suggests that for low viscosity continuous phases the satellite droplet size is affected by the local dynamics of the neck in the timescales very close to the droplet break-up, but as the continuous phase viscosity increases, the viscosity of the continuous phase regulates their size.

Chapter 5: Kinetics of the thinning neck

Introduction

In this chapter the experimental analysis of the thinning neck during the necking stage of the droplet formation process is described. Initially, the neck kinetics of surfactant free solutions are discussed and the thinning rates of the neck are calculated. The same analysis is carried out for the necking stage during emulsification of surfactant solutions and the thinning rates are compared to surfactant free systems. The aim of this chapter is to compare the thinning behaviour of surfactant free system to a system with surfactant and draw conclusions on the presence of surfactant. Finally, this chapter examines the effect of fluid viscosity to the thinning rate of the neck to determine if the further increase of the viscosity of the dispersed phase alters the thinning neck dynamics.

The discussion is limited to a flow rate ratio of 0.2. In this case the droplet formation timescales presented in the previous chapter are closer to the timescales associated with the surfactant mass transport. The aim was to probe experimental conditions where the depletion of surfactant would be impactful. Furthermore, further increasing the fluid flow rate leads to rapid phenomena where the collection optics and resolution of the produced footage is reduced due to the increased contribution of the camera noise due to an increase in the Reynolds number (Riccomi et al., 2018).

5.1. Kinetics of the thinning neck of surfactant free solutions

As the droplet formation process advances the liquid filament connecting the expanding droplet to the bulk of the dispersed phase thins and ruptures releasing the droplet. The variation of neck diameter over time is driven by the neck kinetics describing the thinning process. The analysis begins from the droplet formation process of a solution without surfactant in the three different

continuous phases used previously. The evolution of the neck diameter over time in the necking stage is shown in Figure 5.1 for the surfactant free case for each of the three continuous phases. The discussion is limited to a flow rate ratio equal to 0.2. Time 0 corresponds to the moment of pinch off. Moving along the x-axis one moves towards instances away from the pinch-off.

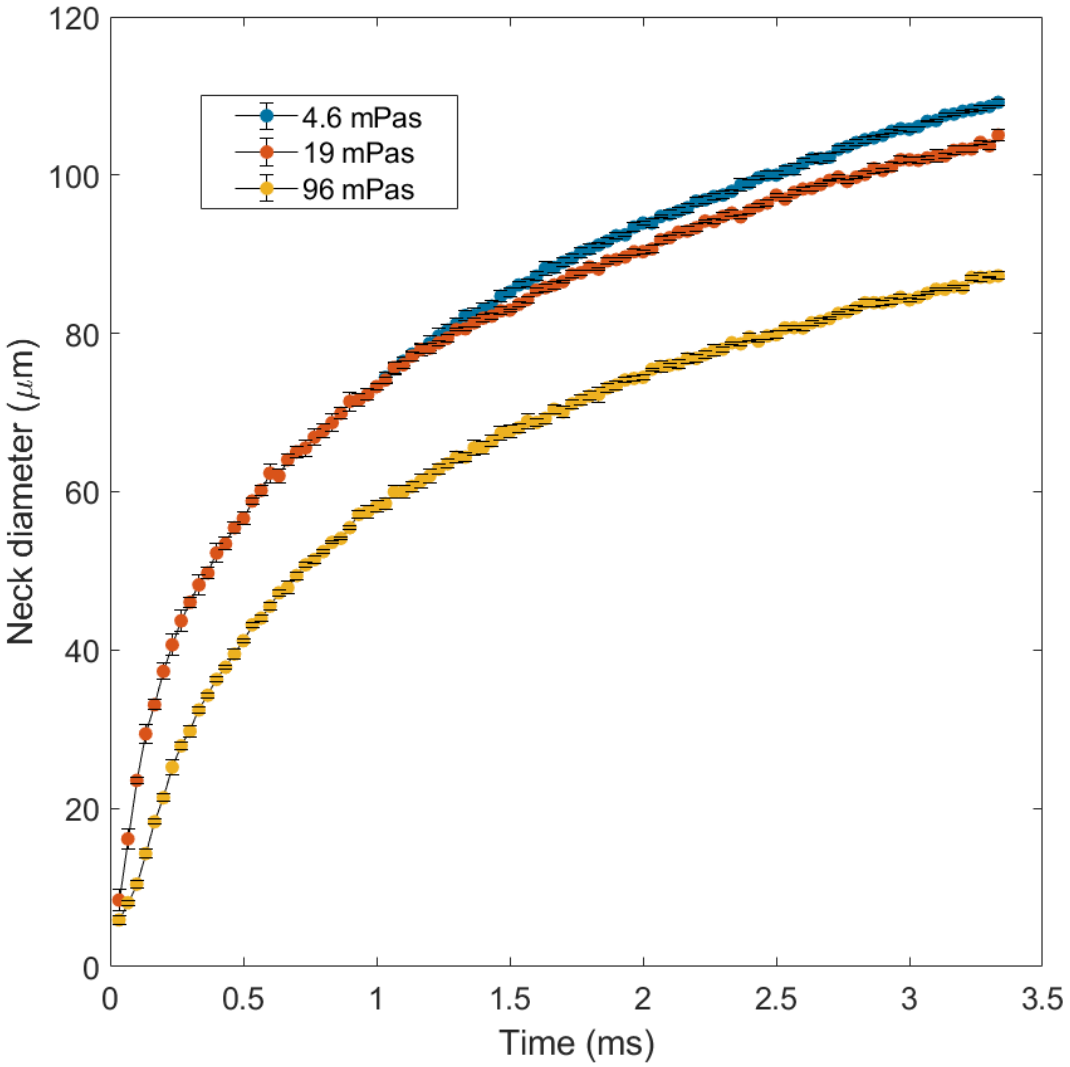


Figure 5.1 Neck kinetics during necking for a solution without surfactant in three different continuous phase viscosities.

From Figure 5.1 two distinct neck kinetics regions are identified. A slower neck thinning for times away from the pinch-off (right-hand side of the figure) and a faster thinning region as the pinch-off is approached (left hand side of the figure).

Using equation 2.16

$$Oh = \frac{\mu_d}{\sqrt{\rho_d \gamma h}}$$

the Ohnesorge number for the studied systems can be calculated. In this study the Ohnesorge number is $8 \cdot 10^{-2} \leq Oh \leq 10^{-1}$. Therefore, inertial thinning kinetics are expected.

For instances close to the neck pinch-off the neck kinetics can enter the visco-inertial regime, described by equation 2.17. Using equations 2.18 and 2.18 the viscous length (l_v) and time (τ_v) scales for the studied systems can be estimated. These are $1 \leq l_v \leq 3$ μm and of the order of 10^{-4} ms respectively. These dimensions are not accessible by the means employed in this study and therefore the only observable kinetics should be inertial.

When the break-up happens inside a viscous fluid, the neck kinetics follow the two fluid Stokes regime in which the neck kinetics are mediated by the viscosity ratio of the two liquid phases (de Saint Vincent et al., 2012). In the experimental systems studied, the droplets are formed inside another fluid. This changes the neck break-up dynamics, and the behaviour of the system is dependent on the viscosity ratio between the two fluids. The two fluid Stokes regime is observed when the magnitude of the length scales of interest is in the order of $l_S = (\mu_c/\mu_d)l_v$. For the fluid used in this study l_s is within observable range only for the most viscous continuous phase of 96 mPa s with l_s = 16 μm for the surfactant free system and 48 for the surfactant systems above the cmc.

The neck diameter data for instances close and away from the pinch-off is fitted to a power law using the non-linear least square method and the thinning exponent is examined. The results are summarised in table 5.1.

Table 5.1 Thinning exponents for solutions without surfactant in three different continuous phase viscosities for time close and away from the pinch-off

	Thinning exponent	
Continuous phase viscosity (mPa s)	Close to the pinch off (A.U.)	Away from the pinch off (A.U.)
4.6	0.88	0.30
19	0.88	0.28
96	0.98	0.31

According to the calculated Ohnesorge number the observed kinetics should be inertial and the exponent should have a value of 2/3. The deviation of the calculated exponents (Table 5.1) from the expected values can be due to the fact that the break-up occurs in a confined geometry. The decrease in the thinning rate was observed for bubble formation in a flow focusing microfluidic device (Garstecki et al., 2005). It was suggested that the geometrical confinement stabilises the thread and the capillary instability that ruptures the neck and the thinning is governed by the imposed flow rates and pressure gradients. In other cases, a similar stabilisation of the liquid thread in a confined geometry was reported (Humphry et al., 2009), while the jet can be completely stable and the capillary instability significantly reduced (Son et al., 2003).

5.2. Kinetics of the thinning neck of surfactant solutions

Similarly, to the solution without surfactant the thinning rate of the neck is examined for surfactant solutions. The neck kinetics for C10TAB solution in three different continuous phase viscosities are shown in Figure 5.2.

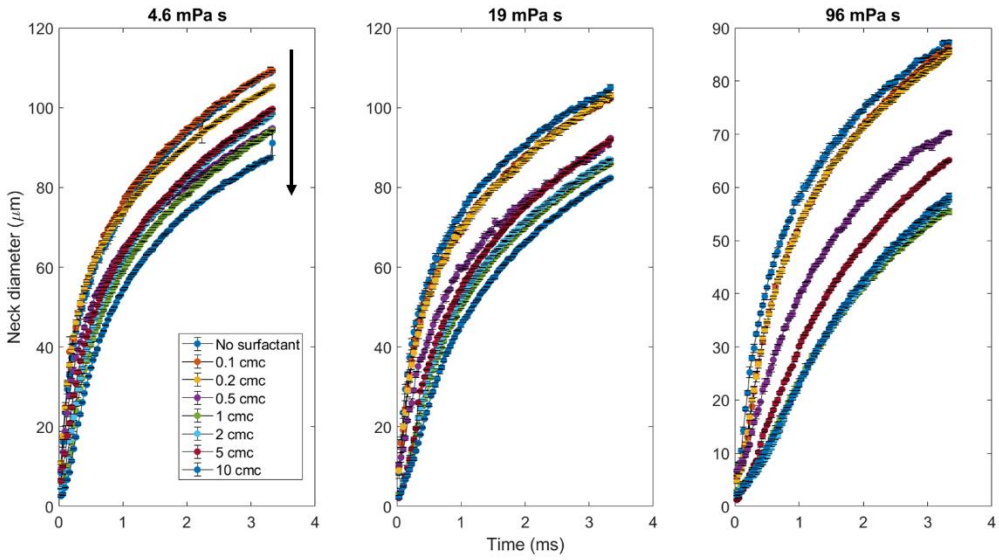


Figure 5.2 Neck kinetics during necking for C10TAB solutions in three different continuous phase viscosities. The arrow shows the increase in concentration.

Similarly to the cases without surfactant, two distinct regimes are present; a slower thinning rate at times away from the break-up and a faster thinning rate, close to the pinch-off. Furthermore, as the surfactant concentration increases the kinetics slow down and the curves follow the decrease in interfacial tension. Similarly, to droplet sizes, neck kinetics cluster for solutions above the cmc suggesting the levelling off of interfacial tension. The thinning rate of the neck is compared to the kinetics of a model case of a surfactant free liquid. Figure 5.3 shows the thinning rate of the neck kinetic curves for different surfactant solutions for instances close to the pinch-off.

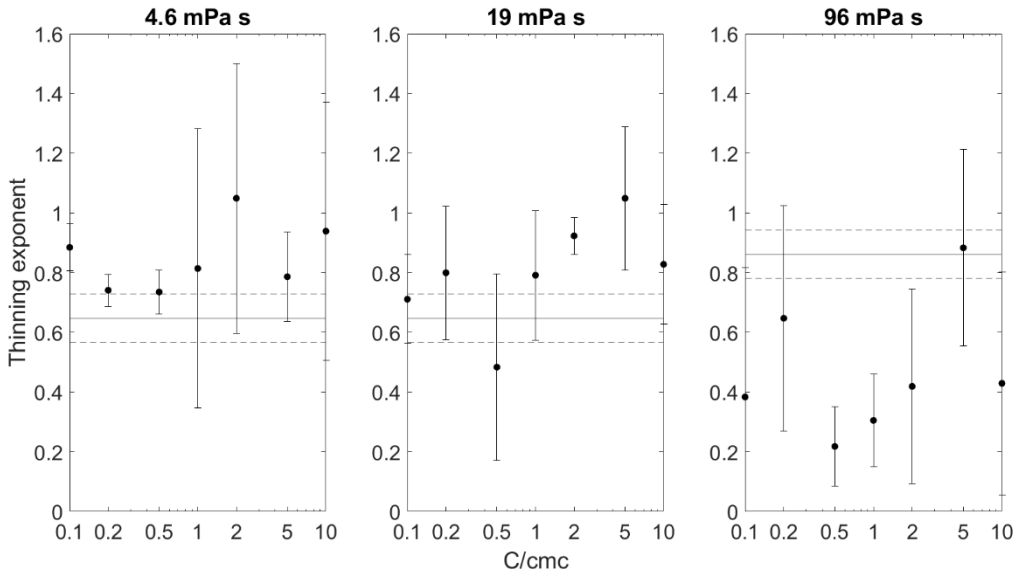


Figure 5.3 Neck thinning rate for different C10TAB solutions in 4.6,19 and 96 mPa s silicone oil for instances close to the break-up. The black horizontal line is the slope of the surfactant free system while the red lines represent the error margins. The solid vertical line marks the cmc of the surfactant

The thinning rate of the neck at instances close to the pinch-off becomes different from the thinning rate of a surfactant free system only for concentrations of surfactant 5 times the cmc and above for the 4.6 mPa s silicone oil. The similarity of the surfactant laden and surfactant free thinning exponents suggest that the phenomena responsible for the replenishment of surfactant on the interface are slower than the deformation of the thinning neck. For smaller concentrations of surfactant, it appears that the neck kinetics display the same thinning exponent as a solution without surfactant. It appears that for low surfactant concentrations the neck in the final stages of the break-up behaves like a surfactant free solution for all surfactant concentrations and for all continuous phase viscosities. As the concentration of surfactant increases the behaviour changes. In the last stages of the break-up the neck displays properties different from a solution without surfactant but only for highly concentrated solutions. As the continuous phase viscosity increases, the neck behaves like a surfactant free solution for all concentrations. The increase in continuous phase viscosity suppresses interfacial flows (Marangoni phenomena) that replenish the surfactant on the interface. The observed behaviour suggests that interfacial phenomena are crucial in equalising surfactant inhomogeneities in the final stages of break-up. The increase in continuous phase viscosity was shown to suppress

interfacial flows during the merging of droplets. In the case of droplet formation, especially when the viscosity ratio is small, it must be considered that, despite the amount of surfactant in the system the behaviour in the final stage of the break-up will be very similar to the behaviour of a surfactant free system. Similarly, the neck kinetics for instances away from the break-up are examined. Figure 5.4 displays the thinning rates of the neck kinetic curves away from the break.

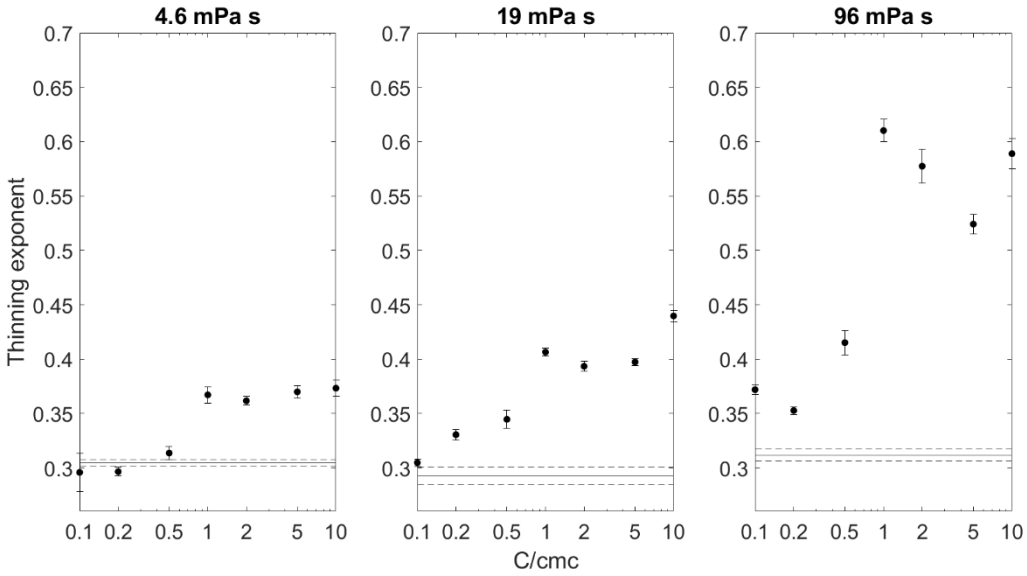


Figure 5.4 Neck thinning rate for different C10TAB solutions in 4.6, 19 and 96 mPa s silicone oil for instances away from the break-up. The black horizontal line is the slope of the surfactant free system while the red lines represent the error margins. The solid vertical line marks the cmc of the surfactant

It is observed that for solutions below the cmc the thinning rate increases as the surfactant concentration increases. Only in the case of the 4.6 mPa s silicone oil, the thinning rate, for solutions below the cmc, is in the range of the solution without surfactant suggesting a similar behaviour. As the concentration reaches the cmc the thinning rate remains constant for different surfactant concentrations. The difference in behaviour between the surfactant solutions and the solution without surfactant suggests, that in the initial stages of the break up the majority of the solutions display a different behaviour than a solution without surfactant. In the case of the 4.6 mPa s silicone oil the break-up is faster, and for low concentration solutions there is competition between the break-up and the replenishment of surfactant on the interface. The replenishment of the surfactant on the interface during these timescales happens due to

Marangoni phenomena on the interface caused by differences in the surfactant surface concentration and the adsorption of surfactant from the bulk of the dispersed phase solution. For small concentrations of surfactant, the adsorption is small, as the majority of the surfactant is found on the interface, therefore the weight falls on interfacial phenomena to redistribute the surfactant along the interface. In the case of the 4.6 mPa s continuous phase, the replenishment of the surfactant happens slower than the break-up. This explains the similarity in the thinning rate between low concentration solutions and the surfactant free system. Only for the break-up occurring in the 96 mPa s silicone oil the calculated exponent reaches the theoretically predicted value for inertial kinetics. In this case, the droplet are smaller than the channel depth (Figure 4.17) and therefore the effect of confinement is reduced. Furthermore, the increase in oil viscosity slows the process down. At the same time, it suppresses interfacial phenomena but it appears that the behaviour is significantly different suggesting that the interface is covered with surfactant. The above behaviour reinforces what was stated in chapter 4, that the timescales associated with the surfactant mass transport fail to describe the surfactant behaviour during droplet formation. According to the timescales presented in Figure 4.6, Figure 4.7 and Figure 4.8, the limiting adsorption timescale and Marangoni timescales are in every case smaller than the deformation timescale suggesting a process which would develop under equilibrium conditions which is not the case as seen above. Similarly, the C12TAB neck kinetics are examined. Figure 5.5 shows the neck kinetics for different C12TAB solutions used.

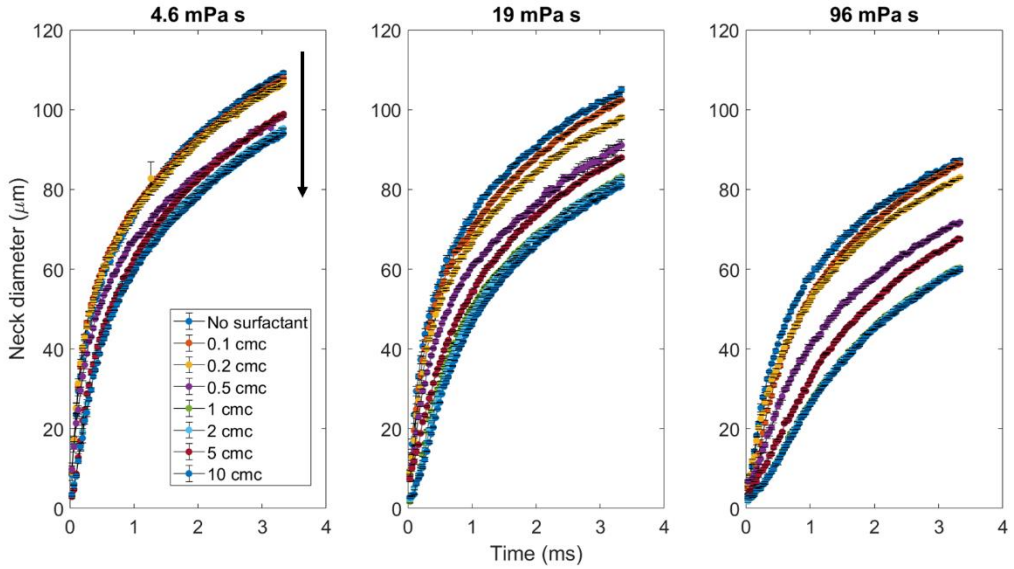


Figure 5.5 Neck kinetics during necking for C12TAB solutions in three different continuous phase viscosities

The neck thinning behaviour displayed by the C12TAB solutions is similar to the C10TAB solutions. The kinetics appear to follow the increase in surfactant concentration and cluster for solutions above the cmc. The thinning rate for instances away and close to the break-up is examined in a similar way as previously. Figure 5.6 shows the thinning rates for the kinetics close to pinch-off.

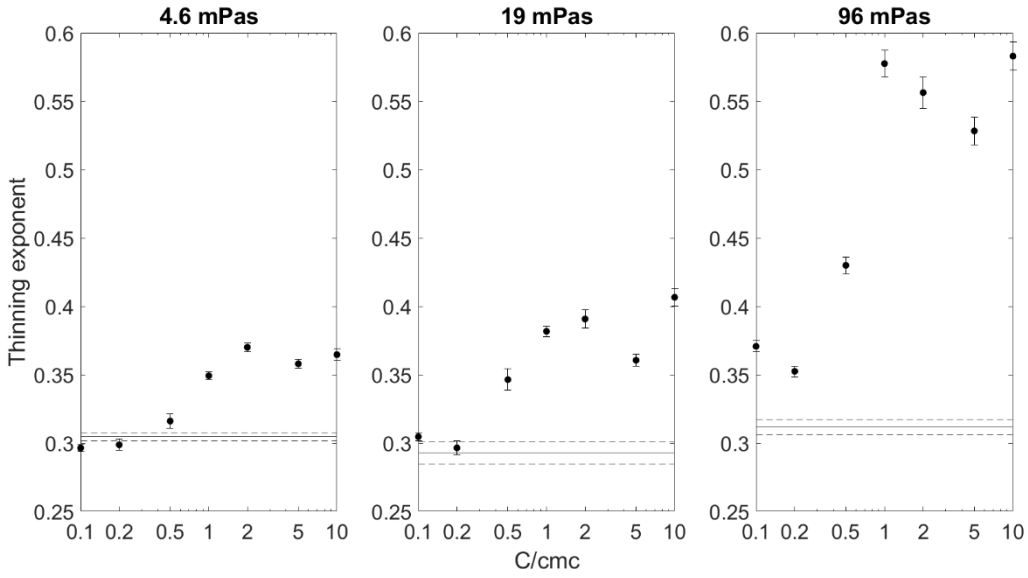


Figure 5.6 Neck thinning rate for different C12TAB solutions in 4.6, 19 and 96 mPa s silicone oil for instances close to the break-up. The black horizontal line is the slope of the surfactant free system while the red lines represent the error margins. The solid vertical line marks the cmc of the surfactant

Similar to the case of C10TAB, for the solutions above the cmc for the 4.6 and 19 mPa s silicone oil, the thinning rate is larger than the rate of a no-surfactant solution, suggesting a different thinning behaviour. For solutions below the cmc the thinning rate is very similar to a surfactant free solution. The kinetics in these time scales for these solutions display the same behaviour as a solution without surfactant, suggesting a depletion of surfactant from the neck area. For the 96 mPa s continuous phase viscosity the thinning rate is the same as the surfactant-free solution. As in the case of C10TAB, in the final stages of break-up, Marangoni phenomena are more important in replenishing the surfactant on the interface. The higher viscosity oil supresses interfacial flows making the replenishment of surfactant through Marangoni phenomena impossible. For the timescales away from the break-up the thinning rates are displayed in Figure 5.7.

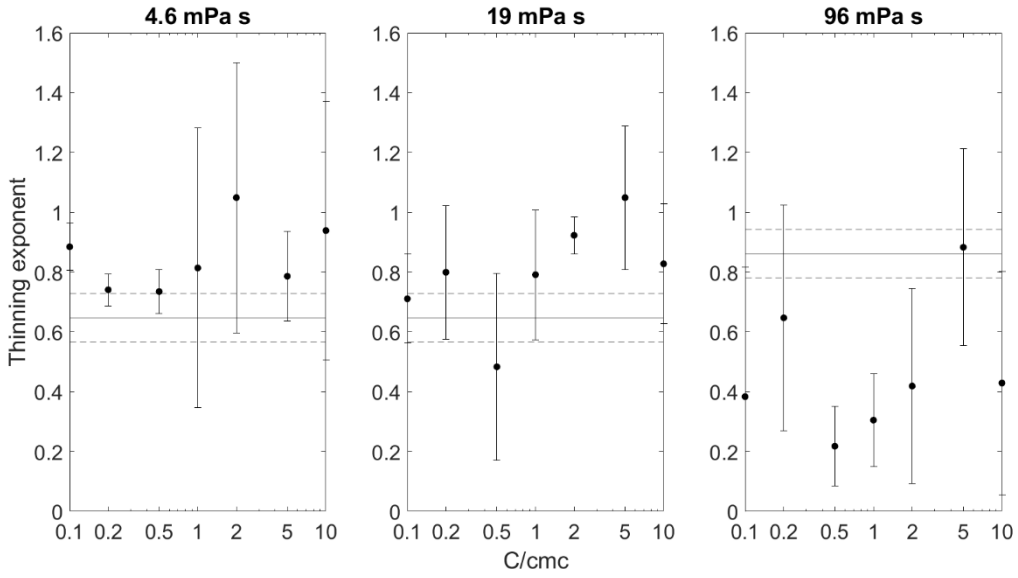


Figure 5.7 Neck thinning rate for different C12TAB solutions in 4.6, 19, 96 mPa s silicone oil for instances away from break-up. The black horizontal line is the slope of the surfactant free system while the red lines represent the error margins. The solid vertical line marks the cmc of the surfactant

Similar to the C10TAB solutions, the thinning rate increases as the surfactant concentration increases and levels of for solutions above the cmc. The expected inertial exponent is reached for the unconfined droplet formation similarly to the case of C10TAB for the 96 mPa s continuous phase only. The behaviour is different from a surfactant free system for all surfactant solutions in all silicone oils except for the low concentration solution in 4.6 mPa s

silicone oil and This behaviour is indicative of depletion of surfactant as the break-up process evolves. In the first stages of the break-up the solutions display a different behaviour from a surfactant free system. As the break-up progresses and the thinning rate of the neck increases depletion phenomena arise. In the case of C12TAB the limiting adsorption timescale is larger than the case of C10TAB as seen in Figure 4.10, Figure 4.11 and Figure 4.12, and Marangoni phenomena are mainly responsible for replenishing the surfactant on the interface. In each case the Marangoni timescale is smaller than the deformation timescale. Nevertheless, it is observed that the thinning rate changes as the process evolves suggesting again that the timescales used in Chapter 4 do not describe the actual behaviour of the surfactant. C16TAB displays a similar behaviour. For solutions below the cmc, and instances close to pinch-off, the slope is the same as the slope of a surfactant free solution. As the concentration increases the thinning rate increases for the cases of 4.6 and 19 mPa s continuous phase viscosities. In the case of 96 mPa s the thinning rate is in the same as a surfactant free solution in each case. In this case, the process is dominated by the viscosity of the continuous phase. When examining instances away from the break-up all solutions display a distinct behaviour from a solution without surfactant for all viscosities. The above analysis showed that the thinning behaviour is different for instance close and away from the pinch-off regardless of surfactant concentration and the thinning behaviour changes as the process evolves.

Furthermore, the above analysis allows to draw conclusions on the acting interfacial tension in the neck region in those timescales. Since the behaviour of all solutions below the cmc, in instances close to the pinch-off, is very close to the behaviour of a surfactant free system, it can be assumed that there might be surfactant depletion in the neck. This can be examined by using the two fluid Stokes model (de Saint Vincent et al., 2012). The model is described by equation 2.19.

$$R(t) = (H\gamma/\mu_1)(t_c - t)$$

By examining the neck kinetics close to pinch of, for t < 1 ms, the appearance of a linear regime is observed. The thinning may enter the Stokes regime when the length scales of interest are in the order of $l_S = (\mu_c/\mu_d)l_v$. For the liquids used in this study l_s is within the observable range only for the most viscous continuous phase of 96 mPa·s with l_S = 16 μm for the surfactant-free dispersed phase and l_S = 48 μm for surfactant concentrations above the cmc.This is presented in Figure 5.8.

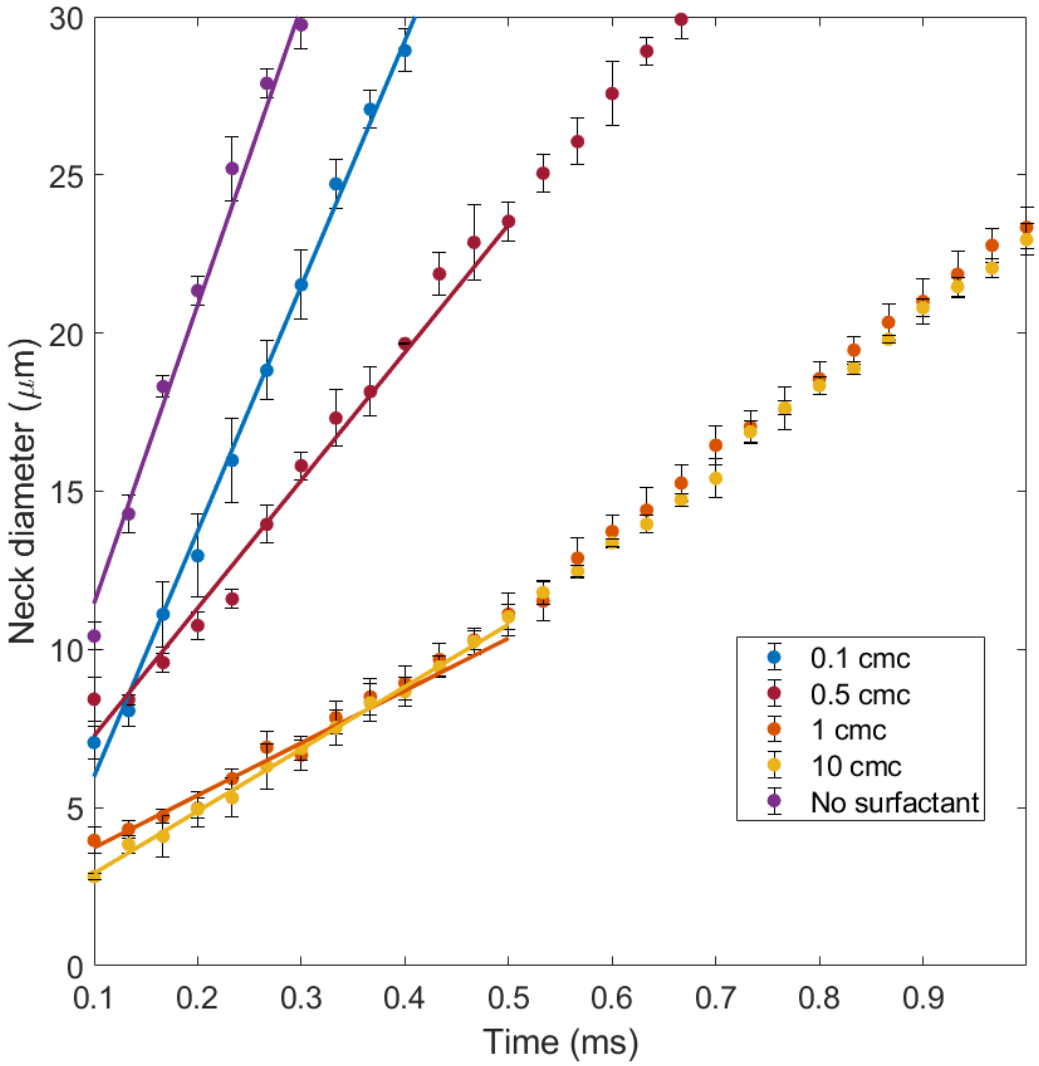


Figure 5.8 Thinning kinetics close to pinch-off for C10TAB solutions.

Using the slope of the surfactant free system the constant H is calculated to be 0.32 which is in line with the predicted literature value of 0.3 (Cohen and Nagel, 2001). The same behaviour is

observed for the C12TAB solution for t < 1 ms. Using the calculated constant H for the surfactant free system the surface tension for the surfactant systems can be calculated using equation 2.19. The results are presented in Figure 5.9.

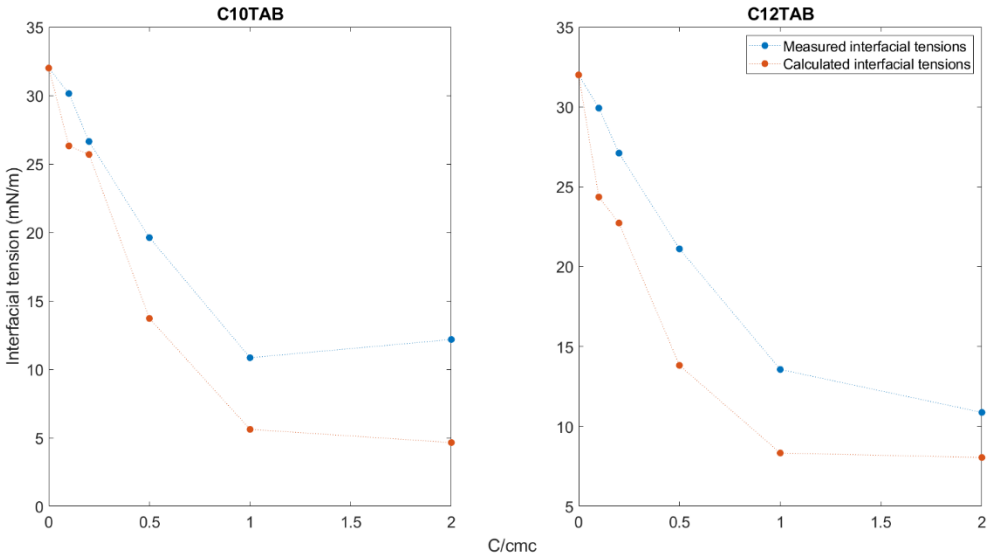


Figure 5.9 Comparison between the measured and calculated interfacial tensions for C10 and C12TAB solutions in the final moments of the neck break-up.

Figure 5.9 shows that the acting interfacial tension in the final stages of the neck thinning is smaller the equilibrium interfacial tensions presented in Figure 4.1. The reduction of the acting interfacial tension leads to a reduction in the capillary pressure driving the thinning of the neck. This suggests that he process evolves slower as it approaches pinch-off and the reduction in capillary pressure can be caused by Marangoni stresses and the redistribution of surfactant on the thinning neck.

5.3. Neck kinetics and thinning rate of a higher viscosity dispersed phase

The neck kinetics of 66% by weight glycerol/water solutions are examined. The increase in glycerol content increases the viscosity of the system by one order of magnitude which in turn reduces the diffusion coefficient by one order of magnitude as well (Cheng, 2008). According to Perkins and Geankoplis the diffusion coefficient of a solute in a binary system can be

estimated using equations 4.2 and 4.3 (Perkins and Geankoplis, 1969). The diffusion coefficients of the surfactants in the 52% and 66% glycerol/water systems are 10^{-10} and 10^{-11} m^2 s^{-1} respectively, while the viscosities are 6 and 70 mPa s. The quantities of surfactant used are the same as previously. The neck kinetics in times away and close to the pinch off are examined and compared. The neck kinetics are similar to the neck kinetics presented previously. Solutions with amounts of surfactant below the cmc display kinetics close to a surfactant free system. Increasing the quantity of surfactant slows the kinetics down as shown previously. An example of the neck kinetics observed is presented in Figure 5.10.

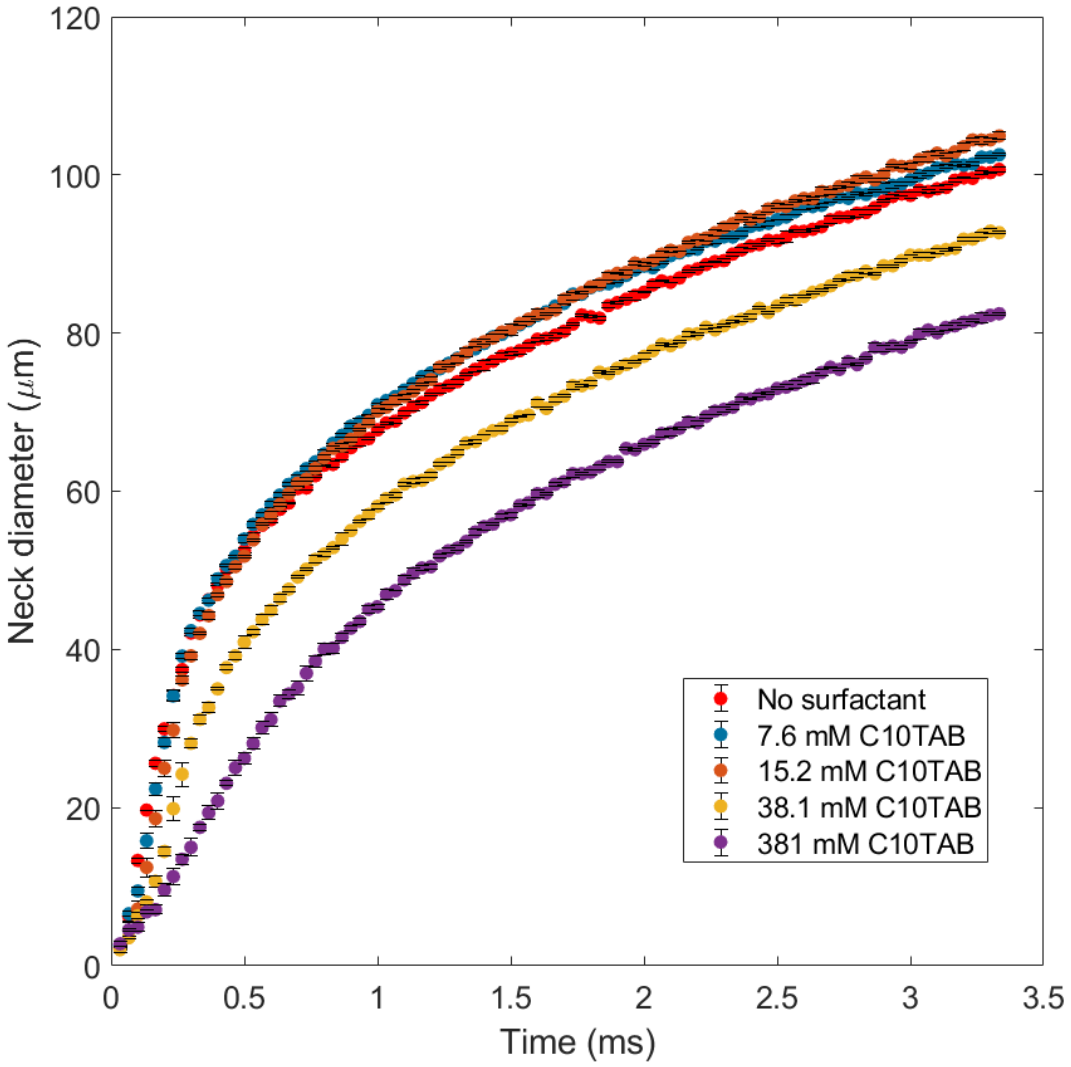


Figure 5.10 Neck kinetics of 70 mPa s C10TAB concentrations. Continuous phase is 4.6 mPa s silicone oil

As in the previous cases two distinct regimes are present. Slow kinetics in times away from the break-up and faster kinetics as the process approaches pinch-off. Increasing the surfactant concentration slows down the kinetics and solutions with quantities of surfactant below the cmc display kinetics very close to a surfactant free system. Figure 5.11 shows the thinning rates of the neck for moments away from the pinch-off for all C10TAB solution using all three continuous phases.

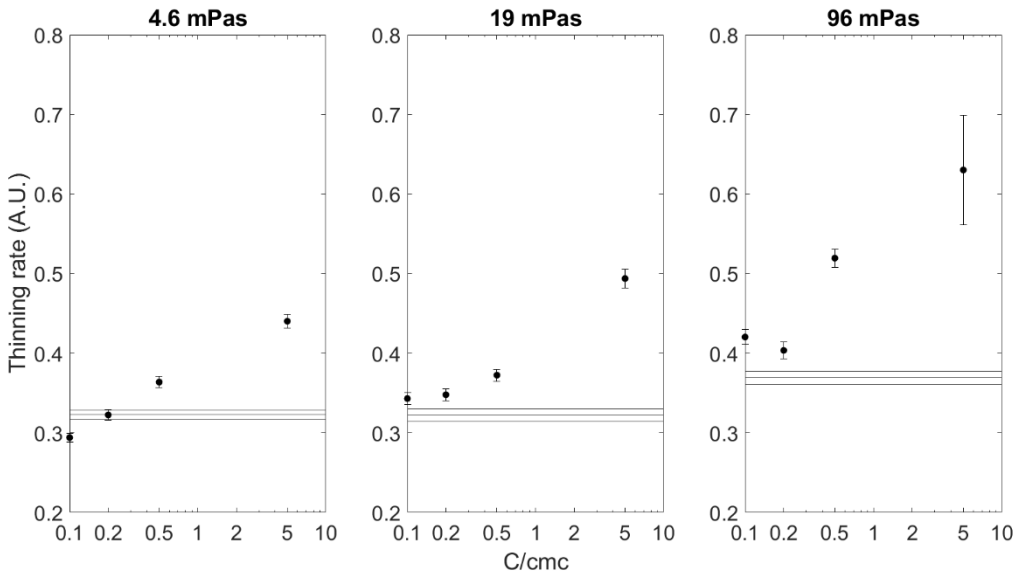


Figure 5.11 Neck thinning rate for instances away from the pinch-off for various 70 mPa s C10TAB solutions in three different continuous phases. Solid black line is the thinning rate of a surfactant free system while the red lines are the error margins. The vertical black lines mark the cmc of the surfactant.

It is observed that the thinning exponents increase with an increase of the surfactant concentration as in the cases presented in section 5.2. When the break-up occurs in the 4.6 mPa s continuous phase the thinning exponents at timescales away from the droplet pinch-off is very similar the thinning exponent of a surfactant free system. When the break-up occurs in the 19 and 96 mPas continuous phases the thinning exponent is different from the surfactant free system suggesting a different thinning behaviour. In the case of the 4.6 mPa s the thinning rates for the solutions with small quantities of surfactant are close to a surfactant free system. In these cases, the system displays a thinning rate very similar to the thinning rate of a surfactant free system. The C12TAB solution displays a similar behaviour. So far, the increase in

viscosity has minimal effect in the behaviour of the systems at timescales away from the pinch-off. Similarly, instances close to the pinch-off are examined and the results are presented in Figure 5.12.

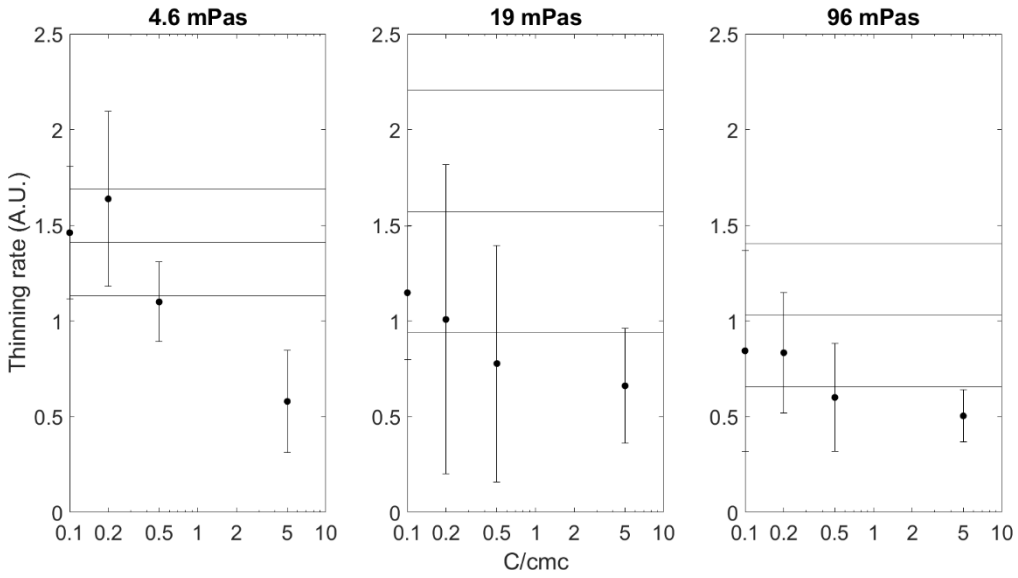


Figure 5.12 Neck thinning rate instances close to the pinch-off for various 70 mPa s C10TAB in three diffrent continuous phases. Solid black line is the thinning rate of a surfactant free system while the red lines are the error margins. The vertical black lines mark the cmc of the surfactant.

As the process approaches pinch-off the kinetics behaviour resembles in all cases the behaviour of a system without surfactant, similarly to the previous cases. This suggests that in the last moments of pinch-off the system displays properties close to a surfactant free system.

The increase in the viscosity of the dispersed phase and the subsequent decrease of the diffusion coefficient of the surfactant species present has minimal effect in the kinetics of the thinning neck for instances away and close to pinch-off. It can be assumed that the local hydrodynamics (i.e. advection) play a much more important role in redistributing the surfactant in the bulk and on the interface of the thinning neck during droplet formation. This was also suggested by the calculated Peclet number in section 2.5.1. A Peclet number on the order of 10^4 suggests that the mass transport phenomena present are governed much more by adevection rather than diffusion. Furthermore, the redistribution of surfactant might rely more on Marangoni

phenomena that redistribute surfactant along the interface rather than the diffusion control phenomena that the increase in the dispersed phase viscosity impacts.

5.4. Conclusions

Key learnings

- Neck kinetics don't follow the predicted inertial regime due to droplet confinement.
- Thinning process is divided in two steps. An initialy slow thinning and a faster thinning as the neck approached pinch-off.
- The calculated thinning exponent increases with an increase of surfactant concentration.
- In the final stages of the break-up the thinning exponent is similar for surfactant laden and surfactant free systems regardless of concentration.

The necking stage of droplet formation has been examined for surfactant free and surfactant laden systems, for three different continuous phase viscosities. It was demonstrated that, for surfactant free systems, the kinetics slow down when the continuous phase viscosity increases. The neck kinetics display two distinct regimes. For instances away from the droplet pinch-off the thinning rate of the neck is slow. As the neck thins further and the droplet detachment approaches the thinning rate increases. This holds for surfactant free and surfactant systems in all continuous phases studied.

After the examination of the surfactant free systems the neck thinning process of surfactant laden systems was studied. In the case when surfactant is present the kinetics slow down following the decrease in equilibrium interfacial tension. The neck kinetics for solutions above the cmc appear to fall over a single curve, suggesting a similar behaviour once the cmc has been reached. Similarly, to the surfactant free system, systems with surfactant are examined,

and the thinning rates of the neck in instances away and close to the pinch off are compared to the thinning rate of a surfactant free system.

The expected inertial kinetics for the neck thinning are not accessed by the current experimental system due to the confined geometry of the microfluidic device. The thinning exponents does not reach the expected value of 2/3. The thinning exponents appears to change according to the surfactant concentration increasing as the concentration increases. Furthermore, the thinning exponent changes as the process approaches pinch-off.

Both in the case of C10TAB and C12TAB, when the droplet break-up occurs in the 4.6 mPa s continuous phase viscosity, solutions with concentrations below the cmc display a thinning exponent similar to the one of a surfactant free system for instances away from the pinch-off. Once the cmc is reached the behaviour differs from the behaviour of the surfactant free system. For instances close to the pinch off the behaviour is in all cases very similar to the surfactant free systems and it differs only for concentrations 2 times the cmc and above.

When the break-up occurs in a 19 mPa s continuous phase the behaviour is different from a surfactant free system both for the C10TAB and C12TAB. For instances close to the pinch off only solutions above the cmc display a different behaviour from a surfactant free system. Finally, when studying the break-up in a 96 mPa s continuous phase, the break-up displays a behaviour similar to a surfactant free system for all solutions for instances close to the pinch-off. For instances away from the break-up of the droplet the behaviour is different for all surfactant solution for both the C10TAB and C12TAB.

The above analysis shows that the neck thinning exponent of the surfactant free systems changes during the process and resembles in some case the surfactant free system. This suggests an increase in the local interfacial tension during droplet formation. This was examined using the two-fluid Stokes model which allows for an estimation of the interfacial tension. The calculated interfacial tension is smaller than the equilibrium interfacial tension,

suggesting a depletion of surfactant from the neck region and a retardation of the break-up process. This can be caused by the presence of Marangoni stresses along the interface of the thinning neck caused by the depletion of surfactant along the neck interface. Solutions above the cmc displayed interfacial tension very close to their equilibrium values.

Lastly, chapter 5 examined the effects of increasing the viscosity of the dispersed phase. It was determined that the increase of the viscosity of the dispersed phase had minimal effect in the neck kinetics in the timescales away from the pinch-off. For instances closer to the pinch-off the thinning rate of a surfactant system becomes smaller that the thinning rate of a surfactant free case suggesting depletion of surfactant from the neck region as demonstrated for the previous cases. From the above results it can be concluded that the local hydrodynamics play a major role in the redistribution of surfactant in the thinning neck region during droplet formation.

In the following chapter, this change in the thinning rate, and this reduction in interfacial tension, will be demonstrated to have an impact on the local velocity fields in the region of the thinning neck. The velocity profiles along the interface for neck diameters approaching pinch off will be examined next.

Chapter 6: Local hydrodynamic phenomena during droplet formation: velocity fields and interfacial topology

Introduction

In this chapter, 2-D velocity fields during droplet formation, obtained from GPV are presented. The magnitude of the local velocity field during droplet formation can provide information on the presence of surfactant and how it affects the droplet formation process. The local distribution of surfactant on the interface affects the local interfacial tension which in turns allows for the presence of Marangoni phenomena which affects the local velocity field. As an example, during the drying of thin polymer films, the evaporation of the solvents creates concentration inhomogeneities on the interface which creates surface tension differences, which in turn create fluid motion (Yiantsios et al., 2015).

This chapter begins by examining the 2-D velocity field during the necking stage of a surfactant free system for each of the three different continuous phases (see §3.1.1). This is followed by a similar analysis for solutions containing either C10TAB or C12TAB below and above the cmc, comparing the velocities fields between surfactant and surfactant free solutions.

Chapter 6 also examines the shape of the interface of the thinning neck. Initially, the shape of the thinning neck for a surfactant free system is analysed and later compared to different surfactant systems to determine if the presence of surfactant has any effect on the shape of the interface.

Finally, the results of the GPV experiments on the expansion stage of droplet formation are presented for solutions with and without surfactant.

6.1. 2-D velocity field during necking for a surfactant free system

Figure 6.1 displays the local velocity field during necking of a surfactant-free system in 4.6 mPa s continuous phase silicone oil. The frame rate selected for these experiments is 30,000 fps and the magnification used is 40×. The magnification results in 0.50 μm pixel^{-1} and 1 frame is 3.3x10^{-5} s. The focal plane investigated is the one covering the central area of the neck, allowing for the optimal observation of the interface.

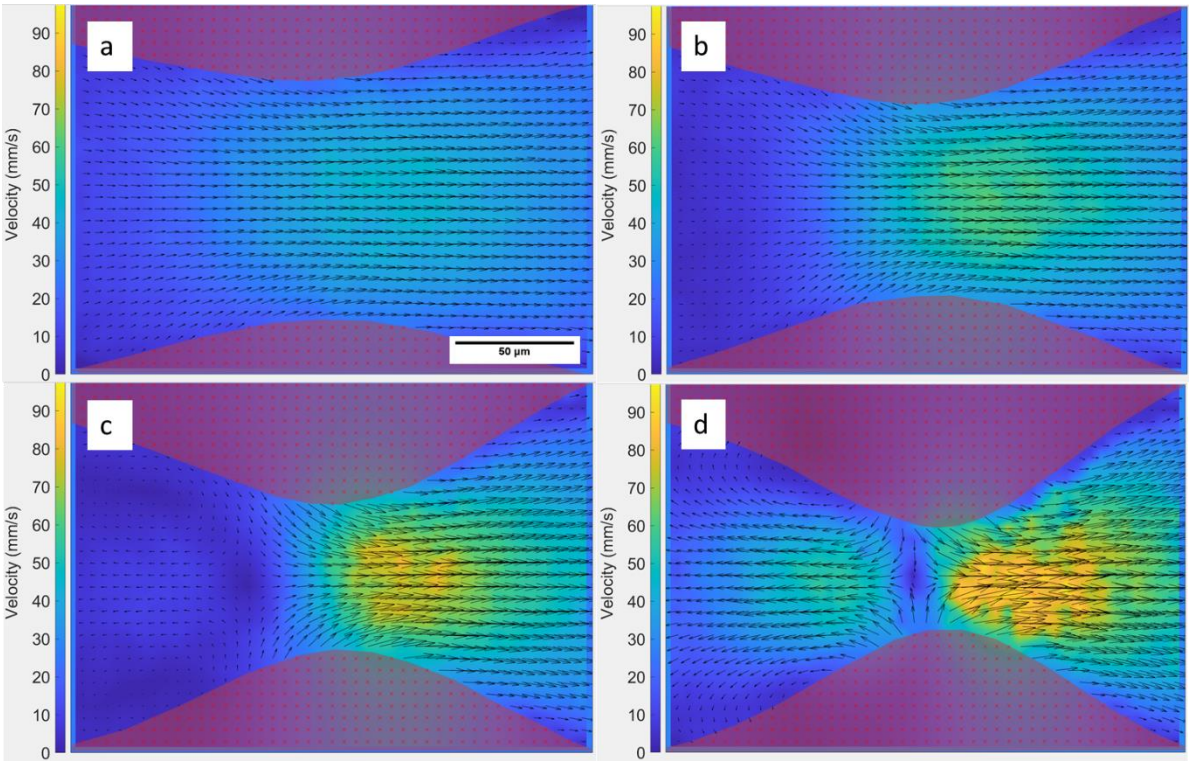


Figure 6.1 Averaged total velocity fields during necking for a surfactant free system. Continuous phase is 4.6 mPa s silicone oil. Neck diameter is a: 100, b:80, c: 60 and d:40 μm.

As the necking stage begins velocities are low and the maximum values are recorded in the centre of the neck and in the thinnest part. As the neck diameter becomes thinner due to the action of the continuous phase, the capillary pressure in the thinnest part of the neck increases, which in turn increases the velocity of the fluid moving through the neck towards the expanding droplet. Capillary pressure is given by

$$P_c = 2\sigma/D_{neck} \tag{6.1}$$

Where σ is surface tension (N m^{-1}), in this case interfacial tension, and D_{neck} is the neck diameter (m) (Kovalchuk et al., 2016). Furthermore, a stagnation zone is formed on the side of dispersed

phase channel. Initially fluid bypasses this low velocity zone and moves towards the outlet channel. As the thinning process progresses fluid is no longer moving towards the outlet channel but is expelled from the neck from both sides. It appears that the neck, in the last stages of necking is stretched in two opposing directions. The action of the continuous phase pushes the neck towards the outlet channel while the flow reversal due to capillary pressure pulls the neck towards the dispersed phase channel. These results are in agreement with experimental studies on emulsification using micro-PIV (Roumpea et al., 2019). Increasing the continuous phase viscosity, the necking process follows the same steps, but a reduction of the velocity magnitude is observed. This can be observed more clearly if the velocity magnitude profiles along the interface are examined, Figure 6.2 displays the velocity magnitude close to the interface of the thinning neck for various neck diameters.

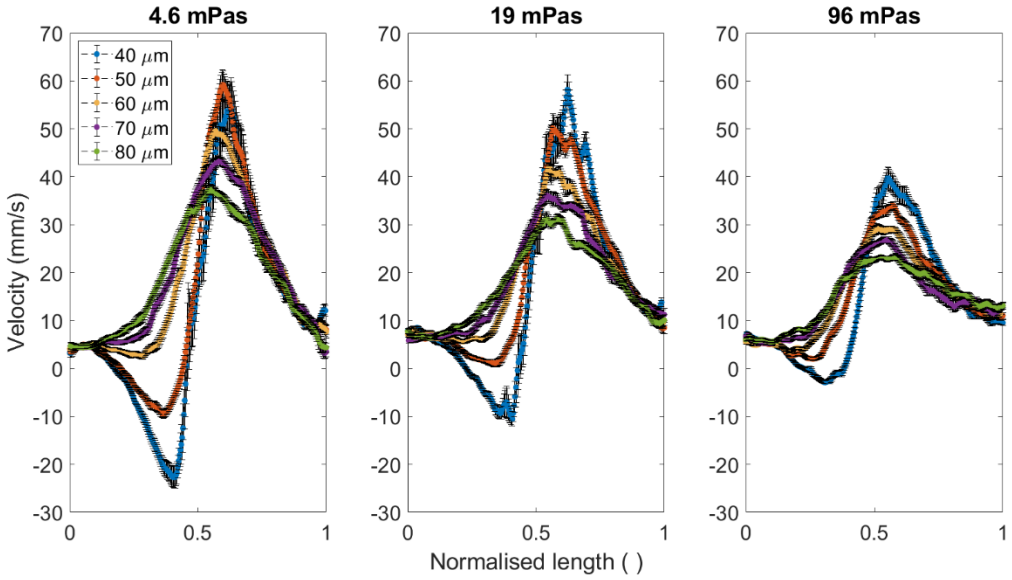


Figure 6.2 Velocities along the interface during the necking stage for a surfactant free system in three different continuous phases.

The interface length is normalised using the maximum length of the interface where the velocities are measured. 0 represents the leftmost part of the interface while 1 is the rightmost. The velocities are measured as close as possible to the interface. The resolution of this measurement is limited by the size of the speckles, which for this study are 3x3 μm in size.

Figure 6.3 is a schematic representation of the neck where the velocities for various neck instances are measured.

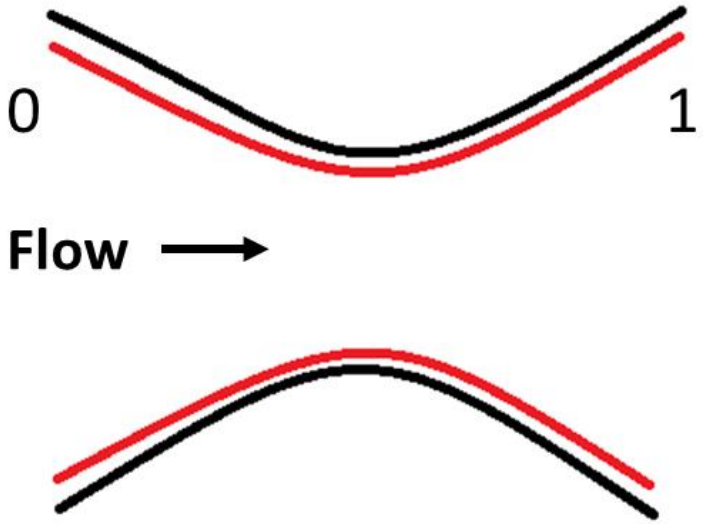


Figure 6.3 Schematic representation of the neck where the velocity profiles are measured. The red line represents the length of the neck where the velocities are measured, where 0 is the start and 1 is end of neck.

The velocities are measured both on the top and bottom side of the neck and averaged since the system is axisymmetric since the neck is focused from the top and bottom continuous phase channels with a flow rate of $Q_c/2$ (Cubaud and Mason, 2008). The error bars presented represent the standard experimental error as used previously. It is observed that as the neck diameter decreases the velocity along the interface increases. Furthermore, is observed that there is a reversal of the velocities along the interface in the side of the neck closer to the dispersed phase channel. The velocities on the left side of the distributions close to the dispersed phase channel display negative values suggesting fluid motion against the action of the continuous phase. In the case of 4.6 mPa s silicone oil, velocities become large and move towards the dispersed phase channel. As the continuous phase viscosity increases this action is smaller. In these cases, the magnitude of the reversal is smaller since the fluid needs to overcome the action of a more viscous continuous phase.

6.2.2-D velocity field during necking for systems with surfactant

The same analysis is performed for different surfactant solutions with concentrations below and above the cmc. The surfactants chosen for this study are the C10TAB and C12TAB and the solutions used have the same equilibrium interfacial tensions. The main idea behind this is that, since the solutions display the same interfacial tension, any differences observed during the droplet formation process can be attributed to the nature of the surfactant. The equilibrium interfacial tensions of the solutions used are summarised in the Table 6.1.

Table 6.1 Equilibrium interfacial tension of the solution used

Concentrations (mM)		Equilibrium interfacial tension
C10TAB	C12TAB	(mN m^{-1})
7.6	2	28.67
15.2	4	26.58
38.1	10	19.5
381	100	12

In Chapters 4 and 5 it was shown how the behaviour of the solution changes depending on concentration. More specifically, Figure 5.11 and Figure 5.12 show that for solutions below the cmc the surfactant solutions display a behaviour very similar to a surfactant free system. This is despite the observation from Figure 4.7, Figure 4.8 and Figure 4.10 that the timescales associated with the surfactant replenishment on the interface are smaller than the droplet formation and deformation timescales for the C10TAB. A similar behaviour is observed for C12TAB. Therefore, the systems to be studies are chosen to have concentration below the cmc where depletion phenomena can manifest.

The necking stage for a surfactant solution follows a similar behaviour, Figure 6.4 displays the 2-D averaged velocities for different diameters of the necking stage for a 2 mM C12TAB solution.

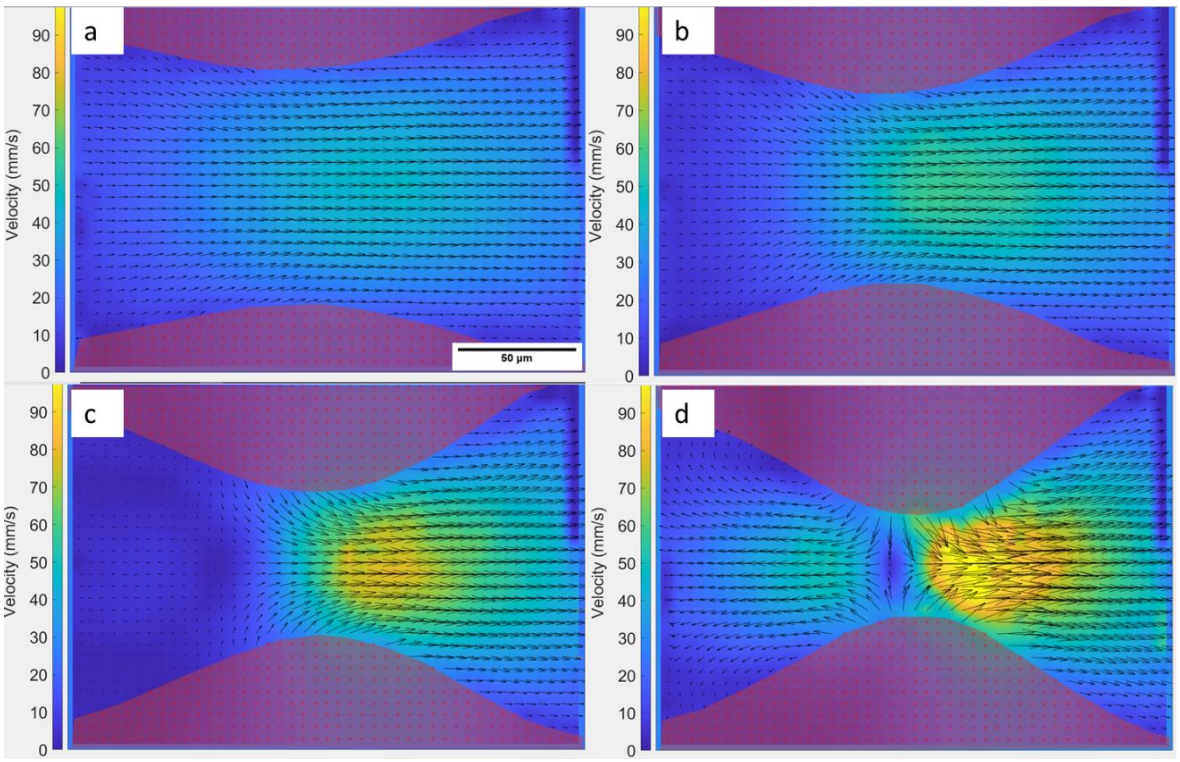


Figure 6.4 Averaged total velocity fields during necking for a 2 mM C12TAB solution. Continuous phase is 4.6 mPa s silicone oil. Neck diameter is a: 100, b:80, c: 60 and d:40 μm.

Similarly, to the surfactant free case an increase of the fluid velocity exiting the neck and the formation of a stagnation zone (panel c) on the side of the neck closer to the dispersed phase channel is observed. Fluid moves due to the action of the syringe pump, unobstructed at first, towards the expanding droplet. As the neck diameter decreases a stagnation zone is formed at the entrance of the neck. Initially fluid moves along the interface and into the neck bypassing the stagnation zone while also creating small recirculation at the side of the neck close to the dispersed phase channel. As the neck diameter keeps decreasing fluid no longer moves through the neck and is only expelled from both sides. A similar behaviour is observed for all surfactant solutions. The velocities close to the interface as the process evolves are also examined and compared to the velocities along the interface of the surfactant free system. Figure 6.5 displays the velocities along the interface for various diameters for the 2 mM C12TAB solution.

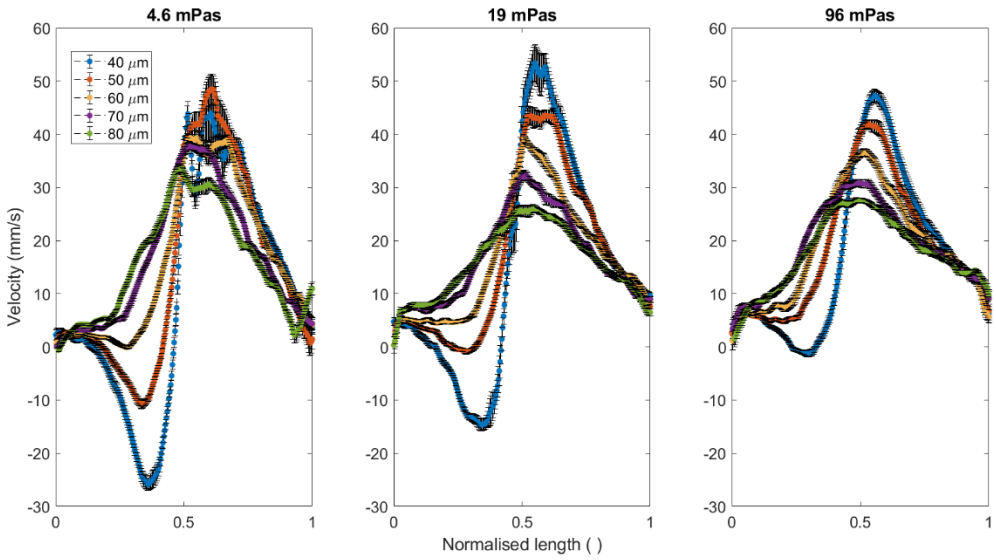


Figure 6.5 Velocities along the interface during the necking stage of 2 mM C12TAB solution in three different continuous phases.

Similarly, to the surfactant free system, as the continuous phase viscosity is increased the velocities close to the interface are smaller. A similar reversal of the flow along the interface, on the side of the neck closer to the dispersed phase channel, is observed for the 4.6 mPa s continuous phase which becomes smaller in magnitude then vanishes completely for the 19 mPa s and 96 mPa s continuous phases respectively. The velocity profiles are similar for other surfactant solutions.

Necking is driven by the capillary pressure squeezing the neck. According to equation 6.1, capillary pressure is a function of neck diameter and interfacial tension. The effect of the addition of surfactant can be understood by looking into the maximum fluid velocities. Figure 6.6 displays the results.

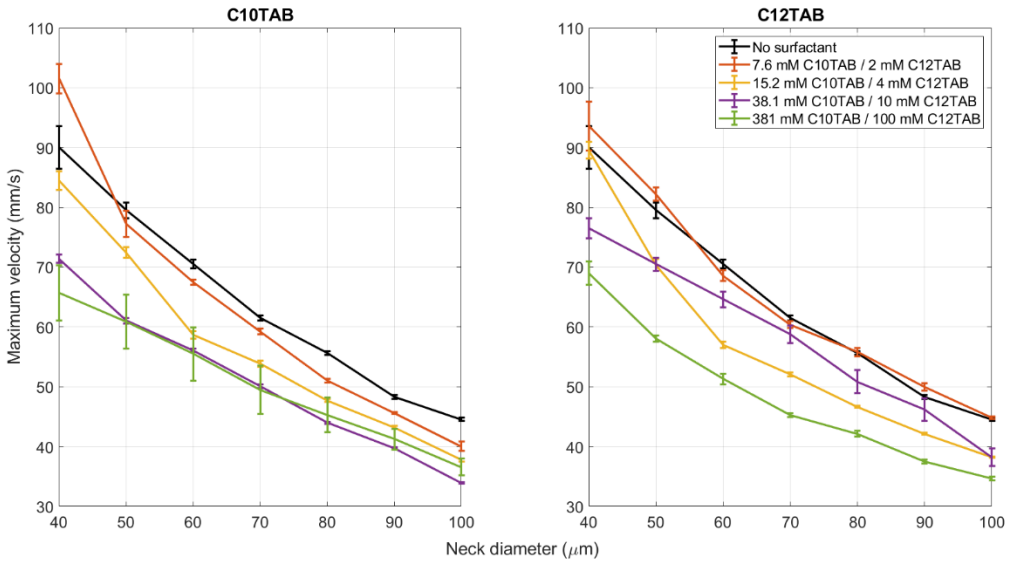


Figure 6.6 Maximum fluid velocity during necking for various solutions. Continuous phase is 4.6 mPa s silicone oil.

It is observed that as the neck diameter decreases the velocity increases. The fluid, under the action of the pump and the drag force of the continuous phase is forced through the neck. As the diameter of the liquid filament decreases the velocity of the liquid moving through it increases. Liquid is expelled from the neck as the capillary instability reduces the diameter of the neck leading to the detachment of the droplet. Increasing the surfactant concentration lowers the maximum fluid velocity since it lowers capillary pressure by lowering interfacial tension according to equation 6.1. The change in maximum fluid velocity follows the change in thinning exponent presented in Figure 5.3 and Figure 5.4. As the thinning rate increase, suggesting a different acting interfacial tension the maximum fluid velocity is reduced. It was demonstrated in the previous chapter that as the neck diameter decreases when small quantities of the surfactant are present the thinning neck displays a behaviour very similar to a surfactant free system (see section 5.2). The velocities along the interface for these solutions are also compared. Figure 6.7, displays the results.

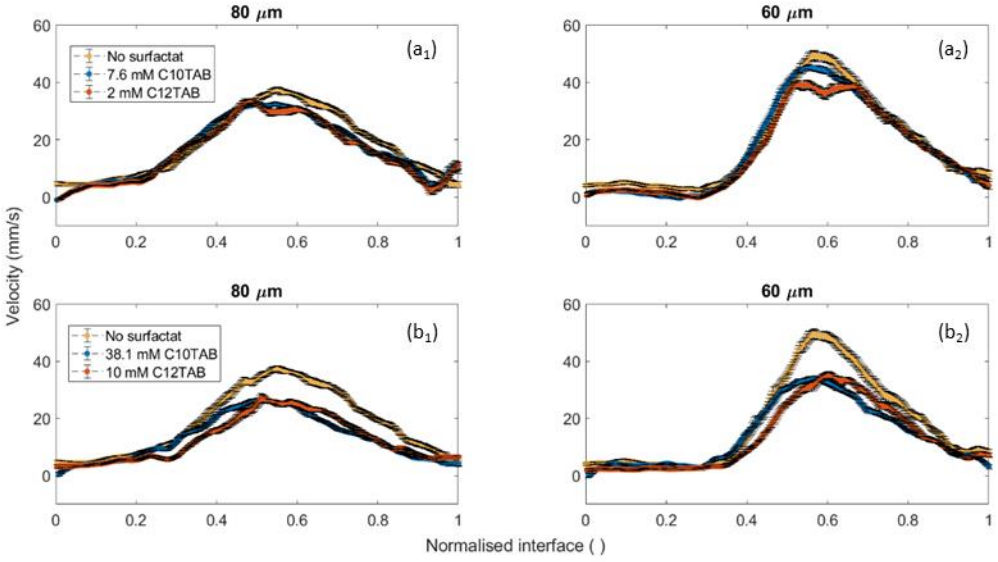


Figure 6.7 Velocity profiles along the interface of the thinning neck. Continuous phase is 4.6 mPa s silicone oil. $a_{1\text{-}2}$: 7.6 mM and 2 mM. $b_{1\text{-}2}$: 38.1 mM and 10 mM.

It is observed that the velocities along the interface for the solution with surfactant appear to be smaller than the surfactant free system. Examining Figure 5.3, Figure 5.4, Figure 5.6, and Figure 5.7 is shown that solutions with small surfactant quantity (below the cmc) display a behaviour very similar to a surfactant-free system for instances away and close to the pinch-off. This suggests a depletion of surfactant from the thinning neck which is responsible for the reduction in interfacial velocities, due to the presence of Marangoni stresses along the interface, caused by the inhomogeneities of the surfactant concentration. Increasing the surfactant concentration leads to a different behaviour for the instances away from the pinch-off, but as the process approaches it, the behaviour still resembles the behaviour of a surfactant free system. The velocity distributions display smaller velocities even for these surfactant concentrations. Similarly, the break-up process and the velocities in a 19 mPa s continuous phase are examined in Figure 6.8.

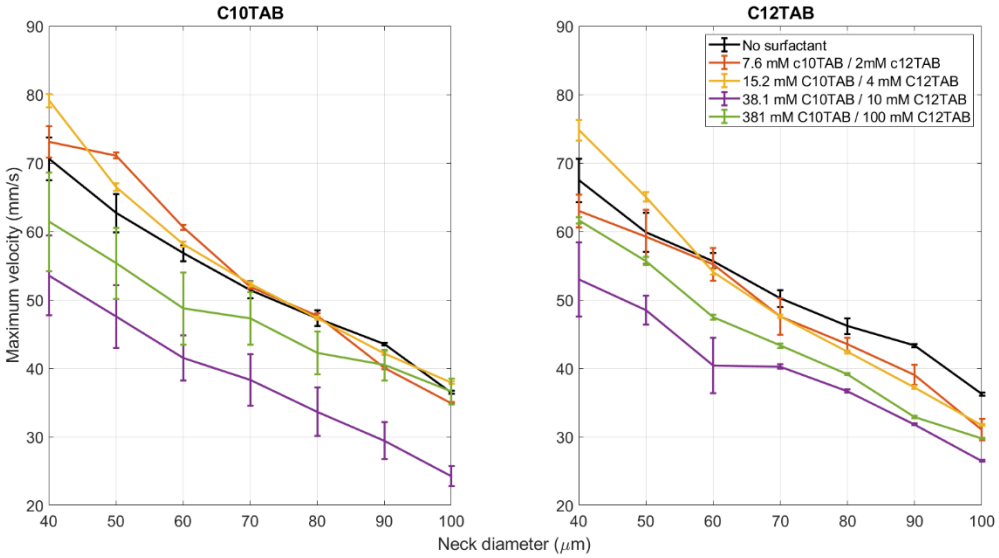


Figure 6.8 Maximum fluid velocity during necking for various solutions. Continuous phase is 19 mPa s silicone oil.

As in the case of the 4.6 mPa s continuous phase the maximum fluid velocity increases as the neck diameter decreases for all surfactant solutions. For small concentration of surfactant, the maximum fluid velocities are very similar with the velocities observed for the surfactant free system, while increasing the surfactant concentration leads to a reduction of the maximum fluid velocity due to a reduction of interfacial tension. The velocities along the interface during the necking stage are displayed in Figure 6.9.

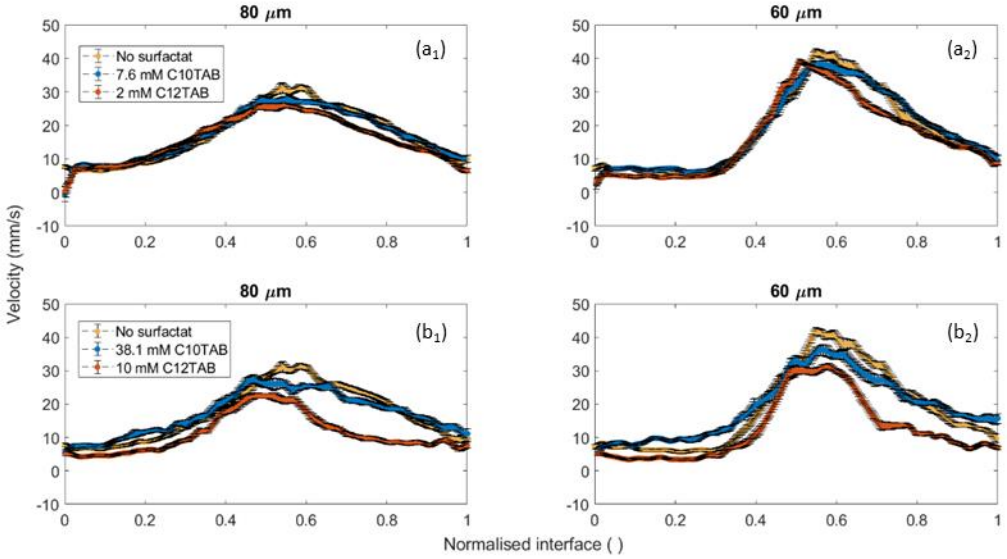


Figure 6.9 Velocity profiles along the interface of the thinning neck. Continuous phase is 19 mPa s silicone oil. $a_{1\text{-}2}$: 7.6 mM and 2 mM. $b_{1\text{-}2}$: 38.1 mM and 10 mM.

In this case the velocities along the interface for the C10TAB solutions appear to be very similar to the velocities of a surfactant free system for all surfactant concentrations. Looking at Figure 5.4 for instances away from the pinch-off the thinning rate for the C10TAB solutions used is quite different from a surfactant free system. When the break-up approaches pinch-off, the thinning behaviour (Figure 5.3) resembles more a surfactant free system and the velocities might be impacted. The velocities along the interface for the C12TAB solutions appear to be smaller than the surfactant free system suggesting the presence of Marangoni phenomena. For instances away from the pinch-off (Figure 5.7) all C12TAB solutions display a different behaviour from a surfactant free system. As the pinch-off approaches the behaviour resembles a surfactant free system (Figure 5.6). C12TAB is found in the system in much smaller quantities due to its smaller cmc. The limiting adsorption timescales for C12TAB solutions presented in 4.2.1.2. show that the droplet formation process occurs faster than the time it takes to replenish the surfactant on the interface. The break-up process is much more affected by the quantity of surfactant in the system explaining the slightly smaller velocities along the interface. Due to the depletion of surfactant along the interface and the larger replenishment timescales, Marangoni stresses arise on the interface which impact the local velocity field. Smaller

velocities are documented for the C12TAB solutions since the absence of surfactant causes a retardation of the interface. Increasing the surfactant concentration above the cmc makes the velocity profiles match the surfactant free system. Lastly, the case of higher continuous phase viscosity is examined. The maximum fluid velocity is displayed in Figure 6.10.

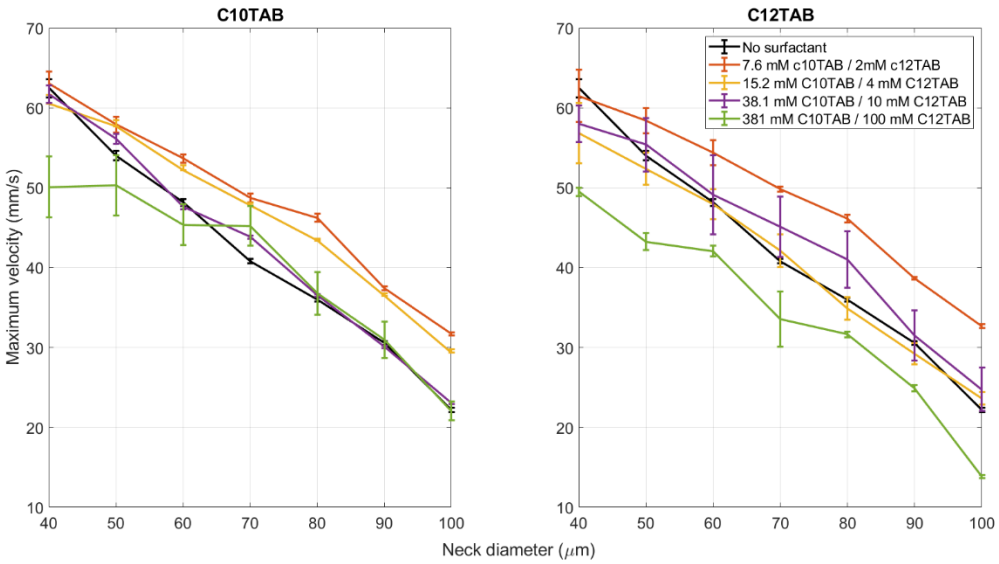


Figure 6.10 Maximum fluid velocity during necking for various solutions. Continuous phase is 96 mPa s silicone oil.

Maximum fluid velocities in this case appear to be much closer to each other. The increase in the continuous phase viscosity leads to a process more dominated by viscosity. The balance of forces during break-up is between inertia, surface tension and viscosity. When including the continuous phase viscosity research has shown that the balance of forces shifts towards viscosity being the more dominant force affecting the break-up of the liquid thread (Lister and Stone, 1998). Furthermore, the difference in equilibrium surface tension between the systems is smaller meaning that the solution will display smaller differences in their maximum fluid velocities. For instances away from the pinch-off the C10TAB solutions display a different behaviour while the pinch off is approached every solution displays a behaviour similar to a surfactant free system. The behaviour is similar for the C12TAB solutions. In this case smaller

differences in the velocity profiles along the interface are expected, the results are presented in Figure 6.11.

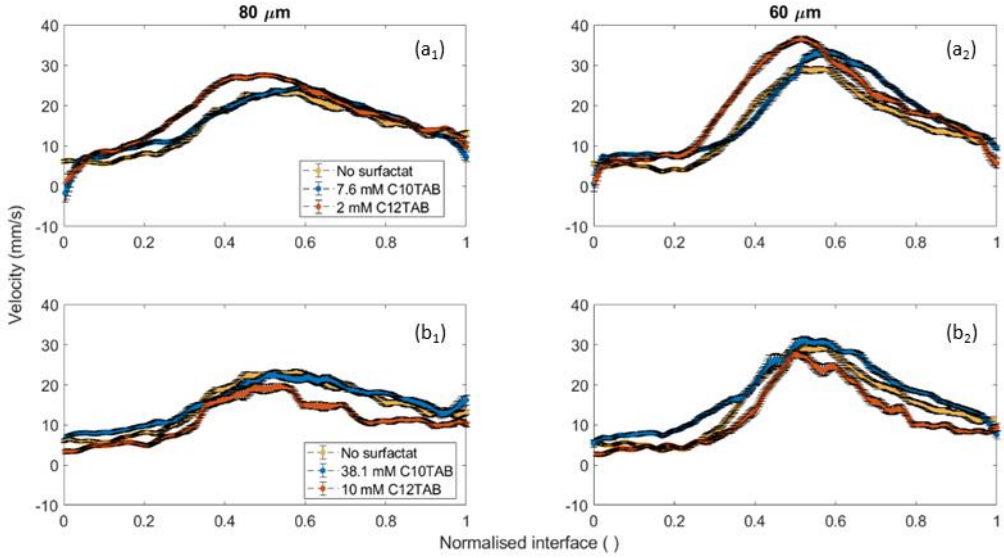


Figure 6.11 Velocity profiles along the interface of the thinning neck. Continuous phase is 96 mPa s silicone oil. $a_{1\text{-}2}$: 7.6 mM and 2 mM. $b_{1\text{-}2}$: 38.1 mM and 10 mM.

It appears that the velocity profiles are much similar to the velocities of a surfactant free systems in most cases. The droplet formation process is significantly slower due to the increase of the continuous phase viscosity and therefore there is more time available for the surfactant mass transport along the interface to take place and cover any inhomogeneities. For the solutions above the cmc the velocity profiles are similar to the distributions for the surfactant free system.

6.3. Examination of the neck shape during the necking stage and self-similarity

In this section, the profiles of the thinning neck for different surfactant, and surfactant free, solutions are examined. As mentioned in §2.5 the shape of the thinning neck should be independent of experimental conditions and is only dictated by the properties of the liquid. To quantitatively examine this the thinning neck is rescaled. The variables for the rescaling of the neck are described by the pair of equations given in (Zhu and Wang, 2019). The equations are,

$$H = h(z)/h_{min} \tag{6.2}$$

$$Z = (z - z_{min})/h_{min} \tag{6.3}$$

where and H and Z are the rescaled coordinates. h_{min} is the minimum neck radius (m), Z is the axial coordinate (m) and z_{min} is the axial coordinate (m) of the neck at the minimum radius. Equations 6.2 and 6.3 are used for the rescaling of the neck for various surfactant solutions and allow the comparison of the shape of the interface. Rescaled interface profiles that are close to each other suggest that the shape of the compared necks is similar.

The rescaled neck profiles for solutions without surfactant for droplet formation in three different continuous phases at various neck diameter instances are presented in Figure 6.12.

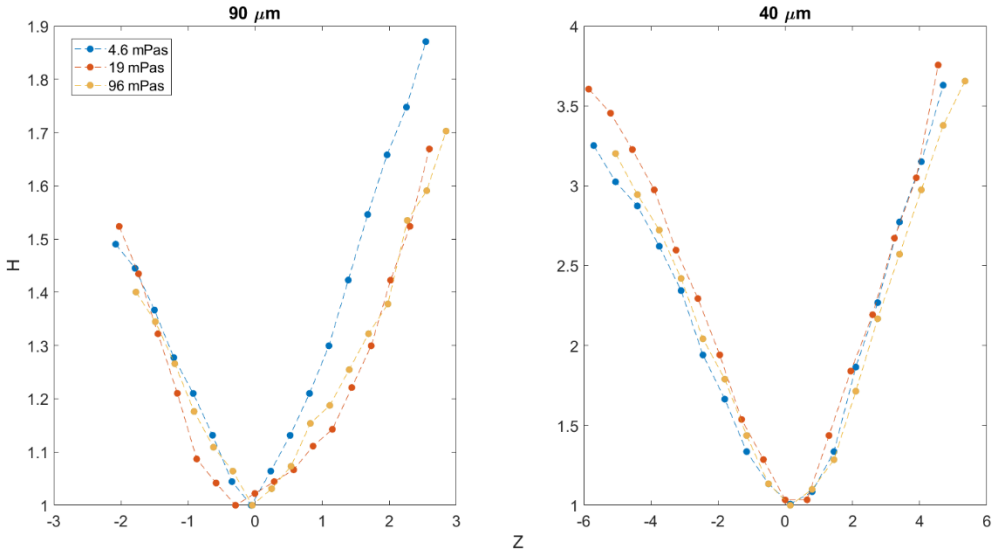


Figure 6.12 Rescaled thinning neck interface profiles for a surfactant free system in three different continuous phase viscosities

It is observed that for larger neck diameters the neck profiles are not similar and there is a dependency on the viscosity ratio between the two phases as is presented in previous literature and mentioned previously. As the diameter of the neck decreases, the profiles become more similar suggesting a universality in the thinning process of the neck. The idea now is if the presence of surfactant affects this behaviour as it did with the maximum fluid velocity and the velocity along the interface. Figure 6.13 displays the results.

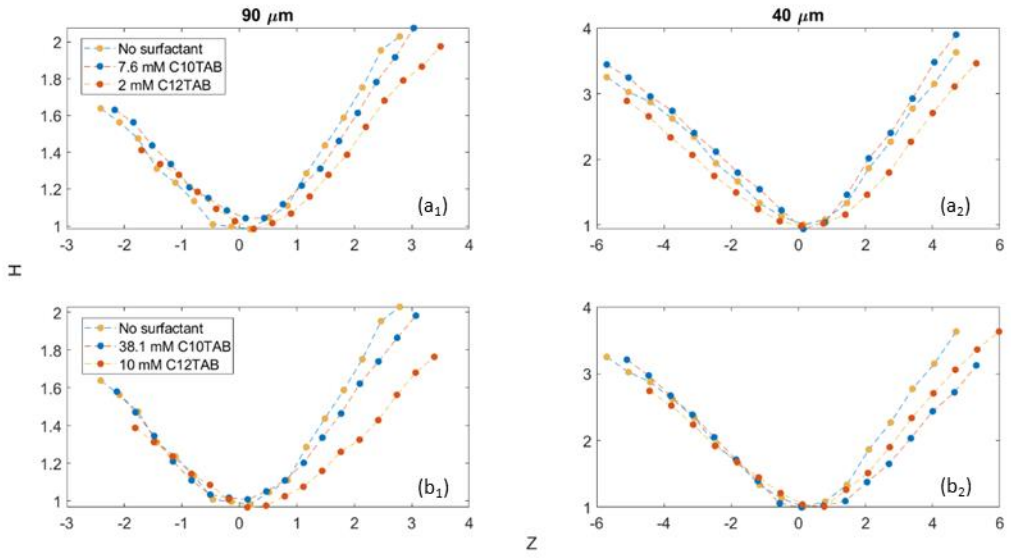


Figure 6.13 Rescaled thinning neck interface for various surfactant solutions in 4.6 mPa s continuous phase. $a_{1\text{-}2}$: 7.6 mM and 2 mM. $b_{1\text{-}2}$: 38.1 mM and 10 mM

Previously the velocity profiles along the interface between surfactant solutions and a surfactant free system were compared and it was demonstrated that increasing the surfactant concentration decreases surface velocities. Similarly, as shown in Figure 6.13, for the small concentrations (a_1) of surfactant the rescaled interface profiles appear to be different from the surfactant free system for both surfactant solutions. Increasing the surfactant concentration (b_1) only makes the differences larger as happened with the velocities along the interface. The presence of the surfactant lowers interfacial velocities due to the presence of Marangoni stresses (as shown previously) which also alters the shape of the interface. In both cases it is observed that as the neck diameter decreases, the neck profiles become more similar (a_2, b_2), during the final stages of the break-up. Chapter 5 showed that as the pinch-off moment approaches the behaviour resembles more a surfactant free system explaining the similarity of the shape of the interface. Similarly, the break-up process in a 19 mPa s continuous phase is examined, Figure 6.14 shows the results.

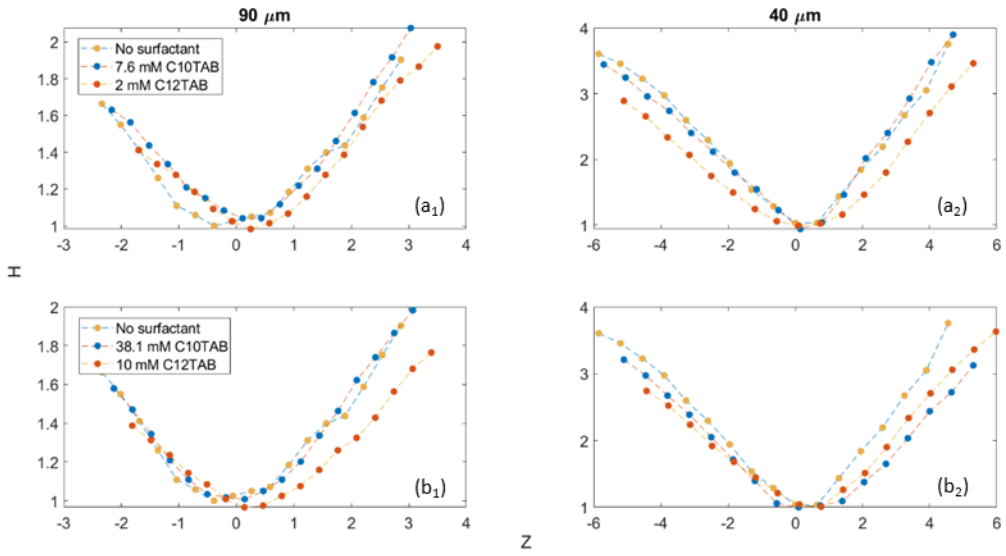


Figure 6.14 Rescaled thinning neck interface for various surfactant solutions in 19 mPa s continuous phase. $a_{1\text{-}2}$: 7.6 mM and 2 mM. $b_{1\text{-}2}$: 38.1 mM and 10 mM.

As in the case of the velocity profiles in Figure 6.2 as the surfactant concentration increases the velocities along the interface become smaller and similarly the rescaled velocity profiles for these solutions are very similar to the surfactant free profile. For the higher concentrations the velocity profile of the 10 mM C12TAB solution is smaller than the 38.1 mM C10TAB and the surfactant free system which is also the case for the rescaled interface profile. This suggests that the presence of Marangoni phenomena alters the shape of the interface. Changing the continuous phase to the 96 mPa s silicone oil leads to a similar behaviour observed in Figure 6.11. The increases in continuous phase viscosity makes the rescaled interface profiles very similar to each other. Lastly, solutions with concentrations of surfactant five times the cmc are examined, the results are presented in the Figure 6.15.

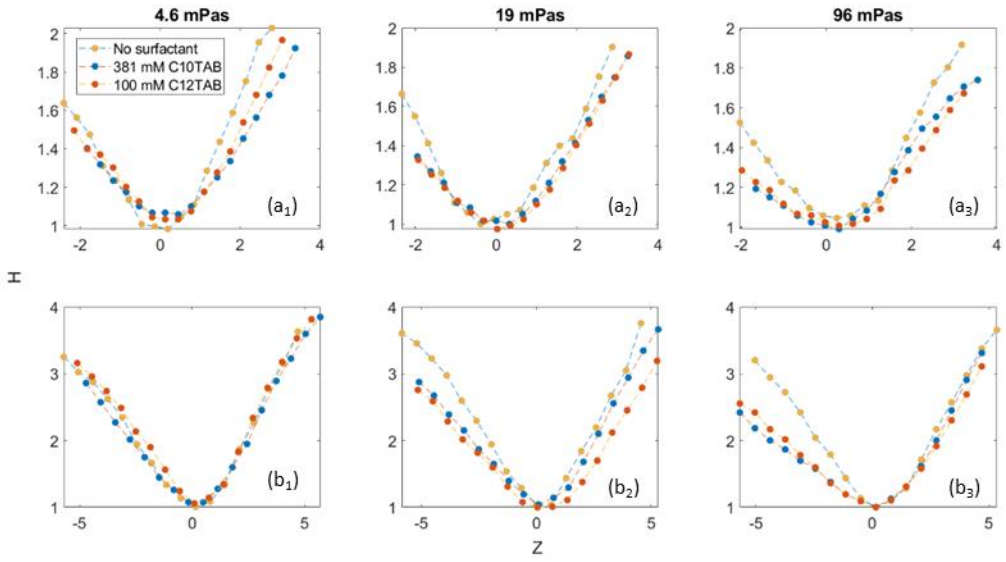


Figure 6.15 Rescaled interface profiles for 5 cmc surfactant solutions in three different continuous phases. $a_{1\text{-}3}$: neck diameter is 80 μm. $b_{1\text{-}3}$: neck diameter is 40 μm.

Increasing the surfactant concentrations has the same effect as increasing the continuous phase viscosity. The rescaled interface profiles appear to be more similar with each other for smaller continuous phase viscosities. For the 19 mPa s continuous phase viscosity the rescaled profiles appear to be different as the break-up approaches, a behaviour similar to the 96 mPa s silicone oil continuous phase. It is observed that increasing the surfactant concentration above the cmc leads to a universal behaviour at neck diameters away from the pinch-off. The profiles appear to be less self-similar once the break-up approaches. In those very short time-scales the deformation of the neck and the fluid velocities become significantly larger and may contribute to the uneven surfactant distribution. Furthermore, it is observed that when the velocities close to the interface are different from the velocities of a surfactant free system the rescaled interface profiles do not match as well. The shape of the neck is affected by the presence of surfactant which in turn affects the local hydrodynamics which alter the local velocity field.

6.4. GPV study of the droplet expansion

The expansion stage of the droplet formation process for a surfactant free system in 4.6 mPa s silicone oil is presented in Figure 6.16. The timeframes presented in each case are 3, 7, 10 and 13 ms after the previous droplet pinch-off event.

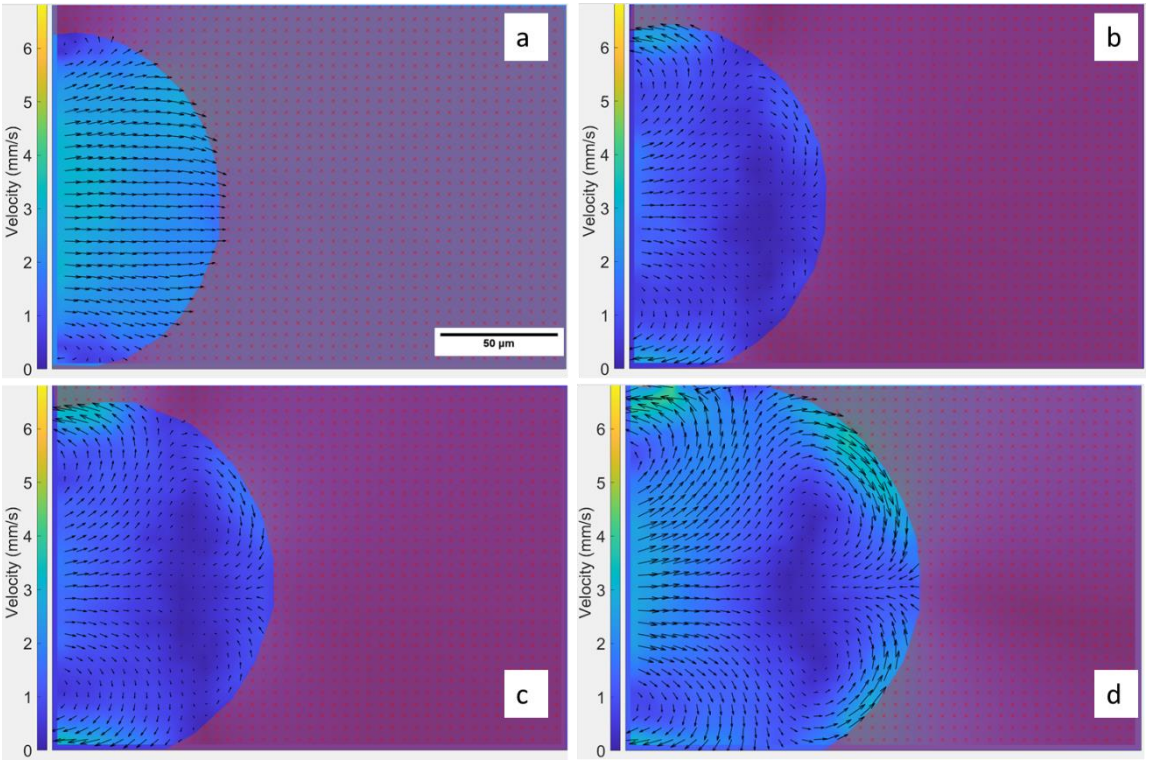


Figure 6.16 Expansion stage of a surfactant free system. Continuous phase is 4.6 mPa s silicone oil. a: 3 ms b: 7 ms. c:10 ms. d: 13 ms after the previous droplet pinch-off

Figure 6.16 shows that the droplet grows by the formation of a stagnation of zone at the tip. As the process advances the stagnation zone moves to centre of the expanding droplet and fluid moves around it. Velocities seem to increase as the process progresses. This mechanism has been documented in literature (Pirbodaghi et al., 2015). Figure 6.16 shows that in the beginning of the process velocities are small and increase as the process develops. The velocity magnitude along the interface is proportional to the viscosity of the continuous phase. During the droplet formation process, the drag force of the continuous phase competes with the surface tension force. Increasing the continuous phase viscosity increases the drag force of the continuous phase which increases interfacial velocities. In the case of the 4.6 mPa s continuous phase the

drag force is small, therefore the difference with the surface tension force is small as well. Furthermore, the absence of surfactant means that the system displays the highest interfacial tension throughout the process. The drag force of the continuous phase encounters a larger resistance due to the high interfacial tension which works against fluid motion on the interface. Similarly, the expansion stage of a surfactant free droplet in a 19 mPa s continuous phase, is presented in Figure 6.17.

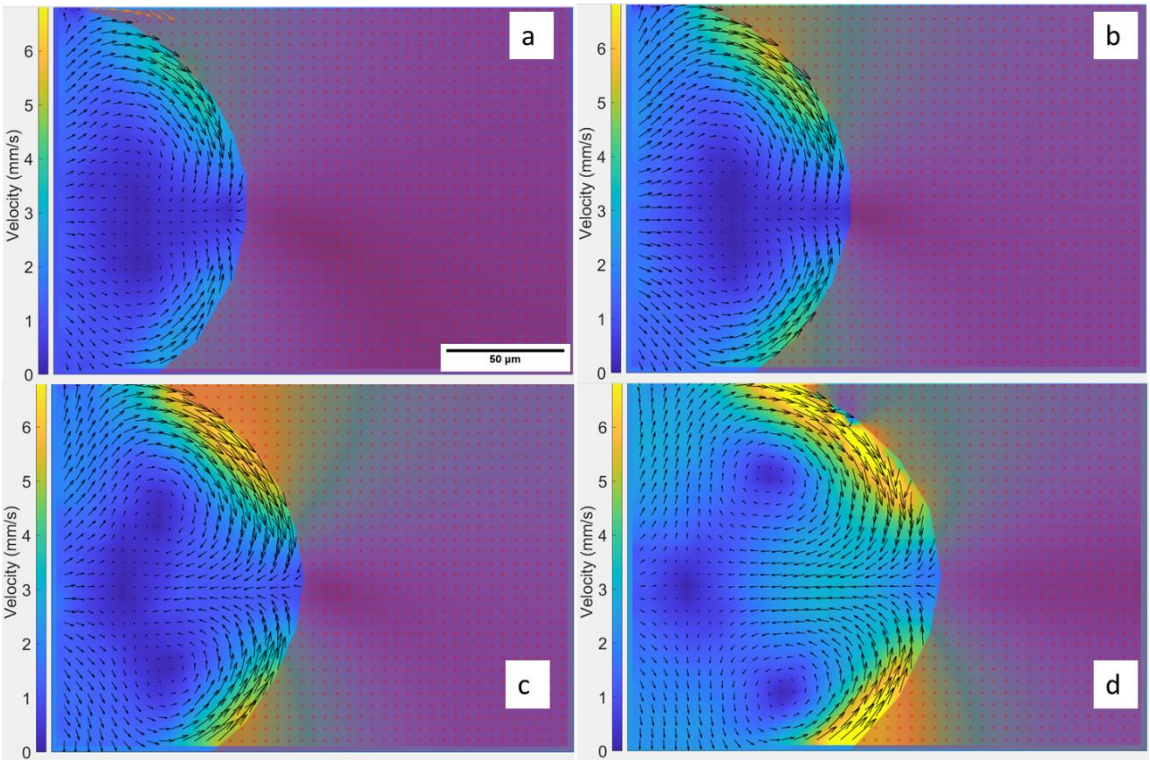


Figure 6.17 Expansion stage of a surfactant free system. Continuous phase is 19 mPa s silicone oil. a: 3 ms b: 7 ms. c:10 ms. d: 13 ms after the previous droplet pinch-off

Examining Figure 6.17 it appears that, in contrast to necking, interfacial velocities appear to be larger as the continuous phase viscosity increases. Furthermore, Figure 6.17 displays the formation of two recirculation zones as the expansion stage progresses. Velocities are higher due to the increase of the continuous phase viscosity because of the increased drag force exerted by the continuous phase. In the case of the 96 mPa s continuous phase a similar behaviour is observed. The velocities are in the same order of magnitude as in the case of 19 mPa s continuous phase and the same recirculation zones are formed. The above results show that for

low viscosity continuous phases the droplet grows with the mechanism proposed by Pirbodaghi and his colleagues. At the first stages of expansion a stagnation zone forms at the tip of the droplet. As the droplet expands fluid moves around that stagnation zone and this zero-velocity area is moved to the centre of the expanding droplet as the process advances. In the cases of more viscous continuous phases a different behaviour is observed. Initially a small recirculation zone is formed at the tip and centre of the expanding droplet. As the process advances this zone separates into two recirculation zones, one at each side of expanding droplet and a stagnation zone is formed at the base of the expanding droplet. That stagnation zone is formed where the fluid recirculating from the tip to the centre of the drop meets the dispersed phases coming into the drop due to the action of the pump. A similar analysis on C10TAB solutions in the same three continuous phases used is performed. Figure 6.18 displays the 2D velocity field during the expansion stage of 38.1 mM C10TAB solution.

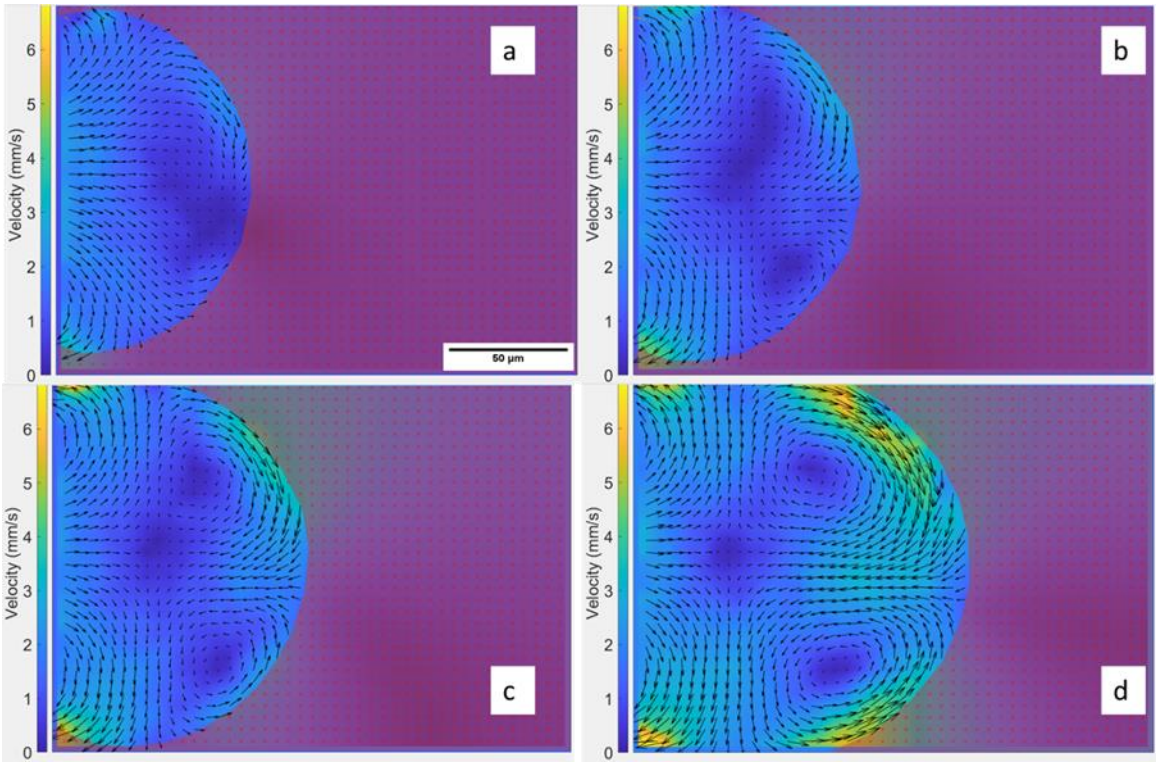


Figure 6.18 Expansion stage of a 38.1 mM C10TAB solution. Continuous phase is 4.6 mPa s silicone oil. a: 3 ms b: 7 ms. c:10 ms. d: 13 ms after the previous droplet pinch-off

In the case of a surfactant free system during droplet formation in 4.6 mPa s silicone oil no significant recirculation is observed. In contrast, in the case of a surfactant system, the

formation of two recirculation zones similarly to the cases of higher viscosity continuous phase for a surfactant free system is observed. The presence of surfactant lowers interfacial tension; therefore, the drag of the continuous phases is larger compared to the surface tension force of the dispersed phase resisting that drag. In the case of a surfactant free system, due to the absence of surfactant, interfacial tension is higher, and the drag force has to overcome a larger obstacle in order to produce recirculation in the expanding droplet. In the case of a surfactant system, this is easier, due to the smaller interfacial tension force. In recent studies, researchers observed recirculation only in a surfactant free system. The absent of recirculation in system with surfactant is attributed to the accumulation of surfactant on the tip of the expanding droplet that creates Marangoni stresses along the interface (Roumpea et al., 2019). It is important to note that the in the study of Roumpeat et. al. researchers used a concentration of surfactant 50 times the cmc. It is possible that with quantities of surfactant that large the difference in surfactant concentration on the interface are large enough to produce high enough Marangoni stresses that do not allow for any recirculation. In contrast this study uses smaller quantities of surfactant and the produced inhomogeneities in surfactant concentration on the interface during expansion might not be equally large. Lastly, Roumpea and their colleagues used microPIV which provided them with a spatial resolution of 11.9x11.9 μm (Roumpea et al., 2019) while in this study the spatial resolution achieved by GPV is 3x3 μm. It is possible that the improved spatial resolution allowed for the observation of the recirculation during the expansion stage in case where it was previously impossible. A solution of 381 mM C10TAB is also studied, a concentration 5 times above the cmc. Figure 6.19 shows the results.

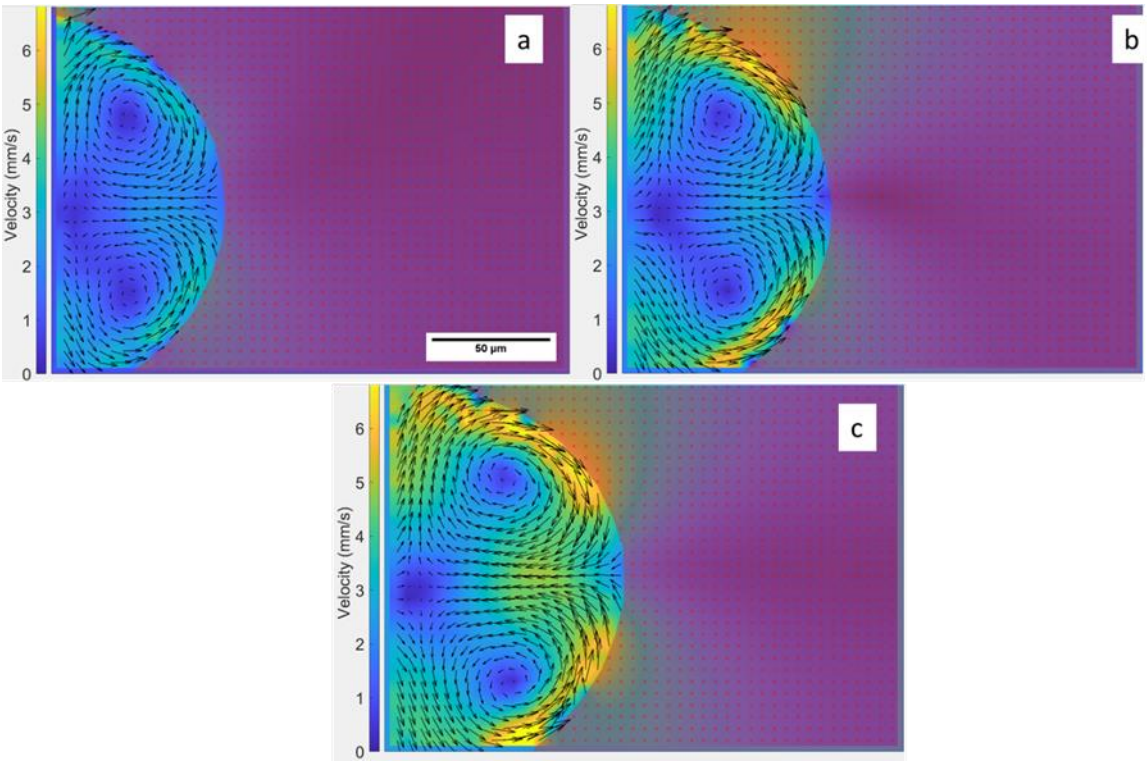


Figure 6.19 Expansion stage of a 381 mM C10TAB solution. Continuous phase is 4.6 mPa s silicone oil. a: 3 ms b: 7 ms. c:10 ms after the previous droplet pinch-off

Similarly, a solution of C10TAB with surfactant concentration 5 times the cmc displays a similar behaviour. The formation of two recirculation zones and a stagnation zone, present from the first stages of expansion, is observed. It is notable to observe that in the final stages, the maximum fluid velocity is 6 mm s^{-1}. In this case, the amount of surfactant in the system is large enough for the system to display an interfacial tension much closer to its equilibrium value. In the case of the 38.1 mM solution the surfactant quantity is limited and the presence of Marangoni stresses along the interface reduces interfacial velocities. Similarly, the expansion stage of 38.1 mM C10TAB solution in 19 mPa s continuous phase is examined, Figure 6.20 shows the 2D velocity fields.

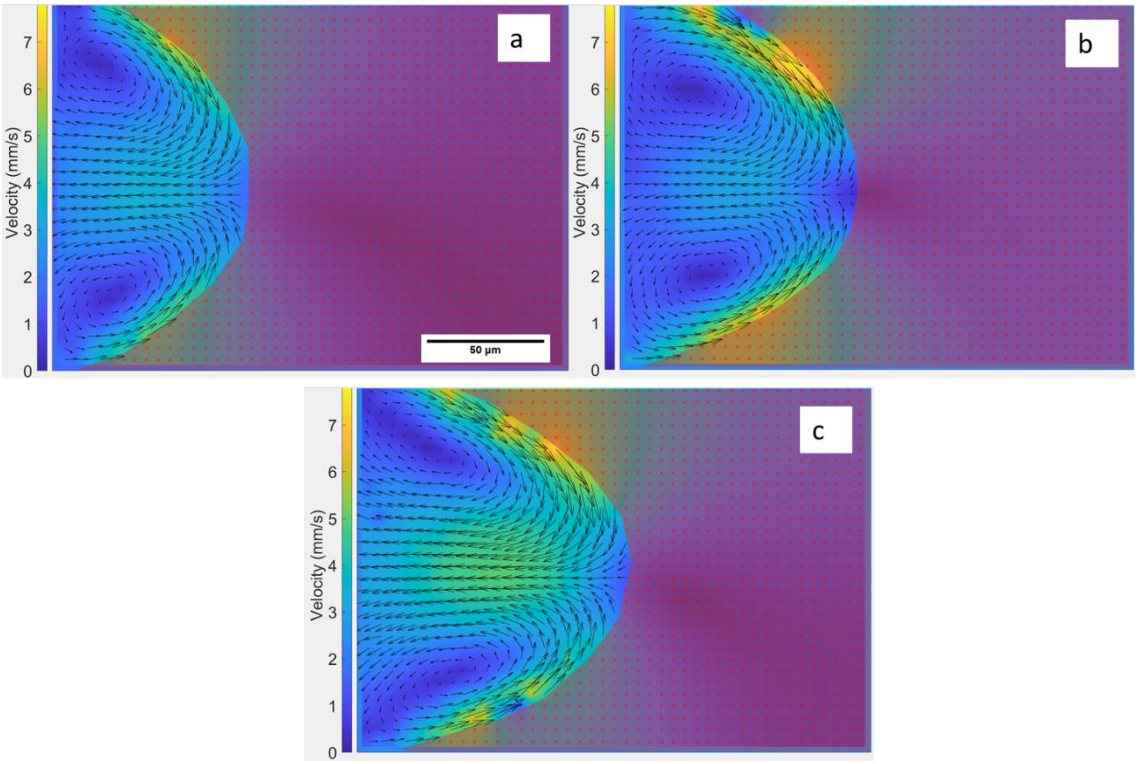


Figure 6.20 Expansion stage of a 38.1 mM C10TAB solution. Continuous phase is 19 mPa s silicone oil. a: 3 ms b: 7 ms. c:10 ms after the previous droplet pinch-off

In the case of 19 mPa s silicone oil and the 38.1 mM C10TAB solution a similar behaviour to the 4.6 mPa s case is observed. Velocities are larger from the surfactant system suggesting the presence of surfactant on the interface that reduces interfacial tension. This reduction in interfacial tension means that the drag of the continuous phase is larger than the surface tension force allowing for the fluid velocities to be larger than the velocities of the surfactant free case. Increasing the quantity of surfactant leads to the same recirculation patterns being formed. The case of the 96 mPa s continuous phase viscosity is also studied. In that case the surfactants solution displayed velocities very similar the surfactant free system. For low viscosity oils the presence of surfactants affects the velocity fields and the velocity magnitudes. More specifically, in the case of 4.6 mPa s continuous phase, the presence of surfactant leads to more recirculation during the expansion stage due to the lower interfacial tension that allows for the continuous phase to drag the interface easier. This relative increase in drag force creates more recirculation in the expanding droplet. As the continuous phase viscosity increases the

velocities along the interface increase. Similarly, when there is surfactant present the velocity magnitude appears to be higher due to the reduction in interfacial tension.

6.5. Conclusions

Key Learnings

- During thinning fluid velocities increases as the neck becomes thinner and a flow reversal is observed after a critical diameter before rupture.
- The velocities close to the thinning interface of the increase as the neck diameter decreases.
- The increase in continuous phase viscosities leads to smaller velocities close to the interface
- The presence of surfactant leads toa reduction in the velocities along the interface for instance close to pinch-off
- Solutions with concentration below the cmc display smaller velocities close to the interface due to the presence of Marangoni phenomena.
- During expansion, recirculation is observed inside the growing droplet proportional to the viscosity of the continuous phase and the quantity of surfactant.
- The shape of the interface is affected by the presence of surfactant. Interfaces are more similar closer to pinch-off due to the depletion of surfactant from that region.

In this Chapter, the velocity profiles during the necking and expansion stages during droplet formation for surfactant free and surfactant systems in three different continuous phase viscosities were examined. Furthermore, the velocities along the interface were studied closely and compared to the surfactant free systems. Chapter 6 also examined the shape of the thinning neck during the necking stage to determine the effect of the redistribution of surfactant to the shape of the interface

It was demonstrated that during the necking stage liquid flows from the dispersed phase channel under the action of the syringe pump towards the expanding droplet. As the neck diameter decreases the movement of the fluid is hindered and a stagnation zone is formed at the base of the neck on the side of the dispersed phase channel. Initially, fluid moves around this stagnation zone, but as the neck becomes thinner due to the action of the continuous phase, fluid flow towards the expanding droplet is stopped and liquid is expelled for the neck. This is the case for surfactant and surfactant free systems in all continuous phases studied.

Examining the velocity fields along the interface reveals that velocities increase as the neck diameter decreases and for the same neck diameter velocities are smaller as the viscosity of the continuous phase increases. This is the case for surfactant and surfactant free systems. Comparing the velocities along the interface for surfactant and surfactant free systems revealed that the velocities along the interface are smaller when surfactant is present especially for concentrations below the cmc.

Furthermore, as the neck diameter decreases the maximum fluid velocity increases. For surfactant solution below the cmc the maximum fluid velocity is very similar to the maximum fluid velocity of a surfactant free system suggesting a similar acting interfacial tension as seen in Chapter 5. Increasing the surfactant concentration leads to smaller maximum fluid velocities.

The shape of the interface was also examined. It was revealed that for surfactant free systems the normalised interface profiles are similar for instances close to the droplet break-up but differ for instances away from the pinch-off. When surfactant is present the shape of the interface is different than the shape of a surfactant free system suggesting that the presence of Marangoni phenomena alters the shape of the interface. The differences persist even for solutions above the cmc for all continuous phase viscosities.

The last part of Chapter 6 examined the 2-D velocity profiles during the expansion stage of droplet formation for surfactant free and surfactant laden systems in three different continuous

phases. It was demonstrated that for the surfactant free system there is significantly more recirculation present as the continuous phase viscosity increases. The velocity magnitude is also increased as the continuous phase viscosity increases.

During the expansion stage the droplet grows towards the outlet channel. On this stage of droplet formation liquid moves into the expanding droplet along the interface and a stagnation zone is formed at the tip. For the case of the 4.6 mPa s continuous phase, this stagnation zone moves towards the centre of the expanding droplet and liquid moves around it. In the case of the 19 mPa s and 96 mPa s continuous phases, in addition to the stagnation zone, two recirculation zones are formed and the velocity magnitudes appear to be larger.

When surfactant is present this recirculation zones appear even in the case of the 4.6 mPa s continuous phase suggesting that during the expansion stage, convective mixing is more prevalent when surfactant is present. It appears that increasing the surfactant concentration leads to an increase in the recirculation inside the expanding droplet.

Chapter 7: Conclusions and future work

7.1 Conclusions

7.1.1. Conclusions regarding droplet sizes

The presence of surfactant during droplet formation affects the size of the produced droplets by reducing interfacial tension. Increasing the quantity of surfactant reduces droplet sizes in all cases regardless of the cmc of the surfactant. Increasing the continuous phase viscosity or the continuous phase flow rate has a similar effect due to the increase of the drag force acting against the interfacial tension force. For every surfactant used droplet sizes decreased even after the concentration of the surfactant was increased above the cmc when the break-up happened in a 19 mPa s continuous phase silicone oil. When the continuous phase was a 4.6 mPa s silicone oil the droplet size distributions for the C10TAB and C12TAB were the same for solutions above the cmc, something that was not observed for the C16TAB. In the case of a 96 mPa s continuous phase case the distributions seem to be similar to each other for high surfactant concentration for all surfactants. The above suggests that in the case of 19 mPa s continuous phase viscosity the transport of surfactant on the interface is reduced due to the suppression of interfacial flows which redistribute surfactant more easily in the case of the 4.6 mPa s oil, making the droplet sizes similar for high concentrations. Furthermore, surfactant solutions with small amounts of surfactant appear to display different droplet size distributions in cases where those should be the same.

It was demonstrated that depending on the continuous phase viscosity the droplet formation process can be modelled based on the capillary number and the volume fraction of the continuous phase. Furthermore, similar previous studies used the same scaling, proving it to be quite insightful (Cubaud and Mason, 2008). The mathematical scaling extracted for each case is:

4.6 mPa s	19 mPa s	96 mPa s (confined)	96 mPa s (unconfined)
$d/h = 0.35\ (a_2Ca_2)^{-0.25}$	$d/h = 0.4\ (a_2Ca_2)^{-0.24}$	$d/h = 0.33\ (a_2Ca_2)^{-0.24}$	$d/h = 0.33\ (a_2Ca_2)^{-0.40}$

For the 4.6 and 19 mPa s continuous phase viscosities the behaviour is very similar and suggests that the action of the continuous phase is more important in our experiments than similar experiments carried out using rectangular microchannels (Cubaud and Mason, 2008). In the case of 96 mPa s the scaling law changes when the droplet diameters become smaller than the channel height. When the droplet are confined the scaling law is very similar the previous scaling laws produced for the lower viscosity continuous phases, while for the unconfined case the exponent becomes smaller suggesting a smaller contribution of the continuous phase to the break-up.

In terms of satellite droplets their size increases with an increase of surfactant concentration and it levels off only for concentrations of surfactant two times above the cmc. Furthermore, increasing the continuous phase viscosity leads to a reduction in satellite droplet sizes. The size of the satellites, changes drastically for high surfactant concentrations in the 96 mPa s continuous phase due to the transition of the droplet formation regime from dripping to jetting. The limitations of the above analysis lie in the fact that the dynamic nature of the surfactant mass transport was not considered. The equilibrium interfacial tension was used in order to calculate the capillary number since there is no measure of dynamic interfacial tension during the emulsification process.

7.1.2. Conclusions regarding the neck kinetics

The thinning rate of the neck can reveal important information regarding the presence of surfactant. It is observed that in every case the thinning rate of the neck displays two distinct behaviours. For times away from the pinch-off the thinning rate is slow, while for times

approaching the pinch-off, the thinning rate is larger. Increasing the surfactant concentration slows down the neck kinetics as it was observed in literature. The neck kinetics cluster for solutions above the cmc suggesting a levelling of interfacial tension.

In the case of the 4.6 mPa s continuous phase the thinning rate of the neck appears to be different from the thinning rate of a surfactant free system only when the surfactant concentration is higher than 0.5 cmc, both for the C10TAB and C12TAB. For moments close to the pinch-off the thinning rate appears to be different only for highly concentrated solutions both for the C10TAB and C12TAB. The above suggests that while in the first stages of the process the solutions displays properties different from a surfactant free system, in the final stages, the behaviour is very similar to a surfactant free system. This suggests, that depletion of surfactant from the thinning neck during the very short final moments of droplet formation might be inevitable.

When the continuous phase is a 19 mPa s silicone oil all solutions display a different thinning rate from a surfactant free system in moments away from the pinch-off. Both for the C10TAB and the C12TAB. When examining instances closer to the droplet pinch-off only solutions with concentrations above the cmc display a different behaviour from a surfactant free system. Using the 19 mPa s continuous phase the process becomes slower. This suggests that the rearrangement of surfactant on the interface has more time available to compete with the deformation of the interface.

Finally, the case of the 96 mPa s continuous phase is examined. In this case for instances away from the pinch-off the solutions display a behaviour different from a surfactant free system. When the process approaches pinch-off the behaviour resembles a surfactant free system. In the case of the 96 mPa s continuous phase the increase in viscosity means an inhibition of surface flows rearranging the surfactant on the interface. Since even for highly concentrated solutions the behaviour is similar to a solution without surfactant, it can be assumed that

Marangoni phenomena on the interface are responsible for the replenishment of surfactant in the final instances of the process.

In all three continuous phases an increase in interfacial tension was observed in the final stages of the break-up for solution below the cmc. The neck kinetics in the final stages are described by the two-fluid Stokes model and that allows for a calculation of the acting interfacial tension as the process approaches pinch-off. For the solutions above the cmc the increase is smaller and the interfacial tension only increases in the very last moments of the break-up. This increase in interfacial tension is in line with the change in the thinning rate as the process approaches pinch-off.

Increasing the viscosity of the dispersed phase leads to a decrease in the diffusion coefficient of the surfactant species present. Increasing viscosity by one order of magnitude leads to a decrease of the diffusion coefficient by the same magnitude. The break-up process is affected since the thinning rates of the neck closer to the pinch-off display a thinning rate smaller than a surfactant free system, while for instances away from the pinch-off the process is not affected. In summary, all solutions display a different behaviour from a surfactant free system in instances away from the pinch-off regardless of the continuous phase viscosity. In contrast, during the final moments of the pinch-off the behaviour resembles the behaviour of a surfactant free system for surfactant solutions below the cmc in the case of the 4.6 mPa s and 96 mPa s continuous phase. In the case of the 4.6 mPa s the process develops faster than the time the surfactant has to repopulate the available interface. While in the case of the 96 mPa s continuous phase the increase in viscosity inhibits surface flows that rearrange the surfactant on the interface.

7.1.3 Conclusions regarding the velocity fields

7.1.3.1 Velocity fields during necking

During necking the velocity in the thinning neck changes drastically. Initially fluid moves from the bulk of the dispersed phase to the expanding droplet due to the action of the syringe pump. As the neck diameter becomes thinner due to the action of the continuous phase a stagnation zone is formed at the base of the neck closer to the dispersed phase inlet. Fluid initially bypasses this stagnation zone and moves into the neck and into the expanding droplet. As the neck diameter keeps decreasing fluid stops passing through the neck and is expelled from both sides leading to the rupture of the liquid filament. This is observed for all surfactant free and surfactant solutions.

The velocities along the interface for a surfactant free system keep increasing as the neck diameter decreases. Increasing the continuous phase viscosity leads to a reduction in the fluid velocities close to the interface, the largest velocities are observed for the lowest viscosity silicone oil. When surfactant is present the velocities along the interface follow a similar behaviour, they increase due to the reduction of the neck diameter and decrease when the break-up happens in a higher viscosity continuous phase.

Examining the maximum fluid velocities exiting the neck it is revealed that, the maximum fluid velocity increases as the break-up process approaches pinch-off which is in line with the reduction in the neck diameter. Increasing the surfactant concentration leads to a reduction in maximum fluid velocities which is caused by a reduction of the capillary pressure forcing the fluid to move out of the thinning neck. Solutions of surfactant below the cmc display maximum fluid velocities similar to a surfactant free system. This behaviour is observed for the 4.6 mPa s and 19 mPa s continuous phase silicone oils. In the case of the 96 mPa s silicone oil the maximum fluid velocities are close to a surfactant free system in all cases.

Comparing the velocities along the interface reveals that for surfactant solutions below the cmc the velocities along the interface are smaller when compared to the velocities of a surfactant free system for the same neck diameter. When the break up happens in a 4.6 mPa s and 19 mPa s continuous phase, the fluid velocities close to the interface for the solutions below the cmc are very similar to a surfactant free system. Considering this, the smaller velocities along the interface can be explained by acting Marangoni phenomena reducing fluid velocities. In the case of 96 mPa s continuous phase the differences are smaller but in this case the process is highly dominated by viscosity which suppresses surface flows.

In summary, it was demonstrated that fluid velocities increase as the neck diameter decreases for all continuous phases and all surfactant solutions. When comparing the velocities close to the interface a reduction is observed in the cases where surfactant is present in small concentrations, suggesting the presence of interfacial stresses acting against the break-up.

7.1.3.2. Velocity fields during expansion

Examining the velocity profiles during the expansion stage reveals that when a surfactant free system is considered the velocity magnitudes appear to be larger as the viscosity of the continuous phase is increased. Increasing the continuous phase viscosity leads to an increase in the drag force exerted by the continuous phase. This means that the interfacial tension force resisting the drag force has a larger competition allowing for larger fluid velocities in the dispersed phase.

In the case of the 4.6 mPa s continuous phase, no recirculation is observed during the expansion stage and the maximum fluid velocities are recorded on the interface. Increasing the viscosity of the continuous phase to 19 mPa s and 96 mPa s two recirculation patters are formed which in later stages merge into a stagnation zone at the centre of the expanding droplet. Fluid moves around that zone towards the tip of the droplet in accordance to the mechanism described in literature.

When surfactant is present higher fluid velocities are observed when the break-up happens in a 4.6 mPa s continuous phase. Furthermore, the formation of two recirculation zones is observed. These recirculation zones are not present when the break-up happens in absence of surfactant. When surfactant is present interfacial tensions are lower suggesting that the drag force from the continuous phase encounters a smaller resistance in moving the fluid along the interface. This allows for higher fluid velocities. Increasing the surfactant concentration above the cmc leads to the same recirculation zones being formed and higher fluid velocities. Increasing the continuous phase viscosity leads to the formation of two recirculation zones and the velocity magnitudes are similar to the surfactant free system.

In summary, the presence of surfactant allows for the formation of two recirculation zones in each case which become more pronounced by the increase in the continuous phase viscosity. This means that when surfactant is present there is an increase in the convective mixing happening during the expansion stage.

7.1.4. Conclusion regarding the self-similarity of the neck

Rescaling the interface profile reveals that the shape of the interface of a surfactant free solution undergoing break-up is the same in the final stage of the process regardless of the viscosity of the continuous phase. In contrast, the shape of the interface for instances away from the break-up is different when the break-up happens in a low viscosity continuous phase.

When surfactant is present and the break-up happens in a 4.6 mPa s continuous phase the interface profile of the interface of the solution with the surfactant with the smallest cmc is different. The interface of the neck when C10TAB is present is very similar to the surfactant free system suggesting that the presence of surfactant does not alter the shape of the interface. In the case of C12TAB the interface profile is different for larger and smaller neck diameters. When the surfactant concentration is increased the behaviour is similar. In the case of droplet formation in a 19 mPa s continuous phase the rescaled interface profiles display a similar

behaviour. For small surfactant concentration only in the case of C12TAB being present in the system the interface profiles are different. Increasing the surfactant concentration leads to differences being observed for both surfactants even in the last moments of the process.

For surfactant solutions above the cmc in the case of a 4.6 mPa s continuous phase the rescaled interface profiles are similar to a surfactant free system. If the viscosity of the continuous phase is increased then the rescaled interface profiles show differences at instances away and close to the break-up.

The profile of the interface is affected by the presence of surfactant. For low surfactant concentrations, solutions with small quantities of surfactant display the largest differences. When the surfactant quantity is increased above the cmc then the increase in continuous phase viscosity leads to differences in the rescaled interface profiles. This suggests that, for small surfactant concentration the surfactant quantity is affecting the surfactant mass transport but as the surfactant quantity is increased, the surfactant transport along the interface is what dominates the surfactant mass transport.

7.2. Future work

In terms of future work, a complete resolution of the velocity field in the continuous oil phase will be most useful. Similar work has been carried out by Roumpea and their colleagues employing micro-PIV to resolve the 2-D velocity field in the oil phase. During this project there have been made attempts to create oil dispersible nanoparticles or nanobubbles but without success. The resolution of the velocity field in the continuous phase can be used to estimate the surface tension force during the break-up (Roumpea et al., 2019). More specifically, since GPV can produce a 2-D velocity field, a 2-D interfacial tension force field can be reconstructed, since the interfacial tension force is unlikely to be uniform during the process. Additionally, 2-D velocity fields captured at different planes can allow researchers to

reconstruct a 3-D velocity of the droplet formation process. This can pave the way for interfacial tension measurements in the timescales of microfluidic droplet formation.

Furthermore, the analysis can be expanded to other droplet formation regimes like jetting or other microfluidic channel geometries in order to validate previous experimental observations carried out in T-Junctions e.g. This study was also limited by the presence of glycerol which needs to be added in order to match the refractive index of the silicone oil. This decreases the diffusion coefficient of the surfactants limiting their mass transport. It might be worth trying some different continuous phases in order to reduce the quantity of glycerol needed.

Droplets in microfluidics can be created under various conditions with shorter or longer time scales. Further probing these timescales will provide valuable information in the whole range of droplet sizes, timescales and applications. Droplet break-up becomes quite rapid, especially in the last instances before pinch-off. Improved camera technologies can give the opportunity to better investigate these short time scales. Furthermore, the nature of GPV, requiring to reduce the numerical aperture of the condenser lens, increasing the depth of the observation field, makes it impossible to get accurate velocity fields in the final short length scales of the process, when the depth of the field of view becomes larger than the diameter of the thinning neck. Even micro-PIV, that extract information from a 2-D region cannot give accurate information during those time scales due to length scales of the tracer particles being very close to the observation length scales. The work carried out by Eggers showed that in those very short time scales the fluid properties are the only determinants of its behaviour, it would thus be interesting to have an experimental observation of that.

Lastly, the employment of Machine Learning (ML) can be useful. ML can be used to create a comprehensive model of droplet formation encompassing all the underlying phenomena and can serve as a fast and reliable tool to predict droplet sizes under many conditions. This can be valuable as it will reduce experimental are research time. The limitations of ML are that in

order for it to be properly applied it requires large amounts of data and the physics of the process are ignored and replaced by statistical observations and correlations. An attempt has been carried out during this project but the ML algorithm produced lacked the data to produce accurate results.

In summary, microfluidic droplet formation, and multiphase flows in general are phenomena that fascinate scientist through the years. Future prospects are only limited by our imagination and the technological capabilities of our time.

Appendix: Encapsulation of hydroxyapatite microparticles in a solid and impermeable shell using microfluidics

A.1. Introduction

In the appendix the work carried out in a short project regarding the encapsulation of microparticles in a solid and rigid shell using microfluidics for the use in Positron Emission Particle Tracking (PEPT) is presented. This part begins by reviewing the literature regarding PEPT in order to underline the limitations of the technique and showcase the motivations of this project. This is followed by the materials and methods used which in part have been described in §3.1 and §3.2. Lastly the formation of solid capsules using microfluidics is described and they are characterised in regards to their ability to encapsulate tracer microparticles and their impermeability.

A.2. Aims and objectives

The aims of this project are to create solid and impermeable capsules using microfluidics. The capsules will be used to encapsulate tracer microparticles used in PEPT. The capsules need to be impermeable for an adequate amount of time in order to allow for a PEPT experiment to take place and be durable enough to resist any mechanical stresses present during experimentation.

A.3. Literature review

PEPT is a velocimetry technique that allows for the reconstruction of the velocity field in opaque systems (Parker et al., 1993). The technique relies on the detection of two γ-photons emitted by the annihilation of a positron and an electron in the close vicinity of a single radioactive tracer particle. The photons are detected and the position of the particle can be

found. One of the limitations of the technique lies in the fact that the radioactivity of the tracer particle is sensitive to the presence of water making the technique impossible in aqueous systems without coating the particle which increases its size (Jacobson et al., 2015).

Positron Emission Particle Tracking (PEPT) is a variant of the medical imaging technique Positron Emission Tomography (PET) and it was developed at the University of Birmingham. The technique utilises a single labelled tracer particle and the aim is to determine the location of the particle as it moves within a piece of opaque equipment as long as it can be fitted between the detectors (University of Birmingham, 2020a). A radioisotope, fluorine-18 in most cases (University of Birmingham, 2020b), is incorporated onto the tracer particle. The isotope undergoes beta decay that results in the emission of a positron. The emitted positron then annihilates with an electron producing a set of back-to-back gamma photons (University of Birmingham, 2020a) which are detected in order to determine the position of the particle. Due to conservation of momentum, the pair of γ-photons follow collinear antiparallel trajectories which allows us for the location of the particle based on the intersection of the photons with the detectors.

Fluorine-18 is produced in the MC40 Cyclotron present in the facility using a helium-3 ion beam. Tracer particles used for PEPT are between 100 μm – 10 mm. Particles that are below 1 mm are activated using an indirect activation approach. In this case the cyclotron beam irradiates deionised water, converting some of the oxygen present in fluorine-18. The tracer particles are then immersed in the water and the water is evaporated. In this way a proportion of fluorine-18 ions attach on the particles. These ions are very reactive and if the particle is exposed to an aqueous solution the fluorine ions contaminate the water (University of Birmingham, 2020b). This is the main drive behind this project. The inability of the small particles to be placed in an aqueous environment limits the applicability of PEPT.

The origins of PEPT got back to PET which was first established in 1970's for medical purposes in order to extract images of organs using positron-emitting pharmaceuticals (Ter-Pogossian et al., 1975). The first use of PET for not medical purposes was carried out at the University of Birmingham in the United Kingdom for the investigation of flow inside engineering equipment (Hawkesworth et al., 1991). The main constrain at the time was the increased cost of the detection equipment but advancements in that field allowed for the consideration of PET as a viable technique for investigations in the physical sciences. The first attempt was carried out in order to investigate the distribution of lubricant in engine systems by labelling either the whole lubricant load or parts of it (Hawkesworth et al., 1991). Other applications involved the study of the displacement of the liquid in geological strata, the fluid transport in fractured rocks and the extrusion process in small moulds. This study showed the capabilities of PEPT in investigating processes that manifest in timescales from milliseconds to days.

In the next years the use of PEPT took off and different groups established their own centres studying the flow fields in fluidised beds, hydro-cyclones and piping systems, involving one or more tracer particles (Stellema et al., 1998, Hoffmann et al., 2005, Chang and Hoffmann, 2015, Langford et al., 2016). PEPT has also been employed for the analysis of suspensions in stirred vessels (Fangary et al., 2002). Furthermore, advancements in PEPT helped validate CFD simulations of agitated suspensions with high volumes of solids (Liu and Barigou, 2015). The uses of PEPT are quite numerous, practically it can be employed to visualise flows in any type of opaque equipment like static mixers or granular screws (Mihailova et al., 2015, Lee et al., 2012). Similarly to PIV and other velocimetry techniques the accuracy of PEPT decreases as the velocities of the fluid increases (Bakalis et al., 2003). One of the final advancements in the field of PEPT comes with the aid of machine learning where researches were able to use machine learning algorithms in order to improve particle location and separation in the case of

multiple traces. The researchers were able to demonstrate that the number of tracers is irrelevant and the algorithms can distinguish between tracers that are up to 2 mm close to each other (Nicuşan and Windows-Yule, 2020). Other fields that deploy the use of PEPT and where the presence of water is constant is the studies on sand. These studies focus on the movement of sand particles after natural disasters or under the wheels of exploratory vehicles. The limitations in observation can be overcome by the use of PEPT (Kinugasa et al., 2015).

The limitations of PEPT described previously is what sparked the start of this project. Microfluidics can be used as a fast and reliable way for the creation of solid particles for the encapsulation and slow release of active species. A recent example is the formation of hydrogel microparticles that are turned solid with the use of UV. These microparticles are able to hold active species in their crosslinked network. The release of the active species can be triggered by outside stimuli (Duncanson et al., 2012, Kong et al., 2012). In the case of protecting the PEPT microparticle from water the goal is not the slow release of active species, but the protection of the particle from coming into contact with water. Therefore, there is need of a rigid shell that acts as a barrier to the outside environment. Such rigid polymer shells can be formed using UV activated adhesives. A common example is NOA 89, which has been used for the formation of microfibers and other structures (Duboin et al., 2013). The researchers were able to create crosslinked polymer structures using a hand held non-focusing UV lamp proving the portability of the technique. NOA 89 has been used to create spherical droplets that can be polymerised under UV inside a microfluidic device (Pluchon et al., 2012). The above studies prove the versatility of commercially available UV curable polymers and the capabilities of microfluidics. In order for this project to be successful a method that creates solid microparticles containing the PEPT tracer particles without the need of observation using handheld UV light source inside a microfluidic device needs to be engineered. The last hurdle to overcome is the trapping of the PEPT tracer particle inside a still liquid polymer droplet.

Droplet microfluidics haven been proven capable for the trapping of bacteria and cells for their study (Eun et al., 2011). Furthermore, microfluidics have been proven able for the formation of double emulsion with a solid shell, acting as carrier capsules for the controlled release of chemicals (Kim et al., 2011). The above studies demonstrate the capabilities of microfluidic encapsulation and the possibility of encapsulating solid microparticles in UV curable polymer droplets.

A.4. Materials and methods

In this section the materials and methods used in this study are described. Some of them have been covered in the previous section so they will not be mentioned again. The materials and methods described are, the UV-lamp setup, the 3D printing of the devices and the fluorescent microscopy.

A.4.1. Microfluidic devices

The microfluidic devices used in this project are presented in the figure below.

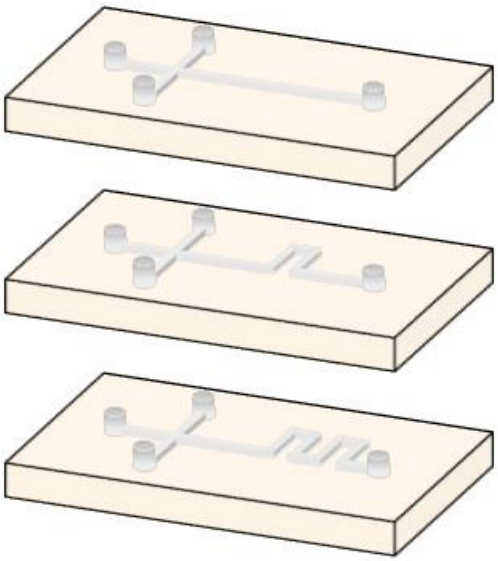


Figure A.1 microfluidic devices used is this project. From top to bottom: straight, serpentine and double serpentine channels

The design of these channels was carried out in a computer aided design software (AutoCAD) (AUTODESK, 2020). The cross section of this device is square measuring 500 μm in width and height. The devices were designed in order to accommodate the microparticles and minimise the risk of microparticle trapping. Another design aspect that had to be considered is the fact that the device needs to fit on a standard glass slide to allow optical observation under a microscope. The devices were 3-D printed due to their larger dimensions that exceed the dimensions applicable for photolithography (MicroChem, 2019). The device rested on 1 mm flat base that was glued to a petri dish. The design process began by design the base and extruding it to 1 mm in height. On the top plane of the base the microfluidic channel was designed and extruded to the desired height.

The design was then exported and 3-D printed. The print was carried out using a Form 2 desktop stereolithography 3-D printer using the clear resin (formlabs, 2018). After the completion of the print, the product needs to be washed in isopropanol and then dried under UV to complete the curing (Formlabs, 2020). It is recommended to print the device with supports, which are later removed after the print is complete.

After the supports are removed the underside of the based is polished using sandpaper to allows for a smoother surface for better adhesion in a petri dish. The microfluidic device was then glued to the petri dish using an epoxy adhesive (Araldite professional adhesives, 2020). After the application of the adhesive the device was left in the petri dish for 24 hours with some weight on top to improve the adhesion. Subsequently the PDMS microfluidic chip was fabricated then in the same way described previously.

A.4.2. Hydroxyapatite micro particles

The microparticles provided were hydroxyapatite microparticles with a nominal diameter of 180-210 μm. They are not radioactively labelled and no preparation is needed.

A.4.3. Droplet formation and encapsulation

The continuous phase used for this study is 4.6 mPa s silicone oil as provided my Merck (Sigma-Aldrich, 2020). The dispersed phase was NOA89 (Norland Products, 2019). The microparticles are dispersed in the NOA and the two fluids moved into 5 mL syringes (Merck, 2020a). For the fluid delivery in the microfluidic device two syringe pumps from WPI were employed (WORLD PRECISION INSTRUMENTS, 2020). A schematic of the experimental set up is presented in Figure A.2.

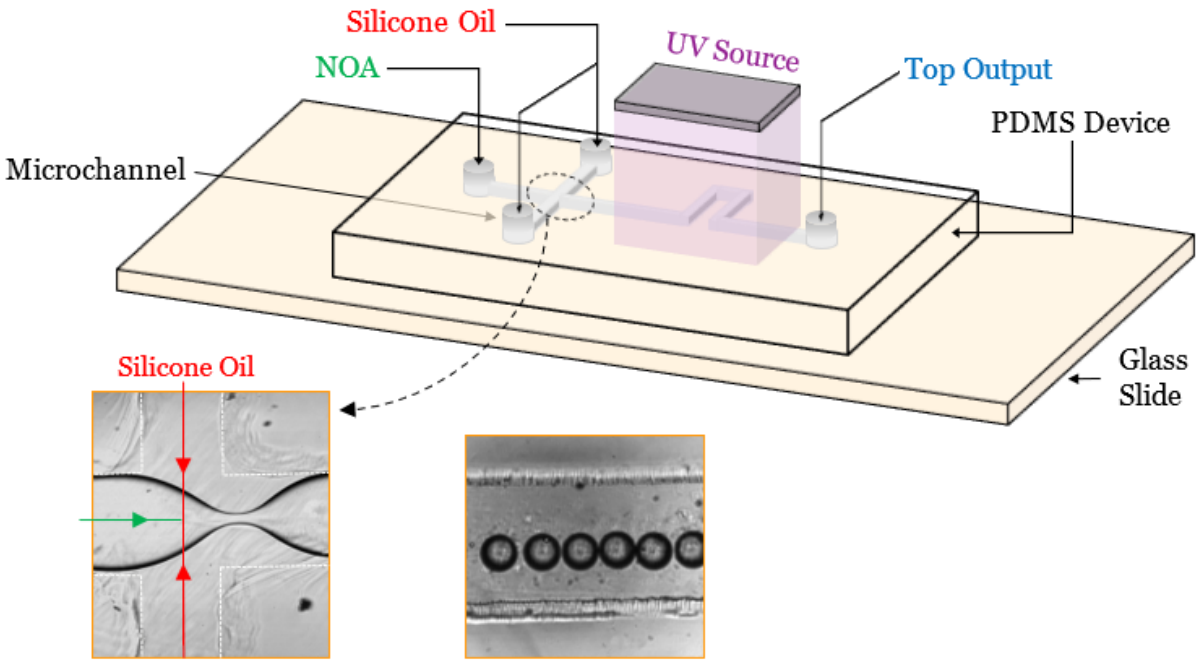


Figure A.2 Schematic of experimental set-up

The characterisation experiments where performed under the same microscope used in the previous study. The polymerisation experiments did not require optical observation and were conducted on a bench top. The whole set up was placed inside a cardboard box with a cut-out on the top where the UV lamp was placed. This was done in order to minimise UV leakage and reduce to a minimum our exposure to UV. The UV source has an 8W lamp and can emit at 350 and 254 nm and no filter is used. The tubing and syringe tips used are the same that were used in the previous study. The conditions are set and left for about 15 mins in order to allow for the

materials to properly flow through the device, after that the UV lamp is turned on and the produced capsules are collected in glass beaker. The device needs to be placed upside down with the glass side face up in order to minimise the adsorption of UV from the PDMS chip.

A.4.5. UV fluorescence

In order to control for the impermeability of the capsules, rhodamine-B (Merck, 2020h) was dissolved into the NOA89 prior to experimentation. Rhodamine-B dissolves well into NOA89 and is incorporated in the solid structured of the polymerised adhesive. By mixing rhodamine with NOA89 and observing its leaking from the polymerised NOA89 droplet will give us a solid indication of the impermeability of the capsules. The adsorption and emission wavelengths of rhodamine-B are 510 and 560 nm respectively (Sakai et al., 2007). The sample was illuminated with a LED UV source (lumencor, 2020). The filter used allowed for a wavelength of 545±25 nm to pass. The light was shinned on to the sample and a snapshot taken. This was carried out immediately after polymerisation, 8, 16 and 32 hours after.

A.5. Results

Initially, the droplet sizes of pure water in three different continuous phases are examined. Figure A.3 shows the results.

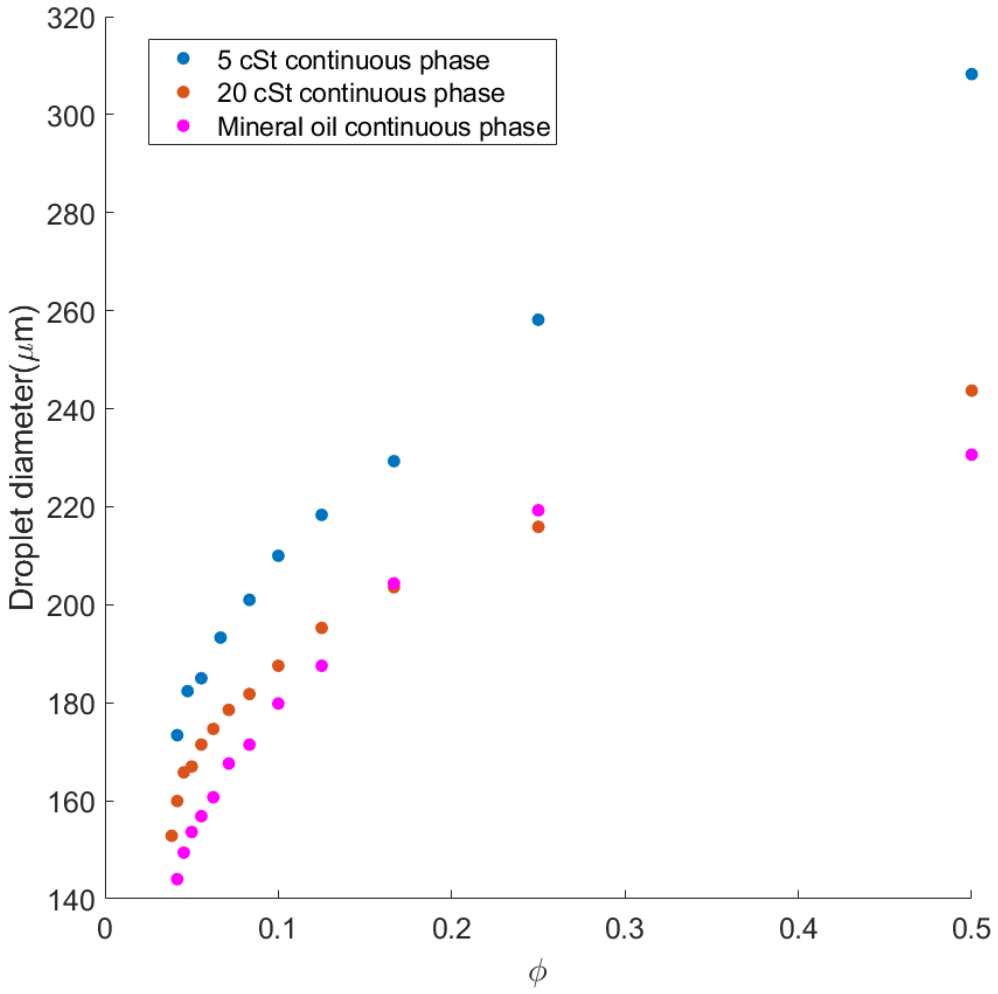


Figure A.3 Water droplet diameters using three different continuous phases

As seen previously, droplet sizes decrease with an increase of continuous phase flow rate (reduction in φ). Furthermore, increasing the continuous phase viscosity for fixed flow rate conditions leads to a reduction in droplet sizes. These experiments were carried out in order to validate the functionality of the microfluidic device without any surfactant present. Similarly, the droplet sizes of NOA89 as the dispersed phase are examined. Figure A.4 displays the results.

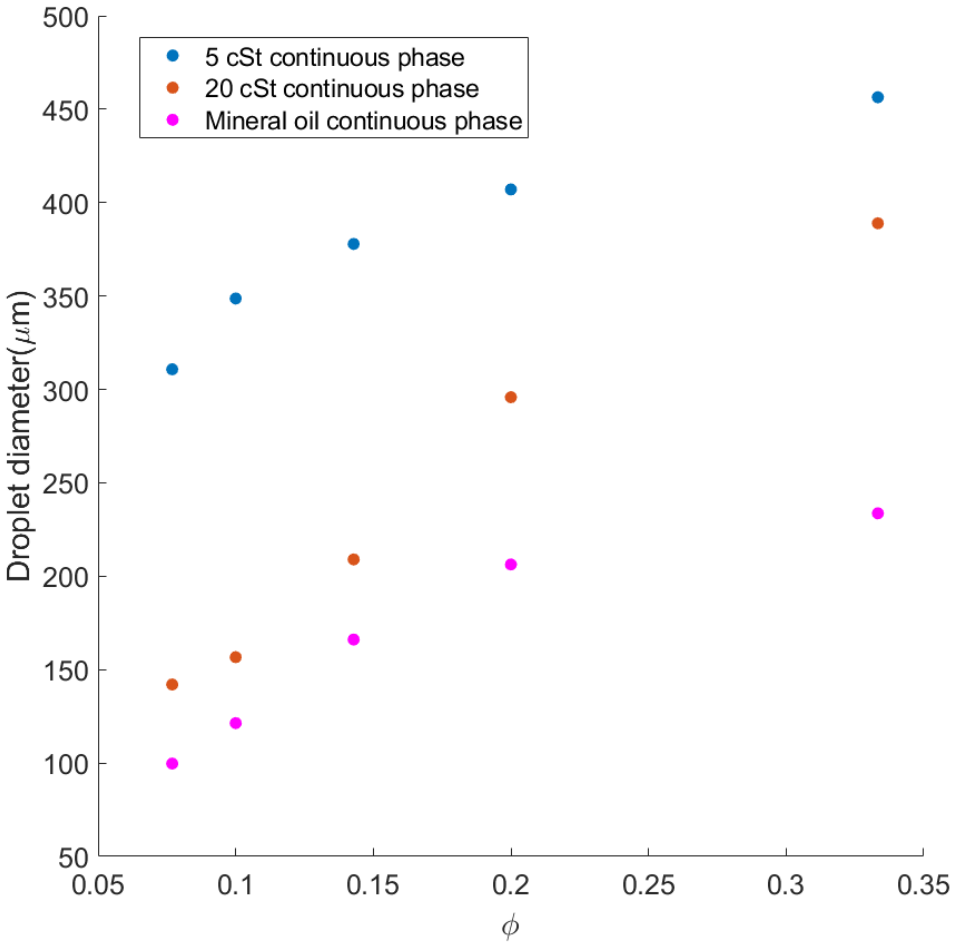


Figure A.4 NOA89 droplet sizes in three different continuous phases

Similarly, to the case of water, a reduction in droplet sizes as the flow rate and the viscosity of the continuous phase are increased is observed. These experiments were carried out in order to determine the conditions that will allow us to encapsulate the microparticles. The droplet size needs to be larger than the microparticle and also smaller than the channel depth. Large enough droplets are needed that will be able to fit the particles and at the same will not interact with the channel walls so they can be easily extractable. Therefore, from the above experiments is observed that for the 19 mPa s silicone oil and the mineral oil, NOA89 droplet sizes are going to be very close to the particle sizes making the encapsulation harder. Following the above the 4.6 mPa s silicone oil was chosen as the continuous phase which produces NOA89 droplet with large enough diameters to encapsulate the particles.

The next step was to try and polymerise the droplets containing particles before they exit the microfluidic device. In this case, the residence time under a UV source is a critical factor. For the first straight microfluidic channel designed the residence time was not enough to polymerise the produced droplets. For this purpose, two more microfluidic devices were designed. One with a single and one with a double serpentine channel. The residence times of the droplets under the UV significantly increased. The results are presented in Figure A.5.

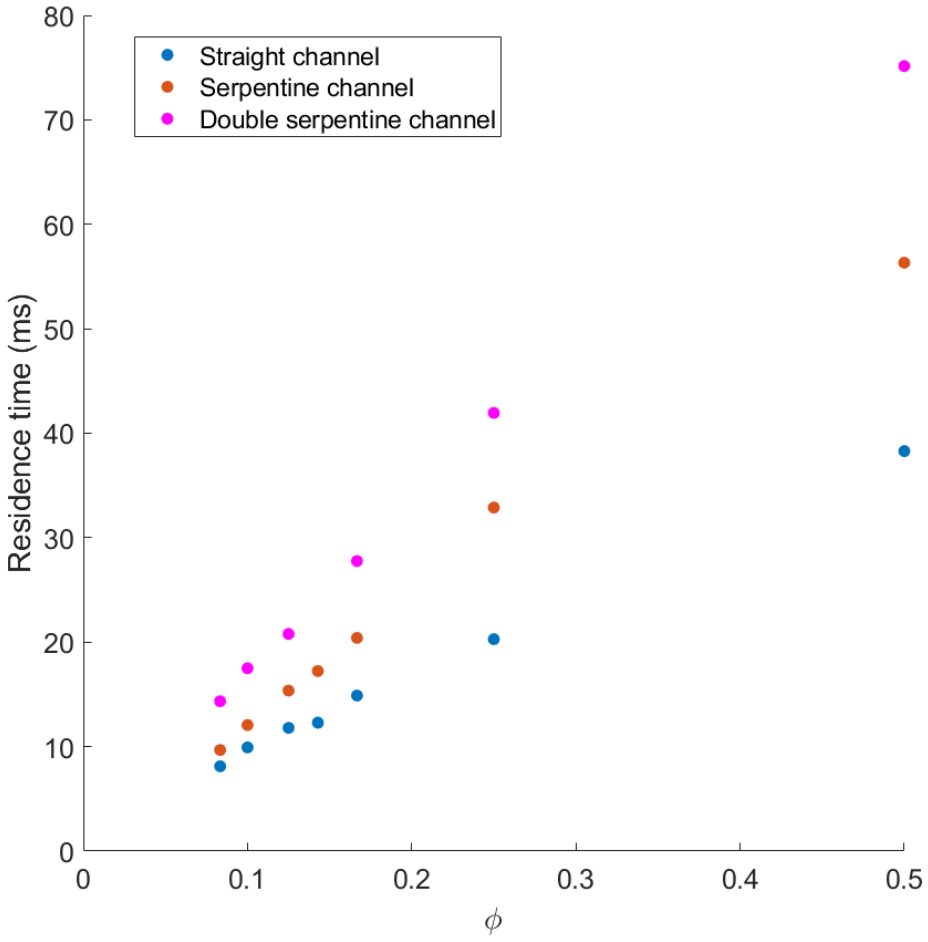


Figure A.5 Residence times of NOA89 Droplets for various flow rate conditions

It is observed that the straight channel allows for the smallest residence times while the longer, serpentine channels, allow for higher residence times. The criterion for residence time that is accommodated is that the NOA89 droplets need to spend a minimum amount of time under the UV, enough in order to allow for the polymerisation to occur. Since there is no need to control

for the maximum residence time, the decision was made to move forward with the double serpentine microfluidic device.

After having validated the functionality of the microfluidic device and having chosen the operating conditions the encapsulation the microparticles without the presence of UV is attempted. The aim is just to further validate the process in terms of functionality once the microparticles are suspended in the dispersed phase. An example of a liquid NOA89 droplet containing a microparticle is shown in Figure A.6.

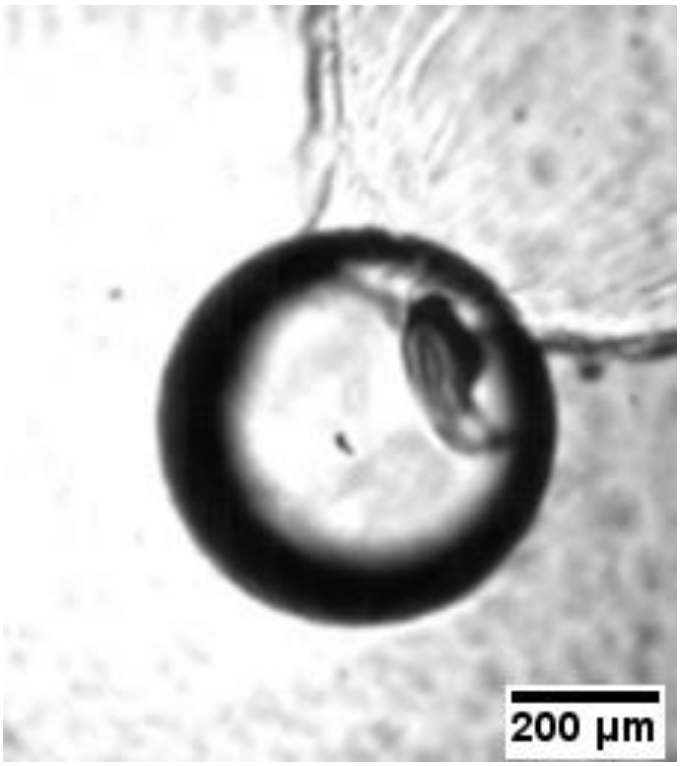


Figure A.6 Microparticle inside a liquid NOA89 droplet

The microparticle are carried with the flow of the dispersed phase. Once the dispersed phase reached the junction of the microfluidic the microparticles end up inside the produced droplets. The next step is to polymerise the droplets containing the microparticle during their time inside the microfluidic channel. The first attempts showed that the UV source was able to only partially polymerise the liquid NOA89 droplets. In order to overcome this obstacle, the UV source was placed closer to the microfluid device at a distance of 50 mm away from it. This resulted in a more complete polymerisation. A final series of experiments was carried out in

order to determine the impermeably of the produced capsules. In these experiments Rhodamine-B was added to the NOA89 prior to polymerisation. Then droplets were produced as previously and the collected solid NOA89 droplets were monitored using fluorescence. The produced capsules appeared to be stable for up to 16 hours, while leaking was detected after that time. Figure A.7 displays these results.

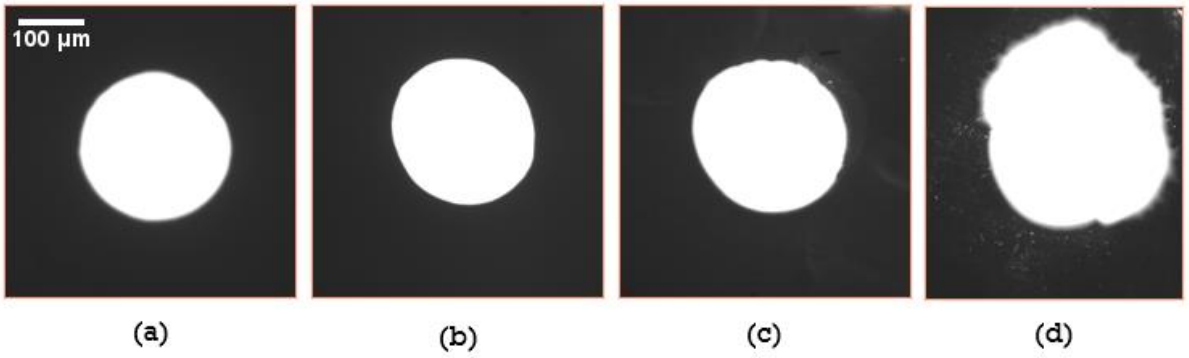


Figure A.7 Fluorescent images of rhodamine-NOA89 solid capsules in various times after formation. a: 0 hours. b: 8 hours. c: 16 hours. d: 32 hours.

It is observed that the particles start breaking-leaking after 8 hours therefore their stability and use should be restricted in time smaller than that. In a typical PEPT experiment, the microparticles would be made radioactive and that activity would last up to two hours. Therefore, the produced capsules can be utilised for PEPT applications in that time window.

A.6. Conclusions and future work

During this short project it was demonstrated that solid NOA89 capsules can be formed using microfluidics in order encapsulate hydroxyapatite microparticles for PEPT applications. NOA89 droplets can be made using a rectangular microfluidic device under various flow rate conditions and with the use of various continuous phases. The microparticles can be dispersed in the liquid NOA89 and then made to flow through the microfluidic device in order for them to get trapped inside a liquid NOA89 droplet. Further down the channel the NOA89 droplet can be polymerised using UV, trapping the microparticle inside a rigid impermeable shell. This

shell is able to maintain its impermeability and not leak for at least 8 hours, which is far more than the duration of typical PEPT experiment.

Future work can involve the investigation of mixtures of NOA89 and photo-initiator substances in order to allow for smaller residence times and simpler microfluidic devices. Furthermore, mechanical testing of the solid particles will be useful in order to determine their ability to withstand extreme forces and determine the limits of their operation.

8. References

ABATE, A. R., LEE, D., DO, T., HOLTZE, C. & WEITZ, D. A. 2008. Glass coating for PDMS microfluidic channels by sol–gel methods. *Lab on a Chip,* 8**,** 516-518.

ADRIAN, R. 1986. Multi-point optical measurements of simultaneous vectors in unsteady flow—a review. *International journal of heat and fluid flow,* 7**,** 127-145.

ADRIAN, R. J. 1984. Scattering particle characteristics and their effect on pulsed laser measurements of fluid flow: speckle velocimetry vs particle image velocimetry. *Applied optics,* 23**,** 1690-1691.

ADRIAN, R. J. 2005. Twenty years of particle image velocimetry. *Experiments in fluids,* 39**,** 159-169.

AGRESTI, J. J., ANTIPOV, E., ABATE, A. R., AHN, K., ROWAT, A. C., BARET, J.-C., MARQUEZ, M., KLIBANOV, A. M., GRIFFITHS, A. D. & WEITZ, D. A. 2010. Ultrahigh-throughput screening in drop-based microfluidics for directed evolution. *Proceedings of the National Academy of Sciences,* 107**,** 4004-4009.

ALAIMO, M., MAGATTI, D., FERRI, F. & POTENZA, M. 2006. Heterodyne speckle velocimetry. *Applied physics letters,* 88**,** 191101.

ALVAREZ, N. J., WALKER, L. M. & ANNA, S. L. 2010. Diffusion-limited adsorption to a spherical geometry: The impact of curvature and competitive time scales. *Physical Review E,* 82**,** 011604.

ANNA, S. L. 2016. Droplets and Bubbles in Microfluidic Devices. *Annual Review of Fluid Mechanics,* 48**,** 285-309.

ANNA, S. L. & MAYER, H. C. 2006. Microscale tipstreaming in a microfluidic flow focusing device. *Physics of Fluids,* 18**,** 121512.

AQUAPEL GLASS TREATMENT. 2020. *{Aquapel Glass Treatment}* [Online]. Available: http://www.aquapel.com/ [Accessed].

ARALDITE PROFESSIONAL ADHESIVES. 2020. *{ARALDITE RAPID 2 X 15ML}* [Online]. Available: https://www.go-araldite.com/products/epoxy-adhesives/araldite-rapid-2-x-15ml-tube [Accessed].

AUTODESK 2020. {versin Q.47.0.0 AutoCAD 2020}.

BAKALIS, S., COX, P., WANG-NOLAN, W., PARKER, D. & RYER, P. F. 2003. Use of Positron-Emission Particle Tracking (PEPT) Technique for Velocity Measurements in Model Food Fluids. *Journal of food science,* 68**,** 2684-2692.

BARBIER, V., TATOULIAN, M., LI, H., AREFI-KHONSARI, F., AJDARI, A. & TABELING, P. 2006. Stable modification of PDMS surface properties by plasma polymerization: application to the formation of double emulsions in microfluidic systems. *Langmuir,* 22**,** 5230-5232.

BARKER, D. & FOURNEY, M. 1977. Measuring fluid velocities with speckle patterns. *Optics letters,* 1**,** 135-137.

BEN-YAKAR, A., CHRONIS, N. & LU, H. 2009. Microfluidics for the analysis of behavior, nerve regeneration, and neural cell biology in C. elegans. *Current opinion in neurobiology,* 19**,** 561-567.

BÉNARD, H. 1900. Les tourbillons cellulaires dans une nappe liquide. *Rev. Gen. Sci. Pures Appl.,* 11**,** 1261-1271.

BHATTACHARYA, S., DATTA, A., BERG, J. M. & GANGOPADHYAY, S. 2005. Studies on surface wettability of poly (dimethyl) siloxane (PDMS) and glass under oxygen-plasma treatment and correlation with bond strength. *Journal of microelectromechanical systems,* 14**,** 590-597.

BREUER, K. S. 2005. *Microscale diagnostic techniques*, Springer.

BROCHARD-WYART, F. & QUÉRÉ, D. 2004. *Capillarity and wetting phenomena: drops, bubbles, pearls, waves*, Springer.

BROGIOLI, D., VAILATI, A. & GIGLIO, M. 2002. Heterodyne near-field scattering. *Applied physics letters,* 81**,** 4109-4111.

BROSSARD, C., MONNIER, J., BARRICAU, P., VANDERNOOT, F.-X., LE SANT, Y., CHAMPAGNAT, F. & LE BESNERAIS, G. 2009. Principles and applications of particle image velocimetry.
BRUUS, H. 2007. *Theoretical Microfluidics*, OUP Oxford.
BUZZACCARO, S., SECCHI, E. & PIAZZA, R. 2013. Ghost Particle Velocimetry: Accurate 3D Flow Visualization Using Standard Lab Equipment. *Physical Review Letters,* 111**,** 048101.
CARRIER, O., DERVIN, E., FUNFSCHILLING, D. & LI, H. 2013. Formation of satellite droplets in flow-focusing junctions: volume and neck rupture. *Microsystem Technologies,* 21.
CERBINO, R. & CICUTA, P. 2017. Perspective: Differential dynamic microscopy extracts multi-scale activity in complex fluids and biological systems. *The Journal of chemical physics,* 147**,** 110901.
CERBINO, R. & TRAPPE, V. 2008. Differential Dynamic Microscopy: Probing Wave Vector Dependent Dynamics with a Microscope. *Physical Review Letters,* 100**,** 188102.
CHANG, T., WATSON, A. & TATTERSON, G. B. 1985. Image processing of tracer particle motions as applied to mixing and turbulent flow—II. Results and discussion. *Chemical engineering science,* 40**,** 277-285.
CHANG, Y.-F. & HOFFMANN, A. C. 2015. A Lagrangian study of liquid flow in a reverse-flow hydrocyclone using positron emission particle tracking. *Experiments in Fluids,* 56**,** 4.
CHEN, Z., MILNER, T. E., DAVE, D. & NELSON, J. S. 1997. Optical Doppler tomographic imaging of fluid flow velocity in highly scattering media. *Optics letters,* 22**,** 64-66.
CHENG, N.-S. 2008. Formula for the viscosity of a glycerol− water mixture. *Industrial & engineering chemistry research,* 47**,** 3285-3288.
CHINAUD, M., VOULGAROPOULOS, V. & ANGELI, P. 2016. Surfactant effects on the coalescence of a drop in a Hele-Shaw cell. *Physical Review E,* 94**,** 033101.
CHRISTOPHER, G. F. & ANNA, S. L. 2007. Microfluidic methods for generating continuous droplet streams. *Journal of Physics D: Applied Physics,* 40**,** R319.
CHUANG, H.-S. & WERELEY, S. 2009. Design, fabrication and characterization of a conducting PDMS for microheaters and temperature sensors. *Journal of Micromechanics and Microengineering,* 19**,** 045010.
CLAUSELL-TORMOS, J., LIEBER, D., BARET, J.-C., EL-HARRAK, A., MILLER, O. J., FRENZ, L., BLOUWOLFF, J., HUMPHRY, K. J., KÖSTER, S. & DUAN, H. 2008. Droplet-based microfluidic platforms for the encapsulation and screening of mammalian cells and multicellular organisms. *Chemistry & biology,* 15**,** 427-437.
COHEN, I. & NAGEL, S. R. 2001. Testing for scaling behavior dependence on geometrical and fluid parameters in the two fluid drop snap-off problem. *Physics of Fluids,* 13**,** 3533-3541.
COLE-PARMER. 2020. *{Masterflex Transfer Tubing, Tygon® ND-100-80 Microbore, 0.020" ID x 0.060" OD}* [Online]. Available: https://www.coleparmer.co.uk/i/masterflex-transfer-tubing-tygon-nd-100-80-microbore-0-020-id-x-0-060-od-100-ft/0641901 [Accessed].
COX, B. 1964. An experimental investigation of the streamlines in viscous fluid expelled from a tube. *Journal of Fluid Mechanics,* 20**,** 193-200.
CRAMER, C., FISCHER, P. & WINDHAB, E. J. 2004. Drop formation in a co-flowing ambient fluid. *Chemical Engineering Science,* 59**,** 3045-3058.
CRASTER, R., MATAR, O. & PAPAGEORGIOU, D. 2009. Breakup of surfactant-laden jets above the critical micelle concentration. *Journal of Fluid Mechanics,* 629**,** 195-219.
CRIMALDI, J. 2008. Planar laser induced fluorescence in aqueous flows. *Experiments in fluids,* 44**,** 851-863.
CROSS, M. C. & HOHENBERG, P. C. 1993. Pattern formation outside of equilibrium. *Reviews of modern physics,* 65**,** 851.
CUBAUD, T. & MASON, T. G. 2008. Capillary threads and viscous droplets in square microchannels. *Physics of Fluids*.

DARHUBER, A. A., VALENTINO, J. P., TROIAN, S. M. & WAGNER, S. 2003. Thermocapillary actuation of droplets on chemically patterned surfaces by programmable microheater arrays. *Journal of Microelectromechanical Systems,* 12**,** 873-879.
DAS, T. & CHAKRABORTY, S. 2013. Perspective: Flicking with flow: Can microfluidics revolutionize the cancer research? *Biomicrofluidics,* 7**,** 011811.
DE GENNES, P.-G., BROCHARD-WYART, F. & QUÉRÉ, D. 2013. *Capillarity and wetting phenomena: drops, bubbles, pearls, waves*, Springer Science & Business Media.
DE SAINT VINCENT, M. R., PETIT, J., AYTOUNA, M., DELVILLE, J. P., BONN, D. & KELLAY, H. 2012. Dynamic interfacial tension effects in the rupture of liquid necks. *Journal of Fluid Mechanics,* 692**,** 499-510.
DEEGAN, R., BAKAJIN, O., DUPONT, T., HUBER, G., NAGEL, S. & WITTEN, T. 1997. Capillary Flow as the Cause of Ring Stains From Dried Liquid Drops. *Nature,* 389**,** 827-829.
DEGENNES, P., BROCHARD-WYART, M. & QUERE, D. 2002. Perles. *Gouttes, bulles, perles et ondes, Belin*.
DENDUKURI, D., PANDA, P., HAGHGOOIE, R., KIM, J. M., HATTON, T. A. & DOYLE, P. S. 2008. Modeling of oxygen-inhibited free radical photopolymerization in a PDMS microfluidic device. *Macromolecules,* 41**,** 8547-8556.
DENDUKURI, D., PREGIBON, D. C., COLLINS, J., HATTON, T. A. & DOYLE, P. S. 2006. Continuous-flow lithography for high-throughput microparticle synthesis. *Nature materials,* 5**,** 365-369.
DONG, T., WEHELIYE, W. H. & ANGELI, P. 2019. Laser induced fluorescence studies on the distribution of surfactants during drop/interface coalescence. *Physics of Fluids,* 31**,** 012106.
DONG, T., WEHELIYE, W. H., CHAUSSET, P. & ANGELI, P. 2017. An experimental study on the drop/interface partial coalescence with surfactants. *Physics of Fluids,* 29**,** 102101.
DOW. 2020. *{SYLGARD 184 Silicone Elastomer Kit}* [Online]. Available: https://www.dow.com/en-us/pdp.sylgard-184-silicone-elastomer-kit.01064291z.html [Accessed].
DU NOÜY, P. L. 1919. A new apparatus for measuring surface tension. *The Journal of general physiology,* 1**,** 521.
DUBOIN, A., MIDDLETON, R., MALLOGGI, F., MONTI, F. & TABELING, P. 2013. Cusps, spouts and microfiber synthesis with microfluidics. *Soft Matter,* 9**,** 3041-3049.
DUDDERAR, T. & SIMPKINS, P. 1977. Laser speckle photography in a fluid medium. *Nature,* 270**,** 45-47.
DUNCANSON, W. J., LIN, T., ABATE, A. R., SEIFFERT, S., SHAH, R. K. & WEITZ, D. A. 2012. Microfluidic synthesis of advanced microparticles for encapsulation and controlled release. *Lab on a Chip,* 12**,** 2135-2145.
EGGERS, J. 1993. Universal pinching of 3D axisymmetric free-surface flow. *Physical Review Letters,* 71**,** 3458-3460.
EGGERS, J. 1997. Nonlinear dynamics and breakup of free-surface flows. *Reviews of modern physics,* 69**,** 865.
EGGERS, J. & VILLERMAUX, E. 2008. Physics of liquid jets. *Reports on Progress in Physics,* 71**,** 036601.
EINSTEIN, A. 1905. On the motion of small particles suspended in liquids at rest required by the molecular-kinetic theory of heat. *Annalen der physik,* 17**,** 208.
ELVEFLOW. 2017. *PDMS: A review - Elveflow* [Online]. Available: http://www.elveflow.com/microfluidic-tutorials/microfluidic-reviews-and-tutorials/the-poly-di-methyl-siloxane-pdms-and-microfluidics/ [Accessed 21/02/2017].
EUN, Y.-J., UTADA, A. S., COPELAND, M. F., TAKEUCHI, S. & WEIBEL, D. B. 2011. Encapsulating bacteria in agarose microparticles using microfluidics for high-throughput cell analysis and isolation. *ACS chemical biology,* 6**,** 260-266.
EVERITT, B. & SKRONDAL, A. 2002. *The Cambridge dictionary of statistics*, Cambridge University Press Cambridge.

FAINERMAN, V., LYLYK, S., AKSENENKO, E., MAKIEVSKI, A., PETKOV, J., YORKE, J. & MILLER, R. 2009. Adsorption layer characteristics of Triton surfactants: 1. Surface tension and adsorption isotherms. *Colloids and Surfaces A: Physicochemical and Engineering Aspects,* 334**,** 1-7.
FAINERMAN, V. & MILLER, R. 2004. Maximum bubble pressure tensiometry—an analysis of experimental constraints. *Advances in colloid and interface science,* 108**,** 287-301.
FANGARY, Y. S., BARIGOU, M., SEVILLE, J. P. & PARKER, D. J. 2002. A Langrangian study of solids suspension in a stirred vessel by Positron Emission Particle Tracking (PEPT). *Chemical engineering & technology,* 25**,** 521-528.
FINN, R. 1999. Capillary surface interfaces. *Notices of the AMS,* 46**,** 770-781.
FORMLABS 2018. {Form 2 Desktop Stereolithography 3D printer.
FORMLABS. 2020. *{Form Wash and Form Cure}* [Online]. Available: https://support.formlabs.com/s/article/Form-Wash-and-Form-Cure?language=en_US [Accessed].
FRUMKIN, A. & GORODETZKAYA, A. 1928. Electrocapillary Phenomena and Layer Formation on the Surface of Liquid Gallium. *Z. Phys. Chem.(Leipzig),* 136**,** 215.
FUARD, D., TZVETKOVA-CHEVOLLEAU, T., DECOSSAS, S., TRACQUI, P. & SCHIAVONE, P. 2008. Optimization of poly-di-methyl-siloxane (PDMS) substrates for studying cellular adhesion and motility. *Microelectronic Engineering,* 85**,** 1289-1293.
GARSTECKI, P., FUERSTMAN, M. J., STONE, H. A. & WHITESIDES, G. M. 2006. Formation of droplets and bubbles in a microfluidic T-junction—scaling and mechanism of break-up. *Lab on a Chip,* 6**,** 437-446.
GARSTECKI, P., STONE, H. A. & WHITESIDES, G. M. 2005. Mechanism for flow-rate controlled breakup in confined geometries: A route to monodisperse emulsions. *Physical review letters,* 94**,** 164501.
GHARIB, M., KREMERS, D., KOOCHESFAHANI, M. & KEMP, M. 2002. Leonardo's vision of flow visualization. *Experiments in fluids,* 33**,** 219-223.
GLAWDEL, T., ELBUKEN, C. & REN, C. L. 2012a. Droplet formation in microfluidic T-junction generators operating in the transitional regime. I. Experimental observations. *Physical Review E,* 85**,** 016322.
GLAWDEL, T., ELBUKEN, C. & REN, C. L. 2012b. Droplet formation in microfluidic T-junction generators operating in the transitional regime. II. Modeling. *Physical Review E,* 85**,** 016323.
GLAWDEL, T. & REN, C. L. 2012. Droplet formation in microfluidic T-junction generators operating in the transitional regime. III. Dynamic surfactant effects. *Physical Review*.
GOLLUB, J. P. & LANGER, J. S. 1999. Pattern formation in nonequilibrium physics. *Reviews of Modern Physics,* 71**,** S396.
GRAF, K. & KAPPL, M. 2003. Physics and chemistry of interfaces/Hans-Jürgen Butt, Karlheinz Graf, Michael Kappl. Butt, Hans-Jürgen.
GRIFFITHS, A. D. & TAWFIK, D. S. 2006. Miniaturising the laboratory in emulsion droplets. *Trends in biotechnology,* 24**,** 395-402.
GROUSSON, R. & MALLICK, S. 1977. Study of flow pattern in a fluid by scattered laser light. *Applied Optics,* 16**,** 2334-2336.
GÜNTHER, A. & JENSEN, K. F. 2006. Multiphase microfluidics: from flow characteristics to chemical and materials synthesis. *Lab on a Chip,* 6**,** 1487-1503.
HAEBERLE, S. & ZENGERLE, R. 2007. Microfluidic platforms for lab-on-a-chip applications. *Lab on a Chip,* 7**,** 1094-1110.
HALE, G. M. & QUERRY, M. R. 1973. Optical constants of water in the 200-nm to 200-µm wavelength region. *Applied optics,* 12**,** 555-563.
HAMLEY, I. W. 2007. Colloids in Introduction to Soft Matter. John Wiley & Sons, Ltd.
HAWKESWORTH, M., PARKER, D., FOWLES, P., CRILLY, J., JEFFERIES, N. & JONKERS, G. 1991. Nonmedical applications of a positron camera. *Nuclear Instruments and Methods in Physics*

Research Section A: Accelerators, Spectrometers, Detectors and Associated Equipment, 310**,** 423-434.
HECHT, E. 2012. *Optics*, Pearson Education India.
HOFFMANN, A. C., DECHSIRI, C., VAN DE WIEL, F. & DEHLING, H. 2005. PET investigation of a fluidized particle: spatial and temporal resolution and short term motion. *Measurement Science and Technology,* 16**,** 851.
HOLTZE, C., ROWAT, A., AGRESTI, J., HUTCHISON, J., ANGILE, F., SCHMITZ, C., KÖSTER, S., DUAN, H., HUMPHRY, K. & SCANGA, R. 2008. Biocompatible surfactants for water-in-fluorocarbon emulsions. *Lab on a Chip,* 8**,** 1632-1639.
HSU, C.-T., SHAO, M.-J. & LIN, S.-Y. 2000. Adsorption Kinetics of C12E4 at the Air− Water Interface: Adsorption onto a Fresh Interface. *Langmuir,* 16**,** 3187-3194.
HUANG, Y., CHOI, K. & HIDROVO, C. H. 2014. The improved resistance of PDMS to pressure-induced deformation and chemical solvent swelling for microfluidic devices. *Microelectronic engineering,* 124**,** 66-75.
HUMPHRY, K. J., AJDARI, A., FERNÁNDEZ-NIEVES, A., STONE, H. A. & WEITZ, D. A. 2009. Suppression of instabilities in multiphase flow by geometric confinement. *Physical Review E,* 79**,** 056310.
HUSNY, J. & COOPER-WHITE, J. J. 2006. The effect of elasticity on drop creation in T-shaped microchannels. *Journal of non-newtonian fluid mechanics,* 137**,** 121-136.
ISMAGILOV, H. S. J. T. R. 2003. A Microfluidic System for Controlling Reaction Networks in Time Angew. *Chem. Int. Ed. 115 2003 792,* 796.
ISRAELACHVILI, J. N. 2011. *Intermolecular and surface forces*, Academic press.
JACOBSON, O., KIESEWETTER, D. O. & CHEN, X. 2015. Fluorine-18 radiochemistry, labeling strategies and synthetic routes. *Bioconjugate chemistry,* 26**,** 1-18.
JAVADI, A., MUCIC, N., KARBASCHI, M., WON, J., LOTFI, M., DAN, A., ULAGANATHAN, V., GOCHEV, G., MAKIEVSKI, A. & KOVALCHUK, V. 2013. Characterization methods for liquid interfacial layers. *The European Physical Journal Special Topics,* 222**,** 7-29.
JIN, F., BALASUBRAMANIAM, R. & STEBE, K. J. 2004. Surfactant adsorption to spherical particles: The intrinsic length scale governing the shift from diffusion to kinetic-controlled mass transfer. *The journal of adhesion,* 80**,** 773-796.
JIN, F. & STEBE, K. J. 2007. The effects of a diffusion controlled surfactant on a viscous drop injected into a viscous medium. *Physics of Fluids,* 19**,** 112103.
KADRI, H. E. L., GUN, R., OVERTON, T. W., BAKALIS, S. & GKATZIONIS, K. 2016. Modulating the release of Escherichia coli in double W1/O/W2 emulsion globules under hypo-osmotic pressure. *RSC Advances,* 6**,** 93694-93706.
KARBASCHI, M., BASTANI, D., JAVADI, A., KOVALCHUK, V., KOVALCHUK, N., MAKIEVSKI, A., BONACCURSO, E. & MILLER, R. 2012. Drop profile analysis tensiometry under highly dynamic conditions. *Colloids and Surfaces A: Physicochemical and Engineering Aspects,* 413**,** 292-297.
KASAGI, N. & NISHINO, K. 1991. Probing turbulence with three-dimensional particle-tracking velocimetry. *Experimental thermal and fluid science,* 4**,** 601-612.
KELLER, J. B. & MIKSIS, M. J. 1983. Surface tension driven flows. *SIAM Journal on Applied Mathematics,* 43**,** 268-277.
KIM, S.-H., KIM, J. W., CHO, J.-C. & WEITZ, D. A. 2011. Double-emulsion drops with ultra-thin shells for capsule templates. *Lab on a Chip,* 11**,** 3162-3166.
KINUGASA, T., KUWAGI, K., LEADBEATER, T. W., GARGIULI, J., PARKER, D. J., SEVILLE, J. P., YOSHIDA, K. & AMANO, H. 2015. Three-dimensional dynamic imaging of sand particles under wheel via gamma-ray camera system. *Journal of Terramechanics,* 62**,** 5-17.
KONG, T., WU, J., TO, M., WAI KWOK YEUNG, K., CHEUNG SHUM, H. & WANG, L. 2012. Droplet based microfluidic fabrication of designer microparticles for encapsulation applications. *Biomicrofluidics,* 6**,** 034104.

KOVALCHUK, N., CHOWDHURY, J., SCHOFIELD, Z., VIGOLO, D. & SIMMONS, M. 2018a. Study of drop coalescence and mixing in microchannel using Ghost Particle Velocimetry. *Chemical Engineering Research and Design,* 132**,** 881-889.

KOVALCHUK, N. M., DUNN, J., DAVIES, J. & SIMMONS, M. J. H. 2019a. Superspreading on Hydrophobic Substrates: Effect of Glycerol Additive. *Colloids and Interfaces,* 3**,** 51.

KOVALCHUK, N. M., JENKINSON, H., MILLER, R. & SIMMONS, M. J. 2018b. Effect of soluble surfactants on pinch-off of moderately viscous drops and satellite size. *Journal of colloid and interface science,* 516**,** 182-191.

KOVALCHUK, N. M., NOWAK, E. & SIMMONS, M. J. H. 2016. Effect of Soluble Surfactants on the Kinetics of Thinning of Liquid Bridges during Drops Formation and on Size of Satellite Droplets. *Langmuir*.

KOVALCHUK, N. M., REICHOW, M., FROMMWEILER, T., VIGOLO, D. & SIMMONS, M. J. H. 2019b. Mass Transfer Accompanying Coalescence of Surfactant-Laden and Surfactant-Free Drop in a Microfluidic Channel. *Langmuir,* 35**,** 9184-9193.

KOVALCHUK, N. M., ROUMPEA, E., NOWAK, E., CHINAUD, M., ANGELI, P. & SIMMONS, M. J. 2018c. Effect of surfactant on emulsification in microchannels. *Chemical Engineering Science,* 176**,** 139-152.

KOVALCHUK, N. M., ROUMPEA, E., NOWAK, E., CHINAUD, M., ANGELI, P. & SIMMONS, M. J. H. 2018d. Effect of surfactant on emulsification in microchannels. *Chemical Engineering Science,* 176**,** 139-152.

KRSTIĆ, M. 2006. Chapter 9 - MIXING CONTROL FOR JET FLOWS. *In:* ROY, G. D. (ed.) *Combustion Processes in Propulsion.* Burlington: Butterworth-Heinemann.

LANGE, N. A. & FORKER, G. M. 1967. Handbook of Chemistry, revised. McGraw-Hill.

LANGFORD, S., WIGGINS, C., TENPENNY, D. & RUGGLES, A. 2016. Positron emission particle tracking (PEPT) for fluid flow measurements. *Nuclear Engineering and Design,* 302**,** 81-89.

LANGMUIR, I. 1917. The constitution and fundamental properties of solids and liquids. II. Liquids. *Journal of the American Chemical Society,* 39**,** 1848-1906.

LANGMUIR, I. 1918. The Adsorption of Gases on Plane Surface of Glass, Mica and Platinum. *Journal of the American Chemical Society,* 40**,** 1361-1402.

LANZILLOTTO, A.-M., LEU, T.-S., AMABILE, M., SAMTANEY, R., WILDES, R., LANZILLOTTO, A.-M., LEU, T.-S., AMABILE, M., SAMTANEY, R. & WILDES, R. A study of structure and motion in fluidic Microsystems. 28th Fluid Dynamics Conference, 1997. 1790.

LEE, K. T., INGRAM, A. & ROWSON, N. A. 2012. Twin screw wet granulation: the study of a continuous twin screw granulator using Positron Emission Particle Tracking (PEPT) technique. *European journal of pharmaceutics and biopharmaceutics,* 81**,** 666-673.

LEVINE, I. N. 2007. *Physical Chemistry (Sie)*, McGraw-Hill Education (India) Pvt Limited.

LI, S., GLYNNE-JONES, P., ANDRIOTIS, O. G., CHING, K. Y., JONNALAGADDA, U. S., OREFFO, R. O., HILL, M. & TARE, R. S. 2014. Application of an acoustofluidic perfusion bioreactor for cartilage tissue engineering. *Lab on a Chip,* 14**,** 4475-4485.

LIAO, Y.-C., SUBRAMANI, H. J., FRANSES, E. I. & BASARAN, O. A. 2004. Effects of soluble surfactants on the deformation and breakup of stretching liquid bridges. *Langmuir,* 20**,** 9926-9930.

LINDKEN, R., ROSSI, M., GROßE, S. & WESTERWEEL, J. 2009. Micro-particle image velocimetry (μPIV): recent developments, applications, and guidelines. *Lab on a Chip,* 9**,** 2551-2567.

LINDKEN, R., WESTERWEEL, J. & WIENEKE, B. 2006. Stereoscopic micro particle image velocimetry. *Experiments in Fluids,* 41**,** 161-171.

LISTER, J. R. & STONE, H. A. 1998. Capillary breakup of a viscous thread surrounded by another viscous fluid. *Physics of fluids,* 10**,** 2758-2764.

LIU, L. & BARIGOU, M. 2015. Lagrangian particle tracking in mechanically agitated polydisperse suspensions: Multi-component hydrodynamics and spatial distribution. *International Journal of Multiphase Flow,* 73**,** 80-89.

LIU, Y., LI, Y., HENSEL, A., BRANDNER, J. J., ZHANG, K., DU, X. & YANG, Y. 2020. A review on emulsification via microfluidic processes. *Frontiers of Chemical Science and Engineering,* 14**,** 350-364.
LUMENCOR 2020. *{SOLA SE Light Engine*

Instruction Manual}.
MAAS, H., GRUEN, A. & PAPANTONIOU, D. 1993. Particle tracking velocimetry in three-dimensional flows. *Experiments in fluids,* 15**,** 133-146.
MAJUMDER, M., RENDALL, C. S., EUKEL, J. A., WANG, J. Y., BEHABTU, N., PINT, C. L., LIU, T.-Y., ORBAEK, A. W., MIRRI, F. & NAM, J. 2012. Overcoming the "coffee-stain" effect by compositional Marangoni-flow-assisted drop-drying. *The Journal of Physical Chemistry B,* 116**,** 6536-6542.
MANZ, A., GRABER, N. & WIDMER, H. Á. 1990. Miniaturized total chemical analysis systems: a novel concept for chemical sensing. *Sensors and actuators B: Chemical,* 1**,** 244-248.
MARANGONI, C. 1865. *Sull'espansione delle goccie d'un liquido galleggianti sulla superfice di altro liquido*.
MARTINO, C., VIGOLO, D., SOLVAS, X. C. I., STAVRAKIS, S. & DEMELLO, A. J. 2016. Real-Time PEGDA-Based Microgel Generation and Encapsulation in Microdroplets. *Advanced Materials Technologies,* 1**,** 1600028.
MASHAGHI, S., ABBASPOURRAD, A., WEITZ, D. A. & VAN OIJEN, A. M. 2016. Droplet microfluidics: A tool for biology, chemistry and nanotechnology. *TrAC Trends in Analytical Chemistry,* 82**,** 118-125.
MCCABE, W., SMITH, J. & HARRIOTT, P. 2005. *Unit Operations of Chemical Engineering*, McGraw Hill.
MCCLEMENTS, D. J. 2016. *Food emulsions : principles, practices, and techniques*.
MCCLEMENTS, D. J. & LI, Y. 2010. Structured emulsion-based delivery systems: controlling the digestion and release of lipophilic food components. *Adv Colloid Interface Sci,* 159**,** 213-28.
MCDONALD, J. C., DUFFY, D. C., ANDERSON, J. R., CHIU, D. T., WU, H., SCHUELLER, O. J. & WHITESIDES, G. M. 2000. Fabrication of microfluidic systems in poly (dimethylsiloxane). *ELECTROPHORESIS: An International Journal,* 21**,** 27-40.
MCNAUGHT, A. D. & WILKINSON, A. 1997. Compendium of chemical terminology. IUPAC recommendations.
MENGER, F. M. 1979. The structure of micelles. *Accounts of Chemical Research,* 12**,** 111-117.
MERCK. 2020a. *{Becton Dickinson hypodermic syringes, polypropylene}* [Online]. Available: https://www.sigmaaldrich.com/catalog/product/aldrich/z192139?lang=en&region=GB [Accessed].
MERCK 2020b. {Decyltrimethylammonium bromide}.
MERCK 2020c. {Dodecyltrimethylammonium bromide}.
MERCK. 2020d. *{Glycerol}* [Online]. Available: https://www.sigmaaldrich.com/catalog/product/sial/g9012?lang=en&region=GB [Accessed].
MERCK. 2020e. *{Hexadecyltrimethylammonium bromide}* [Online]. Available: https://www.sigmaaldrich.com/catalog/product/sigma/h9151?lang=en&region=GB [Accessed].
MERCK 2020f. {Methyl violet}.
MERCK 2020g. {Micro particles based on polystyrene}.
MERCK 2020h. {Rhodamine B}.
MERCK. 2020i. *{Silicone oil viscosity 100 cSt (25 °C)}* [Online]. Available: https://www.sigmaaldrich.com/catalog/product/aldrich/378364?lang=en&region=GB [Accessed].
MICROCHEM 2019. {SU-8 2000 Permanet Epoxy Negative Photoresist.
MIHAILOVA, O., LIM, V., MCCARTHY, M. J., MCCARTHY, K. L. & BAKALIS, S. 2015. Laminar mixing in a SMX static mixer evaluated by positron emission particle tracking (PEPT) and magnetic resonance imaging (MRI). *Chemical Engineering Science,* 137**,** 1014-1023.

MILLER, R., NOSKOV, B. A., FAINERMAN, V. B. & PETKOV, J. T. 2008. Impact of micellar kinetics on dynamic interfacial properties of surfactant solutions. *Highlights in colloid science.* Wiley-VCH.
MIT. 2013. *PDMS / Glass Microfluidics* [Online]. MIT. Available: https://ocw.mit.edu/courses/electrical-engineering-and-computer-science/6-s079-nanomaker-spring-2013/labs/MIT6_S079S13_slides06.pdf [Accessed 20/02/2017].
MÖBIUS, D., MILLER, R. & FAINERMAN, V. B. 2001. *Surfactants: chemistry, interfacial properties, applications*, Elsevier.
MOORE, G. 1980. VLSI, what does the future hold. *Electron. Aust,* 42.
MOYER, M. W. 2011. Organs-on-a-chip for faster drug development. *Scientific American,* 25.
MUCIC, N., JAVADI, A., KOVALCHUK, N. M., AKSENENKO, E. V. & MILLER, R. 2011. Dynamics of interfacial layers—Experimental feasibilities of adsorption kinetics and dilational rheology. *Advances in Colloid and Interface Science,* 168**,** 167-178.
NEUMANN, A. 1979. Surface and Colloid Science, vol. II, ed. RJ Good and RR Stromberg. New York: Plenum Press.
NGUYEN, N. T. & WERELEY, S. T. 2006. Fundamentals and applications of microfluidics, Artech House. *Inc.: Boston, MA, USA*.
NIC, M., HOVORKA, L., JIRAT, J., KOSATA, B. & ZNAMENACEK, J. 2005. *IUPAC compendium of chemical terminology-the gold book*, International Union of Pure and Applied Chemistry.
NICUŞAN, A. & WINDOWS-YULE, C. 2020. Positron emission particle tracking using machine learning. *Review of Scientific Instruments,* 91**,** 013329.
NIKON 2020. {Inverted Microscope ECLIPSE Ti-U Ti-U/B Ti-S Ti-S/L100 Instructions}.
NISISAKO, T., TORII, T. & HIGUCHI, T. 2002. Droplet formation in a microchannel network. *Lab on a Chip,* 2**,** 24-26.
NORLAND PRODUCTS. 2019. *{Norland optical Adhesive 89}* [Online]. Available: https://www.norlandprod.com/adhesives/NOA%2089.html [Accessed].
NOWAK, E., XIE, Z., KOVALCHUK, N. M., MATAR, O. K. & SIMMONS, M. J. 2017. Bulk advection and interfacial flows in the binary coalescence of surfactant-laden and surfactant-free drops. *Soft Matter*.
OTTINO, J. M. 1990. Mixing, chaotic advection, and turbulence. *Annual Review of Fluid Mechanics,* 22**,** 207-254.
PALA ROSAS, I., CONTRERAS, J. L., SALMONES, J., TAPIA, C., ZEIFERT, B., NAVARRETE, J., VÁZQUEZ, T. & GARCÍA, D. C. 2017. Catalytic dehydration of glycerol to acrolein over a catalyst of Pd/LaY zeolite and comparison with the chemical equilibrium. *Catalysts,* 7**,** 73.
PAPAGEORGIOU, D. T. 1995. On the breakup of viscous liquid threads. *Physics of Fluids,* 7**,** 1529-1544.
PARKER, D., BROADBENT, C., FOWLES, P., HAWKESWORTH, M. & MCNEIL, P. 1993. Positron emission particle tracking-a technique for studying flow within engineering equipment. *Nuclear Instruments and Methods in Physics Research Section A: Accelerators, Spectrometers, Detectors and Associated Equipment,* 326**,** 592-607.
PASSERONE, A., LIGGIERI, L., RANDO, N., RAVERA, F. & RICCI, E. 1991. A new experimental method for the measurement of the interfacial tension between immiscible fluids at zero bond number. *Journal of colloid and interface science,* 146**,** 152-162.
PAYNE, B. 1950. OBSERVATIONS ON MICROSCOPE CONDENSERS, OBJECTIVES, AND EYEPIECES. *Journal of the Royal Microscopical Society,* 70**,** 317-341.
PEARSON, J. 1958. On convection cells induced by surface tension. *Journal of fluid mechanics,* 4**,** 489-500.
PERKINS, L. & GEANKOPLIS, C. 1969. Molecular diffusion in a ternary liquid system with the diffusing component dilute. *Chemical Engineering Science,* 24**,** 1035-1042.
PHOTRON. *{FASTCAM SA5}* [Online]. Available: https://photron.com/fastcam-sa-5/ [Accessed].

PIRBODAGHI, T., VIGOLO, D., AKBARI, S. & DEMELLO, A. 2015. Investigating the fluid dynamics of rapid processes within microfluidic devices using bright field microscopy. *Lab on a Chip*.
PLUCHON, D., HUBY, N., MORÉAC, A., PANIZZA, P. & BÊCHE, B. 2012. From Fabrication to Characterization of 3D Organic Microresonators: A Complementary Alliance of Microfluidics and Optics. *Advances in Optical Technologies,* 2012.
POLYNKIN, P., POLYNKIN, A., PEYGHAMBARIAN, N. & MANSURIPUR, M. 2005. Evanescent field-based optical fiber sensing device for measuring the refractive index of liquids in microfluidic channels. *Optics letters,* 30**,** 1273-1275.
PORTER, M. R. 2013. *Handbook of surfactants*, Springer.
RAJ M, K. & CHAKRABORTY, S. 2020. PDMS microfluidics: A mini review. *Journal of Applied Polymer Science,* 137**,** 48958.
RAMMENSEE, S., SLOTTA, U., SCHEIBEL, T. & BAUSCH, A. R. 2008. Assembly mechanism of recombinant spider silk proteins. *Proceedings of the National Academy of Sciences,* 105**,** 6590-6595.
REYNOLDS, O. 1883. XXIX. An experimental investigation of the circumstances which determine whether the motion of water shall be direct or sinuous, and of the law of resistance in parallel channels. *Philosophical Transactions of the Royal society of London***,** 935-982.
RICCOMI, M., ALBERINI, F., BRUNAZZI, E. & VIGOLO, D. 2018. Ghost Particle Velocimetry as an alternative to µPIV for micro/milli-fluidic devices. *Chemical Engineering Research and Design,* 133**,** 183-194.
ROCHÉ, M., AYTOUNA, M., BONN, D. & KELLAY, H. 2009. Effect of surface tension variations on the pinch-off behavior of small fluid drops in the presence of surfactants. *Physical review letters,* 103**,** 264501.
RODRÍGUEZ-HAKIM, M., BARAKAT, J. M., SHI, X., SHAQFEH, E. S. G. & FULLER, G. G. 2019. Evaporation-driven solutocapillary flow of thin liquid films over curved substrates. *Physical Review Fluids,* 4**,** 034002.
ROTEM, A., ABATE, A. R., UTADA, A. S., VAN STEIJN, V. & WEITZ, D. A. 2012. Drop formation in non-planar microfluidic devices. *Lab on a Chip,* 12**,** 4263-4268.
ROUMPEA, E., KOVALCHUK, N. M., CHINAUD, M., NOWAK, E., SIMMONS, M. J. & ANGELI, P. 2019. Experimental studies on droplet formation in a flow-focusing microchannel in the presence of surfactants. *Chemical Engineering Science,* 195**,** 507-518.
SAKAI, M., OHMORI, T. & FUJII, M. 2007. Two-color picosecond time-resolved infrared super-resolution microscopy. *Handai Nanophotonics,* 3**,** 189-195.
SAMANTA, S., LAYEK, R., KAR, S., RAJ, M. K., MUKHOPADHYAY, S. & CHAKRABORTY, S. 2017. Predicting Escherichia coli's chemotactic drift under exponential gradient. *Physical Review E,* 96**,** 032409.
SANTIAGO, J. G., WERELEY, S. T., MEINHART, C. D., BEEBE, D. & ADRIAN, R. J. 1998. A particle image velocimetry system for microfluidics. *Experiments in fluids,* 25**,** 316-319.
SCHINDELIN, J., ARGANDA-CARRERAS, I., FRISE, E., KAYNIG, V., LONGAIR, M., PIETZSCH, T., PREIBISCH, S., RUEDEN, C., SAALFELD, S. & SCHMID, B. 2012. Fiji: an open-source platform for biological-image analysis. *Nature methods,* 9**,** 676-682.
SCHOFIELD, Z., VIGOLO, D., BRILL, A., ALEXIADIS, A. & NASH, G. A Microfluidic Approach to Model Deep Vein Thrombosis. 71st Annual Meeting of the APS Division of Fluid Dynamics, 2018.
SCHRAMM, L. L. 2006. *Emulsions, foams, and suspensions: fundamentals and applications*, John Wiley & Sons.
SHAH, S. K., CHATTERJEE, S. K. & BHATTARAI, A. 2016. Effect of Methanol on Viscosity of Aqueous Solutions of Cationic Surfactants at 298.15 to 323.15 K. *Journal of Chemistry,* 2016.
SHELLEY, L. A., NATHALIE, B. & HOWARD, A. S. 2003. Formation of dispersions using “flow focusing” in microchannels. *Applied Physics Letters,* 82**,** 364-366.

SHINOHARA, K., SUGII, Y., AOTA, A., HIBARA, A., TOKESHI, M., KITAMORI, T. & OKAMOTO, K. 2004. High-speed micro-PIV measurements of transient flow in microfluidic devices. *Measurement science and Technology,* 15**,** 1965.
SI-MAT 2020. {Si-Mat}.
SIGMA-ALDRICH. 2017. *Silicone oil, viscosity 20 cSt* [Online]. [Accessed 20/02/2017].
SIGMA-ALDRICH. 2020. *{Silicone oil viscosity 5 cSt}* [Online]. Available: https://www.sigmaaldrich.com/catalog/product/aldrich/317667?lang=en&region=GB [Accessed].
SINTERFACE. *Maximum Bubble Pressure Tensiometer BPA1S* [Online]. Available: http://www.sinterface.com/products/measurement/tensiometry/maximum_bubble_pressure_tensiometer_bpa1s/index.html [Accessed].
SINTERFACE. 2020. *{Profile Analysis Tensiometer PAT1P}* [Online]. Available: http://www.sinterface.com/products/measurement/tensiometry/profile_analysis_tensiometer_pat1p/index.html#a77 [Accessed].
SON, Y., MARTYS, N. S., HAGEDORN, J. G. & MIGLER, K. B. 2003. Suppression of capillary instability of a polymeric thread via parallel plate confinement. *Macromolecules,* 36**,** 5825-5833.
SONG, H., CHEN, D. L. & ISMAGILOV, R. F. 2006. Reactions in droplets in microfluidic channels. *Angewandte chemie international edition,* 45**,** 7336-7356.
SPELT, J. 1996. *Applied Surface Thermodynamics*, CRC Press.
STEEGMANS, M. L., WARMERDAM, A., SCHROEN, K. G. & BOOM, R. M. 2009. Dynamic interfacial tension measurements with microfluidic Y-junctions. *Langmuir,* 25**,** 9751-9758.
STELLEMA, C., VLEK, J., MUDDE, R., DE GOEIJ, J. & VAN DEN BLEEK, C. 1998. Development of an improved positron emission particle tracking system. *Nuclear Instruments and Methods in Physics Research Section A: Accelerators, Spectrometers, Detectors and Associated Equipment,* 404**,** 334-348.
SZYSZKOWSKI, B. V. 1908. Experimental studies on capillary properties of aqueous solutions of fatty acids. *Z. Phys. Chem,* 64**,** 385-414.
TADROS, T. 2013. Steric Stabilization. *In:* TADROS, T. (ed.) *Encyclopedia of Colloid and Interface Science.* Berlin, Heidelberg: Springer Berlin Heidelberg.
TAKAMURA, K., FISCHER, H. & MORROW, N. R. 2012. Physical properties of aqueous glycerol solutions. *Journal of Petroleum Science and Engineering,* 98**,** 50-60.
TAN, Y.-C. & LEE, A. P. 2005. Microfluidic separation of satellite droplets as the basis of a monodispersed micron and submicron emulsification system. *Lab on a Chip,* 5**,** 1178-1183.
TATE, T. & LONDON, E. 1864. Dublin Philos. Mag. *J. Sci,* 27**,** 176.
TER-POGOSSIAN, M. M., PHELPS, M. E., HOFFMAN, E. J. & MULLANI, N. A. 1975. A positron-emission transaxial tomograph for nuclear imaging (PETT). *Radiology,* 114**,** 89-98.
THIELICKE, W. & STAMHUIS, E. J. 2014. PIVlab – Towards User-friendly, Affordable and Accurate Digital Particle Image Velocimetry in MATLAB. *Journal of Open Research Software* 2**,** e30.
THOMPSON, B. J. 1969. Introduction to Fourier Optics. Joseph W. Goodman. McGraw-Hill, New York, 1968. xiv+ 287 pp., illus. $13.50. McGraw-Hill Physical and Quantum Electronics Series. American Association for the Advancement of Science.
THOMSON, J. 1855. XLII. On certain curious motions observable at the surfaces of wine and other alcoholic liquors. *The London, Edinburgh, and Dublin Philosophical Magazine and Journal of Science,* 10**,** 330-333.
THULASIDAS, T., ABRAHAM, M. & CERRO, R. 1997. Flow patterns in liquid slugs during bubble-train flow inside capillaries. *Chemical Engineering Science,* 52**,** 2947-2962.
TJAHJADI, M., STONE, H. A. & OTTINO, J. M. 1992. Satellite and subsatellite formation in capillary breakup. *Journal of Fluid Mechanics,* 243**,** 297-317.
TOOFAN, M. & TOOFAN, J. 2015. A brief review of the cleaning process for electronic device fabrication. *Developments in Surface Contamination and Cleaning.* Elsevier.

UMBANHOWAR, P., PRASAD, V. & WEITZ, D. A. 2000. Monodisperse emulsion generation via drop break off in a coflowing stream. *Langmuir,* 16**,** 347-351.
UNIVERSITY OF BIRMINGHAM. 2020a. *{Positron Emission Particle Tracking (PEPT) overview}* [Online]. Available: https://www.birmingham.ac.uk/research/activity/physics/particle-nuclear/positron-imaging-centre/positron-emission-particle-tracking-pept/pept-overview.aspx [Accessed].
UNIVERSITY OF BIRMINGHAM. 2020b. *Radioactively Labelled Tracers* [Online]. Available: https://www.birmingham.ac.uk/research/activity/physics/particle-nuclear/positron-imaging-centre/positron-emission-particle-tracking-pept/radioactively-labelled-tracers.aspx [Accessed].
UNIVERSITY OF TORONTO. *Rayleigh-Bénard and Bénard-Marangoni convection* [Online]. Available: https://www8.physics.utoronto.ca/~nonlin/thermal.html [Accessed].
VAN DER GRAAF, S., NISISAKO, T., SCHROËN, C., VAN DER SMAN, R. & BOOM, R. 2006. Lattice Boltzmann simulations of droplet formation in a T-shaped microchannel. *Langmuir,* 22**,** 4144-4152.
VAN STEIJN, V., KREUTZER, M. T. & KLEIJN, C. R. 2007. μ-PIV study of the formation of segmented flow in microfluidic T-junctions. *Chemical Engineering Science,* 62**,** 7505-7514.
VIGOLO, D., RADL, S. & STONE, A. H. 2014. Unexpected Trapping of Particles at a T Junction. *PNAS*.
VINCENT, J. F., BOGATYREVA, O. A., BOGATYREV, N. R., BOWYER, A. & PAHL, A.-K. 2006. Biomimetics: its practice and theory. *Journal of the Royal Society Interface,* 3**,** 471-482.
VIS, M., OPDAM, J., VAN'T OOR, I. S., SOLIGNO, G., VAN ROIJ, R., TROMP, R. H. & ERNÉ, B. H. 2015. Water-in-water emulsions stabilized by nanoplates. *ACS Macro Letters,* 4**,** 965-968.
WALSTRA, P. 1991. Principles of emulsion formation. *Editors: J. Laven, HN Stein***,** 77.
WANG, Z., VOLINSKY, A. A. & GALLANT, N. D. 2014. Crosslinking effect on polydimethylsiloxane elastic modulus measured by custom-built compression instrument. *Journal of Applied Polymer Science,* 131.
WATSON, K. L. 1998. *Foundation science for engineers*.
WEHELIYE, W. H., DONG, T. & ANGELI, P. 2017. On the effect of surfactants on drop coalescence at liquid/liquid interfaces. *Chemical Engineering Science,* 161**,** 215-227.
WEIBEL, D. B. & WHITESIDES, G. M. 2006. Applications of microfluidics in chemical biology. *Current opinion in chemical biology,* 10**,** 584-591.
WIENEKE, B. 2017. *PIV uncertainty quantification and beyond.* Delft University of Technology.
WORLD PRECISION INSTRUMENTS. 2020. *{AL4000-220}* [Online]. Available: https://www.wpi-europe.com/products/pumps-and-microinjection/laboratory-syringe-pumps/al4000-220.aspx [Accessed].
WU, C.-Y., LIAO, W.-H. & TUNG, Y.-C. 2011. Integrated ionic liquid-based electrofluidic circuits for pressure sensing within polydimethylsiloxane microfluidic systems. *Lab on a Chip,* 11**,** 1740-1746.
XIA, Y. & WHITESIDES, G. M. 1998. Soft lithography. *Annual review of materials science,* 28**,** 153-184.
XU, J., DONG, P., ZHAO, H., TOSTADO, C. & LUO, G. 2012. The dynamic effects of surfactants on droplet formation in coaxial microfluidic devices. *Langmuir,* 28**,** 9250-9258.
XU, J., LI, S., LAN, W. & LUO, G. 2008. Microfluidic approach for rapid interfacial tension measurement. *Langmuir,* 24**,** 11287-11292.
XU, Q. & NAKAJIMA, M. 2004. The generation of highly monodisperse droplets through the breakup of hydrodynamically focused microthread in a microfluidic device. *Applied Physics Letters,* 85**,** 3726-3728.
YIANTSIOS, S. G., SERPETSI, S. K., DOUMENC, F. & GUERRIER, B. 2015. Surface deformation and film corrugation during drying of polymer solutions induced by Marangoni phenomena. *International Journal of Heat and Mass Transfer,* 89**,** 1083-1094.
ZEISS MICROSCOPY. *Condenser Light Cones and Numerical Aperture* [Online]. Available: http://zeiss-campus.magnet.fsu.edu/tutorials/basics/condenserlightcones/indexflash.html [Accessed].

ZHANG, H.-Q., SARICA, C. & PEREYRA, E. 2012. Review of high-viscosity oil multiphase pipe flow. *Energy & fuels,* 26**,** 3979-3985.
ZHENG, B., TICE, J. D., ROACH, L. S. & ISMAGILOV, R. F. 2004. A droplet-based, composite PDMS/glass capillary microfluidic system for evaluating protein crystallization conditions by microbatch and vapor-diffusion methods with on-chip X-ray diffraction. *Angewandte chemie international edition,* 43**,** 2508-2511.
ZHOU, J., ELLIS, A. V. & VOELCKER, N. H. 2010. Recent developments in PDMS surface modification for microfluidic devices. *Electrophoresis,* 31**,** 2-16.
ZHU, P., TANG, X., TIAN, Y. & WANG, L. 2016. Pinch-off of microfluidic droplets with oscillatory velocity of inner phase flow. *Scientific reports,* 6**,** 31436.
ZHU, P. & WANG, L. 2017. Passive and active droplet generation with microfluidics: a review. *Lab on a Chip,* 17**,** 34-75.
ZHU, P. & WANG, L. 2019. Droplet pinch-off with pressure fluctuations. *Chemical Engineering Science,* 196**,** 333-343.
ZILLER, M. & MILLER, R. 1986. On the solution of diffusion controlled adsorption kinetics by means of orthogonal collocation. *Colloid and polymer science,* 264**,** 611-615.